ELECTRICAL AND MAGNETIC PROPERTIES OF MAGNETIC ION SUBSTITUTED RELAXOR FERROELECTRIC CERAMICS

By
ADITYANARAYAN H. PANDEY
Enrolment No: PHYS03201204019

Raja Ramanna Centre for Advanced Technology,
Indore-452013, India

A thesis submitted to the
Board of Studies in Physical Sciences

In partial fulfillment of requirements
for the Degree of
DOCTOR OF PHILOSOPHY
of
HOMI BHABHA NATIONAL INSTITUTE

August, 2018

Homi Bhabha National Institute[1]

Recommendations of the Viva Voce Committee

As members of the Viva Voce Committee, we certify that we have read the dissertation prepared by **Adityanarayan H. Pandey** entitled **"Electrical and magnetic properties of magnetic ion substituted relaxor ferroelectric ceramics"** and recommend that it may be accepted as fulfilling the thesis requirement for the award of Degree of Doctor of Philosophy.

Chairperson – Dr. Rama Chari Ramachari **Date:** 3.12.18.

Guide/Convener & Member 1– Dr. S. M. Gupta **Date:** 03.12.18

External Member – Prof. A. K. Nigam **Date:** 03/12/18

Examiner – Prof. A. R. Kulkarni ARKulkarni **Date:** 03.12.18

Member 2- Dr. T. Ganguli **Date:** 03-12-2018

Member 3- Dr. T. K. Sharma **Date:** 03.12.18

Member 4- Dr. M. H. Modi **Date:** 3.12.18

Member 5- Dr. M. K. Chattopadhyay M K Chattopadhyay **Date:** 03/12/2018

Final approval and acceptance of this thesis is contingent upon the candidate's submission of the final copies of the thesis to HBNI.

I/We hereby certify that I/we have read this thesis prepared under my/our direction and recommend that it may be accepted as fulfilling the thesis requirement.

3/12/18

Date: 03/12/2018

Dr. S. M. Gupta

(Guide)

Place: RRCAT, Indore

---

[1] This page is to be included only for final submission after successful completion of viva voce.

STATEMENT BY AUTHOR

This dissertation has been submitted in partial fulfilment of requirements for an advanced degree at Homi Bhabha National Institute (HBNI) and is deposited in the Library to be made available to borrowers under rules of the HBNI.

Brief quotations from this dissertation are allowable without special permission, provided that accurate acknowledgement of the source is made. Requests for permission for extended quotation from or reproduction of this manuscript in whole or in part may be granted by the Competent Authority of HBNI when in his or her judgment the proposed use of the material is in the interests of scholarship. In all other instances, however, permission must be obtained from the author.

Adityanarayan H. Pandey

DECLARATION

I, hereby declare that the investigation presented in the thesis has been carried out by me. The work is original and has not been submitted earlier as a whole or in part for a degree / diploma at this or any other Institution / University.

Adityanarayan H. Pandey

List of Publications arising from thesis

Journal

1. “Investigation of structural, dielectric and ferroelectric properties of Gd-doped lead magnesium niobate ceramics”, **Adityanarayan H. Pandey,** Arvind K. Srivastava, Anil K. Sinha, Surya M. Gupta, *Materials Research Express***, 2015,** *2(9),* 096303.
2. “Raman spectroscopic investigation of Gd-substituted lead magnesium niobate ceramics $Pb_{1-x}Gd_x(Mg_{1+x/3}Nb_{2-x/3})O_3$ $(0 \leq x \leq 0.1)$”, **Adityanarayan H. Pandey,** Vasant G. Sathe, Surya M. Gupta, *Journal of Alloys and Compounds*, **2016**, *682*, 180-187.
3. “Critical slowing down of polar nano regions ensemble in Gd^{3+}-substituted $PbMg_{1/3}Nb_{2/3}O_3$ ceramics”, **Adityanarayan H. Pandey**, S. M. Gupta, N. P. Lalla, A. K. Nigam, *Journal of Applied Physics***,** **2017**, *122*, 044101.
4. “Bipolar electrocaloric effect in $Pb_{1-x}Gd_x(Mg_{1+x/3}Nb_{2-x/3})O_3$ ceramic: Relaxor with super-dipolar glass state”, **Adityanaraya H. Pandey** Surya Mohan Gupta, Anand Mohan Awasthi, *Scripta Materialia*, **2019,** *162*, 1-4.
5. “Effect of hot press sintering temperature on structural, microstructural, vibrational, dielectric, and ferroelectric properties of $PbMg_{1/3}Nb_{2/3}O_3$ ceramics”, **Adityanarayan H. Pandey**, S. M. Gupta, communicated to *Materilaia* **(arXiv:1810.01132).**
6. “Role of charge compensation mechanism on phase, dielectric and ferroelectric properties of aliovalent ion modified $PbMg_{1/3}Nb_{2/3}O_3$ ceramics”, **Adityanaraya H. Pandey**, Surya Mohan Gupta, communicated in *Journal of Solid State Chemistry* **(arXiv: 1811.07384).**
7. “Magnetic and magnetodielectric properties of relaxor Gd-substituted $PbMg_{1/3}Nb_{2/3}O_3$ ceramics”, **Adityanarayan H. Pandey**, S. M. Gupta, A. K. Nigam, to be communicated in *Journal Magnetism and Magnetic Materials*.

Book Chapter

1. “Investigation of re-entrant relaxor behaviour in lead cobalt niobate ceramic”, Adityanarayan H. Pandey, Surya Mohan Gupta, accepted for publication in *IntechOpen publisher* **(arXiv:1810.11513)**.

Conference

1. **“**Field induced polarization and magnetization behaviour of Gd-doped lead magnesium niobate ceramics”, **Adityanarayan H. Pandey**, Surya M. Gupta, Arun K. Nigam; DAE-Solid State Physics Symposium (**DAE-SSPS-2015**), 21-25th December, 2015, Amity University UP, Noida, Uttar Pradesh, India, **AIP Conference Proceedings.**
2. “Raman spectroscopic study of $Pb_{1-x}Gd_x(Mg_{1+x/3}Nb_{2-x/3})O_3$ ceramics”, **A. Pandey**, V Sathe, S M. Gupta; DAE-BRNS National Laser Symposium (NLS-24), 2-5th December, 2015, Madhya Pradesh, India.
3. “Field induced nano to macro domain ferroelectric transition in relaxor lead magnesium niobate ceramic”, **Adityanarayan H. Pandey** and S. M. Gupta, DAE- Solid State Physics Symposium (**DAE-SSPS-2017**), 26-30th December, 2017, BARC Mumbai, India, **AIP Conference Proceedings.**
4. “Observation of positive and negative magnetodielectric effects in relaxor $PbCo_{1/3}Nb_{2/3}O_3$ Ceramic”, **Adityanarayan H. Pandey**, Anand M. Awasthi, and Surya M. Gupta, Oral presentation in **IMF-2017 conference**, San Antonio, Texas, USA.
5. “Positive and negative electrocaloric effect in relaxor ceramic $Pb_{1-x}Gd_x(Mg_{1/3}Nb_{2/3})_{1-x/4}O_3$ ($x = 0.05$)”, **Adityanarayan H. Pandey**, G. Singh, R. Rawat, and S. M. Gupta, Materials and Technologies For Energy Conversion and Storage (**M-TECS-2018**), 26-29th September, 2018, BARC Mumbai, India.

Others

1. “Structural analysis of lead magnesium niobate using synchrotron powder X-ray diffraction and the Rietveld method”, Ashok Bhakar**, Adityanarayan H. Pandey**, M. N. Singh, Anuj Upadhyay, A. K. Sinha, S. M. Gupta, and Tapas Ganguli, *Acta. Cryst. B*, **2016**, *72*, 404-407.
2. “Empirical model studies on relaxor behaviour in $Bi_{2.5}La_{1.5}Ti_3O_{12}$ ceramic”, Rachna Selvamani, **Adityanarayan Pandey**, and S. M. Gupta, *AIP Conference Proceedings***,** **2016**, *1731,* 140047.
3. “Cluster glass like behavior of magnetoelectric $PbNi_{1/3}Nb_{2/3}O_3$ ceramics”, Preeti, **Adityanarayan Pandey**, Rachna Selvamani, Chander Shekhar, and S. M. Gupta, *AIP Conference Proceedings***,** **2017**, *1832,*140021**.**

4. “Effect of processing parameters on micro-structural properties of Lead Magnesium Niobates”, Ashok Bhakar, Adityanarayan H. Pandey, M. N. Singh, Anuj Upadhyay, A. K. Sinha, S. M. Gupta, Tapas Ganguli, and S. K. Rai, *Acta. Cryst. B,* **2017**, *73,* 1095-1104.
5. “Investigation of phase and dielectric properties of lead nickel tantalate ceramics”, Preeti, **Adityanarayan Pandey**, Rachna Selvamani, Chander Shekhar, and S. M. Gupta, *Ferroelectrics,* **2017,** *517*, 1-7.

Adityanarayan H. Pandey

DEDICATED TO MY TEACHERS

ACKNOWLEDGEMENTS

It is a great opportunity to express my gratitude to my Ph.D. guide Dr. S. M. Gupta, for giving all kinds of freedom in carrying out this research work and the successful completion of my thesis work. He has a cool temperament that certainly benefits a person working with him. He has a greatest professional influence on my development as a researcher.

I sincerely give special gratitude to Prof. A. K. Nigam for faithful discussions and suggestions during this thesis work. I am greatly indebted to him for his support, guidance and encouragement throughout the project work. Thanks are also due to Prof. A. K. Nigam for providing magnetic and magnetodielectric measurement facilities.

I am very grateful to Dr. P. A. Naik, Director RRCAT for his continual help during my stay at RRCAT for PhD training. I am extremely thankful to all members of Doctoral Committee for their constructive motivation and guidance. I sincerely thank our HBNI Ph.D. coordination committee members for their continuous care and help during the Ph. D. course and special thank to Dr S. B. Roy for useful discussions. I am very grateful to Dean-Academic and Dean of student affairs HBNI, RRCAT for continual help and necessary support during my Ph.D. course.

I would like to thank all members of LMS, and Indus, RRCAT, UGC-DAE consortium for scientific research, BARC and TIFR who supported directly or indirectly during my experiments. Above all, it would not have been possible for me to achieve this milestone in my research career without encouragement and support from my friends (PhD, MSc and others) and all family members who have dreamed and prayed for my all around success. I sincerely thank all the persons who have helped and supported me directly or indirectly in the course.

.

Contents

Contents……………………………………………………………………………i
Synopsis……………………………………………………………………………iv
List of Figures……………………………………………………………………….xv
List of Tables…………………………………………………………………….xxii
Chapter 1: Introduction 1
1.1 Introduction..1
1.2 Motivation and statement of the present work..5
1.3 Basic topics and literature survey 6
    1.3.1 Dielectrics...6
    1.3.2 Ferroelectrics 10
    1.3.3 Phase transitions 13
    1.3.4 Ferromagnetim 16
    1.3.5 Multiferroics 20
    1.3.6 Relaxor ferroelectrics 24
1.4 Organization of the thesis 29
Chapter 2: Experimental procedure 31
2.1 Introduction...31
2.2 Material synthesis and ceramic processing..32
2.3 Scanning Electron Microscopy (SEM) 34
2.4 Transmission Electron Microscopy (TEM) 36
2.5 X-ray diffraction (XRD) 39
2.6 Raman Spectroscopy...42
2.7 Dielectric spectroscopy..44
2.8 PE loop tracer..46
2.9 Magnetization (SQUID/VSM)..48
2.10 Differential scanning calorimetry (DSC)...50
Chapter 3: Microstructural, vibrational, dielectric and ferroelectric properties correlations in hot-pressed PMN ceramics...52
3.1 Introduction...52
3.2 HP sintered ceramic sample preparation...53
3.3 Results and Discussion 54
    3.3.1 SEM..54
    3.3.2 XRD..55

3.3.3 TEM 57

3.3.4 Raman Spectroscopy 60

3.3.5 Dielectric Spectroscopy 66

3.3.6 Impedance Spectroscopy 78

3.3.7 PE Hysteresis Loop 80

3.4 Conclusion 82

Chapter 4: Investigation of phase formation, microstructural, vibrational, dielectric and ferroelectric properties of Gd-substituted PMN ceramics 83

4.1 Role of charge compensation mechanism on phase, dielectric and ferroelectric properties of aliovalent ion substitution in PMN 83

4.1.1 Introduction 83

4.1.2 Results and discussion 84

4.1.2.1 Examination of phase formation using XRD, EDXS and SEM 84

4.1.2.2 Comparison of dielectric and ferroelectric properties 89

4.1.3 Conclusion 93

4.2 Critical slowing down dynamics of nano-polar dynamics in Gd-doped PMN $Pb_{1-x}Gd_x(Mg_{1+x/3}Nb_{2-x/3})O_3$ ($0 \leq x \leq 0.1$) ceramics 94

4.2.1 Introduction 94

4.2.2 Results and discussion 96

4.2.2.1 Phase formation and structure analysis 96

4.2.2.2 Microstructural examination 101

4.2.2.3 Raman spectroscopy 103

4.2.2.4 TEM 110

4.2.2.5 Dielectric properties 112

4.2.2.6 PE hysteresis loop 120

4.2.3 Conclusion 123

4.3 Electrocaloric behaviour of Gd-substituted PMN $Pb_{1-x}Gd_x(Mg_{1+x/3}Nb_{2-x/3})O_3$ ($0 \leq x \leq 0.1$) ceramics 124

4.3.1 Introduction 124

4.3.2 Electrocaloric behaviour 126

4.3.3 Conclusion 135

Chapter 5: Investigation of magnetic and magnetodielectric properties of Gd-substituted PMN ceramics and its comparison with PCN 136

5.1 Magnetic and magnetodielectric properties of relaxor $Pb_{1-x}Gd_x(Mg_{(1+x)/3}Nb_{(2-x)/3})O_3$ ceramics 136

5.1.1 Introduction 136
5.1.2 Results and discussion..........137
5.1.2.1 Magnetic properties..........137
5.1.2.2 Magnetodielectric studies..........142
5.1.3 Conclusion..........145
5.2 Magnetic and magnetodielectric properties of relaxor $PbCo_{1/3}Nb_{2/3}O_3$ ceramic..........146
5.2.1 Introduction 146
5.2.2 Results and discussion..........146
5.2.2.1 Microstructural and structural studies 146
5.2.2.2 XANES..........148
5.2.2.3 Dielectric spectroscopy 150
5.2.2.4 Polarization..........153
5.2.2.5 Magnetization..........154
5.2.2.6 Magnetodielectric effect..........156
5.2.3 Conclusion..........158
Chapter 6: Summary of novel conclusions and future work..........159
6.1 Summary of novel conclusions..........159
6.2 Future work..........162
References..........163

Synopsis

Relaxor ferroelectrics (RFEs) belong to a special class of ferroelectric materials, which have attracted incredible attention of scientific community for the last half century due to their extraordinary dielectric, piezoelectric, electromechanical, electro-caloric, and pyroelectric properties, which make it technological important materials for piezoelectric/electrostrictive actuators, sensors, and as electro-optic and photorefractive elements [1]. Since its discovery in 1954, lead-based mixed perovskite structures having general formula $Pb(B_1B_2)O_3$ (where $B_1 = Mg^{2+}$, Zn^{2+}, Ni^{2+}, Co^{2+}, In^{3+}, Sc^{3+}, Fe^{3+} etc. and $B_2 = Ti^{4+}$, Zr^{4+}, Nb^{5+}, Ta^{5+}, V^{5+}, Te^{6+}, W^{6+} etc.) are widely studied. Among these, lead magnesium niobate (PMN) is an important and extensively investigated relaxor ferroelectric because of its high frequency dependent diffuse dielectric constant (>20000 at 1 kHz), inability to sustain a remnant polarization until temperatures significantly below the dielectric constant maximum (ε'_m), hysteresis loss free polarization-electric field (*PE*) loop at room temperature. Although X-ray diffraction and neutron diffraction studies revealed average cubic structure having Pm3m crystal symmetry globally, while locally there is a coexistence of polar nano-domains (PNRs) with a rhombohedral R3m symmetry and chemical ordered regions (CORs) with Fm3m symmetry up to 5 K [2]. Therefore, it is believed that the statistical distribution of PNRs and CORs in paraelectric matrix is the origin of its unique ferroelectric properties. These PNRs are permanently correlated dipole moments (giant dipoles) composed of many unit cells, which appear at a temperature T_B ~ 600 K (Burns temperature), which is characterized by deviation form its linear dependence in volume, inverse susceptibility and refractive index [3]. These dynamic PNRs grow in number as well as in size on cooling, causing increase in dielectric constant, and formation of nano domains (elliptical shape with maximum ~ 10 nm size) but a ferroelectric state is not reached at all temperature up to 5 K [4]. Many local experimental tools like Neutron scattering, Raman scattering, Transmission electron microscope (TEM), etc. has been used to establish this phenomena. Along with the PNRs, there are chemically ordered regions (CORs) distributed randomly in the diordered matrix, as confirmed by the presence of superlattice reflection along <111> unit axis in the selected area electron diffraction pattern obtained from <110> reflections. These CORs are described by “Random Layer model” where the (111) planes are occupied by Nb^{5+} cations sequenced with the (111) planes occupied by mixture of Mg^{2+} and Nb^{5+} cations in a ratio of 2:1, causing doubling of unit cell size having Fm3m crystal structure [5]. The average size of the CORs in PMN is ~ 2-5 nm and remains unaffected in the studied temperature range of 5-800 K. These CORs are considered to be the source of quenched random field, which suppreses the growth of PNRs on cooling [6]. The CORs and PNRs are correlated and have been reported to be influenced by the application of an external electric field or chemical substitution with aliovalent ions at the A and B-sites. The size of the CORs in PMN can not be increased by thermal annealing [5]. A ferroelectric rhombohedral crystal structure has been reported below 200 K in poled PMN ceramic, which is associated to the presence of the long range order. On the other hand, the A-site modification of PMN with La results in an increase of size of the CORs and reduction in size of the PNRs, which leads to an increase in the relaxor like dielectric characteristics [7]. Similarly, B-site cation substitution with Ti or Zr in PMN has been reported to reduce the size of the CORs, which results in a growth of the PNRs from nano to micron size [8]. Correspondingly, relaxor like dielectric behavior is changed to normal ferroelectric. Recently, magnetic ion (transition metals or rare-earths) doping in ferroelectric ceramics is being investigated intensely in order to add new functionality namely magnetism to make it multiferroics. The multiferroics are single phase compounds or multiphase composites, which possesses simultaneously two or more primary ferroic orders viz. ferroelectric, ferromagnetic and ferroelastic [9]. At present, multiferroic materials are gaining lot of attention due to its technological importance and scientific challenges as magnetism and ferroelectricity are two independent phenomena. The trivalent rare earth cations substitution at Pb-site in PMN has been correlated with B-site cation ordering using XRD technique. No detailed investigation has been reported for aliovalent gadolinium ion (Gd^{3+}) substitution in PMN.

The nano scale heterogeneity is believed to be a fundamental part of relaxors, but the mechanisms of CORs appearance and incapability of the PNRs growth below the T_m in zero-field condition is still not clear. It is also not clear at what temperature the CORs develop in PMN and how the size of the CORs relate with the sintering temperature. The statistical distribution of the PNRs and CORs is believed to play critical role in exhibiting relaxor behaviour of PMN. The purpose of this study is to investigate origin of the CORs and how substitution of rare earth magnetic Gd-ion at Pb-site in PMN influence the size of CORs which is believed to control the relaxor ferroelectric properties. Furthermore, the magnetic properties of the Gd-substituted PMN is measured for its qualification to multiferroic type-I materials. This thesis work clearly reveals formation of the CORs as soon as perovskite phase is formed during calcination, fact which was not known till now. The size of the CORs seems to remain invariant to hot press sintering temperature but an increase in the average grain size from ~1.1 μm to 2.8 μm enhances the dielectric permittivity from 8800 to 25000 and saturation polarization from 9 to 30 $\mu C/cm^2$, which has been correlated with the core: shell thickness ratio calculated from the core-shell model. Investigations on Gd-substituted lead magnesium niobate ceramics, have been studied and structural, dielectric and ferroelectric properties are correlated with the size of CORs. Microstructural investigation using selected area electron diffraction (SAED) pattern along <110> unit axis has revealed enhancement in intensity of the superlattice reflection spots along ½<111> with increasing Gd-substitution, which reveals enhancement in size of the CORs and reduction in size of PNRs. Dielectric properties analysis reveals critical slowing down of PNRs ensemble resulting to a super-dipolar glass state in Gd-substituted PMN for $x \geq 0.05$. A large degree of diffuseness parameter "δ_A" > 90 for $x \geq 0.05$ is due to an additional disorder arising by the Gd-ions substitution at the Mg-site, which is also confirmed from phase analysis and elemental mapping. Sluggish response of the polar region is exhibited in the low temperature hysteresis P-E loop study of $x \geq 0.05$, suggesting reduction in the co-operative interaction within the PNRs leading to reduction in its size. Finally, an empirical parameter "K" calculated from the temperature dependent of ac-permittivity asserts the existence of super-dipolar glass state for $x \geq 0.05$. This thesis comprised of six chapters and contents of each chapter are outlined concisely in the following manner.

Chapter 1 begins with brief discussion of various topics related to this thesis work listed as, dielectric, ferroelectrics, relaxor ferroelectrics, multiferroics etc. followed by the literature survey on relaxor ferroelectrics and present understanding about the CORs. At the end, motivation behind the present thesis work and work carried out to achieve the goals is presented in concise form.

Chapter 2 describes the sample preparation method (part-1) and experimental techniques (part-2) employed in the present work. In the first part, synthesis and processing of ceramic powder is described in detail, where two step Columbite precursor method is adopted to synthesize ceramic powders with varying compositions and then the compacted powder is sintered at high temperature (~1200 ^{o}C) in closed environment to avoid lead oxide loss to obtain dense (> 95% of theoretical density) ceramics. In later part, various experimental techniques like, x-ray diffraction (XRD), scanning or transmission electron microscopy (SEM or TEM), Raman Spectroscopy, superconducting quantum interference device (SQUID), dielectric properties and ferroelectric properties are outlined and elaborated rigorously. The XRD is used to examine phase formation and crystal structure, SEM is used to image microstructure, TEM and Raman Spectroscopy tools are used to probe local structures. Further, dielectric spectroscopy and PE loop tracer are used to study electrical properties and SQUID is used to investigate the magnetic ordering.

In **Chapter 3**, origin and stability of chemical ordered regions (CORs) and its effect on the dielectric and ferroelectric properties in hot pressed (HP) PMN ceramics is presented. These HP sintered PMN ceramics are prepared by application of uniaxial pressure at various high temperatures (from 800 ^{o}C to 1200 ^{o}C) for 2 hrs time period. Vibrational, microstrcture, ferroelectric and dielectric properties investigation reveals non-stoichiometric chemical ordered regions (CORs) and relaxor like dielectric characteristics in lead magnesium niobate (PMN) ceramics uniaxially hot pressed (HP) at 800 ^{o}C to 1200 ^{o}C. Presence of the PNRs and the CORs in HP PMN ceramics is directly visualized using ⟨110⟩ zone selected area electron diffraction (SAED) pattern along with bright and dark field TEM imaging. Occurance of (½½½) superlattice reflections along <111> in <110> zone axis SAED pattern and the presence of bright nano-meter regions in corresponding dark-field images in 800 ^{o}C hot pressed PMN demonstrates formation of the CORs as soon as perovskite phase is formed during calcination, fact which was not known till now. Lattice constant is observed to be invarint with HP sintering temperature, whereas strain and grain size increases with increase in HP sintering temperature. Raman spectra is de-convoluted using the Pseudo-Voigt peak shape function and 14 de-convoluted peaks with varying FWHM, wave number and intensity are analyzed. Separation between two broad peaks of Nb-O-Nb stretching mode is found to increase from 76.7 to 86.2 cm^{-1} and the red-shift of O-B-O bending modes near 265 cm^{-1} suggest an increase in the polar nano-size regions. Further, Hysteresis loss free “s-shaped” loop with zero remnant polarization has been observed for all HP PMN ceramics at 300 K, whereas typical ferroelectric like P-E hysteresis loop is observed for all HP ceramics except HP800 at 180 K. Dielectric measurements are carried out to analyze the influence of HP sintering temperature on the relaxor dielectric behaviour of the HP-PMN ceramics. In dielectric studies it is found that dielectric constant maximum (ε_m) is increased from 8800 to 25000 and temperature of ε_m (T_m) is shifted from 278 K to 263 K with increasing average grain size from ~1.1 μm to 2.8 μm. Grain size dependence of the ε_m and shifting of the T_m towards lower temperature is correlated with core: shell thickness ratio calculated from the core-shell model. In addition, Relaxation behaviour is investigated using Cole-Cole dielectric relaxation model and frequency dispersion of the T_m is fitted to different interacting and non interacting PNRs models to reveal insight of the interaction among the PNRs.

In **Chapter 4**, structure, microstructure, vibrational, dielectric and ferroelectric properties of Gd-substituted PMN is discussed. This chapter is divided into three sections. Section 4.1 describes the role of charge compensation mechanism on phase, dielectric and ferroelectric properties of aliovalent ion Gd substitution in PMN. In general, aliovalent substitution at Pb-site can be compensated by creating A-site or B-site vacancies or changing the B-site cations ratio. This study clearly shows that Gd substitution in PMN by creating A-site vacancies to compensate charge imbalance leads to the formation of unwanted secondary pyrochlore phase, whereas, no remarkable differences are observed between samples with B-site vacancies or changing B-site cations ratio from the X-ray diffraction patterns, dielectric and ferroelectric hysteresis loops. In section 4.2, Gd-substituted PMN $Pb_{1-x}Gd_x(Mg_{1+x/3}Nb_{2-x/3})O_3$ ($0 \leq x \leq 0.1$) ceramics where charge imbalance is compensated by changing B-site cations ratio is comprehensively studied and compared with B-site vacancies samples. The segregation of second gadolinium niobate phase in Gd-substituted PMN for $x > 0.03$ is independent of the charge compensation mechanisms, which is in contrast to La-doped PMN study where precipitation of second phase was successfully controlled by changing B-site cation ratio [10]. Phase analysis and elemental mapping has revealed segregation of MgO for $x \geq 0.05$, which is due to Gd-substitution at Mg-site in PMN. Raman active stretching mode of Nb-O-Mg (A_{1g}, ~ 780 cm^{-1}) and Nb-O-Nb (~ 500-600 cm^{-1}) have been used as probe to determine the effect of Gd-ions on the size of chemical ordered regions (CORs) and polar nano-regions (PNRs) in PGMN ceramics. The red shift in A_{1g} as well as Nb-O-Nb stretching modes and the intensity ratio of A_{1g} and P_2 modes has been shown to increase with increasing Gd-concentration which is due to enhancement of CORs and reduction in PNRs size. Similarly, microstructural investigation using selected area electron diffraction (SAED) pattern along <110> unit axis has revealed enhancement in intensity of superlattice reflection spots along ½<111> with increasing Gd-substitution, which reveals enhancement in size of the CORs and reduction in size of PNRs. From dielectric study, an increase in the relaxor like dielectric characteristics is also found consistent with the proposed trend of CORs and PNRs sizes in Gd-substituted PMN ceramics. The fitting parameters obtained from the fitting of T_m (f) to the power law suggest critical slowing down of PNRs ensemble resulting in a super-dipolar glass state. The sluggish response of the polar region is exhibited in the hysteresis P-E loop, also suggests reduction in the correlation within the PNRs leading to reduction in its size. In section 4.3, another interesting feature of ferroelectrics i.e., electrocaloric (EC) effect of Gd-substituted PMN ceramics is evaluated by an “indirect method”. EC materials have tremendous potential for broad range of solid state cooling devices such as temperature regulations for sensors, electronic devices and medical equipments and on-chip cooling etc. The EC effect is examined by calculating the electrocaloric temperature change (ΔT_{EC}) from temperature dependent PE hysteresis loop using thermodynamic Maxwell equation. Temperature dependence of the PE hysteresis loop reveals an anomalous behaviour around glass transition temperature T_g, which is in the vicinity of a crossover from low temperature negative EC effect to high temperature positive EC effect. This anomaly has been addressed in this chapter by evoking critical slowing down dynamics of polar nano-domains against temperature.

Chapter 5 is divided into two sections. Section 5.1 describes the magnetic and magneto dielectric properties of Gd-substituted PMN ($0 \leq x \leq 0.1$, PGMN) ceramics in which the charge imbalance due to Gd-substitution at A-site is compensated by changing B-site cations ratio. The field induced magnetization (M-H) is observed to vary linearly at room temperature and non- linearly at 5 K for all the PGMN ceramic samples. The saturation magnetization at 5 K is found to increase linearly from ~1.0 to 11.5 emu/gm with increasing Gd-concentrations. The temperature dependence magnetization M(T) measured between 300 K - 5 K under the applied magnetic field of 100 Oe does not show any sign of saturation at low temperature but the temperature dependence of inverse susceptibility plot depicts deviation from its straight line dependence below ~120 K, implying development of local magnetic correlations. A frequency independent prominent peak is also noticed around 120 K in real and imaginary parts of ac-susceptibility measurement for Gd-doped PMN ceramics. The fitting of high temperature inverse susceptibility data using Curie-Weiss law for PGMN ceramics gives realistic value of the Curie constant and negative value of the Curie-Weiss temperature θ_p. The magnetodielectric effect ($\%MD = (\varepsilon'(9T)-\varepsilon'(0T))/\varepsilon'(0T)*100$) depicts positive and negative MD for all PGMN ceramics implying weak coupling between magnetic and dielectric properties. Such positive and negative MDs are also observed in disordered double perovskite ceramics where single MD peak is reported in B-site ordered phase [11]. Therefore, it is believed that disorder in distribution of magnetic ion in ferroelectric host is responsible for such positive and negative MDs. Section 5.2 describes synthesis and characterization of the PCN prepared for comparing the magnetic and magneto dielectric properties of the PGMN with lead cobalt niobate (PCN) in which B-site is occupied with magnetic Co^{3+} ion. The room temperature M-H curve of the PCN shows linear variation of magnetization with magnetic field, suggesting paramagnetic behavior of this sample at 300 K. However, a weak M-H hysteresis is observed near 5 K. The inverse susceptibility plot of

PCN also depicts deviation from straight line near ~130 K. The C-W fitting in high temperature region of PCN also yields negative value of θ_p, confirms predominant AFM interactions in the PCN sample. Therefore, susceptibility measurement and M-H curve strongly suggests development of interaction between the magnetic moments for both PGMN and PCN ceramics at low temperatures. The MD effect of the PCN depicts positive and negative values similar to the PGMN ceramics implying coupling between magnetic and dielectric properties.

In **Chapter 6**, presents the summary of the work done and conclusions drawn from the above described thesis work along with the future scope of this work. The main findings are given below:

- The chemically ordered regions (CORs) in PMN is believed to form as soon as perovskite phase is formed during calcination at 800 ^{o}C and remains unaffected with HP-sintering temperature. Grain size dependence on the ε_m and T_m suggests an important role of the core-region which overcomes effect of the shell-regions in micron or above sized grains. The ratio of core to shell region thickness is found to increase with increasing grain size.
- The charge imbalance due to aliovalent ion Gd^{3+} substitution at Pb^{2+} site with changing B-site cations ratio in Gd-PMN successfully control the formation of unwanted secondary pyrochlore phase. It was impossible to avoid the secondary pyrochlore phase when the charge imbalance is compensated by creating A-site vacancies. Segregation of the gadolinium niobate phase in Gd-substituted PMN (PGMN) for $x > 0.03$ is observed to an inherent part and unavoidable no matter what the charge compensation mechanisms is used.

- Detailed temperature dependent dielectric properties analysis in Gd-substituted PMN for $x \geq 0.05$ revealed the critical slowing down of dynamics of the PNRs ensemble to result in a super-dipolar glass state.
- Field induced magnetization and magnetodielectric effect studies suggested weak magnetodielectric coupling in Gd-doped PMN. These results are compared with the lead cobalt niobate (PCN) in which B-site is occupied with a magnetic ion and found consistent.

At the end, future work is suggested along with a possible way to achieve.

References

1. K. Uchino, S. Nomura, L. E. Cross, S. J. Jang, and R. E. Newnham, Appl. Phys., 51 (1980) 1142-1145; K. Uchino, Relaxor Ferroelecric Devices, Ferroelectrics, 151 (1994) 321-330.

2. A. A. Bokov, Z.-G. Ye, J. of Mat. Sci. 41, 31-52 (2006); A. A. Bokov and Z.-G. Ye, J. of Advanced Dielectrics 2(2), 1241010 (2012).

3. G. Burns and F. H. Dacol, Sol. Stat. Comm. 48, 853(1983).

4. D. Fu, H. Taniguchi, M. Itoh, S. Ya Koshihara, N. Yamamoto, and S. Mori, Phys. Rev. Lett. 103, 207601(2009).

5. P. K. Davies and M. A. Akbas, J. Phys. Chem. Solids 61, 159-166(2000); M. A. Akbas and P. K. Davies, J. Am. Ceram. Soc. 83(1), 119-123 (2000).

6. V. Westphal, W. Kleemann, and M. D. Glinchuk, Phys. Rev. Lett. 68, 847 (1992); A. K. Tagantsev and A. E. Glazounov, Phys. Rev. B 57, 18 (1998).

7. J. Chen, H. M. Chan, and M. P. Harmer, J. Am. Ceram. Soc. 72, 593-598 (1989); D. M. Fanning, I. K. Robinson, S. T. Jung, E. V. Colla, D. D. Viehland, and D. A. Payne, J. Appl. Phys. 87[2], 840 (2000).

8. H.Q. Fan, L.T. Zhanga, L.Y. Zhang, and X. Yao, Solid State Comm. 111, 541 (1999); G. Singh, V.S Tiwari, and V.K Wadhawan, Solid State Comm. 118[8], 407 (2001).

9. H. Schmid, Ferroelectrics 162, 317 (1994); N. A. Hill, J. Phys. Chem. B 104, 6694 (2000).

10. S. M. Gupta and D. Viehland, J. of Appl. Phys. 80, 5875 (1996).

11. L. Y. Wang, Q. Li, Y. Y. Gong, D. H. Wang, Qing Qi Cao, and Y. W. Du, J. Am. Ceram. Soc. 97[7], 2024–2026 (2014).

List of Figures

Fig. 1.1. (a) ABO_3 perovskite structure, (b) Model for relaxor where PNRs and CORs represent the polar nano region and chemically ordered region, respectively, dispersed in paraelectric matrix and (c,d) show two models of arrangement of COR (ref [11])..................2

Fig. 1.2. A physical picture showing temperature dependent evolution of PNRs and CORs in PMN (ref [11]). 4

Fig. 1.3. Schematic figures between dielectric constant vs frequency showing various polarization mechanisms. 10

Fig. 1.4. (a) PE hysteresis loop for ferroelectrics and (b) Temperature dependent of dielectric permittivity showing paraelectric to ferroelectric phase transition below Curie temperature, T_c. 12

Fig. 1.5. (a) Free energy (G) vs polarization (P) schematic plot for a second order phase transition, (b) Polarization and inverse susceptibility plot for a second order phase transition. 14

Fig. 1.6. (a) Free energy (G) vs polarization (P) schematic plot for a first order phase transition, (b) Polarization and inverse susceptibility plot for a first order phase transition...16

Fig. 1.7. (a) Typical *M-H* hysteresis loop for ferromagnetic materials, (b-e) Schematic picture of conversion of a multi-domain state into a single domain state under the application of magnetic field..17

Fig. 1.8. (a) Schematic 3d and 4s densities of states, $D(E)$, in first-row transition metals. The horizontal lines show the positions of the Fermi levels in Zn, Cu, Ni, Co, Fe, and Mn. (b) 3d and 4s up- and down-spin densities of states in first-row transition metals, with exchange interaction included [ref. (42)]. 19

Fig. 1.9. Multiferroic materials combine the properties of ferroelectrics and magnets [ref. (47)]..22

Fig. 1.10. Type I multiferroics where the origin of ferroelectricity is different (a) lone pair, (b) bond+site-centred charge ordering (c) geometric frustration mechanism [ref. (47)].........22

Fig. 1.11. Type II multiferroics (a) ferroelectricity is caused by a particular type of magnetic spiral, (b) ferroelectricity appears for collinear magnetic structures [ref. (47)]. 23

Fig. 1.12. Temperature dependent dielectric plot of canonical relaxors (e.g., PMN) showing different temperature regions. 25

Fig. 1.13. A conceptual picture of composition fluctuation model that believes the broad dielectric permittivity is result of the distribution in the Curie temperature of polar 'micro' regions of different sizes. 26

Fig. 2.1. Flowchart of synthesis of PMN ceramic using two step Columbite precursor method 32

Fig. 2.2. Schematic diagram of FE-SEM experimental set-up consists of several important parts including a vacuum system, an electron gun, magnetic lenses, various signal detectors, a sample stage and a control system [ref. 60)]. 35

Fig. 2.3. (a) Schematic diagram of TEM system consist of power supply, vacuum, lighting, imaging and recording systems (b) dark field imaging (c) and bright field imaging [ref. 61)]. 37

Fig. 2.4. Schematic diagram of XRD mechanism reflection of x-ray by lattice planes of a crystalline sample satisfying Bragg's condition. 40

Fig. 2.5. Schematic diagram of Raman Spectroscopy platform set-up consists of excitation source (laser), sample illumination and collection system, monochromator and detector. 43

Fig. 2.6. Schematic of dielectric cell designed for dielectric measurement in the temperature range of 100 to 450 K 45

Fig. 2.7. Schematic diagram of Sowyer-Tower circuit for the P-E loop measurement. 47

Fig. 2.8. (a) Schematic diagram of vibrating sample magnetometer (VSM), (b) basic principle of SQUID magnetometer 49

Fig. 2.9. Schematic diagram of DSC set up for heat capacity measurement 50

Fig. 3.1. Schematic diagram of HP sintering set-up 53

Fig. 3.2. FESEM micrograph of fractured surface of hot pressed PMN ceramics sintered at different temperatures a) HP800, b) HP900, c) HP1000, d) HP1100, and e) HP1200. 55

Fig. 3.3. Comparison of XRD patterns of Hot pressed PMN ceramics sintered at different temperatures from 800 ^{o}C to 1200 ^{o}C (HP800 to HP1200) and indexed using JCPDS 27-1199; secondary pyrochlore phase present in HP800 and HP900 are highlighted using '*'. Inset shows FWHM of (111) and (211) peak (after subtracting instrumental broadening) against HP-temperature. 56

Fig. 3.4. (a-i) Comparion of the bright field images (a-c), selected area electron diffraction along <110> unit axis (d-f) and dark field images (g-i) for HP800, HP900 and HP1200 ceramics. Presence of superlattice reflection along ½ <111> axis is shown by an arrow. 59

Fig. 3.5. (a) Comparison of room temperature Raman spectra of various HP PMN ceramics, (b,c) Deconvolution of Raman spectra of HP1200; plus, marks represent the raw data, solid

red line is the fitted data using Pseudo-Voigt peaks (green color) and the linear background line is given for clarity. 61

Fig. 3.6. (a-c) HP sintering temperature dependence of few frequency modes, and (d-f) HP sintering temperature dependence of FWHM of various modes for PMN ceramics.............. 63

Fig. 3.7. Real and imaginary parts of complex dielectric constant as function of temperature at selected frequencies of hot pressed PMN ceramics sintered at different temperatures, (a) HP800, (b) HP900, (c) HP1000, (d) HP1100, and (e) HP1200. 66

Fig. 3.8. Comparison of temperature dependence of (a) dielectric constant and (b) loss tangent at 1 kHz frequency; inset plots ε_m and T_m at 1 kHz frequency as a function of hot pressed sintering temperature 70

Fig. 3.9. (a) Normalized curve ($\varepsilon/\varepsilon_m$ vs T/T_m) of hot pressed PMN ceramics sintered from 800 ^{o}C to 1200 ^{o}C, (b) Representative fitting ($1/\varepsilon$ vs T) of HP1100 ceramic sample by Curie-Weiss Law, (c) Representative fitting ($1/\varepsilon$ vs T) of HP1100 ceramic sample by Eq. (3.2); inset of Fig. 3.8(c) shows δ_A variation of HP sintering temperature, (d) Comparison of the Vogel-Fulcher (red curve), and stretched exponential power law (green curve) and critical slowing down model (blue curve)for all HP PMN ceramics where open symbols represent the temperature of $\varepsilon_m(T_m)$ in the frequency range 0.1-100 kHz. 73

Fig. 3.10. (a,b) Frequency dependence of real (ε') and imaginary (ε'') parts of complex dielectric constant at selected temperatures between 240 K - 280 K for HP 900 PMN ceramic sample, where symbols represent the experimental data points and red solid lines are fitting to Eq. (3.10), (c-e) Variation of the Cole-Cole fitting parameter: (c) $\Delta\varepsilon$, (d) α, and (e) τ_o with temperature for HP PMN ceramics sintered from 800 ^{o}C to 1200 ^{o}C. 74

Fig. 3.11. (a) Impedance spectra of HP1100 measured at 700 K (black solid spheres) is fitted using equivalent circuit scheme using grain and grain boundary contributions, (b) Temperature evolution of impedance spectra of HP1100 measured at 650 K, 675 K, and 700 K fitted using equivalent circuit scheme, (c) Impedance spectra of different HP sintered ceramics measured at 700 K fitted using equivalent circuit scheme. 77

Fig. 3.12. (a-c) Comparison of PE hysteresis loop of HP sintered PMN ceramics (from 800 ^{o}C to 1200 ^{o}C) at $E = 15$ kV/cm and $f = 50$ Hz (a) $T = 300$, (b) $T = 220$ K, and (c) $T = 180$ K, (d-f) Comparison of temperature dependent parameters (d) P_{max}, (e) P_r, and (f) E_c of HP PMN ceramics. 81

Fig. 4.1. Comparison of XRD pattern of the PGMN4 powders sintered at 1200 ^{o}C, where the perovskite phase is indexed by JCPDS 27-1199 and few minor peaks pyrochlore phase are marked by "*"and GdNbO4 marked by "+" MgO is marked by an arrow; inset (a) shows the

(½ ½ ½) supperlattice reflection resulting from the doubling of unit cell (Fm3m crystal symmetry), inset (b) is enhanced view in 2θ ragne27^o - 33^o to depict the secondary phases, and inset (c) shows formation of % perovskite phase in PGMN4 ceramics in comparison to PMN. 86

Fig. 4.2. Comparison of scanning electron micrographs of the fractured surface of sintered ceramics (a) PMN, (b) PGMN-VA, (c) PGMN-VB, and (d) PGMN-R and the spherical grains (size < 1 μm) confirming the second phase are marked by arrow. 87

Fig. 4.3. SEM micrograph of the fractured surface of (a) PMN, (b) PGMN-VA, (c) PGMN4-VB, and (d) PGMN4 ceramic sample along with Pb, Gd, Mg, and Nb elemental mapping showing uniform distribution of these ions in the perovskite grains and presence of the $GdNbO_4$ and MgO phases. 88

Fig. 4.4. Temperature dependence of the dielectric constant and loss tangent variations at different frequencies in the 100 Hz to100 kHz range for (a) PMN, (b) PGMN-VA, (c) PGMN-VB, and (d) PGMN-R ceramics, respectively. 91

Fig. 4.5. (a) Comparison of temperature dependence of dielectric constant and loss tangent at 1 kHz frequency for PGMN4 ceramics, (b) Comparison of normalized plot $\varepsilon'/\varepsilon'_m$ vs T/T_m of PGMN4 ceramics; inset plots shows variation of diffuseness parameter, δ_A, calculated using Eq. (4.2). 92

Fig. 4.6. Comparison of PE-loop recorded at (a) 300 k and (b) 180 K when 20 kV/cm field applied at 50 Hz frequency for PGMN4 ceramics along with PMN. 93

Fig. 4.7. Comparison of the XRD patterns of $Mg_{(1+x)/3}Nb_{(2-x)/3}O_{4-x/2}$, compositions $x = 0.01$ to 0.1 (MN1 to MN10) calcined at 1200 ^{o}C revealing coexistence of orthorhombic (Pbcn space group) $MgNb_2O_6$ and hexagonal (P-3c1 space group) $Mg_4Nb_2O_9$ phases, where $Mg_4Nb_2O_9$ phase is marked by "*;" Inset of figure depicts $Mg_4Nb_2O_9$ phase variation with increasing Mg^{2+}/Nb^{5+} cations ratio. 97

Fig. 4.8. Comparison of XRD pattern of the PGMN10 powder calcined at different temperatures between 800 and 1200 ^{o}C (designated as CP800 to CP1200), where the perovskite phase is indexed by JCPDS 27-1199 and few minor peaks pyrochlore phase are marked by "*" un-reacted Gd_2O_3 aremarked by "#" and $GdNbO_4$ marked by "+", MgO is marked by an arrow. 98

Fig. 4.9. Comparison of room temperature XRD pattern of ceramics $Pb_{1-x}Gd_xMg_{(1+x)/3}Nb_{(2-x)/3}O_3$, for $0.01 \leq x \leq 0.1$, (designated as PGMN1 to PGMN10) sintered at 1200 ^{o}C for 2 h; where secondary phase $GdNbO_4$ marked by "+" and MgO is marked by an arrow. 99

Fig. 4.10. Rietveld fitted XRD pattern of sintered $Pb_{1-x}Gd_xMg_{(1+x)/3}Nb_{(2-x)/3}O_3$, for $0 \leq x \leq 0.1$ ceramics, where open black circles represent the raw data, the solid red line is the fitted data using space group Pm3m for perovskite PMN and space group I2/c for $GdNbO_4$ along with the difference between the observed and calculated intensity. 101

Fig. 4.11. (a-e) Comparison of scanning electron micrographs of the fractured surface of sintered $Pb_{1-x}Gd_xMg_{(1+x)/3}Nb_{(2-x)/3}O3$, for x = 0.01, 0.03, 0.05, 0.08, and 0.1 ceramics, respectively; (f) energy dispersive spectra taken from the spherical grains confirming the $GdNbO_4$ phase. 102

Fig. 4.12. (a) SEM micrograph of the fractured surface of PGMN5 ceramic sample along with (b) Pb, (c) Gd, (d) Mg, and (e) Nb elemental mapping showing uniform distribution of these ions in the perovskite grains and presence of the $GdNbO_4$ and MgO phases. 103

Fig. 4.13. Raman spectra of pure PMN and Gd^{3+}-substituted PMN $Pb_{1-x}Gd_x(Mg_{1+x/3}Nb_{2-x/3})O_3$ (for $0 \leq x \leq 0.1$) ceramics 104

Fig. 4.14. (a,b) Deconvolution of Raman spectra of PGMN5 ceramic sample, where open circle represent the raw data, solid red line is the fitted data using Pseudo-Voigt peaks (green colour) and the linear background line is given for clarity. The composition (for $0 \leq x \leq 0.1$) evolutions of (c) bending mode of O-B-O near 260 cm^{-1}, (d) stretching mode of Pb-O bond near 150 cm^{-1}, (e) peak position around 490 cm^{-1} (P_1) and 580 cm^{-1} (P_2), (f) peak position difference of P_1 and P_2 and (g) variation of A_{1g} mode (~780 cm^{-1}) 106

Fig. 4.15. Comparison of the bright field images (a)–(c), selected area electron diffraction along <110> unit axis (d)-(f) and dark field images (g)-(i) for PMN, PGMN5, and PGMN10 ceramics. The presence of superlattice reflection along ½<111> axis is shown by an arrow. 111

Fig. 4.16. (a)-(f) Temperature dependence of the dielectric constant [$\varepsilon'(T)$] and loss tangent [tan $\delta(T)$] behavior at different frequencies in the 0.1-100 kHz range for $Pb_{1-x}Gd_xMg_{(1+x)/3}Nb_{(2-x)/3}O_3$, for x = 0, 0.01, 0.03, 0.05, 0.08, and 0.1 ceramics, respectively. ... 114

Fig. 4.17. Comparison of the $\varepsilon'(T)/\varepsilon'_m(T)$ versus T/T_m curves at 1 kHz frequency for different "x". Inset of figure depicts the variation of temperature of dielectric maxima (T_m at 1 kHz) with "x". 116

Fig. 4.18. Temperature dependence of $1/\varepsilon'(T)$ and $\varepsilon'(T)$ along with its fitting to Eq. (4.2) for x = 0.1, Inset of figure shows variation δ_A fitting parameter calculated by fitting temperature dependent dielectric constant (f = 1 kHz) with Eq. (4.2) against "x". 117

Fig. 4.19. (a) Comparison of the Vogel-Fulcher (green curve) and critical slowing down dynamics (red curve) fitting of PMN and PGMN10 ceramics, (b) All PGMN ceramics fitted

by critical slowing down dynamics with bounding *zv* high value to ~14, where open symbols represent the temperature of ε_m (T_m) in the frequency range of 0.1–100 kHz and the red solid line is fitting to Eq. (4.8). 119

Fig. 4.20. Comparison of PE-loop recorded at (a) 300 K and (b) 170 K when15 kV/cm field applied at 50 Hz frequency for PMN to PGMN10 ceramics. (c) Comparison of the effect of Gd-concentration on the (c) P_{max} and (d) P_r and P_{max} against ac-drive amplitude applied at 50 Hz at 300 K and 170 K, respectively. 122

Fig. 4.21. Temperature dependent *ε'* and tan *δ* of $Pb_{1-x}Gd_xMg_{1+x/3}Nb_{2-x/3}O_3$ ceramic of *x* = 0.1 at different frequency. Inset of the figure shows fitting of all PGMN ceramics to the Eq. 1. 127

Fig. 4.22. Temperature dependent *P-E* hysteresis loop of $Pb_{1-x}Gd_xMg_{1+x/3}Nb_{2-x/3}O_3$ ceramics recorded at 50 Hz; **(a)** *x* =0, **(b)** *x* = 0.01, **(c)** *x* = 0.05, and **(d)** *x* = 0.1. 129

Fig. 4.23. Temperature dependent polarization behaviour of $Pb_{1-x}Gd_xMg_{1+x/3}Nb_{2-x/3}O_3$ ceramics at different electric fields; **(a)** *x* = 0, **(b)** *x* = 0.01, **(c)** *x* = 0.05, and **(d)** *x* = 0.1. 130

Fig. 4.24. Heat capacity (C_p) as a function of temperature for $Pb_{1-x}Gd_xMg_{1+x/3}Nb_{2-x/3}O_3$ ($0 \le x \le 0.1$) ceramics measured using differential scanning calorimetry (DSC). 131

Fig. 4.25. Electrocaloric temperature change (ΔT_{EC}) as a function of temperature at different applied electric field for $Pb_{1-x}Gd_xMg_{1+x/3}Nb_{2-x/3}O_3$ ceramics **(a)** *x* = 0, **(b)** *x* = 0.01, **(c)** *x* = 0.05, and **(d)** *x* = 0.1, **(e)** comparison of ΔT_{EC} as a function of temperature for different compositions ($0 \le x \le 0.1$) at ***E*** = 15 kV/cm. 132

Fig. 5.1. (a) Temperature dependence of susceptibility plot $Pb_{1-x}Gd_x(Mg_{1/3}Nb_{2/3})_{1-x/4}O_3$ for *x* = 0.01 to 0.1 fitted by the Curie-Weiss law; inset shows ZFC-FC magnetization plot for *x* = 0.02 sample, (b) Temperature dependence of inverse susceptibility plot $Pb_{1-x}Gd_x(Mg_{1/3}Nb_{2/3})_{1-x/4}O_3$ for *x* = 0.01 to 0.1 showing deviation from linear dependence. 137

Fig. 5.2. *M-H* curve of Gd-substituted PMN ceramics [$Pb_{1-x}Gd_x(Mg_{1/3}Nb_{2/3})_{1-x/4}O_3$ for *x* = 0.01 to 0.1] at a) T = 300 K, b) T = 5 K; upper inset shows normalized M/M_o vs μ_oH/T plot of Gd-PMN ceramics fitted by Brillouin function and lower inset depicts the enlarge view of *M-H* hysteresis plot of 1Gd-PMN and 10Gd-PMN ceramics. 138

Fig. 5.3. Temperature dependence of (a) real (*χ*') and (b) imaginary (*χ*'') parts of ac magnetic susceptibility at H = 10 Oe field and at different frequencies; upper inset shows enlarged view of *χ*' around the peaks and lower inset depicts the second derivative plot of *χ*' for 5Gd-PMN ceramic sample. 140

Fig. 5.4. (a) Temperature dependence of real (*ε*') permittivity of 10Gd-PMN ceramic sample at H = 9 T magnetic field at different frequencies from 10 Hz - 200 kHz; inset shows cluster glass model fitted to ln f vs T_m plot, Temperature dependence of *ε*', (b) below 250 K and (c) above 250 K at H = 0 T and H = 9 T field of "x" = 0.1 (10Gd-PMN) ceramic sample at 1 kHz. 141

Fig. 5.5. Temperature dependence of (a) magneto-dielectric (%*MD*), and (b) magneto-loss (%*ML*) behaviour of "x" = 0.1 at different frequencies from 100 Hz to 100 kHz. 143

Fig. 5.6. a) Magnetic field dependence of real (*ε*') and imaginary (*ε*") parts of complex permittivity at T = 40 K and 1 kHz frequency, b) Time dependence of *ε*' and *ε*" in variation of magnetic field; inset depicts aging of 10Gd-PMN ceramic sample at 40 K. 144

Fig. 5.7. Room temperature (a) XRD, (b) Raman spectra, (c) SEM micrograph and (d) SAED pattern along <110> pattern of PCN ceramic sample 147

Fig. 5.8. Room temperature (a) Co K-edge and (b) Nb K-edge XANES spectra of PCN ceramic along with their respective standard samples 149

Fig. 5.9. Temperature dependence of (a) real part (*ε*'), (b) imaginary part (*ε*"), (c) loss tangent (tan δ) of complex permittivity, (d) Curie-Weiss and Modified Curie-Weiss fit to 1/*ε*' vs T plot, (e) temperature dependence of relaxation frequency fitted using cluster glass model in region I and II for PCN ceramic sample, and (f) temperature dependence of ac-conductivity of PCN at 100 Hz is fitted by Arrhenius law. 151

Fig. 5.10. *P-E* hysteresis of PCN ceramic sample at different temperatures, (a) 275 K, (b) 180 K and (c) 80 K, (d) Temperature dependence of P_{max}, P_r and E_c of PCN ceramic sample for E = 10 kV/cm applied electric field. 153

Fig. 5.11. (a) Temperature dependent susceptibility and inverse susceptibility plot of PCN ceramic where high temperature linear region above ~150 K is fitted using Curie-Weiss law, (b) Field dependent magnetization at 300 K and 5 K 155

Fig. 5.12. a) Temperature dependence of real (*ε*') and imaginary (*ε*") parts of complex dielectric permittivity of PCN ceramic sample at H = 0 T and H = 9 T magnetic field at 10 kHz frequency, b) Temperature dependence of magnetodielectric (%MD) and magnetoloss (%ML) of PCN at 10 kHz. 156

Fig. 5.13. (a) Comparison of magnetodielectric effect, and (b) magnetization of 10Gd-PMN and PCN ceramic samples 157

List of Tables

Table 3.1. Variation of the lattice parameter, % pyrochlore phase, density, grain size, dielectric properties, and field induced polarization of hot pressed PMN ceramics. 54

Table 3.2. Parameters of the Curie-Weiss law, Quadratic law (Eq. 2) and Variation of ΔT_m (=$T_{m100\text{kHz}}$ -$T_{m100\text{Hz}}$), $\Delta\varepsilon_m$ (= $\varepsilon_{m100\text{Hz}}$ –$\varepsilon_{m100\text{kHz}}$) and Mydosh parameter "*K*" (=ΔT_m / (T_m x Δlog (*f*))) for various HP sintered PMN ceramics. 58

Table 3.3. Corrected dielectric constant, grain and grain boundary thicknesses calculated using series and logarithmic mixing rules for HP PMN ceramics. 68

Table 3.4. Parameters of the (a) Vogel-Fulcher [Eq. (3.7)] and (b) power law [Eq. (3.8)], and (c) critical slowing down model [Eq. (3.9)] fit of frequency dependent T_m for various HP sintered PMN ceramics. 75

Table 3.5. (a) Grain and grain boundary resistance (R_g (Ω) and R_{gb} (Ω)), (b) Grain and grain boundary capacitance (C_g (f) and C_{gb} (f)) of HP-PMN ceramics obtained from equivalent circuit fitting. 78

Table 4.1. Variation of the lattice parameter, % perovskite phase, grain size, dielectric properties, and field induced polarization of PGMN ceramics. 84

Table 4.2. Phase analysis of $Pb_{1-x}Gd_xMg_{(1+x)/3}Nb_{(2-x)/3}O_3$, for $0.00 \leq x \leq 0.1$, (designated as PMN to PGMN10) calcined and sintered powders at 800 °C and 1200 °C, respectively. 95

Table 4.3. Variation of the lattice parameter, grain size, dielectric properties and field induced polarization of $Pb_{1-x}Gd_xMg_{(1+x)/3}Nb_{(2-x)/3}O_3$, for $0.00 \leq x \leq 0.1$ ceramics. 100

Table 4.4. Parameters of the Vogel-Fulcher (Eq. 5), strecthed exponential power law (Eq. 6) and Cluster glass model (Eq. 7) fit of frequency dependent T_m and a parameter $t^* = (T_f - T_o)/T_f$ calculated by replacing $T_f(\omega)$ by $T_m(\omega)$ and Vogel-Fulcher temperature (T_o). 109

Table 5.1. Variation of the parameters, temperature independent magnetic susceptibility (χ_o), curie constant (*C*), paramagnetic Curie temperature (θ_p) and μ_{eff} of $Pb_{1-x}Gd_x(Mg_{1/3}Nb_{2/3})_{1-x/4}O_3$, for $0.01 \leq x \leq 0.1$ ceramics. 139

Table 5.2. Structure parameters obtained after Rietveld refinement of lead cobalt niobate ceramic sample for Pm3m crystal symmetry 148

Table 5.3. Model fitting to dielectric data of PCN ceramic sample in various regions 151

Chapter 1
Introduction

1.1 Introduction

The study of condensed matter physics is effectively divided into investigations of ordered (heterostructures, crystals) and disordered (liquids, amorphous materials) systems. Remarkably, relaxor ferroelectrics stretch these classifications and derive their outstanding dielectric, electromechanical, electro-caloric, and pyroelectric properties from this combination of features [1,2]. The term '*relaxor*' refers to its dielectric maximum over a broad temperature range, rather than a sharp Curie–Weiss divergence, and its frequency dependent dielectric response. Out of RFEs family, Pb-based mixed perovskite structure having general formula $Pb(B_1B_2)O_3$ (where $B_1 = Mg^{2+}$, Zn^{2+}, Ni^{2+}, Co^{2+}, In^{3+}, Sc^{3+}, Fe^{3+} etc. and $B_2 = Ti^{4+}$, Zr^{4+}, Nb^{5+}, Ta^{5+}, V^{5+}, Te^{6+}, W^{6+} etc.) are widely studied. Lead magnesium niobate (PMN) is the first relaxor ferroelectric discovered in the late 1950s, has received special recognition due to their extraordinary properties viz., high dielectric constant (~20,000) over a wide temperature range near room temperature, inability to sustain a remnant polarization until temperatures significantly below the dielectric constant maximum (ε'_m), hysteresis loss free polarization-electric field (*P-E*) loop at room temperature [3]. PMN has the ABO_3 cubic perovskite structure with a mixed B-site. X-ray and neutron diffraction studies confirm the cubic symmetry of PMN with space group Pm3m down to 5 K [4]. However, at present widely accepted picture of PMN is unveiled by local probes (e.g., diffused neutron scattering, TEM and Raman spectroscopy etc.); where coexistence of chemical ordered regions (CORs) with a Fm3m symmetry and polar nano regions (PNRs) with a rhombohedral R3m symmetry is observed in paraelectric matrix with a cubic Pm3m symmetry as shown in Fig. 1.1 [5-7]. It is believed that the presence of PNRs is responsible for the high dielectric and piezoelectric properties of relaxors. These PNRs are permanently correlated dipole moments (giant dipoles) composed of many unit cells, which appear at a temperature T_B ~ 600 K (Burns temperature), which is characterized by deviation from its linear temperature dependence in volume, inverse susceptibility and refractive index [8]. Microstructural evolution with temperature has revealed an increase in number and size of the PNRs on cooling below the T_B and these PNRs are reported to become static around $T^* \simeq$ 400 K [9-11]. Finally PNRs collapse around the CORs into elliptical shape with maximum size of ~10-20 nm near ~220 K, as measured by TEM and diffused neutron scattering (Fig. 1.2) [10,11]. The interaction/coupling between the PNRs is not sufficiently strong in order to get long range ordering.

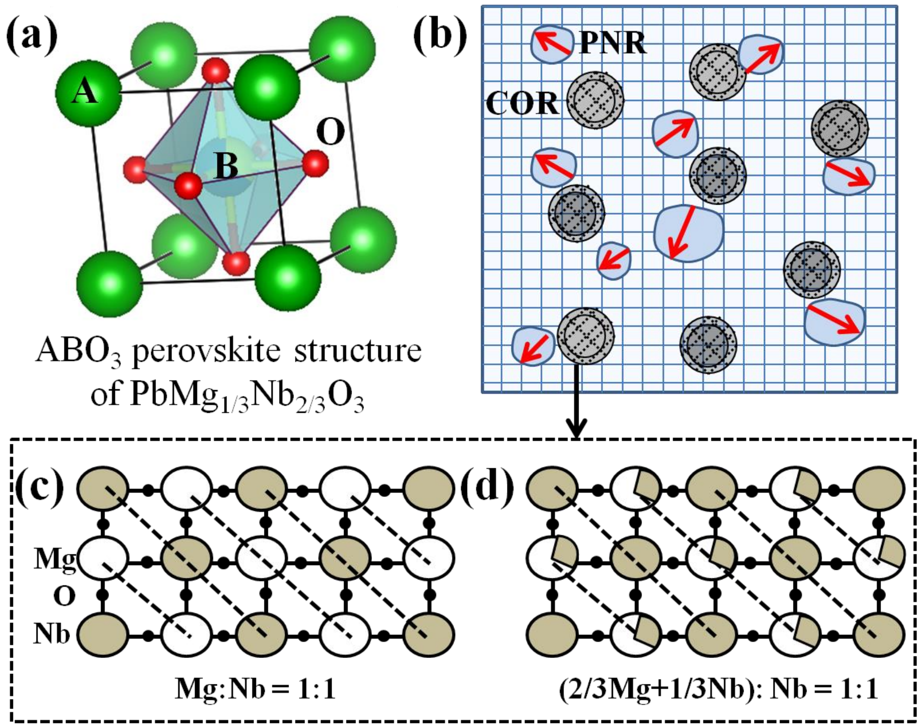

Fig. 1.1. (a) ABO_3 perovskite structure, (b) Model for relaxor where PNRs and CORs represent the polar nano region and chemically ordered region, respectively, dispersed in paraelectric matrix and (c,d) show two models of arrangement of COR (ref [11])

There has been a growing interest in understanding the CORs that occurs due to ordering of B-site cations. Initially two models proposed to describe the CORs [12] (Fig.

1(c,d)): (i) “space charge model” where Mg and Nb occupy (111) adjacent plane in such a way that Nb-deficient negatively charged region is surrounded by Nb-rich positively charged disordered non-stoichiometric matrix, and (ii) “random-site model” where every other (111) plane of B-site sublattices is occupied by Nb cations and the rest of the planes of the B-site sublattices are occupied randomly by Mg and Nb in a ratio of 2:1. High-resolution Z-contrast image investigations have strongly supported the random-site model to describe the chemical ordering [13]. However, this model does not explain why the ordered regions do not grow with thermal annealing. Disability to grow the ordered region with heat treatment favours the space charge model in which the local charge imbalance created by the short range CORs is compensated by the opposite charged disordered regions. But, in contrary to the earlier discussed two models of a binary distribution of CORs within a disordered matrix, using a combination of aberration-corrected scanning transmission electron microscopy experiment and simulations, Cabral *et al.* has recently shown that the degree of ordering smoothly varies within a COR and approaches a minimum at anti-phase boundaries [14]. They also suggested that this new model provides a starting point to connect relaxor behavior with the interplay of local chemistry and structure. Experimentally it is shown that number and size (~ 2-5 nm) of the CORs remains unchanged in temperature range of 15-800 K and also has no influence of thermal annealing [15]. The CORs are believed to be the source of quenched random field which is believed to be responsible for suppressing growth of the PNRs [16]. It is believed that the statistical distributions of the PNRs and CORs are responsible for typical relaxor behaviour of PMN.

The CORs and PNRs are correlated and have been reported to be influenced by the application of an external electric field or chemical substitution with aliovalent ions at A and B-sites [17-25]. A ferroelectric rhombohedral structure has been reported below 200 K in poled PMN ceramic, which is associated to the presence of the long range order [17,18]. The

A-site modification of PMN with La results in an increase of size of the CORs and reduction in size of the PNRs, which leads to an increase in the relaxor like dielectric characteristics [19-22]. Similarly, B-site cation substitution with Ti or Zr in PMN has been reported to reduce the size of the CORs, which results in a growth of the PNRs from nano to micron size [22,25]. Correspondingly, relaxor like dielectric behavior is changed to normal ferroelectric one.

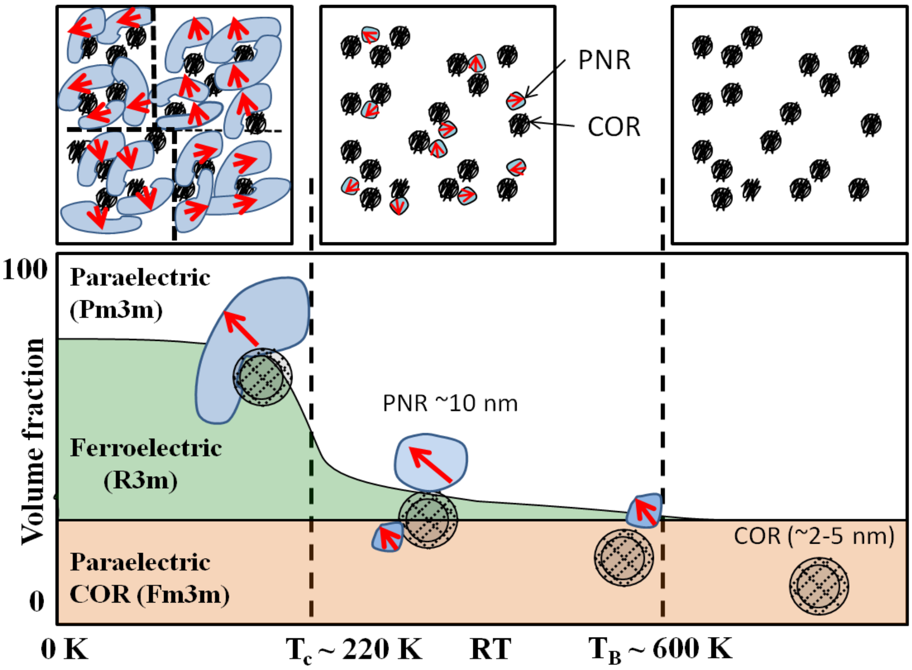

Fig. 1.2. A physical picture showing temperature dependent evolution of PNRs and CORs in PMN (ref [11]).

Relaxor like dielectric characteristics are recently reported for lead-free and homo-valent $Ba(Zr_x,Ti_{1-x})O_3$ system. Difference in polarizability between the Ti and Zr ions has been found essential for the formation of small embedded polar nanoregions [26]. However, in PMN, the random electric fields arising from the mixed B sub-lattice ions, the strong short-range interactions between lead-centered electrical dipoles, and the competition between ferroelectric and anti-ferroelectric interactions, has been proposed to result in a complex nano-domain structure [26]. The nanoscopic heterogeneity seems to be an inherent part of relaxors, but the mechanisms of how PNRs appear and evolve upon cooling are currently pursued worldwide.

1.2 Motivation and statement of the present work

Presently, researchers have emphasized the importance of multiple inhomogeneities (such as PNRs and CORs in disordered matrix) and competing ferro-antiferro interactions, which influence local atomic displacements and material properties [27]. Pb-based relaxor ferroelectric class, particularly PMN represents a valuable material, as new experimental methodologies are being developed to determine local structure and to correlate local structure with material performance.

Recently, magnetic ion (transition metals or rare-earths) doping in ferroelectric ceramics is being investigated intensely in order to add new functionality namely magnetism to make it multiferroics. The multiferroics are single phase compounds or multiphase composites, which possesses simultaneously two or more primary ferroic orders viz. ferroelectric, ferromagnetic and ferroelastic [28]. At present, multiferroic materials are gaining lot of attention due to its technological importance and scientific challenges as magnetism and ferroelectricity are two independent phenomena. The trivalent rare earth cations substitution at Pb-site in PMN has been correlated with B-site cation ordering using XRD technique [29]. No dielectric and microstructure investigation has been reported for aliovalent gadolinium ion (Gd^{3+}) substitution in PMN.

It is clear from above discussions that the nano scale heterogeneity is believed to be a fundamental part of relaxors, but the mechanisms of CORs appearance and incapability of the PNRs growth below the T_m in zero-field condition is still not clear. It is also not clear at what temperature the CORs develop in PMN and how the size of the CORs relate with the sintering temperature. The statistical distribution of the PNRs and CORs is believed to play critical role in exhibiting relaxor behaviour of PMN. The purpose of this study is to investigate origin of the CORs and how substitution of rare earth magnetic Gd-ion at Pb-site in PMN influence the size of CORs which is believed to control the relaxor ferroelectric properties. Furthermore, how rare earth magnetic Gd-ion influence the size of CORs and dielectric properties of PMN is thoroughly investigated. The magnetic properties of the Gd-substituted PMN is measured for its qualification to multiferroic type-I materials. This thesis work clearly reveals formation of the CORs as soon as perovskite phase is formed during calcination, fact which is not known till now. The size of the CORs seems to remain invariant to hot pressed sintering temperature but an increase in the average grain size enhances the dielectric permittivity and saturation polarization, which is correlated well with the core: shell thickness ratio calculated from the core-shell model. Finally, the study of electrocaloric effect in PMN and Gd-substituted PMN ceramics gives new insight into these materials and opens a practical way of refrigeration in upcoming era.

1.3 Basic topics and literature survey

1.3.1 Dielectrics

Dielectrics are insulating ceramic materials and are used in many applications such as capacitors, memories, sensors and actuators [30]. The term dielectric is referred as the ability of a material to store electrical energy. When the dielectric material is placed in the electric field, polarization is caused by induced dipole moment or by rotation of permanent electric dipoles present in material. The induced dipole moment (p) is proportional to the local electric field (E), $p = \alpha E$ (α is the polarizability of the atom or molecule) and the total induced dipole moment per unit volume is called polarization (P). Basically there are four possible mechanisms of polarization [31] viz., i) Electronic polarization involves the separation of the centre of the electron cloud around an atom with respect to the centre of its nucleus under the application of electric field, ii) Ionic polarization is due to small displacement of ions from their equilibrium positions and hence inducing a net dipole moment under the application of external field, iii) Dipolar/orientation polarization is mainly due to orientation of molecular dipoles in the direction of applied field which would otherwise be randomly distributed due to thermal randomization, and iv) Space charge/interface polarization involves limited movement of charges resulting in alignment of charge dipoles under applied field which generally happens at the grain boundaries or any other interface such as electrode-material interface. Qualitatively, it can seen that in the above mentioned mechanisms, unlike masses of the entities to be displaced, with mass increases from electronic to ionic to dipolar polarization. This has a direct correlation with the frequency of the applied field as shown in Fig. 1.3. Intuitively, we can say that heavier the particular entity more is the time spent in displacing it. As a consequence, electronic polarization is the fastest and typically persists at frequencies between ~10^{13}-10^{15} Hz. In contrast, ionic polarization is sluggish and typically occurs at frequencies between ~10^{9}-10^{13} Hz whereas dipolar polarization participating motion of molecules occurs below 10^{9} Hz. Interface or space charge polarization occurs at frequencies below 50 Hz.

The dielectric response appears as the results of the cumulative effect of the microscopic displacement of charge carriers under the influence of an external applied electric field. It is estimated by measuring capacitance which is a measure of the ability of any two conducting plates in proximity to store a charge Q, when V is potential difference is applied across them. The capacitance C is given as [32]

$$C = Q/V \text{ and } C = \frac{\varepsilon_o A}{d} \tag{1.1}$$

where electric field $E = V/d$, ε_o is the permittivity of free space (8.854×10^{-12} F/m), d is the distance between the plates, A is the area of the plates. The value of capacitance increases when a dielectric material is inserted between the plates. The dielectric constant (ε) of the material is given as the ratio of the permittivity of the inserted dielectric material ε_m to that with the free space.

$$\varepsilon = \frac{\varepsilon_m}{\varepsilon_o} \tag{1.2}$$

Now it is important to establish a relationship between the polarization P in the dielectric material and its dielectric constant ε in order to obtain a quantitative understanding of its dielectric properties. The total electric displacement field *D*, in a dielectric caused by some external field E is given as

$$D = \varepsilon_o \varepsilon E = \varepsilon_o E + P \tag{1.3}$$

$$P = \varepsilon_o E(\varepsilon - 1) = \varepsilon_o \chi E \tag{1.4}$$

where χ is electrical susceptibility which is nothing but the ratio of polarized charge or excess charge to the surface charge in a vacuum capacitor and defined as

$$\chi = \varepsilon - 1 = \frac{P}{\varepsilon_o E} \tag{1.5}$$

If the applied voltage is replaced by the AC voltage source than dielectric constant becomes a complex quantity.

$$\varepsilon^* = \varepsilon' + j\varepsilon'' \text{ and } \tan\delta = \frac{\varepsilon'}{\varepsilon''} \tag{1.6}$$

where ε^* is the complex dielectric constant which consist of real part *ε'* which is measure of energy stored and imaginary part *ε''* is the measure of the loss or dissipative energy from the applied electric field (includes the effects of both dielectric loss and conduction loss), tan δ is the dissipation factor/loss tangent/loss angle (the ratio of the imaginary part of the dielectric constant to the real part). The reciprocal of dissipation factor i.e., $(\tan \delta)^{-1}$ described as the quality factor (Q factor) of the material is generally utilized to evaluate the figure of merit (FOM) in high frequency applications. Further, The real and imaginary parts of complex dielectric response of non-interacting dipolar system is described by Debye relaxation equation given as follows [33]

$$\varepsilon' = \varepsilon_\infty + \frac{\varepsilon_s - \varepsilon_\infty}{1 + \omega^2\tau^2} \tag{1.7}$$

$$\varepsilon'' = \frac{(\varepsilon_S-\varepsilon_\infty)\omega\tau}{1+\omega^2\tau^2} \tag{1.8}$$

where $\tau = 1/1\pi f$ is relaxation time (the time required for dipoles to orient in an electric field along the direction of applied field), ω is frequency of applied signal, ε_∞ and ε_s are high and low frequency dielectric responses, respectively. There are many drawbacks associated with this model. This model doesn't assume the shape of the molecule, but in reality molecules can have different shapes which affect the dielectric properties. This model also assumes that the dipoles are non-interacting, but in solid phase the dipoles are not independent in their response to an alternating field. This model also considers a single relaxation time but depending upon the axis of rotation and due to defect the material has distribution of relaxation time. In practice there are different models viz., Cole-Cole [34], Cole-Davidson [35] and Havriliak-Negami [36] models used to describe the relaxation of a different kind of materials such as ceramics, polymers and glasses etc., given as follows

$$\varepsilon^* = \varepsilon_\infty + \frac{\varepsilon_S-\varepsilon_\infty}{1+(j\omega\tau_{cc})^{1-\alpha}} \tag{1.9}$$

$$\varepsilon^* = \varepsilon_\infty + \frac{\varepsilon_S-\varepsilon_\infty}{(1+j\omega\tau_{cd})^{\beta}} \tag{1.10}$$

where τ_{cc} and τ_{cd} are the mean relaxation times and α, β are a constant for a given material, having a value $0 < \alpha < 1$ and $0 < \beta < 1$. Combining two dispersion equations (Cole-Cole equation and Cole-Davidson equation) Havriliak and Negami proposed a function for the complex dielectric constant as

$$\frac{\varepsilon^*-\varepsilon_\infty}{\varepsilon_S-\varepsilon_\infty} = \frac{1}{(1+(j\omega\tau_{HN})^{1-\alpha})^{\beta}} \tag{1.11}$$

This function generates the previously discussed relaxations as special cases. When $\beta = 1$ the circular arc shown above is generated. When $\alpha = 0$ the skewed semicircle is obtained. When $\alpha = 0$ and $\beta = 1$ the Debye function is obtained. It has been suggested that the "α" parameter represents a quantity that denotes chain connectivity and β is related to theoretical density fluctuations of polymers.

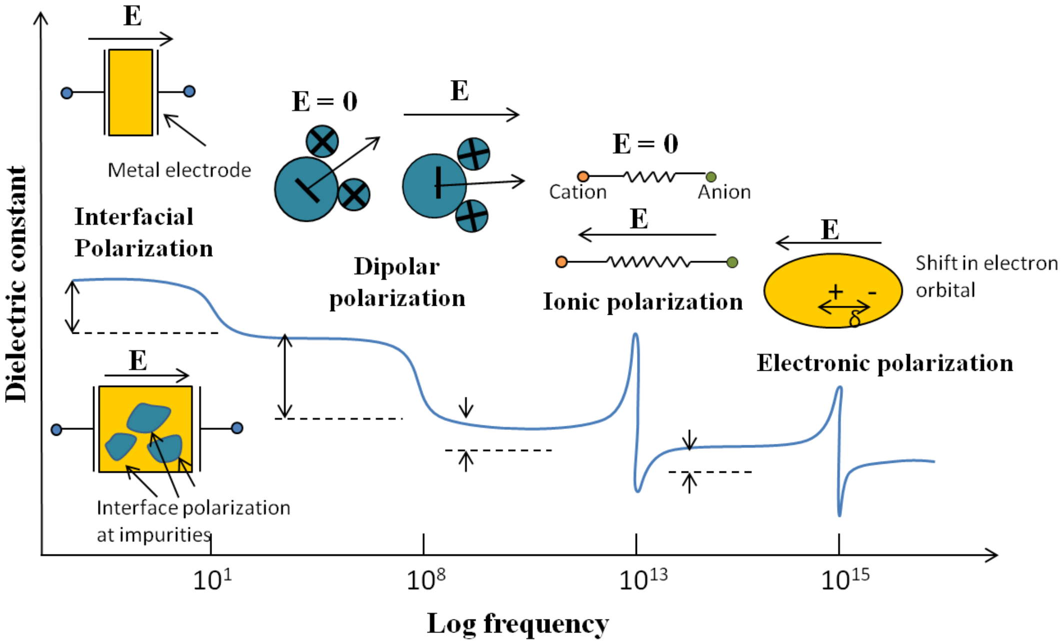

Fig. 1.3. Schematic figures between dielectric constant vs frequency showing various polarization mechanisms.

The dielectric ceramic materials are broadly classified into two categories depending on the Polarization vs. Electric field (*P*-*E*) curve [31], i.e., (i) In linear dielectrics, dielectric constant increases linearly with the applied field followed by an increase in the polarization depending upon the polarization mechanisms, and (ii) Non-linear dielectrics show large dielectric constants, non-zero polarization in the absence of electric field and nonlinearity in the dielectric constant and polarization. These dielectrics show exceptional effects such piezoelectricity (coupling of strain and electric field), pyroelectricity (temperature dependence of the polarization) and ferroelectricity (presence of large polarization in absence of electric field i.e. spontaneous polarization). Further, Ferroelectric ceramics is described in detail in next section.

1.3.2 Ferroelectrics

Ferroelectric ceramic materials are basically polar dielectrics, in which spontaneous electric polarization can be reversed or reoriented by the application of sufficiently high external electric field over a range temperature. Rochelle salt $KNaC_4H_4O_6.4H_2O$ is the first ferroelectric material discovered by Valasek *et al.* in 1921 [37]. Afterwards, for many years this discovery did not boost much excitement possibly due to the world war. A huge leap in the research on ferroelectric materials came in 50's after the discovery of barium titanate ($BaTiO_3$), which led to its use in capacitor, actuator, transducer and sensor devices etc. Subsequently, many other ferroelectric ceramics have been developed, including perovskites and mixed perovskites such as $KNbO_3$, $PbTiO_3$, PMN, and PZT etc. or more complex structures such as Aurivillius phases or tungsten bronzes.

Ferroelectric materials are identified by the occurrence of ferroelectric hysteresis-loop in the polarization (P) vs electric field (E). This P-E hysteresis loop in ferroelectric materials is a consequence of the energy barrier when switching from one polarization direction to another (domain-wall switching) [38,39]. Regions of similar polarization directions in a ferroelectric material are called ferroelectric domains which are separated by domain walls. The thickness of the domain wall ranges typically from 1-10 lattice parameters across. The 180^o domains are considered to have an abrupt change in the polarization direction and the 90^o domain walls are thicker than that of the 180^o domain walls. The angle between the directions of polarization on either side of the wall is the characteristic of domain walls. The domain walls are generally formed to reduce the energy of the system. The grain size, crystal symmetry, magnitude of spontaneous polarization, defect structure, as well as the sample geometry and the method of preparation contribute to the size and structure of these domains [38,39]. The application of an external electric field to a ferroelectric material leads to the growth of the domains in which the polarization orientation is parallel to the direction of application of the electric field. The growth of the domains is followed by a domain wall movement. The spontaneous polarization of a ferroelectric material is called the remanent polarization (P_r), the electric field required to decrease the polarization to zero is called the coercive field (E_c), and the saturation polarization is denoted as P_s, as shown in Fig. 1.4(a).

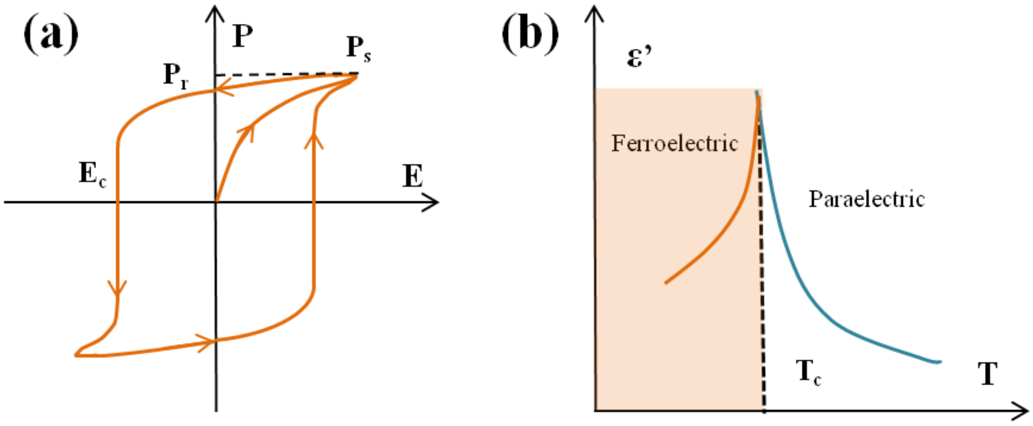

Fig. 1.4. (a) PE hysteresis loop for ferroelectrics and (b) Temperature dependent of dielectric permittivity showing paraelectric to ferroelectric phase transition below Curie temperature, T_c.

Ferroelectric materials are polar crystals, crystal symmetry plays crucial role in the origin of ferroelectricity. Amongst the 32 crystal classes, 11 cannot show ferroelectricity because they are centrosymmetric and the application of an electric field; these materials are polarized linearly, exhibiting a dielectric polarization. Remaining 21 crystal classes are piezoelectric crystals (with the exception of one), which means that the application of a mechanical strain causes an electric current to flow in a certain direction through these materials. Of the 20 piezoelectric classes, 10 have a single polar axis per unit cell and therefore these are spontaneously polarized [39], which is temperature dependent (also called pyroelectrics). A material can be ferroelectric only in certain temperature range because of its crystal structure or symmetry, responsible for spontaneous polarization (P_r). The highest symmetry phase compatible with ferroelectric structure is termed as paraelectric phase. This high temperature paraelectric phase undergoes to a ferroelectric phase through a phase transition below certain temperature called phase transition temperature or Curie point (T_c). This transition is connected with a lowering of crystal symmetry which leads to appearance of the spontaneous polarization. Due to lowering of symmetry the ferroelectric phase always has a lower symmetry than the paraelectric one. Moreover, bulk properties of material such as dielectric permittivity, heat capacity, refractive index etc. show an anomaly in the vicinity of the phase transition temperatures. The dielectric permittivity (ε') shows a sharp peak at the Curie temperature (T_c) and follows the Curie-Weiss law (for $T > T_c$) given as follows (Fig. 1.4(b)) [31,39]

$$\varepsilon = \varepsilon_\infty + \frac{C}{(T-T_c)} \tag{1.12}$$

where C is Curie constant, T_c is the Curie temperature; ε_∞ is the dielectric permittivity contribution due to electronic polarizability. Here, ferroelectric phase transitions are categorised into two parts [39], i) displacive type where the ferroelectric transformation is due to displacement of an ion with respect to another (e.g. $BaTiO_3$, $PbTiO_3$, and PZT etc.) and ii) order-disorder type where ferroelectric phase transition is associated with the individual ordering of ions (e.g. KH_2PO_4 and $NaNO_2$ etc).

1.3.3 Phase transitions

Thermodynamic theory is developed to understand the ferroelectric phase transitions [31,39]. This general theory is applicable for ferroelectric, magnetic, structural and even superconducting phase transitions etc. Phase transitions are classified as first order and second order phase transition. In modern time, Landau theory classifies the type of phase transition which is related to two important concepts: Broken symmetry and the order parameter. A phase transition is usually accompanied by some broken symmetry, i.e., when macroscopic conditions are changed (Temperature is decreased, or the pressure is increased, or external field is applied) one or more symmetry elements may disappear: This is broken symmetry and because of transition from low to high symmetry phase, there is a physical quantity P, Polarization in this case (or Magnetization in magnetic case) called Order parameter is generated. Free energy of system is expressed in terms of order parameter near

T_c and working around other thermodynamic parameters to predict the nature of phase transition.

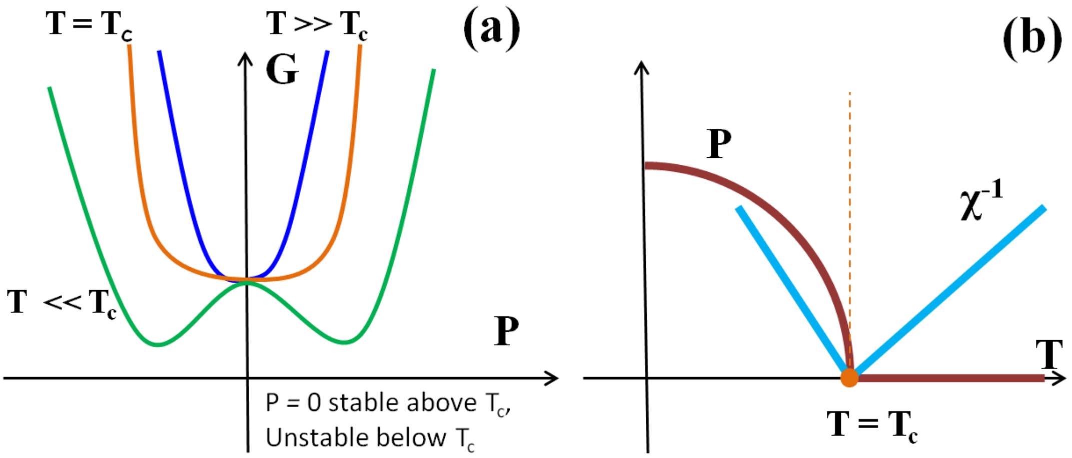

Fig. 1.5. (a) Free energy (*G*) vs polarization (*P*) schematic plot for a second order phase transition, (b) Polarization and inverse susceptibility plot for a second order phase transition.

Ferroelectric materials manifest various types of couplings between physical properties and can be displayed mathematically as [31,39]

$$G = G(P_x, P_y, P_z, \sigma_x, \sigma_y, \sigma_z, \sigma_{yz}, \sigma_{zx}, \sigma_{xy}, T) \tag{1.13}$$

The value of the independent variables can be obtained in thermal equilibrium at the free energy minimum. For uniaxial ferroelectrics, free energy can be expressed in terms of polarization skipping the stress field. Here, the source of free energy is determined for a strain free and unpolarized crystal to be zero.

$$G = \frac{1}{2}\,a\,P^2 + \frac{1}{4}\,b\,P^4 + \frac{1}{6}\,c\,P^6 + \ldots\ldots. - EP \tag{1.14}$$

where parameter *a* [= $a_o(T\text{-}T_c)$] is temperature dependent. As it a phenomenological theory, values of the other constants are small, or large, or positive, or negative subject to the order of phase transition. The order of phase transition is defined in the Ehrenfest idea in which the order of the lowest derivatives of the free energy shows a discontinuity at the transition [31,39]. More universally it is latent heat, which is present or not. Mainly there are two types of phase transitions illustrated as follows, (i) When the value of *b* is small and positive, and *c* = 0, the ferroelectric transition occurs at a temperature $T = T_c$ that is called as *second order* *transition*. In such condition, free energy as function of polarization develops continuously when temperature is changed i.e. from a single minima curve at $P = 0$ when $T < T_c$ to a plot with two minima at $P = +P_o$ and $-P_o$ when $T > T_c$. Two curves begin to be nearly connected if with temperature 'a' changes continuously and changes sign at T_c which is shown in Fig. 1.5. The spontaneous polarization, P_o, can be evaluated by substituting $E = 0$ in Eq. 1.14 and maintaining only two lowest order terms since all the coefficients i.e. a_o, b and c are positive. The polarization can be expressed as

$$P_o = \pm\sqrt{\frac{a_0(T_c - T)}{b}} \text{ for } T < T_c \text{ and } P_0 = 0 \text{ for } T > T_c \tag{1.15}$$

And dielectric susceptibility can be estimates as

$$\chi^{-1} = 2a_0(T_c - T) \text{ for } T < T_c \text{ and } \chi^{-1} = a_0(T - T_c) \text{ for } T > T_c \tag{1.16}$$

Showing that susceptibility will have a divergence at $T = T_c$ or its reciprocal (i.e. dielectric stiffness) will vanish at $T = T_c$ as shown in Fig. 1.5. In real materials, susceptibility reaches very large values near T_c. (ii) Second condition is to consider that when $a < 0$, $b < 0$ but $c > 0$. This means that G vs P curve has three equivalent minima, one for $P = 0$ and the remaining two for $P \neq 0$ at the same temperature i.e. at the same value of 'a' at a temperature $T = T_o$, Curie temperature, which is more than T_o. This leads to the G vs P curve as shown in Fig. 1.6(a). The essential characteristic of this phase transition is that polarization i.e. the order parameter drops from $P \neq 0$ to zero discontinuously at $T = T_c$ and is called as *first order phase transition*. This is also certainly manifested by a discontinuity in the inverse dielectric susceptibility as shown in Fig. 1.6(b). For example, solid-liquid phase transition is a first order phase transition while in different ferroelectrics; $BaTiO_3$ and $PbTiO_3$ are best examples of first order transition. The polarization can be revealed as

$$\text{for } T < T_c,\ P_o^2 = \frac{|b| + \sqrt{b^2 - 4ac(T - T_c)}}{2c} \text{ and for } T > T_c,\ P_o = 0 \tag{1.17}$$

and dielectric susceptibility can be expressed as

$$\text{for } T > T_o,\ \chi^{-1} = a(T - T_c) \text{ and for } T < T_o,\ \chi^{-1} = a(T - T_c) + 3bP_o^2 + 5cP_o^4 \tag{1.18}$$

The fact that there are three minima at $T = T_c$ which is reflected in case the T_c is reached while cooling or heating. More precisely, the material will be in other of the two non-zero polarization states if material is heated from an initial temperature that is lower than T_c whereas, if it is cooled from a temperature higher than T_c, the sample will be in paraelectric state. This produces in thermal hysteresis when these materials are heated and cooled around T_c.

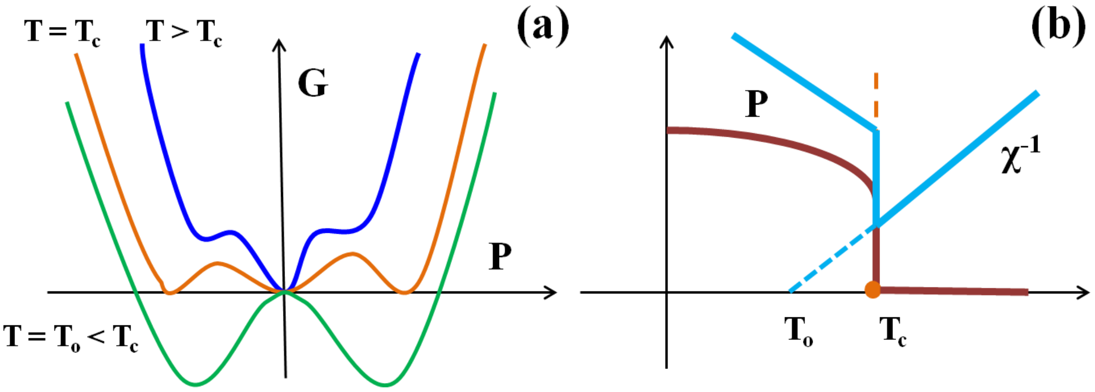

Fig. 1.6. (a) Free energy (*G*) vs polarization (*P*) schematic plot for a first order phase transition, (b) Polarization and inverse susceptibility plot for a first order phase transition.

1.3.4 Ferromagnetim

Magnetic ceramic materials possess extra-ordinary properties such as strong magnetic coupling, high electrical resistivity and low loss features which is used for variety of applications variety of applications such spin valves, high frequency applications, data storage, tunnel junctions etc. [31,40] Depending on the value of magnetic susceptibility (defined as, $\chi_m = M/H$) magnetic materials are divided into diamagnetic, paramagnetic, ferromagnetic, antiferromagnetic and ferromagnetic etc. [31,40] Permanent magnetic moment arising from spin and/or orbit is the origin of magnetization (*M*) in all magnetic materials. In paramagnetic materials, atoms have a permanent non-zero net magnetic moment due to the sum of orbital and spin magnetic moments. But, in addition to permanent magnetic moments as contained in paramagnetic materials, ferromagnetic materials consist of ordered regions or domains of single orientation of magnetic moment giving rise to large finite magnetization in the absence of a magnetic field, much like polarization in ferroelectric materials. This phenomenon is discovered below Curie temperature T_c and above T_c materials show paramagnetic behaviour. Mainly ferromagnetic behaviour is observed in elemental metals such as iron, nickel, cobalt and gadolinium etc. [40]. Though, many oxides such as CrO_2, EuO, and $Y_3Fe_5O_{12}$ etc. are ferromagnetic oxides. These oxides also show conduction and behave like metals. When a varying magnetic field is applied to a ferromagnetic material, the material exhibits a ferroelectric-like hysteresis loop between magnetization (*M*) and the magnetic field (*H*) due to existence of domains as shown in Fig. 1.7(a).

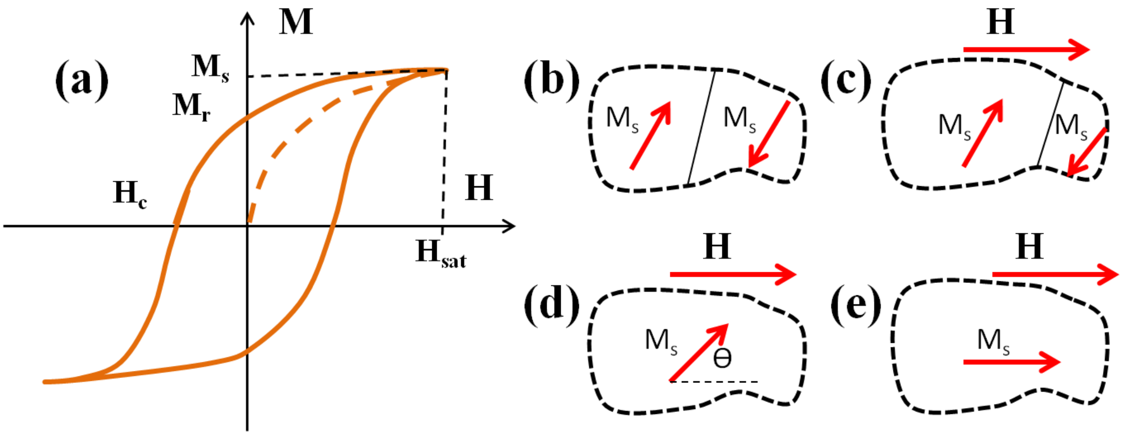

Fig. 1.7. (a) Typical *M-H* hysteresis loop for ferromagnetic materials, (b-e) Schematic picture of conversion of a multi-domain state into a single domain state under the application of magnetic field.

A ferromagnetic material in demagnetized state is divided into a number of small regions called domains akin to ferroelectric materials. There are basically four types of energy viz., exchange energy, magnetostatic energy, anisotropy energy and magnetoelastic energy, available for the formation of domains in ferromagnetic materials [41]. Each domain is spontaneously magnetized to the saturation value M_s, but the direction of magnetization of different domains is such that sample has zero magnetization. The process of magnetization is converting sample from a multi-domain state into a single domain state, magnetized in the same direction as the applied field which is shown in Fig. 1.7(b-e). The dashed line in Fig.

1.7(b) encloses a portion of a crystal in which there are parts of two domains; the boundary separating them is called as domain wall. The two domains are spontaneously, magnetized in opposite direction, so that the magnetization of this part of the crystal is zero. In Fig. 1.7(c), a field H has been applied, causing the upper domain to grow at the expense of the lower one by downward motion of the domain wall, until in Fig. 1.7(d) the wall has moved right out of the region considered. Finally, at still higher applied field the magnetization rotates into parallelism with the applied field and the material is saturated, as in Fig. 1.7(e). During this entire process there has been no change in the magnitude of the magnetization of any region.

There are two phenomenological theories of ferromagnetism which successfully explained many of the properties of ferromagnetic materials: the *Curie-Weiss localized-moment theory* and the *Stoner band theory* of ferromagnetism. Weiss in 1907 postulated that an internal "*Molecular field*" acts in ferromagnetic materials to align the magnetic moments parallel to each other [41,42]. But currently it is interpreted that the origin of this molecular field to be the quantum mechanical exchange energy, which causes electrons with parallel spins (and therefore parallel magnetic moments) to have a lower energy than electrons with antiparallel spins, all other aspects being equal. The molecular field is very high below the Curie temperature (T_c); hence, the sample gets magnetized with the application of external applied field. At sufficiently high temperatures, the magnetic moments are randomly orientated (paramagnetic behavior), as the thermal energy (kT) is larger than the orientation energy of the molecular field. The Weiss localized-moment picture explains the experimentally observed Curie-Weiss law behavior for the susceptibility (χ) of large number of magnetic materials,

$$\chi = \frac{C}{(T-T_c)} \tag{1.19}$$

There is a divergence in the magnetic susceptibility at the Curie temperature when the magnetic moments orient spontaneously even in the absence of the applied magnetic field.

The susceptibility of many antiferromagnets and ferrimagnets is also well described within the localized-moment picture.

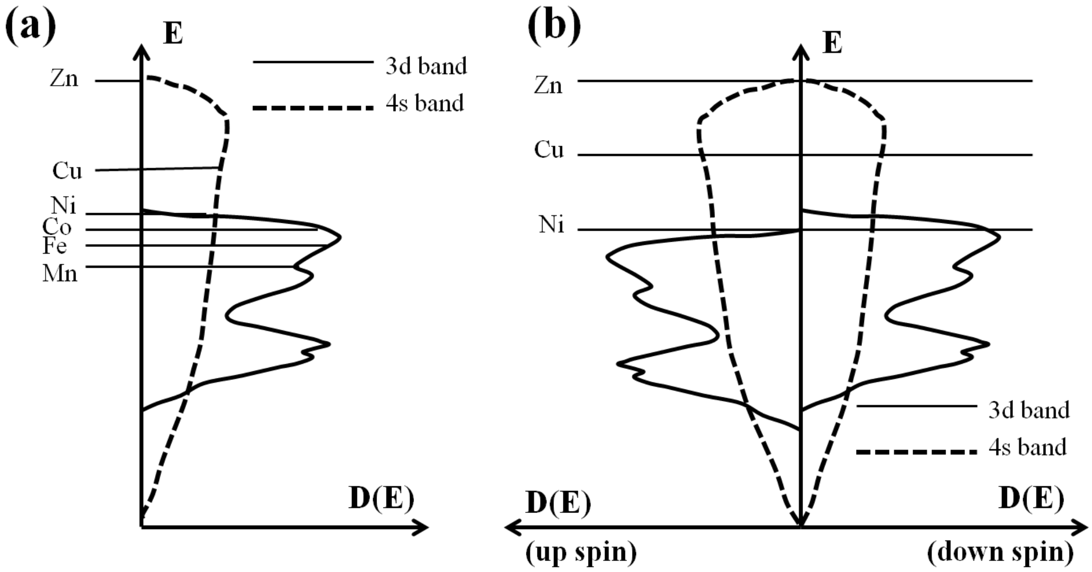

Fig. 1.8. (a) Schematic 3d and 4s densities of states, *D*(*E*), in first-row transition metals. The horizontal lines show the positions of the Fermi levels in Zn, Cu, Ni, Co, Fe, and Mn. (b) 3d and 4s up- and down-spin densities of states in first-row transition metals, with exchange interaction included [ref. (42)].

The Weiss localized-moment theory breaks down in one important aspect; however, it is unable to give explanation for the measured values of the magnetic moment per atom in a few ferromagnetic materials, particularly in ferromagnetic metals. There are two significant discrepancies [41,42]. First, according to the Weiss theory, the magnetic dipole moment on each atom or ion should be the same in both the ferromagnetic and paramagnetic phases which does not agrees with experiments. Second, in the localized-moment theory, the magnetic dipole moment on each atom or ion should correspond to an integer number of electrons. Again, this is not observed experimentally. These results are explained by using the Stoner band theory of ferromagnetism. In the *Stoner band theory*, the exchange energy is the fundamental driving force for ferromagnetism, which is minimized when all of the electrons have the same spin [42]. Opposing the alignment of spins is the increased band energy involved in transferring electrons from the lowest band states (occupied equally with up- and down-spin electrons) to band states of higher energy. This band energy prohibits simple metals from being ferromagnetic. In the elemental ferromagnetic transition metals Fe, Ni, and Co, the position of the Fermi energy is in overlapping region of 3d and 4s bands, as shown schematically in Fig. 1.8(a). As a result of the overlap between the 4s and 3d bands, the valence electrons partially occupy both the 3d and 4s bands. The 4s bands are wide, with a low density of states at the Fermi level. Consequently, the energy that is needed to promote a 4s electron into a vacant state so that it could reverse its spin is more than that which is gained by the resulting decrease in exchange energy, and so the 4s bands are not spin polarized. In contrast, the 3d band is narrow and has a much higher density of states at the Fermi level. The large number of electrons near the Fermi level lowers the band energy needed to reverse a spin, and the exchange effect governs. The exchange interaction produces an exchange potential that finally shifts the energy of the 3d band for electrons with one spin direction relative to the band for electrons with the opposite spin direction, giving the exchange-split band structure shown in Fig. 3.8(b).The magnetic moment does not certainly correspond to an integer number of electrons, since the electrons are shared between partially filled 4s, $3d^{up\text{-}spin}$ and $3d^{down\text{-}spin}$ bands.

In reality, materials evidently do not behave completely like either of these elementary models, although one or other is usually a moderately logical description in maximum cases. To illustrate, rare-earth magnets carry highly localized f electrons that are better explained by the Weiss localized moment theory, whereas, in metallic ferromagnets the magnetic order, occurring from the less strongly localized d orbitals, is Stoner-band-like.

1.3.5 Multiferroics

Coupling phenomena between different physical properties within a material is an important part of the science and technology. Origin and understanding of these phenomena leads novel applications of such materials in different area. Current impetus in such field is on the coupling between electricity and magnetism and the material in which both order is present are known as multiferroics (Fig. 1.9). In 1994, H. Schmid first defined multiferroics as single phase materials which simultaneously possess two or more primary ferroic properties i.e., ferroelectricity, ferromagnetism, ferroelasticy, ferrotoroidicity etc. [43]. In this section mainly we will discuss about the coupling of first two ferroic properties, electricity and magnetism called magnetodielectric (ME) effect. The understanding of the ME effect can be obtained by expanding the free energy in electric fieled E and magnetic field H given as follows [44,45],

$$F(E,H) = F_o - P_i^s E_i - M_i^s H_i - \frac{1}{2}\varepsilon_o \varepsilon_{ij} E_i E_j - \frac{1}{2}\mu_o \mu_{ij} H_i H_j - \alpha_{ij} E_i H_j - \frac{1}{2}\beta_{ijk} E_i H_j H_k - \frac{1}{2}\gamma_{ijk} H_i E_j E_k - \cdots \tag{1.20}$$

where i, j and k are directions, P^s and M^s are the spontaneous polarization and magnetization, ε and μ are the electric permittivity and magnetic permeability, α is the linear magnetoelectric couping parameter. β and γ express bilinear magnetoelectric coupling. Thermodynamic order parameters [i.e., $P(E,H)$ and $M(E,H)$] can be obtained by differentiation the Eq. 1.20 by thermodynamic driving parameter (i.e., E or H),

$$P(E,H) = \frac{\partial F}{\partial E_i} = P_i^s E_i + \varepsilon_o \varepsilon_{ij} E_j + \alpha_{ij} H_j + \frac{1}{2}\beta_{ijk} H_j H_k + \cdots \tag{1.21}$$

$$M(E,H) = \frac{\partial F}{\partial E_i} = M_i^s H_i + \mu_o \mu_{ij} H_j + \alpha_{ij} E_j + \frac{1}{2}\gamma_{ijk} E_j E_k + \cdots \tag{1.22}$$

In Eq. 1.21, setting $P^s{}_i = 0$, $E_i = 0$, and in Eq. 1.22, setting $M^s{}_i = 0$, $H_i = 0$, we obtain

$$P(H) = \alpha_{ij} H_j + \frac{1}{2}\beta_{ijk} H_j H_k + \cdots \tag{1.23}$$

$$M(E) = \alpha_{ij} E_j + \frac{1}{2}\gamma_{ijk} E_j E_k + \cdots \tag{1.24}$$

Equations 1.23and 1.24 express the magnetic (electric) induced polarization (magnetization). Recently, the boundary conditions of linear ME coupling is discussed by W. F. Brown [46] and the coupling coefficient is expressed by:

$$\alpha_{ij} < \sqrt{\varepsilon_o \mu_o \varepsilon_{ii} \mu_{jj}} = \frac{\sqrt{\varepsilon_{ii} \mu_{jj}}}{c_o} \tag{1.25}$$

The above equation (Eq. 1.25) highlights that large linear ME coupling can be gotten by large electric permittivity and magnetic permeability even without ferroic orders.

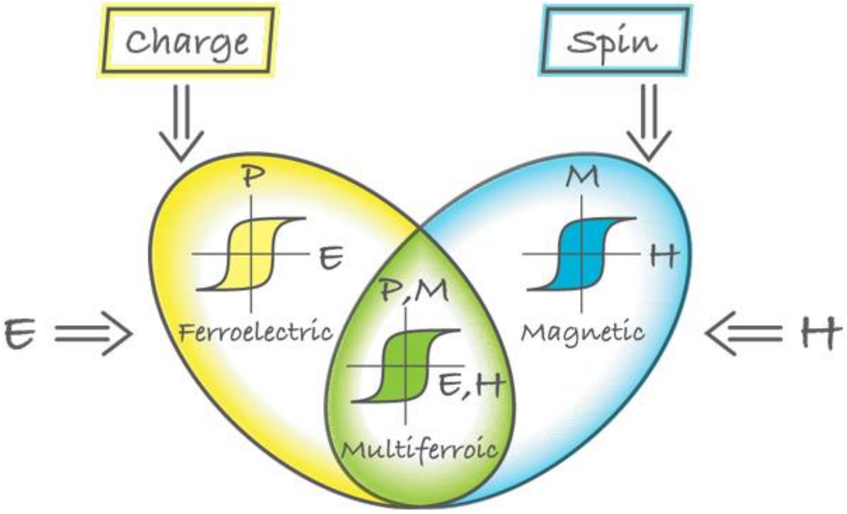

Fig. 1.9. Multiferroic materials combine the properties of ferroelectrics and magnets [ref. (47)].

inly two groups viz., type I and type II.

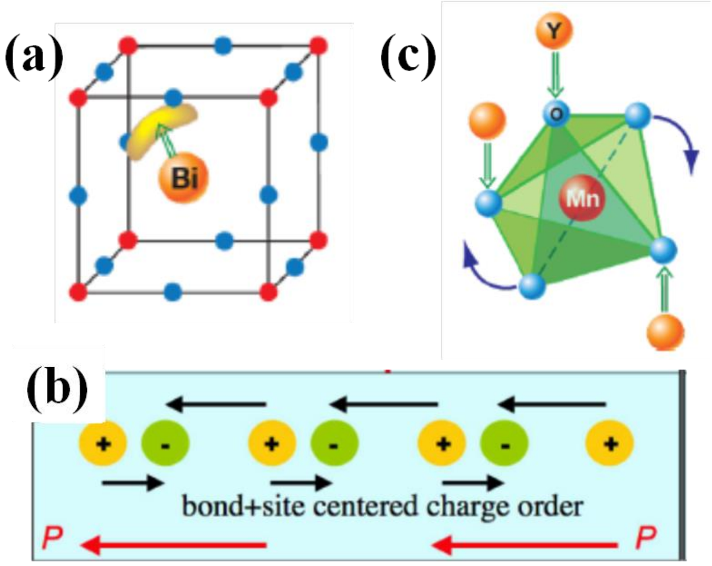

Fig. 1.10. Type I multiferroics where the origin of ferroelectricity is different (a) lone pair, (b) bond+site-centred charge ordering (c) geometric frustration mechanism [ref. (47)].

The microscopic origin of magnetism is basically the same in all magnets, i.e., the presence of localized electrons, mostly in the partially filled *d* or *f* shells of transition-metal or rare-earth ions, which have a corresponding localized spin, or magnetic moment where exchange interactions between the localized moments lead to magnetic order [45]. However, the situation with ferroelectrics is totally different. There are several different microscopic origins of ferroelectricity, and accordingly one can have different types of multiferroics. The multiferroic materials are divided into ma

The Type-I multiferroics are the materials which have different sources of ferroelectricity and magnetism with the two effects being quite independent of each other [44,45,47]. Unfortunately, the coupling between magnetism and ferroelectricity in these materials is usually weak. The materials challenge for this group of multiferroics is to keep all their positive features, but enhance this coupling. These are often good ferroelectrics, and the critical temperatures of the magnetic and ferroelectric transitions can be well above room temperature. Depending on the mechanism of ferroelectricity in them there are some examples of type I are $Pb(Fe_{1/2}Nb_{1/2})O_3$, $BiFeO_3$, $BiMnO_3$, $LuFe_2O_4$, Fe3O$_4$, and $YMnO_3$ etc., which display lone pair, charge order and geometrical frustration mechanisms, respectively, as shown in Fig. 1.10(a-c) [47].

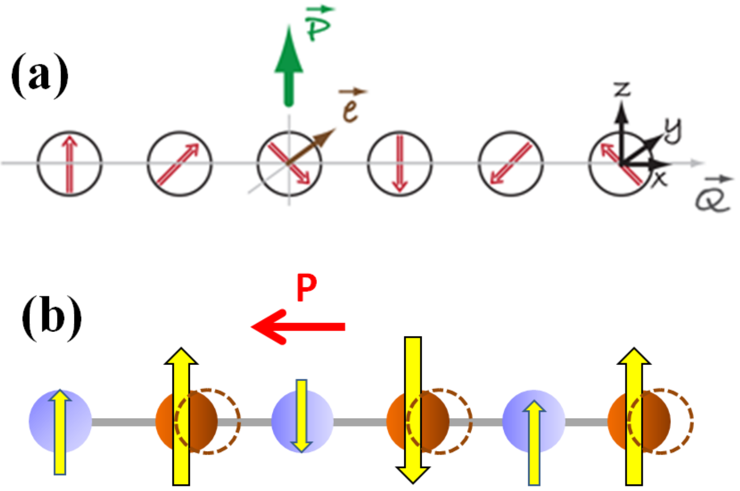

Fig. 1.11. Type II multiferroics (a) ferroelectricity is caused by a particular type of magnetic spiral, (b) ferroelectricity appears for collinear magnetic structures [ref. (47)].

The biggest excitement nowadays is caused by the discovery of a novel class of multiferroic materials are Type-II multiferroics (also called Magnetic multiferroics) which show ferroelectricity in their magnetically ordered state and that too of a particular type of magnetism. Moreover, very strong coupling between ferroelectric and magnetic order parameters has also been observed. From the point of view of the mechanism of multiferroic behaviour, one can divide type-II multiferroics into two groups [45,47]: those in which ferroelectricity is caused by a particular type of magnetic spiral (e.g., $TbMnO_3$, $TbMn_2O_5$, $MnWO_6$, and $Ni_3V_2O_8$ etc.) and those in which ferroelectricity appears even for collinear magnetic structures (e.g., $RMnO_3$) as shown in Fig. 1.11.

1.3.6 Relaxor ferroelectrics

Relaxor ferroelectrics (RFEs) are compositionally disordered systems belonging to a subclass of ferroelectrics having disorder in the arrangement of different ions on the crystallographically equivalent sites [2,3,10]. Most of the well known RFEs are complex compounds with the perovskite ABO_3 structure having disorder at A/B-sites. The typical examples are $Pb(Mg_{1/3}Nb_{2/3})O_3$, $Ba(Zr_xTi_{1-x})O_3$, $Pb_{1-x}La_x(Zr_{1-y},Ti_y)_{1-x/4}O_3$ and $Na_{0.5}Bi_{0.5}TiO_3$ etc. RFEs hold variety of novel properties, like giant dielectric constants, hysteresis-free high electromechanical response, and exceptional electro-optic properties, useful for technological applications [1,3,10]. L. E. Cross in 1987 proposed the name *relaxor ferroelectric*, designated to the materials which satisfy the three succeeding aspects [2]: (i) The temperature-dependent dielectric permittivity shows a broad and smeared maximum, (ii) The temperature for the maximum dielectric permittivity is frequency-dependent, i.e., the presence of “dielectric relaxations”, and (iii) There is no macroscopic symmetry breaking as a function of temperature.

In context of physical properties of RFEs, there are different temperature regions outlined as shown in Fig. 1.12 (for e.g., consider PMN) [5,48], (i) Region I ($T > T_B$): RFEs are paraelectric at high temperatures. (ii) Region II ($T^* < T < T_B$): local radomly oriented polarization grow below Burns temperature, T_B, is characterized by deviation form its linear dependence in volume, inverse susceptibility and refractive index. (iii) Region III ($T_f < T < T^*$): At the intermediate temperature T^*, the glassy polarization fluctuations start to become static. Also usually T^* can be understood as the upper limit of polar glass-like freezing dynamics, whereas the freezing temperature T_f determines the lower limit. (iv) Region IV ($T < T_f$): Below T_f, the local polarization is frozen i.e., ergodicity is broken T_f near or below and REF systems possess nonergodic behaviour; however, the macroscopic symmetry of high-temperature states is conserved. Further, various models have been reviewed in a nutshell which developed the understanding physics of relaxor ferroelectrics [49,50]:

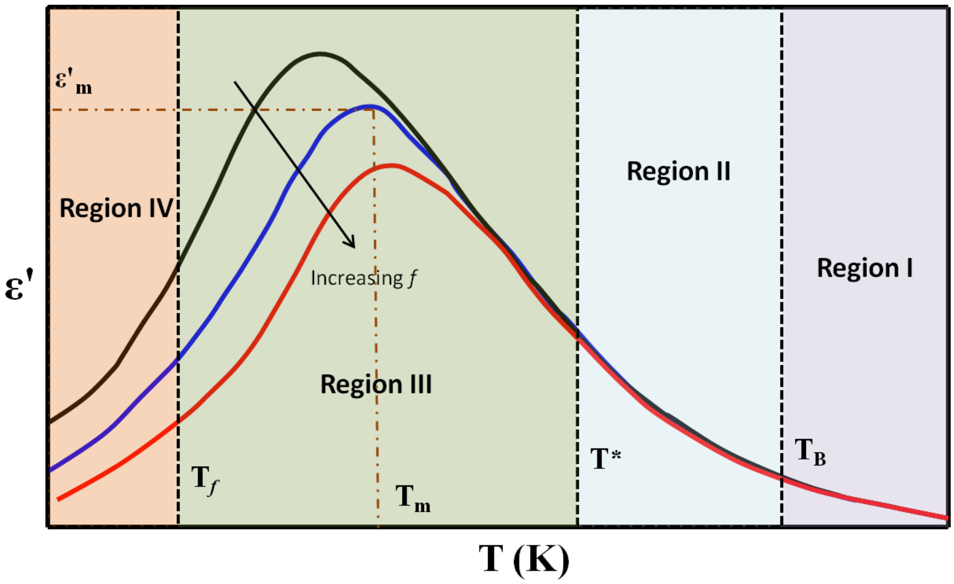

Fig. 1.12. Temperature dependent dielectric plot of canonical relaxors (e.g., PMN) showing different temperature regions.

Composition Fluctuation Model: Smolensky, Kirillov and Isupov assumed that the compositional inhomogeneities (i.e., random distribution of ions at cationic site) in complex perovskites produce distinct local Curie temperatures which have a Gaussian distribution about the mean Curie temperature [51]. As a consequence, the broad maximum of dielectric permittivity is interpreted in terms of a diffused phase transition comprising of a series of local phase transitions. The nature of local transitions are believed to be of the first order, giving rise to mostly non-interacting polar 'micro' regions of different sizes in the non-polar matrix above the mean Curie transition and thermal fluctuations assumed to flip the emerging polar regions. Below the mean Curie temperature, the thermally activated reorientation of the polar regions freezes and simultaneously percolated throughout the whole volume. This model gives the empirical quadratic relationship for the reciprocal real part of linear permittivity ε' defined as

$$\frac{\varepsilon'}{\varepsilon'_m} = 1 + \frac{(T-T_m)^2}{2\delta_m^2} \tag{1.26}$$

where ε'_m is the maximum value of dielectric permittivity at T_m which is assumed to be the mean Curie temperature and parameter δ_m signifies diffuseness of the phase transition. This model eventually established an intuitive image of how the compositional inhomogeneity smears out the ferroelectric phase transition. But this model is inadequate for many complex perovskites having B-site random cations which do not show any diffuse phase transition.

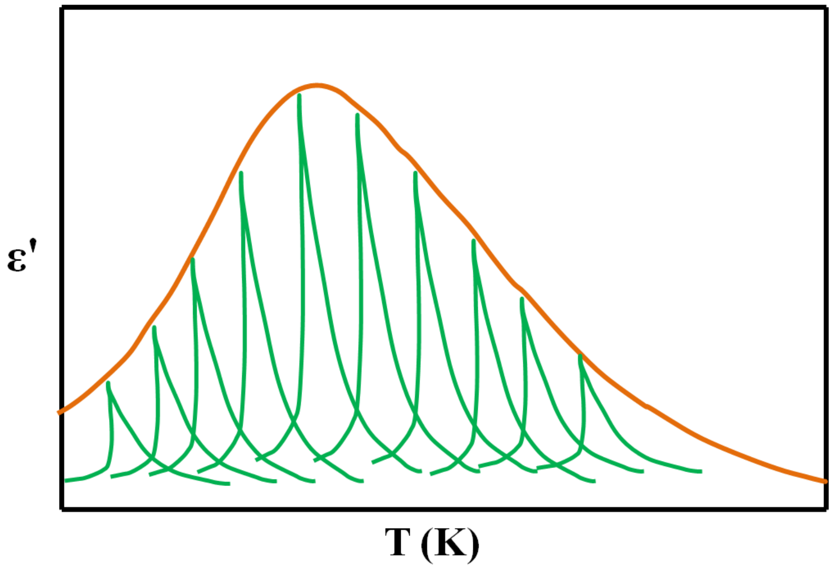

Fig. 1.13. A conceptual picture of composition fluctuation model that believes the broad dielectric permittivity is result of the distribution in the Curie temperature of polar 'micro' regions of different sizes.

Superparaelectric model: L. E. Cross postulated that the small sized noninteracting polar clusters exist in RFEs which permit dynamical (thermal) disordering over specific range of sizes analogous to spin clusters in the superparamagnetic state [2].These polar clusters have different environment around them in different directions due to asymmetrical potential energy well caused by internal compositional inhomogeneities. Therefore, it is anticipated that due to asymmetrical potential the local symmetry will be lower than the global symmetry and this asymmetry around the polar clusters is believed to be responsible for broad and frequency dependent dielectric permittivity in RFEs. Since these PNRs are non-interacting in nature they obey a Debye type relaxation and follow Arrehenius relation

$$\omega = \omega_o e^{\left(\frac{E_a}{k_B T}\right)} \tag{1.27}$$

where $\omega_o(=1/\tau_o)$ is the attempt frequency or Debye frequency, E_a is the activation energy of the relaxation process for thermally activated process and directly related to the cluster size and k_B is the Boltzmann constant. Eq. 1.28 suggests that the motion of the polar clusters can frozen at $T = 0$ K implying infinite broadening of relaxation time at 0 K. Bell calculated the dielectric response using superparaelectric model and showed frequency dependent dielectric response, local polarization fluctuation above Curie temperature, and a departure from Curie-Weiss law [52]. However, using Eq. 1.28, Kirilov and Isupov obtained physically unrealistic value of attempt frequency and activation energy for PMN [53].

Dipolar Glass Model: In analogy with magnetic spin glasses, Viehland *et al.* [54] introduced dipolar glass model considering interaction among polar clusters. They suggested that individual polar clusters interact with each other by means of dipolar interactions. As the temperature decreases, the strength of the interactions increases and at sufficiently low temperature, T_f, the dynamics of polar regions will freeze into metastable or frustrated states such that polarization of polar regions may not change due to the presence of the random fields produced by the structural disorder. The ergodicity is broken T_f near or below and REF systems possess nonergodic behaviour. In spin glasses the nonergodic behaviour is explained by a multivalley potential whose some barriers are so high that the time needed to overcome them is larger than any practically reasonable observation time. Thus, the spin glass cannot reach all the configuration states during the observation time, and consequently, the usual thermodynamic averaging and the time averaging give different results. The temperature dependence of the permittivity maximum is successfully modelled by the Vogel-Fulcher relationship given as follows

$$\omega = \omega_o e^{\left(\frac{E_a}{k_B(T-T_f)}\right)} \tag{1.28}$$

where $\omega_o(=1/\tau_o)$ is the attempt frequency or Debye frequency, E_a is the activation energy of the relaxation process, and T_f is the characteristic Vogel-Fulcher freezing temperature. But, Tagantsev *et al.* has argued that Vogel-Fulcher relationship in relaxor ferroelectrics does not necessarily imply a "freezing" in the system [55]. Instead Vogel-Fulcher relationship can be observed in any system where the distribution of relaxation times has some regular temperature dependence and does not necessarily require manifesting a freezing at the freezing temperature.

Random-Field Model: In 1992, Westphal, Kleemann and Glinchuk proposed a microstructural picture of RFEs that the nonergodic relaxor state is composed of polar nanodomains discretely separated by domain walls, i.e., a ferroelectric nanodomain state [16,56,57]. They suggested that the low temperature features manifested by PMN may not be completely the result of a glassy material, but could also be characterized by a system in which the structural phase transition into a ferroelectric state is destroyed by local quenched random fields, produced by compositional fluctuations with 1:1 Nb^{5+} and Mg^{2+} chemical ordered regions in the perovskite B-site. According to this model the polar nanodomains have well defined polarization contrarily to the polarization degeneracy of polar cluster fluctuations proposed by dipolar-glass model. It is thought that the random fields are the result of quenched high temperature states such as lattice defects or inevitable impurities and these random fields and random interactions among the defects and the polar nanodomains brings about the freezing transition into a glassy state, anticipating the frequency dependence of the permittivity. Their argument is also supported by different experimental evidences: The presence of highly sluggish relaxation in the submillihertz regime during a field cycling well-below T_f, the presence of Barkhausen jumps implying discontinuous domain rearrangements, the occurrence of an extra peak in the influence of an ordering field in both ε' and ε'', the broadness and the position of which decrease with an increasing electric field, the presence of a power-law decay of the isothermal remanent polarization that signifies the reconstruction of a nanodomain state at zero field etc. [49,50]. This idea of the 'random-field-induced' nano domain state has been supported steadily over the last three decades. Despite extensive experimental and theoretical investigations there are many arguments on whether relaxors transform into glassy state or a nano-domain [49,50].

1.4 Organization of the thesis

This thesis contains six chapters which are organized as follows: The sample preparation method and various experimental techniques employed in the present work are described in chapter 2. Chapter 3 outlined the origin and stability of chemical ordered regions and correlation among microstructural, vibrational, dielectric and ferroelectric properties in hot pressed (HP) PMN ceramics is presented. Chapter 4 is divided into three sections. In these sections, we have discussed the role of charge compensation mechanism on phase, dielectric and ferroelectric properties of aliovalent ion (Gd^{3+}) substitution in PMN (Section 4.1), critical slowing down dynamics of nano-polar dynamics in Gd-substituted PMN $Pb_{1-x}Gd_x(Mg_{1+x/3}Nb_{2-x/3})O_3$ ($0 \leq x \leq 0.1$) ceramics (Section 4.2) and electrocaloric behaviour of Gd-substituted PMN $Pb_{1-x}Gd_x(Mg_{1+x/3}Nb_{2-x/3})O_3$ ($0 \leq x \leq 0.1$) ceramics (Section 4.3). Chapter 5 is divided into two sections. The magnetic and magneto-dielectric properties of Gd-substituted PMN $Pb_{1-x}Gd_x(Mg_{1+x/3}Nb_{2-x/3})O_3$ ($0 \leq x \leq 0.1$) ceramics are discussed in first section (Section 5.1). The second section describes the synthesis and characterization of the PCN prepared for comparing the magnetic and magneto dielectric properties of the PGMN with lead cobalt niobate (PCN) in which B-site is occupied with magnetic Co^{3+} ion (Section 5.2). Conclusions and proposed future work are discussed in chapter 6.

Chapter 2

Experimental procedure

2.1 Introduction

In this chapter, synthesis procedure and characterization techniques have been described. The desired perovskite phase of hot pressed lead magnesium niobate (PMN), Gd-sustituted PMN and lead cobalt niobate (PCN) is synthesized by solid state reaction technique. It is widely known that the main difficulty in the fabrication of PMN is the formation of undesired pyrochlore phase along with the perovskite phase. Swartz and Shrout [58] opted a novel approach called Columbite precursor route to avoid the formation of pyrochlore phase given as follows.

$$\mathrm{MgO + Nb_2O_5 \rightarrow MgNb_2O_6} \tag{2.1}$$

$$\mathrm{PbO + 1/3\ MgNb_2O_6 \rightarrow Pb(Mg_{1/3}Nb_{2/3})O_3} \tag{2.2}$$

This chapter first describes the processing technique, utilized to prepare the ceramic specimens. In later part, various experimental techniques are outlined and elaborated rigorously. The X-ray diffraction (XRD) is used to examine phase formation and crystal structure, scanning electron microscopy (SEM) is used to image microstructure, transmission electron microscopy (TEM) and Raman Spectroscopy tools are used to probe local structures. Further, dielectric spectroscopy and PE loop tracer are used to study electrical properties and superconducting quantum interference device (SQUID) is used to investigate the magnetic ordering.

2.2 Material synthesis and ceramic processing

The calcined powder of PMN and Gd-substituted PMN were synthesized by the two step Columbite precursor method (Fig. 2.1) using high purity chemicals: PbO (99.9%), Gd_2O_3 (99.99%), MgO (99.95%), Nb_2O_5 (99.9%) [59]. In first step, the columbite precursor ($MgNb_2O_6$, magnesium niobate) was prepared by mixing predetermined amounts of MgO and Nb_2O_5 in ethanol and ball milled in zirconia bowl for 24 hours using zirconia grinding media. The slurry was dried in oven at 70 ^oC and the dried powder was calcined at 1200 ^oC for 2 hours. The calcined powder was once again ball milled for 24 hours and dried similarly

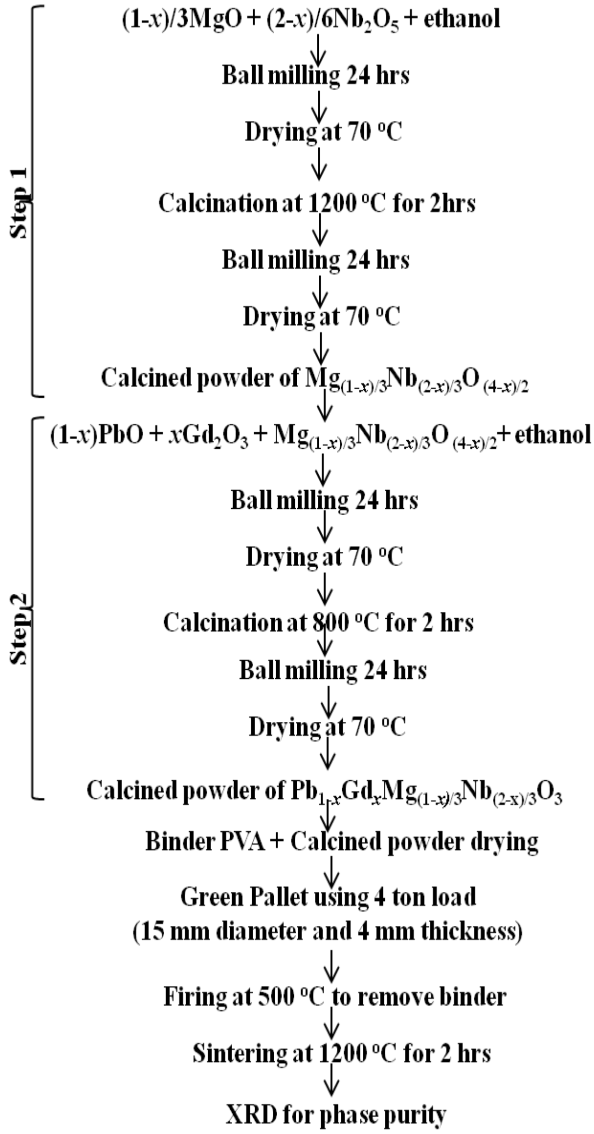

Fig. 2.1. Flowchart of synthesis of PMN ceramic using two step Columbite precursor method

as mentioned above. The single-phase formation was verified by comparing the data with standard JCPDF card 33-875. Then in second step, the Columbite precursor was mixed and ball milled with stoichiometric proportion of PbO and Gd_2O_3 powders and calcined powder at 800 °C for 2 hours. Here, the pyrochlore phase is prevented by eliminating PbO and Nb_2O_5 reaction. The solid state reactions for this route of perovskite PMN formation is:

$$(1+x)/3\ MgO + (2-x)/6\ Nb_2O_5 \rightarrow Mg_{(1+x)/3}Nb_{(2-x)/3}O_{(4-x)/2} \tag{2.3}$$

$$(1-x)\ PbO + x\ Gd_2O_3 + Mg_{(1+x)/3}Nb_{(2-x)/3}O_{(4-x)/2} \rightarrow Pb_{1-x}Gd_x(Mg_{1+x/3}Nb_{2-x/3})O_3 \tag{2.4}$$

The calcined powders were mixed again and pressed into cylinders (15 mm diameter with 5-6 mm thickness) using polyvinyl alcohol (PVA-3mol%) as a binder and a uni-axial hydrostatic pressure of 200 MPa. These cylinders were fired at 1200 °C for 2 hours after binder burnout at 450 °C for 4 hours. These cylinders were fired in closed alumina crucible, in order to minimize lead oxide loss. The sintered blocks were then cut into thin disks and polished on different grades of emery papers to obtain parallel surfaces. The polished surfaces were ultrasonically cleaned to remove dust particles.

Further, the density of the sintered pellets is measured by Archimedes' method working on the principle of Archimedes' liquid displacement where distilled water is used as a displacement media. First, ceramic pellet is weighed in air then the weight of the sample is measured by fully dipping in distilled water. Using these measurements, the density of the sample (ρ_{exp}) is calculated by using following formula:

$$\rho_{exp} = \frac{W_{air}}{W_{air}-W_{water}}\rho_{water} \tag{2.5}$$

where 'W_{air}' is weight of the sample in air, 'W_{water}' weight of the sample dipped in distilled water, and ρ_{water} is the density of the distilled water (1.00 gm/cc). The theoretical density or the single crystal density is determined from the volume of the unit-cell by using following formula:

$$\rho_{theory} = \frac{MxZ}{N_A xV} \tag{2.6}$$

where M is the molecular weight of the sample, Z is the number of atoms per unit cell, N is Avogadro number and V is the volume of the unit cell, calculated from the measured lattice parameters. The experimentally measured densities are then compared with the theoretically calculated values. It is observed these values of all ceramic pellets lies more than 97 % of the theoretical densities.

2.3 Scanning Electron Microscopy (SEM)

Scanning electron microscopy is a versatile tool to acquire microstructural, compositional information by collecting and analysing electron–specimen interaction products in the length scale ranging from few μm to nm. Although the theory and idea for building an SEM was developed by Knoll in early 1935 but first commercial SEM was manufactured in 1965. The working principle of SEM is based on the interaction between high-energy electrons and materials, where an electron beam passing through a specimen leads to different types of interaction products, including auger electrons, backscattered electrons, secondary electrons and characteristic x-rays. In SEM, backscattered electrons and secondary electrons are used for imaging to acquire structural information and the surface morphology of materials while characteristic x-rays are collected for compositional analysis [60].

A typical SEM is generally consists of several important parts including a vacuum system, an electron gun, magnetic lenses, various signal detectors, a sample stage and a control system as shown in Fig. 2.2. Electrons are generated from an electron filament and accelerated through the voltage difference between a cathode and an anode in the electron gun. A high-energy focused electron beam is then formed by focusing the electrons through a series of magnetic lenses. After passing through the scanning coils, the electron beam is directed onto the specimen. When the electron beam interacts with a specimen on the surface, some secondary electrons are generated. These secondary electrons are weakly bound, conduction-band electrons that possess relatively low energy. Some secondary electrons are absorbed by the specimen, while others escape from the specimen's surface. The escaped secondary electrons that carry information about the sample surface will then be captured by a secondary electron detector that is located 52° from the angle of the microscopic column. The collected secondary electrons contain information about the surface morphology of the specimen, which can be seen from the image variation. As the generation of secondary electrons' signal is affected by the topography of the specimen surface, the edges of the sample surface produce more secondary electrons, which make them brighter than other parts of the image.

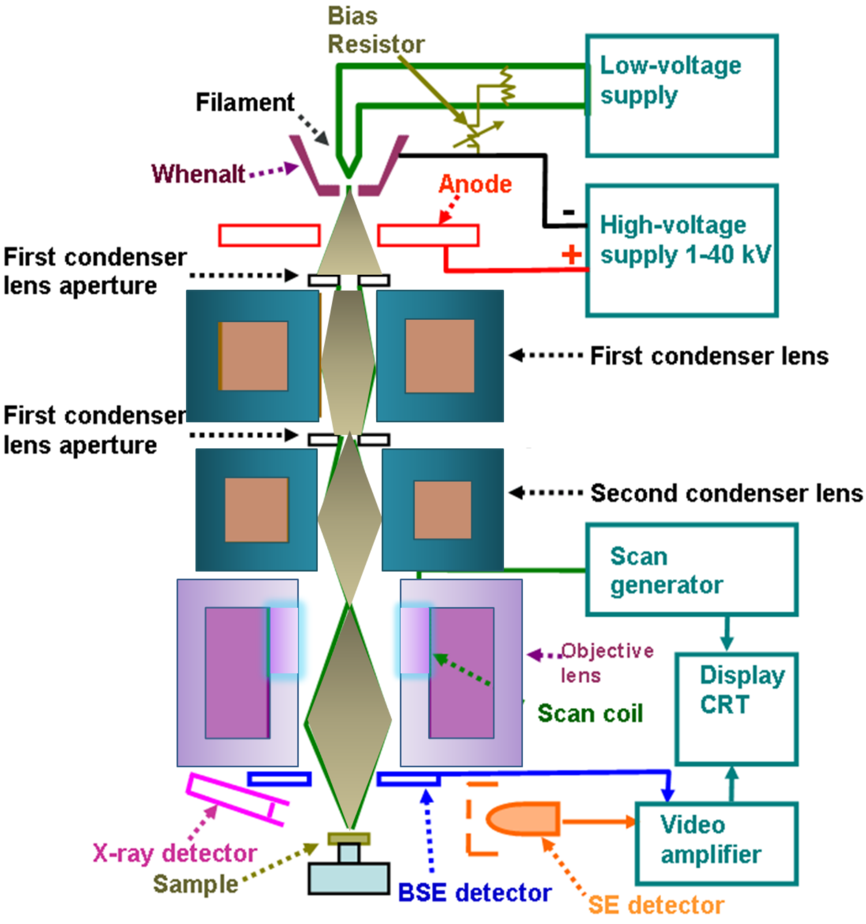

Fig. 2.2. Schematic diagram of FE-SEM experimental set-up consists of several important parts including a vacuum system, an electron gun, magnetic lenses, various signal detectors, a sample stage and a control system [ref. 60)].

In present thesis work, SEM is performed on the fractured surfaces which are sputtered by gold. Field Emission Scanning Electron Microscope (FE-SEM, Carl Zeiss, SIGMA) equipped with energy dispersive spectroscopy (Oxford Inca X-Act LN2 free) is used for grain size, morphology and elemental determination from fractured surface.

2.4 Transmission Electron Microscopy (TEM)

Electron microscopy came in to the picture after the proposal of French physicist de Broglie in 1925 that microscopic particles acquire both wave-like characteristics and particle [61]. As the wavelength of high-energy electrons is much shorter than visible light, electrons were first considered for imaging small objects that are invisible under visible light. On comparison with visible light, high-energy electrons carry much shorter wavelengths, providing theoretically extremely high resolution for the TEM of less than ~ 0.1 nm. Because of the extremely high resolution, the TEM has unanimously become the most dynamic structural characterisation tool for condensed matter and material science.

The basic working principle of the TEM is identical to that of the optical microscope, though the light source is electrons in place of the visible light. There are generally five important components in a commercial TEM: power supply, vacuum, lighting, imaging and recording systems. In the lighting system, electrons are produced by an electron gun which can be either thermionic-emission sources or field-emission sources. These generated electrons in electron gun are accelerated at very high voltages (80-1000 kV) producing flow of high-energy electrons. The high-energy electron flow is refined by passing it through the condenser lens and then focused onto the specimen. A thin specimen thickness of less than a few hundred nanometres is usually required to enable electrons to forward scatter and/or transmit through the specimen for conventional TEM imaging, whereas high resolution TEM imaging constraints specimen thickness less than 100 nm. The structural information for the specimen can be obtained by observing the forward scattering and/or transmitting electrons. After passing through the specimen, the electron beam is focused by the objective lens and magnified by the intermediate lens. The image and diffraction pattern are then projected onto the imaging screen.

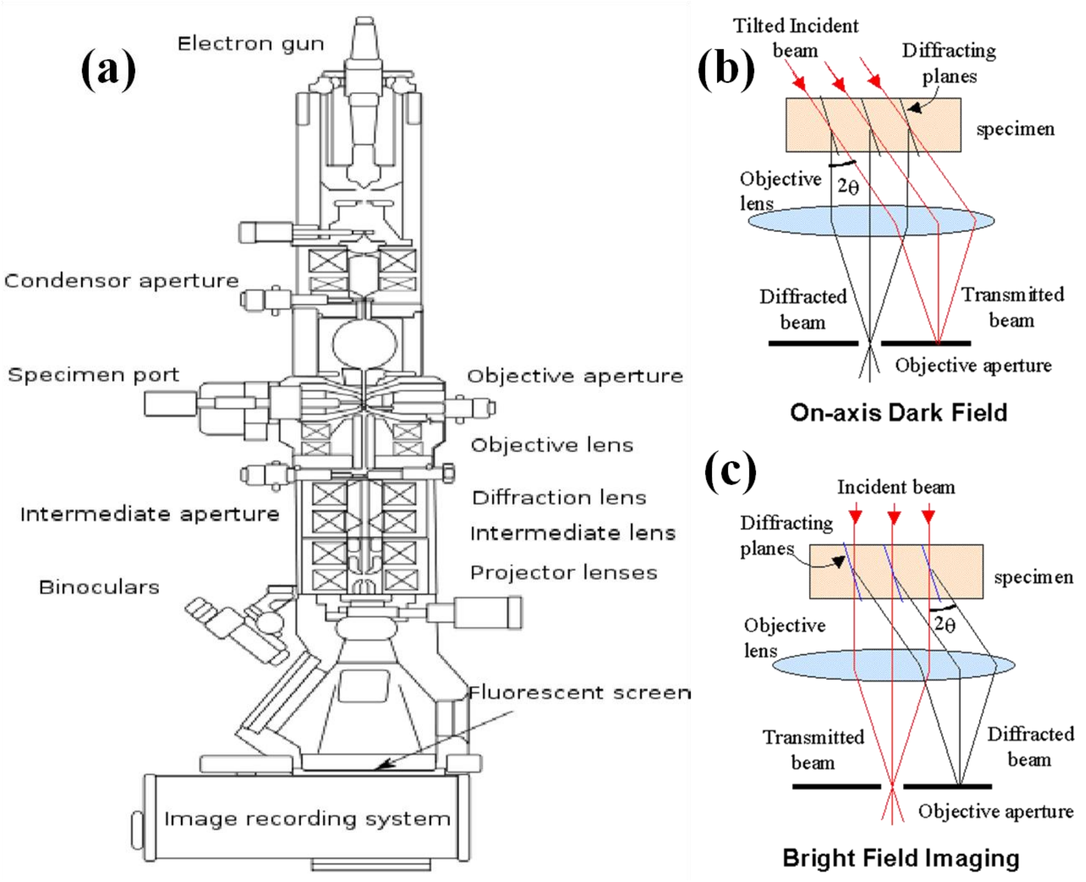

Fig. 2.3. (a) Schematic diagram of TEM system consist of power supply, vacuum, lighting, imaging and recording systems (b) dark field imaging (c) and bright field imaging [ref. 61)].

In addition to the real space imaging of the specimen, information about crystal structures from the reciprocal space is also recorded through electron diffractions. In present-day TEMs, the imaging mode and the diffraction mode can be easily replaced for one another which is depicted in Fig. 2.3, where the electron paths is shown for both the imaging and the diffraction modes. Two special planes, the back focal plane and the image plane, form in the TEM column. The diffraction pattern is located on the back focal plane, which contains structural information about materials in the reciprocal space. An objective aperture can be used to allow one (or several) of the scattered beams to pass through for imaging. A dark-field image is formed using a scattered beam. A bright-field image is formed using the transmitted beam in which an area of interest consisting of desired information can be selected by inserting an intermediate aperture. A subsequently obtained diffraction pattern is termed the selected area's electron diffraction pattern. Finally, an image or an electron diffraction pattern can be seen on the viewing screen after the object in the image plane or the back focal plane has been magnified by the projection lens. Photographic films were once used to record images. Today, images can be observed and recorded by a high-resolution charge-coupled device (CCD) camera. By using a state-of-the art CCD camera, in-situ TEM experimental processes can be video recorded to understand the dynamic structural evolution of materials under various conditions.

While TEM has been a powerful tool for the structural characterisation of materials and biological specimens, there is number of problems also existing in the current TEM system. The TEM samples preparation is a time-consuming process because the sample thickness is generally restricted to less than a few hundred nanometres. Within this thickness range, most oxide materials, including multiferroic materials, can easily be destroyed. Special precaution is required to avoid physical and chemical destruction during the sample preparation process. In addition, structures and/or chemical compositions that are sensitive to the electron beam can be altered or damaged by overexposure.

In present thesis work, TEM specimens are prepared by ultrasonically drilling 3-mm discs which were mechanically polished to ~100 µm. The center portions of these discs are then further ground by a dimpler to ~10 µm, and argon ion-milled (operating at 2-6 KeV) to perforation. The TEM studies are done on a Phillips CM200 microscope operating at an accelerating voltage of 200 kV.

2.5 X-ray diffraction (XRD)

The X-rays are an electromagnetic radiation of very short wavelength ~1 Ǻ which can be produced by the quick deceleration of rapidly moving electrons at a target material (made of Cu or Mo) or anode. The wavelength range of X-rays is ~ 0.1 to 100 Ǻ, but for the purpose of X-ray crystallography can be reduced to ~ 0.6 - 3.0 Ǻ. The diffraction of X-rays was first established by Max von Laue using copper sulphate crystal as the diffracting grating. This discovery was straight away noticed by W. H. Bragg and W. L. Bragg, who used X-rays diffraction (XRD) as a tool to determine structure of crystals. W. L. Bragg noticed that XRD act like a 'reflection' from the planes of atoms within the crystal and the reflection appeared only when constructive interference condition is satisfied. Fig. 2.4 depicts Bragg reflection from a set of crystal planes having a spacing 'd_{hkl}'. The path lengths of interfering beam must differ by an integral multiple of wavelength in order for the occurrence of constructive interference, which is expressed by the Bragg equation as follows [62]

$$2d_{hkl}\,sin\theta_{hkl} = n\lambda \tag{2.7}$$

where dhkl is the interplanar spacing between the crystal planes (*hkl*), θ_{hkl} is the specific Bragg angle at which diffractions from these planes are observed, n is an integer number and λ is the wavelength of X-rays. A polycrystalline sample or finely ground crystalline powder containing large number of randomly oriented crystals is placed in the path of a monochromatic X-ray beam, diffraction occurs only for the crystals planes which happen to be oriented at the Bragg angle (θ) to the incident beam. The scattered beams for each set of planes having miller indices (*hkl*) will be recorded at the appropriate 2θ angle as shown in Fig. 2.4. It can be noticed that only space group information can be determined using Eq. (2.5). Moreover details about the atoms and their Wyckoff positions are determined by relative intensities of Bragg peaks. The intensity of a Bragg peak with set of crystal planes (hkl) is given by

$$I_{hkl} \, \alpha \, |F_{hkl}|^2 \tag{2.8}$$

$$F_{hkl} = \sum_i f_i \, e^{2\pi i(hx'_i+ky'_i+lz'_i)} \tag{2.9}$$

where, F_{hkl} is the structure factor, f_i is the atomic form factor of the ith atom in the unit cell, (x'_i, y'_i, z'_i) is the fractional atomic positions of the ith atom in the unit cell. Summation is performed over the entire atoms in the unit cell. The proportionality includes the multiplicity for that family of reflections and other correction factors like absorption, geometrical factors, temperature dependence and polarization factors etc. As the temperature increases, peak intensity (or Bragg peaks) will decrease since spacing of the planes will not be correctly defined. In this work, the x-ray diffraction is carried out on the calcined powders using Rigaku powder diffractometer, with Cu-K_α radiation, operated at 40 kV, 30 mA in the Bragg-Brentano geometry. XRD data is recorded for ranging 2θ of 15° - 95°. In this case sample stage is rotating to avoid the preferred orientation of set of crystal planes. Further, rietveld refinement of room temperature XRD patterns of ceramic samples is carried out using Fullprof program to find out lattice parameter, phase purity, crystal symmetry, Wyckoff position of atoms etc. [63].

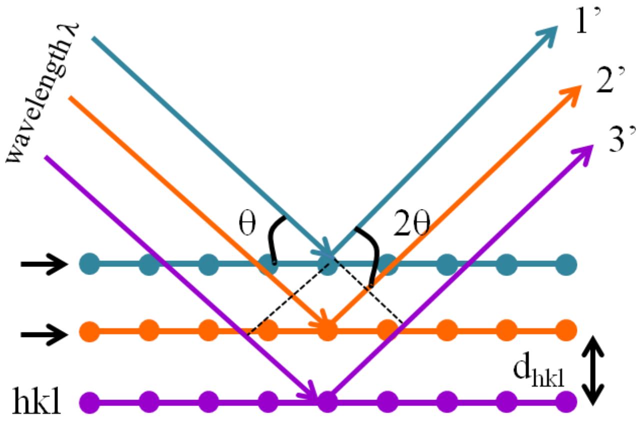

Fig. 2.4. Schematic diagram of XRD mechanism reflection of x-ray by lattice planes of a crystalline sample satisfying Bragg's condition.

Rietveld refinement technique is a robust approach for refining crystal-structure details from X-ray and neutron powder diffraction data. It determines the intensity at particular angle of the powder diffraction data, constructed on the given parameters, and fits calculated data to the experimentally observed data by a least square fitting method. The quantity minimized in the least square fitting method is residue (S_y) given as follows

$$S_y = w_i(Y_i - Y_{ci})^2 \tag{2.10}$$

where, Y_i is the observed intensity at the ith point, Y_{ci} is the corresponding calculated intensity and w_i is the weighting factor. Since the S_y value highly dependent on the actual estimates of several parameters, therefore the refinement program also authorize user to change some of the parameters acceptable for the better agreement between experimental observed and calculated data. Finally a minimization is achieved by performing several non-linear least squares cycles. The measure of fitness between experimentally observed and calculated pattern is quantitatively evaluated by agreement factors, i) R_p - profile, ii) R_{wp} – weighted profile, iii) R_{exp} – expected weighted profile, iv) R_B – Bragg factor, v) χ^2 - goodness of fit, defined as follows

$$R_p = \frac{\sum_i |Y_{io} - Y_{ic}|}{\sum_i Y_{io}} \tag{2.11}$$

$$R_{wp} = \left[\frac{\sum_i w_i(Y_{io} - Y_{ic})^2}{\sum_i w_i Y_{io}^2}\right]^{1/2} \tag{2.12}$$

$$R_{exp} = \left[\frac{N-P}{\sum_i w_i Y_{io}^2}\right]^{1/2} \tag{2.13}$$

$$R_B = \frac{\sum_i |I_{ko} - I_{kc}|}{\sum_i I_{ko}} \tag{2.14}$$

$$\chi^2 = \frac{\sum_i w_i(Y_{io} - Y_{ic})^2}{N-P} = \left(\frac{R_{wp}}{R_{exp}}\right)^2 \tag{2.15}$$

where, N and P are the number of profile points and refined parameters respectively. I_{ko} and I_{kc} are the observed and calculated intensities of corresponding K-Bragg peak. Rietveld refinement is not structure determination, it refines the given structure. To start refining a structure, an initial model (even if incomplete) is necessary. This model for the structure is supposed to be obtained from a crystal structure solver program or by any other mean. In refinement, Pseudo-Voight function is used to define peak shape and background is modelled using a sixth order polynomial. We have refined scale factor, zero correction, background, lattice parameter, half-width, position co-ordinates, isothermal, asymmetry, composition parameters.

2.6 Raman Spectroscopy

Raman scattering spectroscopy is an effective tool to get more insight into the local distortion, disorder and the strain present in the ceramic materials because the vibrational spectrum has typically shorter length scale than required for the diffraction experimental. The local symmetry of Pb-based mixed perovskite materials is different from the global symmetry, therefore Raman scattering is a useful technique to study the dynamics of structure by analyzing the characteristic modes associated with nano regions. Here, selection rules are very sensitive to the local and global symmetries.

The inelastic scattering of light predicted by Smekal in 1923 was first experimentally observed by an Indian scientist Dr. C.V. Raman in 1928, is called “Raman effect”. Raman spectroscopy measures Raman shift which is based on the phenomenon called Raman scattering [64]. When a monochromatic light of frequency ν_o is directed on a crystal, the scattered light is of two types, i) Rayleigh Scattering, having frequency the same as incident beam and is stronger, and ii) Raman scattering having frequencies $\nu_o \pm \nu_m$, where ν_m is the vibrational energy of the scattered crystal. This is very weak effect. The line $\nu_o + \nu_m$ is called antiStokes and $\nu_o - \nu_m$ is called Stokes lines. In crystalline solids, The Raman effect deals with phonons, instead of molecular vibrations. The fundamental requirement of a vibrational mode or phonon is to be spectroscopically Raman active. In order to generate a Raman peak or Raman active mode, the incident phonon must change the bond polarizability and in order to identify the Raman-active modes, the group theory delivers a set of selection rules based on symmetry operations. Also a phonon can be Raman active only in the crystal with no center of inversion. A typical Raman spectrometer consists of excitation source (laser), sample illumination and collection system, monochromator and detector as shown in Fig 2.5. As Raman Effect is a weak effect, laser proved to be ideal source due to its high power, monochromaticity, small diameter and ease to focus.

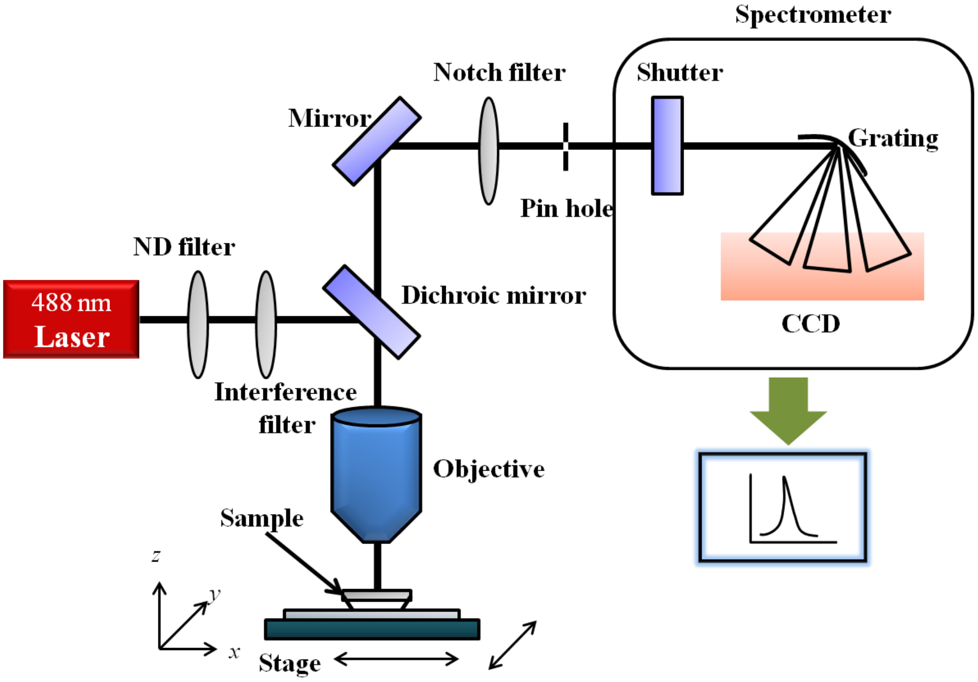

Fig. 2.5. Schematic diagram of Raman Spectroscopy platform set-up consists of excitation source (laser), sample illumination and collection system, monochromator and detector.

In this work, room temperature Raman spectra of the sintered ceramics is recorded by using LABRAM HR-800 spectrometer equipped with a 488 nm excitation source and a CCD detector giving real spectral resolution of better than 0.5 cm-1. The Jandel ‘peakfit’ software is used for deconvolution of the overlapping modes. The fitting of the whole spectra has been carried out by using Pseudo Voigt peak-shape functions ($PV = p \times L + (1-p) \times G$, $0 \leq p \leq 1$, where L and G stand for Lorentzian and Gaussian, respectively) to determine the characteristic parameters of all the Raman bands, like intensity, full width at half maximum (FWHM) and peak position.

2.7 Dielectric spectroscopy

When the dielectric material is placed in the electric field, polarization is caused by induced dipole moment or by rotation of permanent electric dipoles present in material [31]. The induced dipole moment (p) is proportional to the local electric field (E), $p = \alpha E$ (α is the polarizability of the atom or molecule) and the total induced dipole moment per unit volume is called polarization (P). The possible sources of polarizations in dielectric materials are electronic polarization, ionic polarization, dipolar or orientation polarization and space charge polarization. Electronic polarization occurs because of the shift of electronic charge cloud of an atom in respect of the positive nucleus under the influence of electric field. In case of ionic polarization, the net induced dipole moment is due to the displacement of positive and negative ions from their equilibrium positions. In polar dielectrics, the orientation of molecular diploes under the influence of electric field gives rise to the net polarization. In space charge polarization or interfacial polarization, the small distance migration of the tapped charges in interfaces of material contributes to the total polarization.

The macroscopic behaviour of dielectrics can be recognized by placing the dielectric slab in between the parallel plate capacitor. When an electric field is applied between the plates, the interactions are drawn by the dielectric constant or also called relative permittivity, ε ($\varepsilon = \varepsilon_m/\varepsilon_o$, ε_m is the permittivity of the medium and ε_o = 8.85 x 10^{-12} F/m is the permittivity of the free space). The dielectric constant reveals the ability of a dielectric material to store charge. The dielectric constant (ε^*) of the material is a complex quantity and is expressed mathematically as following

$$\varepsilon^* = \varepsilon' + i\varepsilon'' \tag{2.16}$$

where ε' is the real part of the dielectric constant which measures the capability of material to store charge and ε'' is the imaginary part of the dielectric constant which measure of loss in the dielectric material. Dielectric constant of a material is determined by measuring its capacitance (*C*) in parallel plate geometry and using geometrical constants given as

$$\varepsilon' = \frac{C\,x\,d}{\varepsilon_0 x\,A} \tag{2.17}$$

where '*d*' is electrode spacing, '*A*' is the electrode area. Similarly the imaginary part of the dielectric constant is determined from the loss factor (tan*δ*) given as

$$\varepsilon'' = \varepsilon' x\ tan\delta \tag{2.18}$$

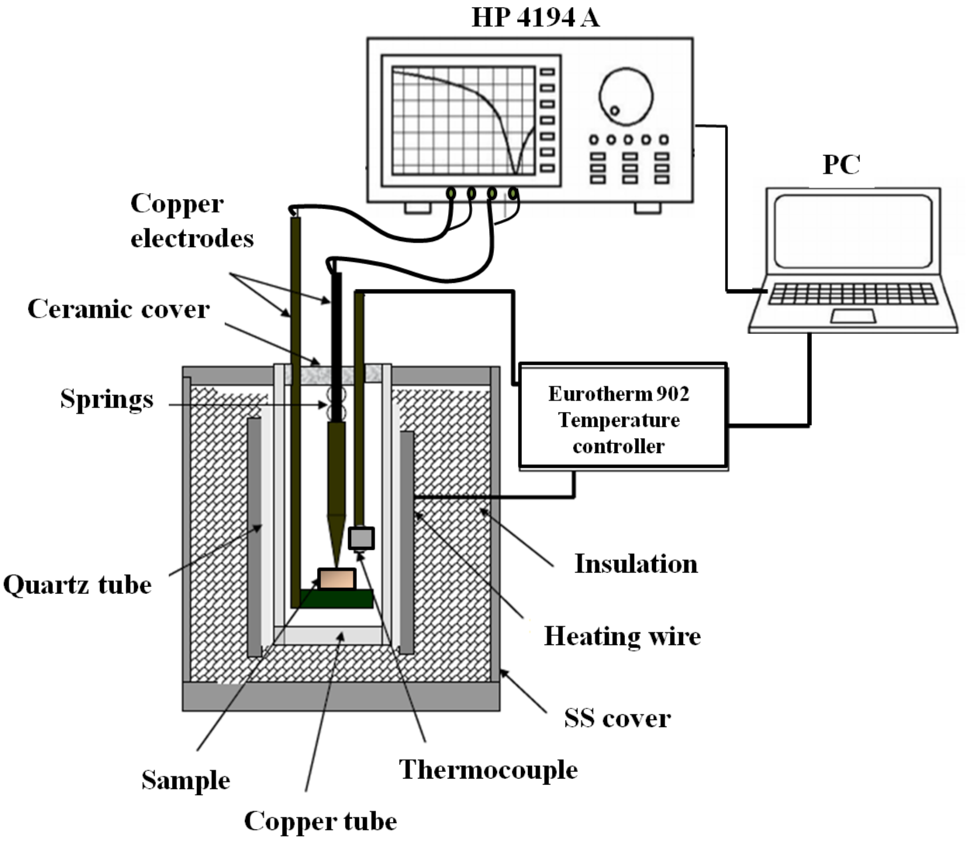

Fig. 2.6. Schematic of dielectric cell designed for dielectric measurement in the temperature range of 100 to 450 K

In this work, the dielectric measurement is carried out on sintered discs of diameter ~ 12 mm and thickness ~ 1 mm. The sintered disks are polished on different grades of emery papers to obtain parallel surfaces. The polished surfaces are ultrasonically cleaned to remove dust particles. The sample is sputter coated with gold followed by a thin coating of silver paste (dried at 450 ^{o}C for 2 minutes) to insure good electrical contact. The dielectric response has been measured using a Hewlett-Packard 4194A impedance analyser, which can cover a frequency range from 0.1 kHz to 100 kHz. For low temperature measurements, the sample is placed in a Delta Design 9023 test chamber, which can be operated between -180 and +200 ^{o}C. The sample temperature is measured using a Eurotherm temperature controller via a K-type thermocouple mounted directly on the ground electrode of the sample fixture. The analyser, test chamber and Eurotherm temperature controller is interfaced with computer to collect data at 20 different frequencies while cooling at a rate of 2 K/min. The dielectric constant of magnetic ion doped ceramics is also measured as a function of temperature and magnetic field. The dielectric response in a magnetic field is called magneto-dielectric (MD) and is defined by using %MD parameter given as

$$\%MD = \frac{\{\varepsilon'(T,H) - \varepsilon'(T,0)\}}{\varepsilon'(T,0)} x100 \tag{2.19}$$

2.8 PE loop tracer

The existence of spontaneous polarization and ferroelectric hysteresis loop is the hallmark evidence of the ferroelectricity in materials, in which the polarization (P) can be switched hysteretically by application of external electric field (E). As a result, the ferroelectric hysteresis loop is also called *P-E* loop. The *P-E* loop tracer is an important tool to characterize the ferroelectric properties of ferroelectric materials as it measures the important parameters, such as the maximum polarization (P_{max}) in an applied electric field, the remnant polarization (P_r) and the coercive electric field (E_c).

A traditional and frequently specified method for the P-E loop measurement is called Sawyer-Tower circuit [39], which consists of an oscilloscope, a signal generator (E), a reference capacitor C_o, and another capacitor C_x with the ferroelectric sample to be measured, as shown in Fig. 2.7. In this method, the signal generator generates an AC electric signal in the circuit, which changes the current and charge in the electronic devices. The reference capacitor C_o and the sample capacitor C_x are filled with the same amount of charge Q, as they are connected in series. The quantity plotted on the horizontal axis is proportional to the field ($E = V_x/d$) across the sample. The voltage V_y across sample capacitor C_o is proportional to the charge Q by $V_y = Q/C_o = (A/C_o)P \propto P$ (A and P are electrode area and polarization of the sample, respectively). The voltage is examined by the vertical plates of the scope and converted into polarization of the sample; hence the ferroelectric hysteresis loop can be directly shown on the oscilloscope. In the Sawyer-Tower circuit, the reference capacitor C_o will induce a back voltage to the sample, and a parasitic capacitance C_p is inevitable during the charge and discharge process, which will perturb the ferroelectric hysteresis. To overcome these shortcomings, an integrated circuit with the virtual ground technique is implemented for the Premier II-type ferroelectric hysteresis loop measurement system designed by Radiant Company. Using this measurement system, the ferroelectric samples can be effectively and accurately measured with a frequency range of 0.03-100 kHz, charge range of 0.80 fC-5.26 mC, and voltage range from ~10 to 10 kV.

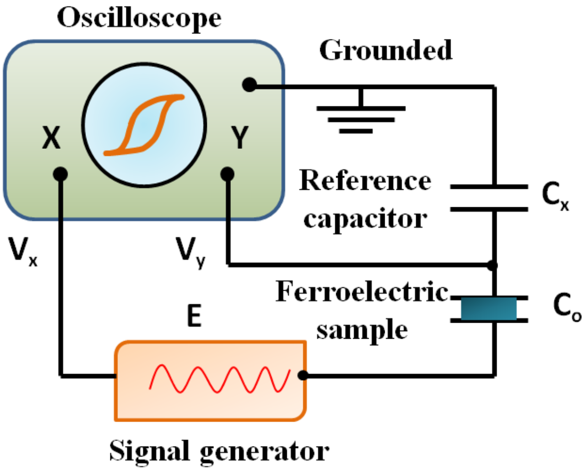

Fig. 2.7. Schematic diagram of Sowyer-Tower circuit for the P-E loop measurement.

In this work, field induced polarization (PE hysteresis loop) are measured at 50 Hz using Precision workstation of Radiant Technology, USA. For low temperature PE loop measurement, ceramic sample is kept in cold finger set up merged in liquid nitrogen and temperature of the sample is measured using RTD sensor mounted directly on the ground electrode of the sample fixture. All the HP-sintered ceramics are tested up to maximum 15 kV/cm external field applied at 50 Hz. Application of more than 15 kV/cm at lower frequencies are not carried out due to sample fixture limitation.

2.9 Magnetization (SQUID/VSM)

Magnetization measurements of magnetic samples are performed using Vibrating Sample Magnetometer (VSM) and Superconducting Quantum Interference Device (SQUID) magnetometer. The basic working principle of VSM is based on Faraday's Law of Induction (i.e. changing magnetic flux produces an electric field). The generated electric field can be measured that gives information about the changing magnetic field. A VSM works by first placing the sample to be studied in a constant magnetic field. Magnetic sample will be magnetized in the magnetic field by aligning the individual magnetic spins or the magnetic domains under the application of field. The magnetic dipole moment of the sample generate magnetic field around the sample (sometimes called the magnetic stray field) and as the sample vibrates (i.e. moved up and down), the magnetic stray field will be changed as a function of time and a set of pick-up coils will sense the same. According to Faraday's Law of induction the alternating magnetic field will cause an electric field in the pick-up coils. This current is directly proportional to the magnetization of the sample. The induction current is amplified by a transimpedance amplifier and lock-in amplifier. The assorted components are connected to computer interface. By means of controlling and monitoring software, the system can show the data on how much the sample is magnetized and how its magnetization depends on the strength of the constant magnetic field [65].

SQUID is a device used for measuring very small magnetic signals or magnetic moments via the quantum interference effect of the superconductor, due to its sensitivity to the magnetic flux [65]. The fundamental building block of the SQUID is called Josephson tunnel junction, which consists of two pieces of superconductors divided by a thin barrier layer. When the Josephson tunnel junction is attached to a superconducting circuit, a kind of macroscopic quantum interference phenomenon takes place i.e., the voltage across the Josephson tunnel junction displays a periodic function with the change of magnetic flux inside the circuit. When a magnetic sample is moving in the superconducting coil, the change in the external magnetic flux will induce a change in superconducting current in the circuit. Due to the coupling attenuation in the SQUID, the changed current will change the magnetic flux in the Josephson tunnel junction and finally change the voltage of the device. SQUID is actually a magnetic flux-voltage converter which can output voltage with amplitude proportional to the detected magnetic signal, as shown in Fig. 2.8(b). The minimum magnetic flux which can cause quantum interference phase change in the Josephson tunnel junction is a single flux quantum (μ_o = 2.07 x 10^{-15} Wb), thereby the SQUID has an ultra-high-sensitivity in detecting the magnetization.

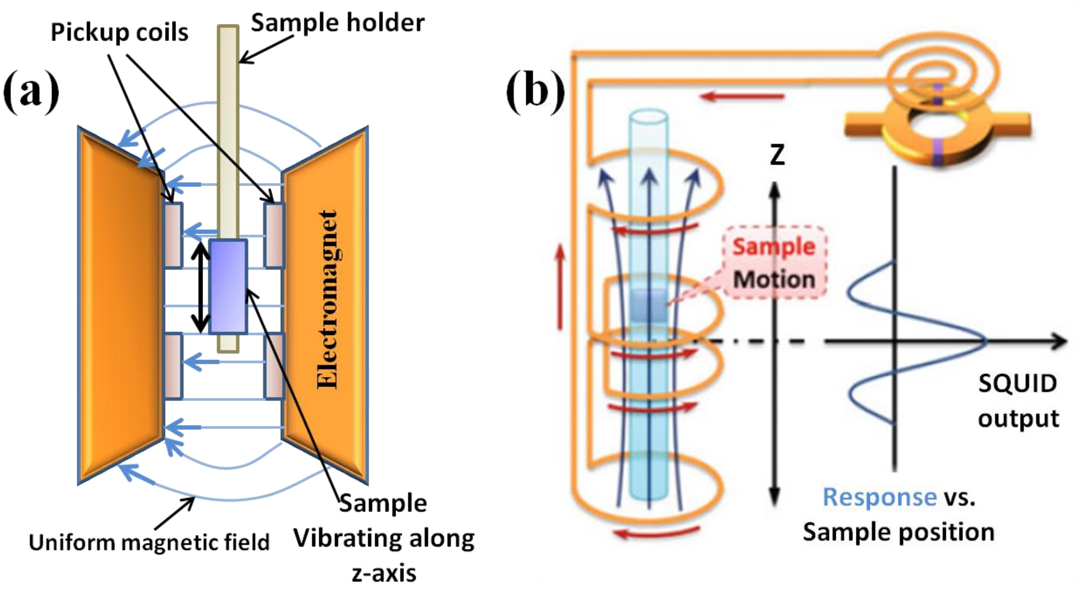

Fig. 2.8. (a) Schematic diagram of vibrating sample magnetometer (VSM), (b) basic principle of SQUID magnetometer

In addition to the function of accurate magnetization measurement, the VSM and SQUID are also an integrated magnetic property measurement system (MPMS) controlled by a computer with the ability of measuring all kinds of magnetic properties, such as saturated magnetization, coercivity, Curie temperature, and susceptibility, under variable temperatures and magnetic fields. The MPMS employs a heater and liquid helium cooling system to control the temperature and utilizes the superconducting coil to generate strong and precision magnetic fields.

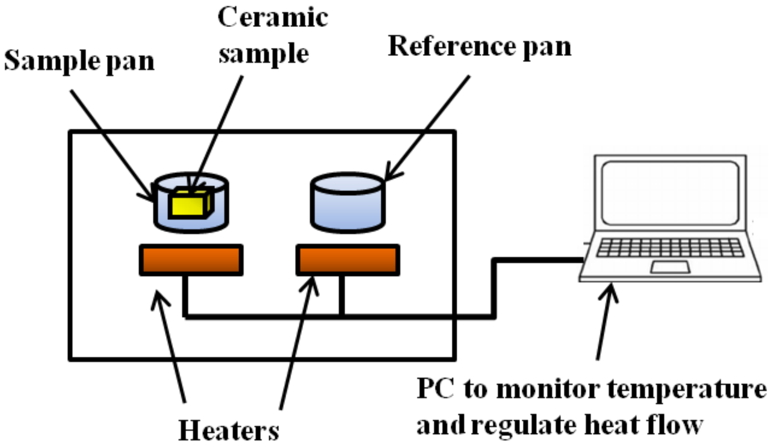

Fig. 2.9. Schematic diagram of DSC set up for heat capacity measurement

2.10 Differential scanning calorimetry (DSC)

Differential scanning calorimetry (DSC) is one of the thermo-analytical techniques used to determine the temperature and heat flow associated with transition in materials as a function of temperature and time. This measurement provides qualitative and quantitative details about physical and chemical changes that involve endothermic or exothermic processes or changes in heat capacity. The heat capacity of a substance is defined, as the quantity of heat energy required to raise the temperature of one gram of the substance for one degree centigrade without changing its state. In DSC, only a few mg of material are required to run the analysis. A differential calorimeter measures the heat of sample relative to a reference. A differential scanning calorimeter heats the sample with a linear temperature ramp. DSC is a technique in which the difference in the amount of heat required to increase the temperature of a sample and reference are measured as function of temperature. Both the sample and reference are kept at approximately the same temperature throughout the experiment. Generally, the temperature program for a DSC analysis is designed such that the sample holder temperature increases linearly as a function of time. DSC is the most often used thermal analysis method, primarily because of its speed, simplicity, and availability.

In present study, low temperature heat capacity (LT-C_p) of Gd-substituted PMN ceramic pellets is measured in the temperature range of 120 - 300 K using a commercial differential scanning calorimeter (STAR^E DSC-1, Mettler Toledo) at the heating rate of 2 ^{o}C/min. For heat capacity measurements, flat ceramic sample is stuck in the sample-pan using Si-grease, and the LT-C_p data is recorded during the warming mode; grease contribution subtracted online using the reference pan with ~same-quantity of the grease.

Chapter 3

Microstructural, vibrational, dielectric and ferroelectric properties correlations in hot-pressed PMN ceramics

3.1 Introduction

In ferroelectric and relaxor ferroelectric ceramics, grain size has been reported to influence the dielectric permitivity, spontaneous polarization and piezoelectric properties [66-70]. Reduction in the ε' with reduction in the grain size has been explained by using a core-shell model, where presence of a dead grain boundary layer on the surface of each grain is assumed. The dead grain boundary layer has lower permittivity and is possibly composed of amorphous PbO or pyrochlore second phase. For PMN, reduction in grain size leads to decrease in the maximum dielectric permitivity (ε_m) and high temperature shift of the T_m (temperature of ε_m), that has been described by pinning of the PNRs by the grain boundaries in small sized grains, which prevent its flipping. Carreaud *et al.* [68] reported the disappearance of dielectric relaxation and vanishing of the correlations between polar nanoregions PNRs below 30 nm grain size of PMN. It is also suggested that continuous disappearance of the correlation among the PNRs due to continuous reduction of the grain size leads to non interacting PNRs state. Moreover, Grigalaitis *et al.* [69] has shown a progressive transformation from the Vogel-Fulcher like to the Arrhenius like (super paraelectric state) slowing down of the PNRs dynamics in the PMN with reduction of the grain size from 2 μm to 15 nm. Interestingly, ferroelectric to relaxor transformation is also observed with reduction of the grain size in solid solution PMN-PT(65/35) [70]. Smaller correlation length has been reported in small sized grains, which is responsible for transformation of long range to short range order.

The nanoscopic heterogeneity is believed to be an inherent part of relaxors, but the mechanisms of how CORs appear and inability of the PNRs to grow to micron size below the Tm in zero-field is still not clear. It is also not clear at what temperature the CORs develop in PMN and how the size of the CORs relate with the sintering temperature. It is believed that the statistical distributions of the PNRs and CORs play critical role in exhibiting typical relaxor behaviour of PMN. The purpose of the present study is to investigate origin of the CORs in hot pressed PMN and how sintering temperature affects the size of the CORs, PNRs and relaxor properties. Present study clearly reveals the presence of the CORs and relaxor-like dielectric characteristics in PMN ceramic hot pressed at 800 °C under 100 MPa, which then thoroughly characterized for microstructural, dielectric and ferroelectric properties.

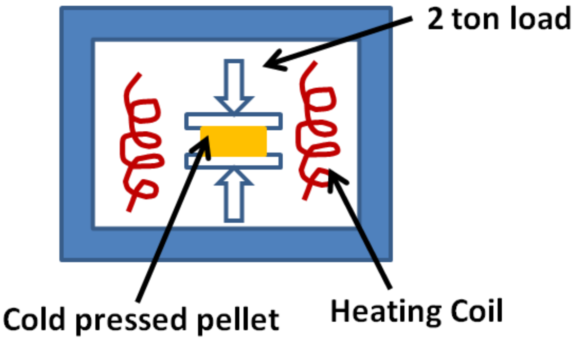

Fig. 3.1. Schematic diagram of HP sintering set-up

3.2 HP sintered ceramic sample preparation

Lead magnesium niobate (PMN) calcined powder is synthesized by the Columbite precursor method using high purity chemicals: PbO (99.9%), MgO (99.95%), Nb2O5 (99.9%) as described in [ref. (59)]. Single perovskite phase has been confirmed in the PMN powder calcined at 800 °C for 2 hours. The calcined powder is mixed with polyvinyl alcohol (PVA-3mol%) binder and pressed into cylinders (15 mm diameter with 5-6 mm thickness) using a uni-axial pressure of 200 MPa. These green ceramics are first heated at 450 °C for 4 hours to remove binder and then hot pressed (HP) under 100 MPa uniaxial pressure at different temperatures from 800 °C to 1200 °C for 2 hours. The PMN ceramic hot pressed at 800, 900, 1000, 1100 and 1200 °C are designated as HP800, HP900, HP1000, HP1100 and HP1200. The density of sintered pellets is determined by liquid displacement method (the Archimedes Method). The density of the ceramic is found to increase from 76% to 99% of the theoretical value with increasing the HP sintering temperature.

Table 3.1. Variation of the lattice parameter, % pyrochlore phase, density, grain size, dielectric properties, and field induced polarization of hot pressed PMN ceramics.

PMN Samples	**Lattice Parameter (Å)**	**% Pyro**	**Density % of Theoretical**	**Grain Size (μm)**	***f* = 1 kHz**		**P_{max} ($\mu C/cm^2$) E=15kV/cm**
					ε'_m	T_m **(K)**	
HP800	4.048	1.7	78%	1.1	8800	278	9.0
HP900	4.047	1.9	95%	1.2	19900	271	13.6
HP1000	4.047	-	98%	1.3	21000	268	16.3
HP1100	4.047	-	99%	1.5	24500	266	16.6
HP1200	4.047	-	99%	2.8	25000	263	16.8

3.3 Results and Discussion

3.3.1 SEM

Microstructure images recorded from the fractured surface of HP800 to HP1200 samples are shown in Fig. 3.2. For HP800, grains are spherical-like displaying large open pores, which is consistent with its density reported in Table 3.1. On the other hand, well defined large grains with minimal open porosity are seen for HP1200. Increase in the hot-pressing temperature reveals change in the morphology of the grains from smooth grain surface to well defined facets of the grains having sharp grain boundaries. It may be noted that change in the grain morphology of HP800 and HP1200 is consistent with the first to third stage of sintering as the temperature is increased. Average grain size has been measured using the linear intercept method. Increase in HP sintering temperature from 800 to 1200 °C causes an increase in the average grain size from 1.1 μm to 2.8 μm. These images clearly reveal minimal porosity indicating good sintered ceramics for all the samples except HP800. Table 3.1 also compares the average grain size and the sintered density observed for the HP-PMN sample.

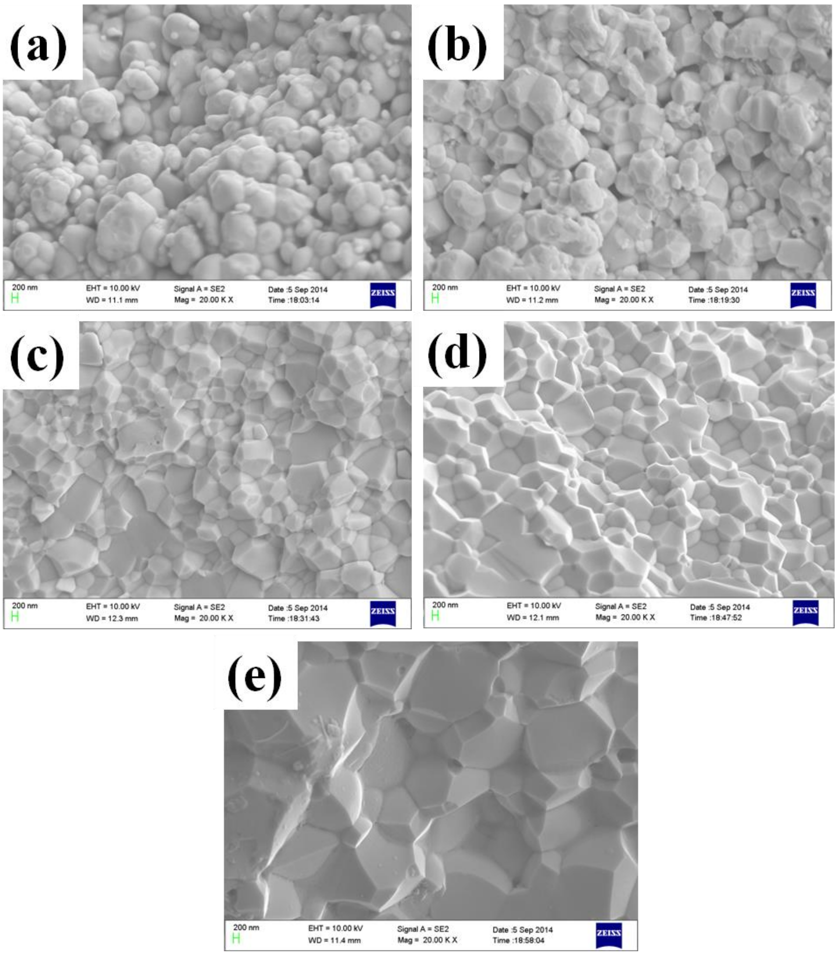

Fig. 3.2. FESEM micrograph of fractured surface of hot pressed PMN ceramics sintered at different temperatures a) HP800, b) HP900, c) HP1000, d) HP1100, and e) HP1200.

3.3.2 XRD

Figure 3.3 compares room temperature X-ray diffraction (XRD) pattern of HP800 to HP1200 ceramics. All the major peaks are indexed with the perovskite phase of the PMN

(JCPDS 27-1199) confirming pseudo-cubic crystal structure having Pm3m space group. A small amount of pyrochlore phase (JCPDS 37-0071, marked by *) has been observed for the HP800 and HP900 ceramics. The relative intensities of the (222) pyrochlore peak (IPyro) and the (110) perovskite PMN peak (IPMN) have been used to determine the volume fraction of pyrochlore and perovskite phase using Eq. 3.1 and are presented in Table 3.1.

$$Pyro/PMN\ (\%) = \frac{(I_{Pyro/PMN})}{I_{Pyro}+I_{PMN}} x100 \tag{3.1}$$

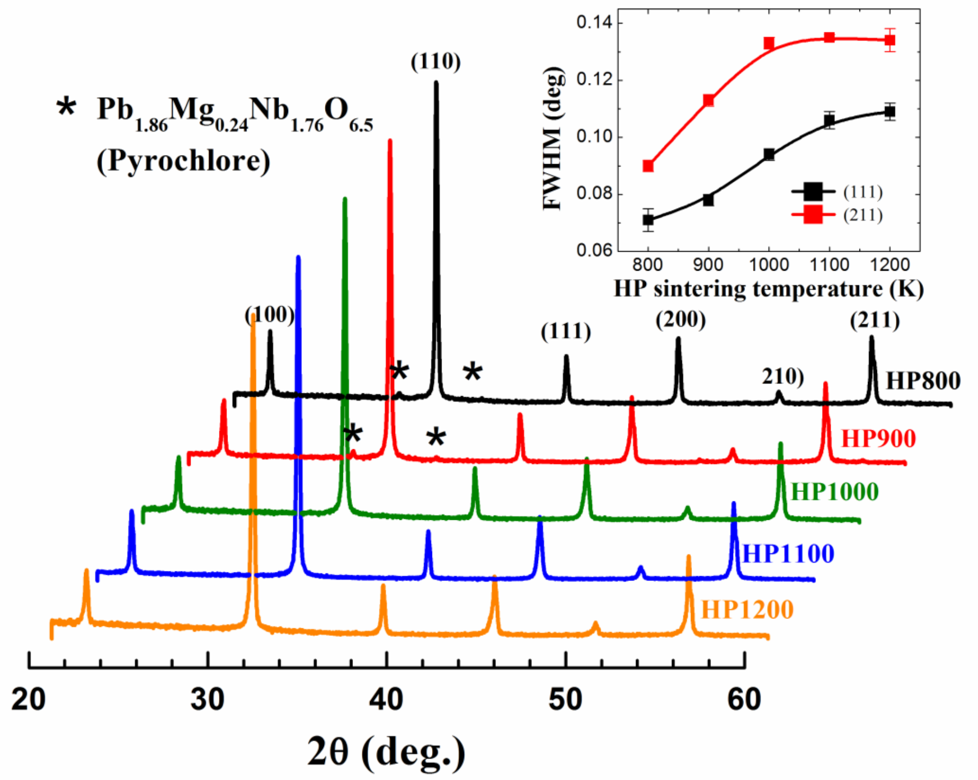

Fig. 3.3. Comparison of XRD patterns of Hot pressed PMN ceramics sintered at different temperatures from 800 ºC to 1200 ºC (HP800 to HP1200) and indexed using JCPDS 27-1199; secondary pyrochlore phase present in HP800 and HP900 are highlighted using '*'. Inset shows FWHM of (111) and (211) peak (after subtracting instrumental broadening) against HP-temperature.

The pyrochlore phase < 2 wt.% for the HP800 and HP900 ceramics may be due to poor control of environment for controlling lead oxide loss during sintering. Single perovskite phase has been obtained in all the other PMN ceramics hot pressed above 900 ºC, which is also evident in Fig. 3.3. In the structural analysis, Pm3m symmetry is considered for the perovskite phase. No change in the lattice parameter is found with increasing hot pressed temperature. The lattice constant (*a* ~4.0467 Å) has been found consistent with earlier reports, where no grain size effect on the crystal lattice parameter is reported in the PMN having particle size greater than 15 nm [68].

The Full Width at Half Maximum (FWHM) of all the major peaks are found to increase with increasing temperature of hot press. The inset of Fig. 3.2 shows variation of FWHM for (111) and (211) peaks after subtracting the FWHM of standard (Si) sample (removing instrumental broadening). It depicts enhancement in the FWHM from 0.071^o to 0.109^o for (111) and 0.09^o to 0.134^o for (211) with increasing the HP temperature from 800 ^oC to 1200 ^oC. It is generally believed that increase in the FWHM is correlated with grain size and/or strain [71]. Since the average grain size is larger than 1 μm and observed to increase with the HP temperature, therefore the increase of the FWHM implies enhancement in strain in the HP PMN ceramics.

3.3.3 TEM

Presence of the PNRs and the CORs in HP PMN ceramics is directly visualized using <110> zone selected area electron diffraction (SAED) pattern along with bright and dark field TEM imaging. The TEM observations have been used to study the effect of HP sintering temperature on the local chemical ordering of the B-site cations. Figure 3.4(a-i) represents comparison of the bright-field, SAED pattern and dark-field imaging of HP800, HP900, and HP1200 ceramics. Figure 3.4(a-c) shows local random contrasts representing the polar nano-domains at room temperature. The average size of these polar nano-domains is measured to be less than 5 nm, which is consistent with the earlier reports describing its presence below the Burns temperature (T_B ~ 650 K). In comparison to HP800, it is also observed that number-density of nano-regions is increased with increasing HP sintering temperature; implying increase of the PNRs. Increase of the number-density of PNRs is also consistent with Raman spectroscopic analysis as reported in the following section. These PNRs are an order of magnitude smaller than a typical FE domain, which is in agreement with the earlier reported TEM study on PMN and other Pb-based relaxors [72].

Table 3.2. Parameters of the Curie-Weiss law, Quadratic law (Eq. 2) and Variation of ΔT_m (=$T_{m100kHz}$ - T_{m100Hz}), $\Delta \varepsilon_m$ (= ε_{m100Hz} –$\varepsilon_{m100kHz}$) and Mydosh parameter “*K*” (=ΔT_m / (T_m x Δlog (*f*))) for various HP sintered PMN ceramics.

PMN Samples	**Curie-Weiss Law**		**Quadratic Law**			**ΔT_m (K)**	**$\Delta \varepsilon_m$**	**“*K*”**
	C x 10^5 (K^{-1})	**θ_{CW} (K)**	**T_A (K)**	**ε_A**	**δ_A**			
HP800	1.1719	380.3	268.7	8990	57.7	11.3	872	0.013
HP900	2.0153	387.5	259.4	20773	50.5	14.0	2639	0.015
HP1000	1.7204	381.6	255.5	22061	48.9	14.2	3236	0.016
HP1100	1.8901	383.8	246.9	26739	47.5	15.0	4707	0.017
HP1200	1.5455	387.4	246.7	26723	44.1	14.8	4913	0.017

According to the chemical formula of PMN ($PbMg_{1/3}Nb_{2/3}O_3$), 1:2 ordering of Mg/Nb is anticipated as reported for $BaMg_{1/3}Nb_{2/3}O_3$. Instead of 1:2 stoichiometric ordering, non-stoichiometric 1:1 ordering has been reported for the PMN so far indicating FCC symmetry of the superstructure with doubling of the unit cell in direct-space, where Mg and Nb are sitting in alternate layers stacked along <111> according to the widely accepted ‘*random layer model*’ [13,73-75]. Figure 3.4(d-f) compares the <110> zone SAED patterns corresponding to HP800, HP900, and HP1200 ceramics. Apart from the allowed strong reflections, originating from the basic perovskite structure, extra weak spots at (½½½) reciprocal positions along <111> (F-spots, super-lattice reflections) are also clearly evident, as marked by arrow. These super-lattice reflections signify local chemical-ordering in some regions of the sample. Such ordering also causes doubling of the unit cell. Presence of these F-spots even for HP800 sample clearly reveals that nonstoichiometric ordering is inherent to PMN ceramic. It occurs during calcination itself and remains unaffected even after high temperature sintering. Any change in the intensity of F-spots signifies change in the size of

CORs. Figures 3.3(d-f) do not show any vivid variation in intensities of F-spots with HP sintering temperature. The intensity of the F-spot is identical to that of the atmospheric pressure sintered PMN sample (at 1200 °C) reported earlier [59]. The invariance in the intensity of (½½½) super-lattice reflections with HP sintering implies that the size CORs does not change, which is also confirmed further with dark field images. Figure 3.4(g-i) shows dark-field image collected at room temperature using the (½½½) super-lattice reflections for HP800, HP900 and HP1200 ceramics, respectively. In these images, the white spots representing nonstoichiometric 1:1 Mg/Nb ordered CORs are dispersed randomly in disordered matrix and confined to domains less than 5 nm. The reason for stability of the CORs in PMN against coarsening, arising upon thermal annealing, is reported to relate with its inability to undergo phase-separation into perovskite and pyrochlore.

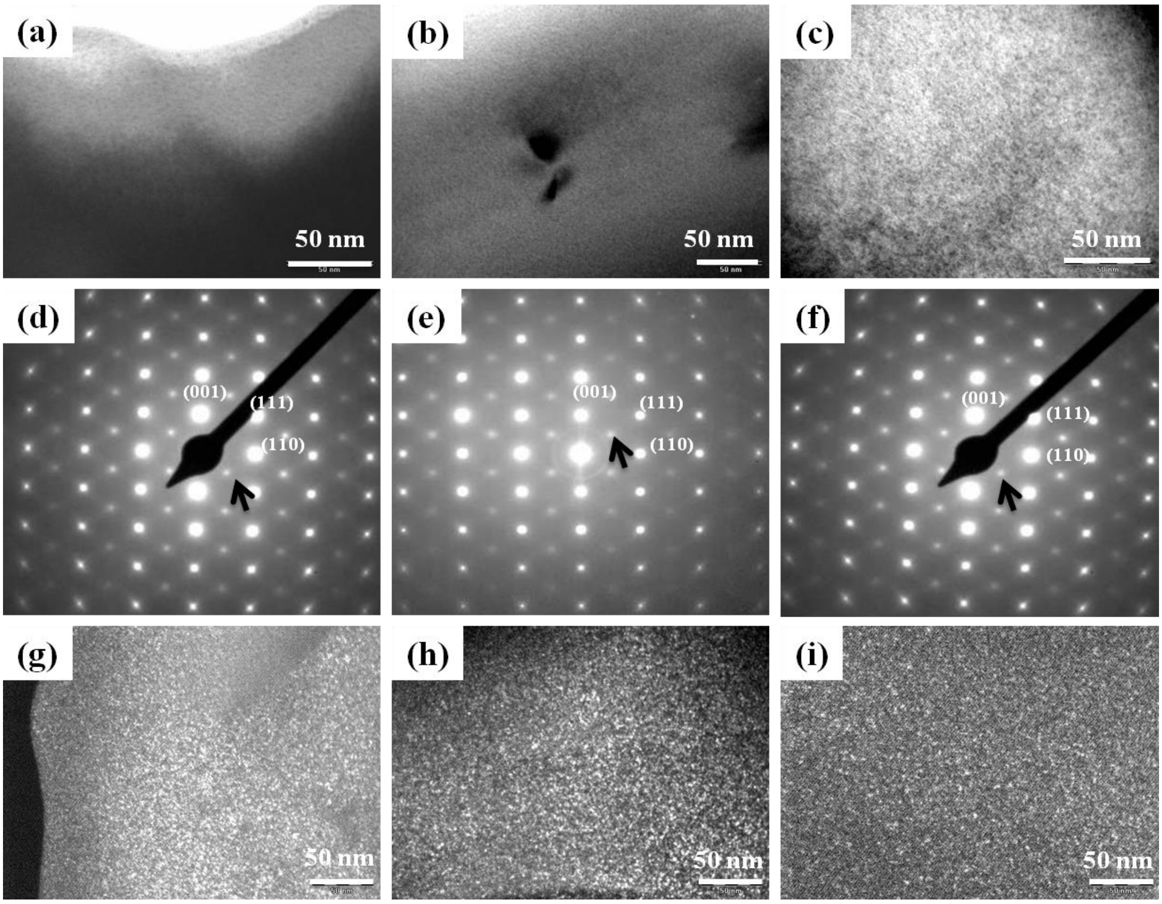

Fig. 3.4. (a-i) Comparion of the bright field images (a-c), selected area electron diffraction along <110> unit axis (d-f) and dark field images (g-i) for HP800, HP900 and HP1200 ceramics. Presence of superlattice reflection along ½ <111> axis is shown by an arrow.

TEM studies thus show the presence of F-spots in HP800 samples, which is hot pressed at the temperature of the calcination, revealing that the nonstoichiometric CORs as inherent part of PMN and remains unaffected even after sintering. There is no change in the intensity of (½½½) superlattice reflection and the size of nano-regions in dark-field images. These results imply that 1:1 Mg/Nb non-stoichiometric CORs are stable and do not get influenced by HP sintering temperature. The consequences of enhancement of the PNRs on dielectric properties are discussed in next section.

3.3.4 Raman Spectroscopy

Raman scattering spectroscopy is an effective tool to investigate the local structures of Pb-based mixed perovskite materials, where the local symmetry is different from the global symmetry. Raman spectra of the PMN has been reported in which a major broad bands below 1000 cm^{-1} are observed because of the site, chemical and structural disorder. The Raman spectrum of all the hot pressed PMN ceramics, as compared in Fig. 3.5(a), reveals many broad and overlapping Raman bands, indicating the presence of large disorder and different local structure, because for an ideal cubic perovskite ABO_3 structure with Pm3m space group, the first-order Raman modes are forbidden by symmetry [76]. Origin of the Raman bands of PMN is due to the CORs and PNRs with Fm3m and R3m space group, respectively. Based on the space group, group theory analysis suggests the presence of 20 active modes: 4 active Raman modes ($A_{1g} + E_g + 2F_{2g}$) for Fm3m symmetry and 16 active Raman modes ($7A_1 + 9E$) originating from R3m symmetry (Z = 2, doubling of unit cell). Four allowed Raman active modes for Fm3m symmetry, are located near 50 & 260 cm^{-1} (F_{2g} modes), 570 cm^{-1} (E_g mode) and 790 cm^{-1} (A_{1g} mode), which are experimentally observed for all the HP-PMN samples and consistent with the earlier report. The multiple heterogeneities i.e., site disorder, presence of the CORs and PNRs, cause the broadening and overlapping of the Raman active modes [76-81].

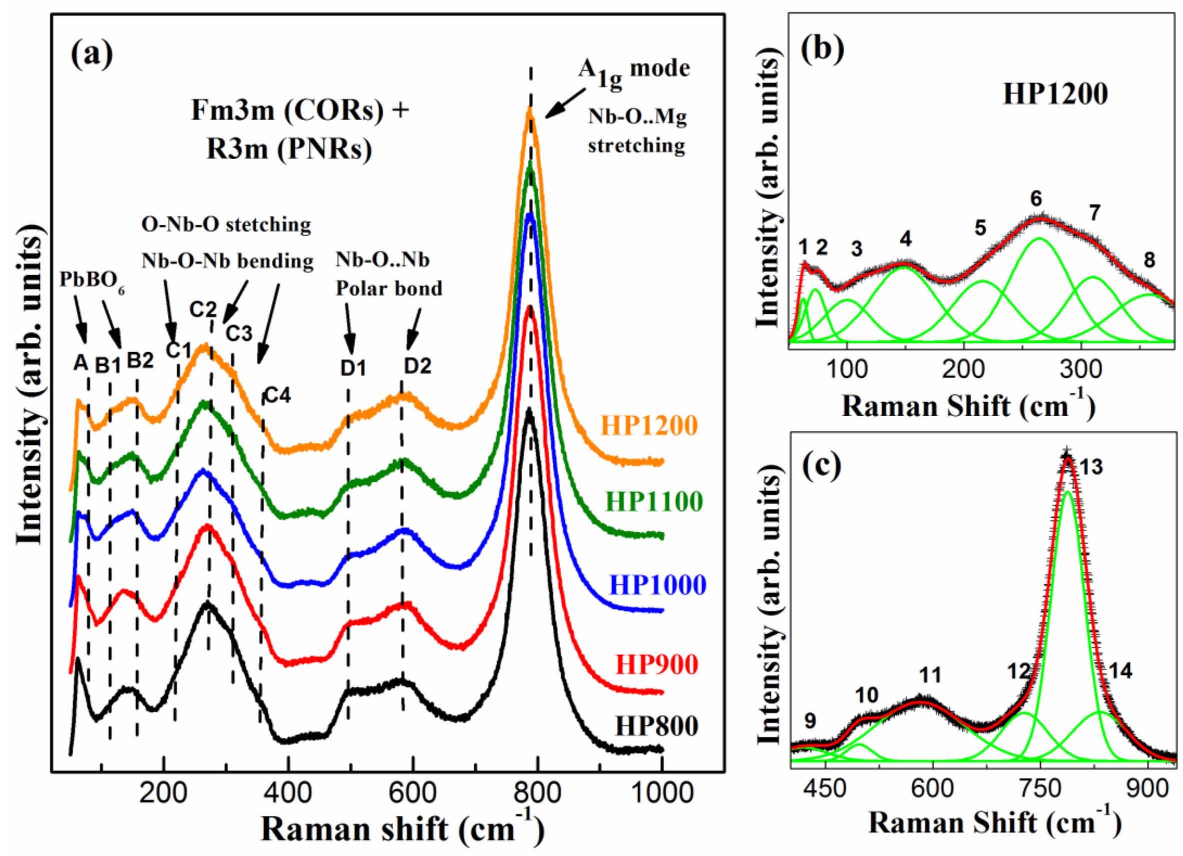

Fig. 3.5. (a) Comparison of room temperature Raman spectra of various HP PMN ceramics, (b,c) Deconvolution of Raman spectra of HP1200; plus, marks represent the raw data, solid red line is the fitted data using Pseudo-Voigt peaks (green color) and the linear background line is given for clarity.

No evidence of disappearance of the old modes or appearance of new modes is observed with increasing HP sintering temperature, confirming the same macroscopic phase structure. These spectra are corrected by Bose factor and normalized by the intensity of 788 cm^{-1} ‘A$_{1g}$’ mode of PMN. For conveyance, the Raman spectra are divided into three regions (i) low frequency region (up to ~ 150 cm^{-1}) attributed to the Pb-BO$_6$ stretching modes, (ii) intermediate frequency region (from ~ 150 to 600 cm^{-1}) consisting stretching mode of Nb-O-Nb bond (near 500 to 600 cm^{-1}) and Mg-O-Mg bond (near 420-430 cm^{-1}) and bending mode of O-B-O bond (near 260-270 cm^{-1}) and (iii) high frequency region (from ~ 600 to 1000 cm^{-1}) assigned to the stretching mode of Nb-O-Mg bonds. The splitting of modes around the 150, 260 and 500 cm^{-1} is a direct indicator of lowering of the local symmetry. The width of the Raman line suggests ordering of the structure.

In consistency with the earlier report, the Raman spectra have been de-convoluted using the Pseudo-voigt peak shape function [79]. Figure 3.5(b,c) shows representative Raman spectra of HP1200 de-convoluted into 14 peaks with varying intensity, wave number and FWHM. The soft modes at ~50 cm^{-1} are not apparent, due to the experimental limitation. Similarly, the Raman spectra are de-convoluted for all HP800 to HP1200 samples. It is observed that number of the modes is less than that expected from the group theory analysis, which is attributed to the overlapping of the Raman modes due to the presence of disorder [78]. Figure 3.6(a,b) shows Raman shift and FWHM of various modes against HP-sintered temperature.

In region I, three modes near 70, 100 and 150 cm^{-1} are generally reported at room temperature. The mode near 70 cm^{-1} has been reported to disappear with increasing temperature above T_m, which reveals local structural phase transition. The intensity of this mode is found to increase with HP-temperature suggesting strong rhombohedral distortion locally. Other two modes near 100 and 150 cm^{-1}, as indicated by dotted line B_1 and B_2 in Fig. 3.5(a), are red shifted (from 110.0 to 100.1 cm^{-1} and 152.3 to 148.3 cm^{-1}) with increasing HP-temperature, also shown in Fig. 3.6(a). The red shift in B_1 and B_2 modes suggests reduction in the force constant of Pb-BO$_6$ bond with increasing HP-temperature, since these modes are assigned to relative motion of Pb-ions against the rigid oxygen octahedral involving motion of B-atom. The intensity and FWHM of ~ 150 cm^{-1} mode is found to increase from 0.12 to 0.20 and 56.9 to 64.2 cm^{-1}, respectively with increasing HP-temperature, as shown in Fig. 3.6(b). The intensity and FWHM of ~150 cm^{-1} mode has been reported to decrease with increasing pressure, which has been correlated with the suppression of the dynamical coupling between the off-centred Pb and B-site cations in PST [82]. An increase in the intensity and FWHM of ~B_2 mode may be related to enhanced coupling between Pb and B-site cations with increasing HP-temperature.

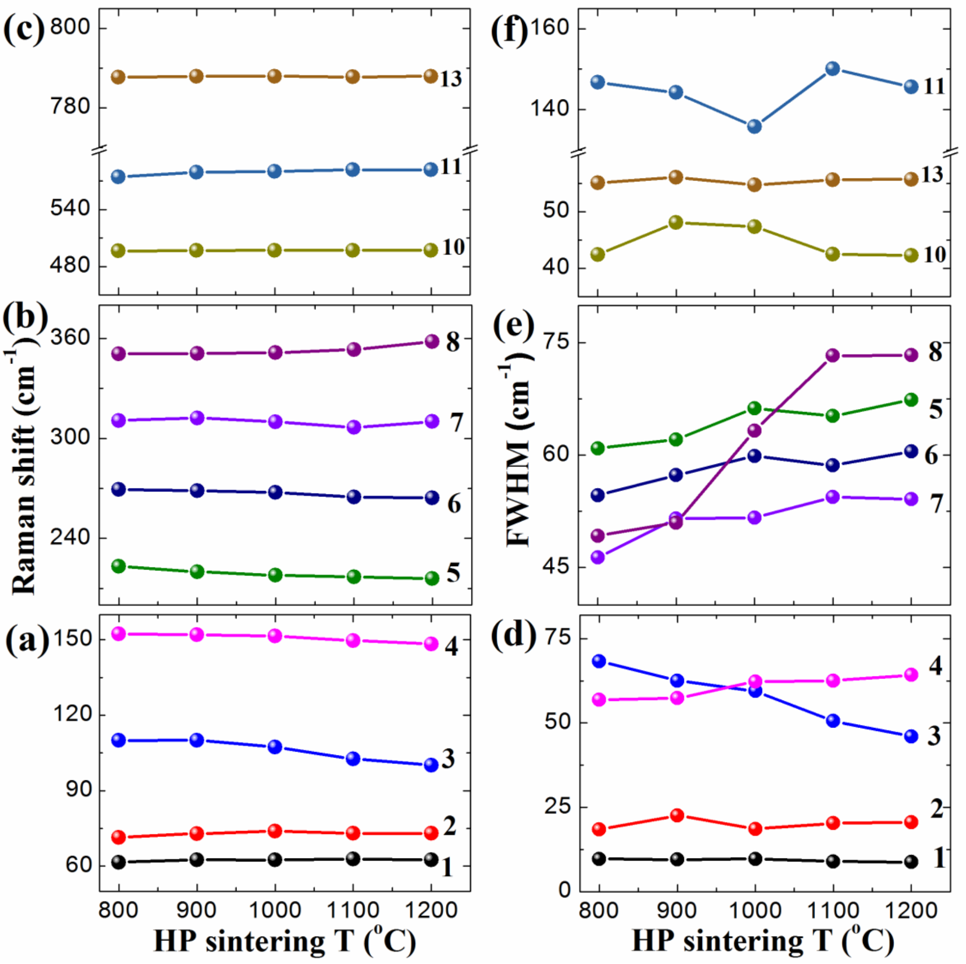

Fig. 3.6. (a-c) HP sintering temperature dependence of few frequency modes, and (d-f) HP sintering temperature dependence of FWHM of various modes for PMN ceramics.

In region II, the wide band from 200 cm^{-1} to 400 cm^{-1} consists of 4 Raman modes in which a broad mode centred near ~265 cm^{-1} related to O-B-O bending has two shoulders at ~223 and ~310 cm^{-1} and the fourth mode is near ~350 cm^{-1}, as marked C_1 to C_4 in Fig. 3.5(a). The Raman shifts of these peaks are consistent with the earlier reports [76-79]. The C_1 and C_2 mode are found red shifted [from 223.1 & 269.4 cm^{-1} (HP800) to 216.0 & 264.4 cm^{-1} (HP1200)]. The C_3 mode does not shift but C_4 mode is blue shifted (from 350.8 to 358.2 cm^{-1}) with increasing HP temperature. The FWHM of C_1, C_2 and C_3 mode is increased ~6-8 cm^{-1} and for C_4 mode it is increased ~24 cm^{-1} with increasing HP temperature. The intensity of C_1,

C_2 and C_3 mode is decreased ~15% but for C_4 it is increased ~30% with increasing HP temperature. The C_2 mode has been shown to shift to higher frequency with La-doping, which is related with decrease reduced mass of B-site [76]. The C_2 mode is observed due to the presence of off-centred displacement of the B-cations from their cubic positions in the PNRs. The shift in frequency of C_2 mode has also been related with cation movement from the centre inside the oxygen octahedron. It is known that the cation movement inside the oxygen octahedron leads to a distortion of the centre-symmetric structure. Shifting of C_2 mode to higher frequency with La-doping in PMN has been related to the cation moving towards the centre, which means decrease in the polar charge separation leading to reduction in the size of PNRs. It may be inferred that shifting of C_2 mode to lower frequency with increasing HP-temperature should cause shifting of B-site cation away from the centre leading to an increase in the distortion, which should result in larger sized PNRs. The Raman activity of C_3 and C_4 modes is caused by dynamical off-centred structural fluctuations due to electron-phonon coupling. The C_3 and C_4 mode are reported to associate with coherent off-centred shifts of Pb-atoms with respect to the oxygen atom planes perpendicular to cubic body diagonal [83]. The intensity ratio of C_4/C_3 mode (ρ) is reported to sensitive to the correlation length of coherent Pb-shifts along <111> directions when vibrations modes in $PbSc_{0.5}Ta_{0.5}O_3$ and $PbSc_{0.5}Nb_{0.5}O_3$ are compared. Larger value of "ρ" has been reported for sample exhibiting correlation among the orientations of the lone pairs within one Pb-O plane if B-site stoichiometric ordering exists. The value of "ρ" has been found to increase from 0.55 to 0.77 exhibiting enlargement of the coherence length of off-centred Pb-shifts with increasing HP-temperature, implying reduction in the disorder at the B-site.

In region III, frequency range of ~500-800 cm^{-1}, two broad peaks are assigned to the Nb-O-Nb stretching mode, as denoted by D_1 and D_2 [Fig. 3.5(a)]. The origin of the Nb-O-Nb stretching mode is ascribed to the displacement of Nb^{5+} from the centre in NbO_6 octahedral cage, which evolves below the Burns temperature and responsible for the formation of the PNRs [77,78]. The separation between D_1, D_2 broad peaks is increased upon cooling, which has been related to the size of the static PNRs [77,78]. With increase of HP temperature from 800 to 1200 ^oC, peak position of D_1 doesn't show any variation but D_2 mode is blue shifted from 573.2 cm^{-1} to 583.2 cm^{-1}. Thus, the separation between D_1 and D_2 increases from 76.7 cm^{-1} to 86.2 cm^{-1}, suggesting an increase in the PNRs size, which is consistent with earlier reports where Gd or La-substitution in PMN has resulted in decrease in the separation between these two modes because of the reduced PNRs size [80]. The intensity ratio (I_{D2}/I_{D1}) increases from 2.52 (HP800) to 3.54 (HP1200) is also consistent with increase in size of the PNRs observed from red-shift of O-B-O bending (C_2) mode.

In region III, the most intense mode is observed near 780 cm^{-1}, which has been designated as A_{1g} mode and assigned to the stretching mode of the B_1-O-B_2 bond (here Nb-O-Mg). Two contributions are reported to associate with the A_{1g} mode, i.e., chemical ordered 1:1 regions and polar vibrations of oxygen-ions in Mg-O-Nb bonds [77]. After fitting Raman spectra of all HP ceramics it is observed that peak position, intensity, and FWHM of A_{1g} mode (~ 788 cm^{-1}) do not show any variation with HP temperature, which implies no change in the size of the B-site cation ordered region. This A_{1g} mode corresponds to Fm3m symmetry and is observed in most of Pb based mixed perovskites. This A_{1g} mode is very sensitive to the B-site ordering [81]. It has been reported that the chemical ordered regions can be enhanced by aliovalent ion (e.g. La^{III}, Eu^{III}, Er^{III} etc.) doping for Pb^{II} or W^{VI} site for Nb^{V} and Mg^{II}- cations. For example, when the ordered regions are increased, the intensity of the stretching mode of Nb-O-Mg bond (~780 cm^{-1}) is increased whereas the intensity of the stretching mode of Nb-O-Nb bond (~600 cm^{-1}) is decreased. The intensity ratio of these two modes is reported to relate directly to the enhancement of the chemically ordered region [76,79]. The intensity ratio of the stretching mode of Nb-O-Mg bond (~780 cm^{-1}) and the intensity of the stretching mode of Nb-O-Nb bond (~600 cm^{-1}) is calculated from the background subtracted Raman data and the ratio is found to remain invariant ~5.1-5.2 with increasing HP temperature from 800 to 1200 °C.

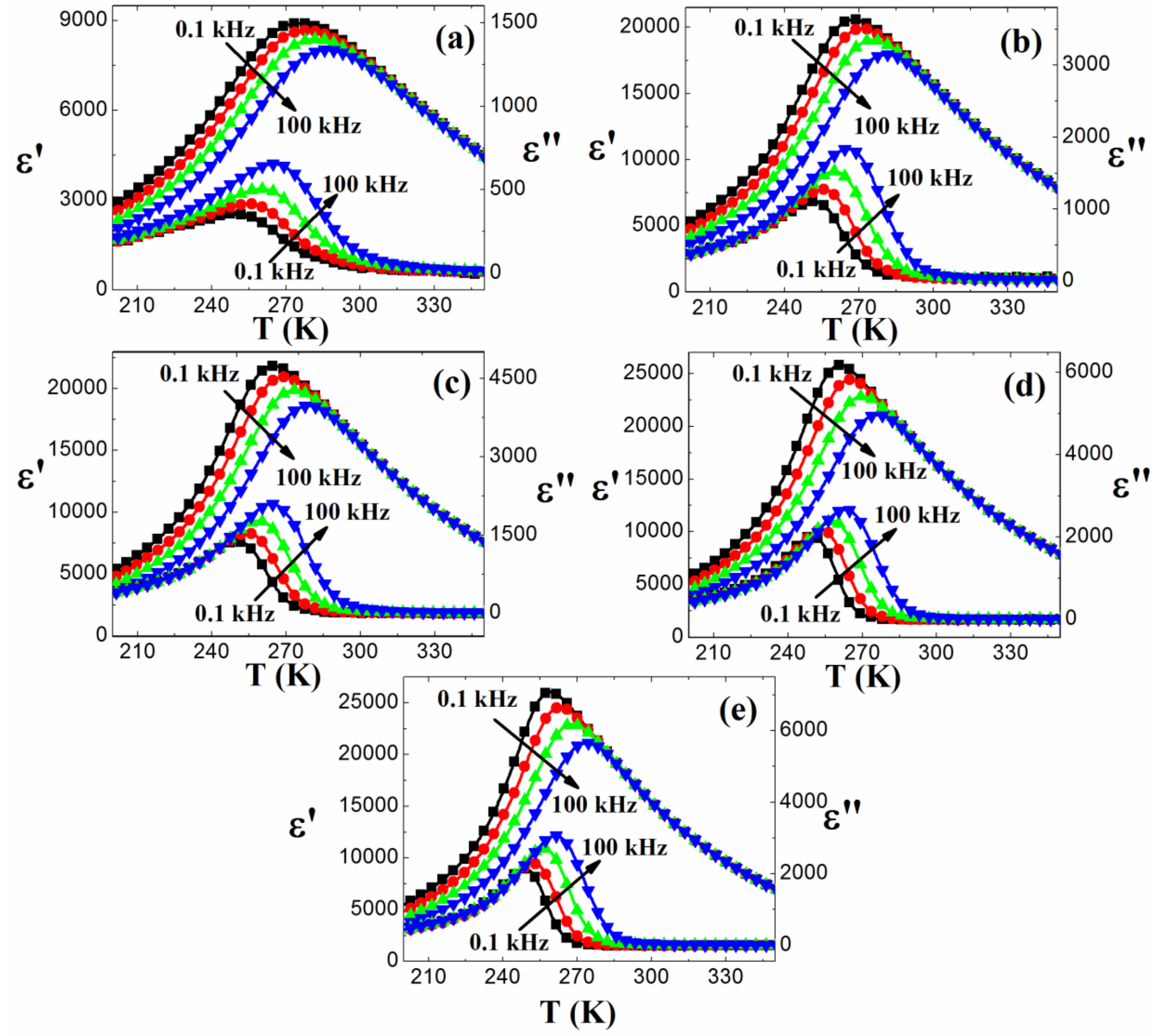

Fig. 3.7. Real and imaginary parts of complex dielectric constant as function of temperature at selected frequencies of hot pressed PMN ceramics sintered at different temperatures, (a) HP800, (b) HP900, (c) HP1000, (d) HP1100, and (e) HP1200.

3.3.5 Dielectric Spectroscopy

Dielectric measurements are carried out to analyse the influence of HP temperature on the relaxor dielectric behaviour of the HP-PMN ceramics. The real (*ε'*) and imaginary (*ε''*) parts of complex dielectric constant (*ε**) as a function of temperature for HP800 to HP1200 ceramics at selected frequencies are shown in Fig. 3.7(a-e). The $\varepsilon'(T)$ and $\varepsilon''(T)$ for all HP samples show broad dielectric maxima (ε_m) with strong frequency dispersion near T_m (T of ε_m peak) i.e. T_m shifts progressively towards higher temperature with increasing frequency. This frequency dispersion clearly indicates that the relaxation process of dynamic PNRs occurs at multiple time scale [3]. Typical relaxor like dielectric characteristics has been observed for HP800 ceramics also. It may be noted that the PMN powder is calcined at 800 ^{o}C and the same powder is hot pressed at 800 ^{o}C. The relaxor like dielectric characteristic of HP800 suggests that the local chemical heterogeneity remains unaffected with the HP-temperature. Figure 3.8(a,b) compares $\varepsilon'(T)$ and $\varepsilon''(T)$ curves at 1 kHz frequency for different hot pressed ceramics. Inset of the Fig. 3.8(b) shows that with increase of the HP temperature, the ε_m increases from 8800 (HP800) to 25000 (HP1200) and the T_m shift from 278 K to 263 K, which is in good agreement with the earlier reports [68]. The ε'_m and T_m at 1 kHz for all HP ceramics are also shown in Table 3.1. Increase in the ε'_m is due to the increase in number or/and size of the PNRs and interaction between them, which is because of increase in the average grain size from 1.1 µm to 2.8 µm. In the later part of this section, this is explained by considering core-shell model. Figure 3.9(a) compares effect of the HP-temperature on the $\varepsilon'(T)$ curves at 1 kHz frequency in reduced form $\varepsilon'/\varepsilon'_m$ vs T/T_m. The broadness around the T_m is reduced with increasing HP-temperature, which implies reduction in the degree of cation's site disorder at the B-site. Decrease in the value of the T_m with increasing HP-sintering temperature is consistent with enhanced correlation among the PNRs. Relaxor dielectric characteristics are generally expressed by degree of diffuseness and correlation length among the PNRs. Interacting PNRs should grow on cooling and enhance their correlation length, leading to a ferroelectric long range ordered (for large correlation length) or short range ordered nano-domains (for smaller correlation length). For ferroelectrics, the temperature dependence of $\varepsilon'(T)$ in paraelectric regions can be related with the Curie-Weiss law [$\varepsilon'(T,\omega)$

= $C/(T - \theta_{CW}]$; where C is Curie constant and θ_{CW} is the Curie-Weiss temperature, are constants, whereas for relaxor ferroelectric, deviation from the Curie-Weiss fitting is reported below the T_B [84], as shown in Fig. 3.9(b) and values of fitting constants are presented in Table 3.2. Recently, modified form of the Curie-Weiss relation (Eq. 3.2) has been shown to fit the $\varepsilon'(T)$ above the ε_m [85].

$$\frac{\varepsilon_A(\omega)}{\varepsilon'(T,\omega)} = 1 + \frac{(T - T_A(\omega))^2}{2\delta_A^2} \tag{3.2}$$

where $\varepsilon_A(>\varepsilon_m)$, $T_A(<T_m)$ and δ_A (called degree of diffuseness) are adjustable parameters, practically independent of frequency and valid for long range of temperatures above the ε_m. Figure 3.9(c) shows fitting of the $\varepsilon'(T)$ above the ε_m to Eq. 3.2 for HP1100 ceramic and the fitting parameters are reported in Table 3.2 along with that for other hot pressed ceramics. The δ_A is observed to decrease from ~55 to 42.5 with increasing HP temperature. Higher value of the δ_A is reported to relate directly with enhancement of the degree of diffuseness [85]. Thus increase in HP temperature leads to decrease in the degree of diffuseness, which is due to lesser chemical/charge disorder at the B-site.

Table 3.3. Corrected dielectric constant, grain and grain boundary thicknesses calculated using series and logarithmic mixing rules for HP PMN ceramics.

Sample	**K_{obs} (1kHz)**	**Porosity (%)**	**K_{corr} (1kHz)**	**Average grain-size (µm)**	**Th-Core (µm)**	**Th-Shell (nm)**	**Ratio core/shell**
HP-800	8800	22	12523	1.1	1.030	70	15
HP-900	19900	5	21471	1.2	1.176	24	49
HP-1000	21000	2	21642	1.3	1.275	25	51
HP-1100	24500	1	24871	1.5	1.486	14	106
HP-1200	25000	1	25378	2.8	2.780	20	139

The reduction in dielectric permittivity with decreasing grain size has been explained by a core-shell model [66], which assumes the existence of a dead layer encapsulating each grains, and permittivity of the layer is much lower than the grain. The dielectric constant and porosity of the sample as a function of HP-temperature is presented in Table 3. It may be noticed that the sample PMN-HP800 has sintered density much lower as compared to all other samples, which has sintered density > 95% of the theoretical value. In order to compare the dielectric constant with the grain size, the dielectric maximum has been corrected for the porosity present in the sample using Rushman and Striven equation [86] given as:

$$K_{corr} = K_{obs} \text{x} \frac{(2+V_2)}{2(1-V_2)} \tag{3.3}$$

where K_{obs} is the experimental value at T_m and V_2 is the volume fraction of porosity present in the sample. Here the porosity is assumed to be not interconnected. The corrected dielectric maximum value for each sample is shown in Table 3.3. The dielectric constant dependency on the grain size in PMN has been explained according to a logarithmic mixing rule [87]:

$$\ln K_{obs} = V_{shell}\ lnK_{shell} + V_{core}\ lnK_{core} \tag{3.4}$$

where K_{shell} and V_{shell} and K_{core} and V_{core} are the dielectric constant and volume of the shell and core regions, respectively. Assuming the K_{core} of 28000 (single crystal of PMN) and a K_{shell} of 300, the grain boundary thickness has been calculated and reported in Table 3.3. It may be noticed that the thickness of the shell decreases from 70 nm to 20 nm and the thickness of the core is increased monotonically. A ratio of core to shell thickness has clearly revealed an increasing trend from 15 to 139 with increasing HP-temperature or grain size, which is consistent with the increased dielectric constant value.

In smaller sized grains, regions near grain boundary may have more probability of restricting thermal activity of larger polar regions, which are associated with the lower frequencies. This means, the dielectric permittivity will have more contribution from the thermally active smaller volume polar regions, which are associated with the higher frequency. This results in shifting of the T_m to higher frequency regime, which is consistent with the increase in T_m observed. A decrease in the dissipation factor for smaller grain sized PMN-HP800 sample is also consistent with this mechanism.

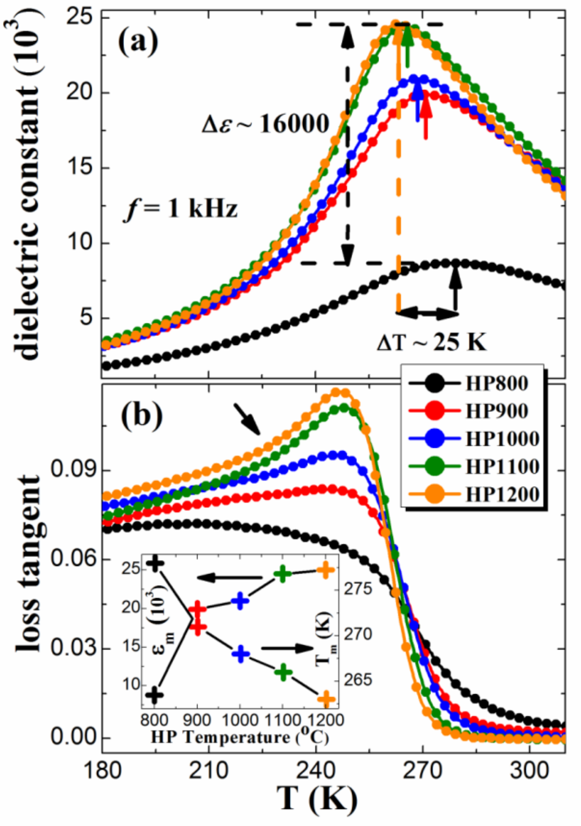

Fig. 3.8. Comparison of temperature dependence of (a) dielectric constant and (b) loss tangent at 1 kHz frequency; inset plots ε_m and T_m at 1 kHz frequency as a function of hot pressed sintering temperature

The strong frequency dependent dielectric behaviour of all HP ceramics is a consequence of statistical distribution of the PNRs over wide range of temperatures. Depending upon the strength of interaction among the polar nano-domains, the frequency dispersion of the T_m can be fitted with (i) Arrhenius relation [Eq. 3.5] if there is no correlation among the PNRs (ii) Vogel-Fulcher relation [(Eq. 3.6] if frustrated interaction among the PNRs leads to freezing of the polar cluster fluctuations at finite temperature (T_f) [54], (iii) stretched exponential relation [Eq. 3.7] if continuous slowing down of dynamics of the PNRs is considered and freezing of the PNRs takes place only at 0 K [88] and (iv) power law of critical dynamics [Eq. 3.8] if frustrated interaction among the PNRs result into a critical slowing down of PNRs dynamics at a temperature (T_g) [89].

$$\omega = \omega_o e^{\left(\frac{-E_a}{k_B T_m}\right)} \qquad (3.5)$$

$$\omega = \omega_o e^{\frac{-E_a}{k_B(T_m - T_f)}} \tag{3.6}$$

$$\omega = \omega_o e^{\left(\frac{-E_a}{k_B T_m}\right)^p} \tag{3.7}$$

$$\omega = \omega_o \left(\frac{T}{T_g} - 1\right)^{zv} \tag{3.8}$$

where, ω_o is attempt frequency ($\tau_o = \omega_o^{-1}$ is the microscopic time associated with flipping of fluctuating dipole entities), E_a is activation energy, k_B is Boltzmann constant, T_f is Vogel-Fulcher temperature where freezing of polar cluster fluctuations take place, p (>1) is related with the degree of dielectric relaxation in relaxors, T_g is glass transition temperature and zv is critical dynamic exponent. Figure 3.9(d) compares fitting of frequency dependence of the $T_m(f)$ to Eq. 3.6-3.8 for all HP ceramics. The corresponding fitted parameters for HP800 to HP1200 are reported in Table 3.4 along with the goodness of fit. The open symbols represent experimental data points and solid line represents the fitted curve. Accurate value of the T_m is determined by fitting the $\varepsilon'(T)$ curve for each frequency in a narrow temperature range around the T_m. It is observed that the fitting parameter (ω_o and E_a) obtained from the Arrhenius relationship fitting do not correspond to any physical significance. The fitting parameter T_f, determined from Eq. 3.6 for HP1200, is in close proximity of ergodic to non-ergodic transition reported earlier for PMN [90]. It has been argued that there might be no freezing of dynamics of the PNRs below the T_f, because the order-disorder transition should have accompanied with an anomaly in the temperature dependence of dielectric constant. No such abnormality in dielectric properties is reported around the T_f so far for the PMN. Thus the $T_m(f)$ for the PMN may not be related with the freezing of the polar nano-domains fluctuations. Here the T_f is considered as the temperature below which the distribution of relaxation time diverges. Decrease in the T_f with increase in the HP-temperature is due to reduce B-site cation disorder. The fitting parameters ω_o and E_a for the HP1200 are consistent with the earlier report [59]. The attempt frequency (ω_o) is found to increase from 10^{12} Hz to

10^{14} Hz with increasing HP-temperature. The attempt frequency (ω_o) beyond > 10^{14} has no physical significance. An increase of activation energy from 0.055 (HP800) to 0.105 (HP1200) can be understood if reduction in B-site cation disorder leading to enhancement in correlation between the PNRs is considered. The value of parameter p is also used to show the interaction and dynamic correlation between the PNRs [88]. The value of p^{-1} characterises the degree of dielectric relaxation strength among normal ferroelectric ($p^{-1} = 0$), Debye medium ($p^{-1} = 1$) or pure glassy ($p^{-1} = 2$) and relaxor ferroelectrics ($0 < p^{-1} < 1$) [88]. The validity of this relationship is verified for various relaxor ferroelectric systems, e.g., PMN, PMN-PT, PNN, PNN-PT, La-PMN, Gd-PMN, etc. The fitting parameters obtained from the fitting of $T_m(f)$ with Eq. (3.7) shows decrease of the value of p from 16.6 to 9.7 with increasing HP-temperature, which is consistent with its inverse relation against dielectric strength, as reported among normal ferroelectric, Debye medium, pure glassy or relaxor ferroelectrics. The attempt frequency ~ 10^8-10^9 Hz and activation energy ~ 0.03 eV is also reasonable to its physical process. The stretched exponential power law fitting suggests enhancement in the dielectric relaxation strength with increasing HP-temperature. Figure 3.8(d) also compares the fitting of $T_m(f)$ with Eq. 3.8 for all HP ceramics and ω_o, $z\nu$ parameters are presented in Table 3.4. The fitted parameters of HP800 are ω_o ~ 5.37±7.1 x 10^{16} Hz, T_g = 264.5±0.6 K, and $z\nu$ = 10.0±0.4. With increasing HP temperature, the ω_o remains unchanged ~10^{16} Hz. Recently in PMN, nonergodic ferroelectric cluster glass ground state (also known as "super-dipolar" glass) is reported to emerge from high temperature PNR ensemble under random electrostatic interaction [91]. A static glass temperature (T_g = 238 K) is reported from fitting of the $T_m(f)$ of ε' to Eq. 3.8 in frequency range 1 x 10^{-3} Hz to 2 x 10^{-2} Hz [50]. The pre-factor "τ_o" and $z\nu$ values are in accordance with the mesoscopic size of the PNR around T_g. The fitting of temperature dependence of the permittivity ε' to Eq. 3.8 in frequencies 10^2 Hz to 10^5 Hz has shown strong deviation above ~245 K for PMN. The parameters "$\omega_o = \tau_o^{-1}$", T_g and $z\nu$ of all other HP ceramics are reported in Table 3.3. It may be noticed that no reduction in "τ_o" ~10^{-17} s is observed, whereas T_g is decreased from 248 to 204 K with increasing HP-temperature, which can be inferred no critical slowing down of dynamics of PNRs ensemble (cluster).

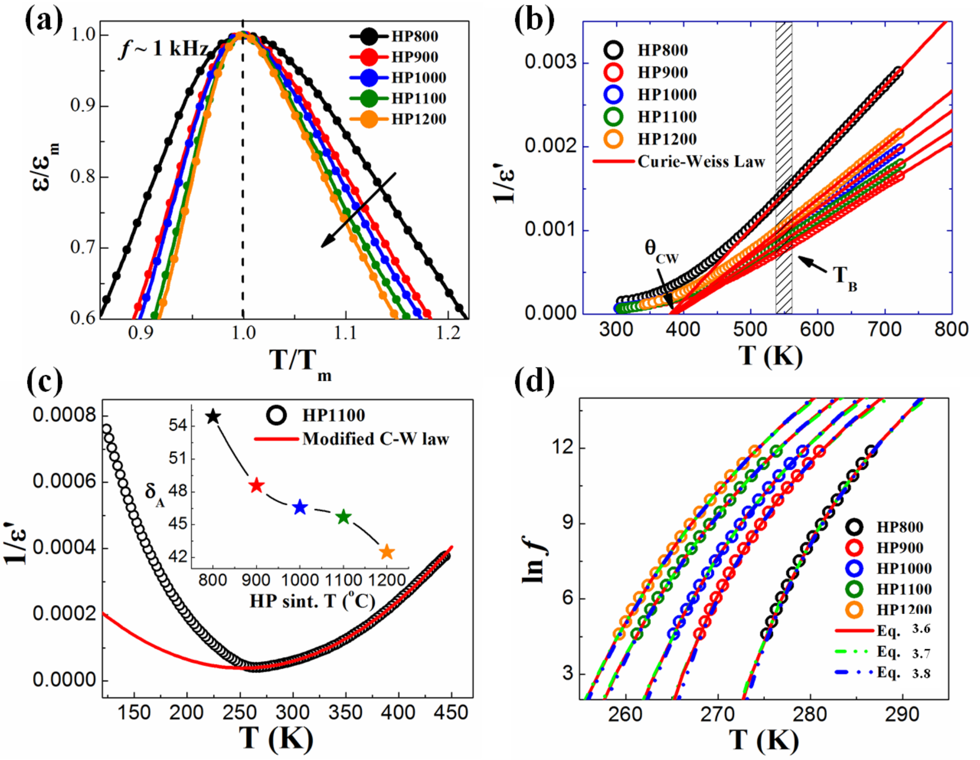

Fig. 3.9. (a) Normalized curve ($\varepsilon/\varepsilon_m$ vs T/T_m) of hot pressed PMN ceramics sintered from 800 °C to 1200 °C, (b) Representative fitting ($1/\varepsilon$ vs T) of HP1100 ceramic sample by Curie-Weiss Law, (c) Representative fitting ($1/\varepsilon$ vs T) of HP1100 ceramic sample by Eq. (3.2); inset of Fig. 3.8(c) shows δ_A variation of HP sintering temperature, (d) Comparison of the Vogel-Fulcher (red curve), and stretched exponential power law (green curve) and critical slowing down model (blue curve)for all HP PMN ceramics where open symbols represent the temperature of $\varepsilon_m(T_m)$ in the frequency range 0.1-100 kHz.

The frequency dependent $\varepsilon'(T)$ data is further analysed to get more insight into the PNR dynamics. The frequency dependent T_m between two frequencies is defined by an empirical (also known as Mydosh parameter) parameter "K" = ΔT_{max} / [T_{max} x $\Delta\log(f)$], which has been reported to distinguish between spin glass (SG), cluster glass (CG) and superparamagnetic (SPM) states in magnetic materials [92]. The smaller values of "K" ~0.005-0.01 is generally reported for SG with strongly interacting spins, ~ 0.03-0.06 for CG weakly interacting spins and larger value > 0.1 for non-interacting spins for SPM system [92]. Similarly, the value of

"*K*" can be used to distinguish between dipolar glass, super-dipolar glass (CG) and super-paraelectric (SPE) states. The related shift $\Delta T_{max}/T_{max}$ is calculated with change of frequency between 100 Hz and ~ 150 kHz. The values of "*K*" are presented in Table 3.2, which increases from 0.013 to 0.017 with increasing HP-temperature, indicating an increase in the frequency dispersion of T_m. It seems the PNRs ensemble state is not a dipolar glass state or a non-ergodic ferroelectric cluster-glass state in all HP ceramics. The cooperation between the PNRs is increasing with increasing grain size, which is consistent with increase in $\Delta\varepsilon$ from 872 to 4913, as reported in Table 3.2.

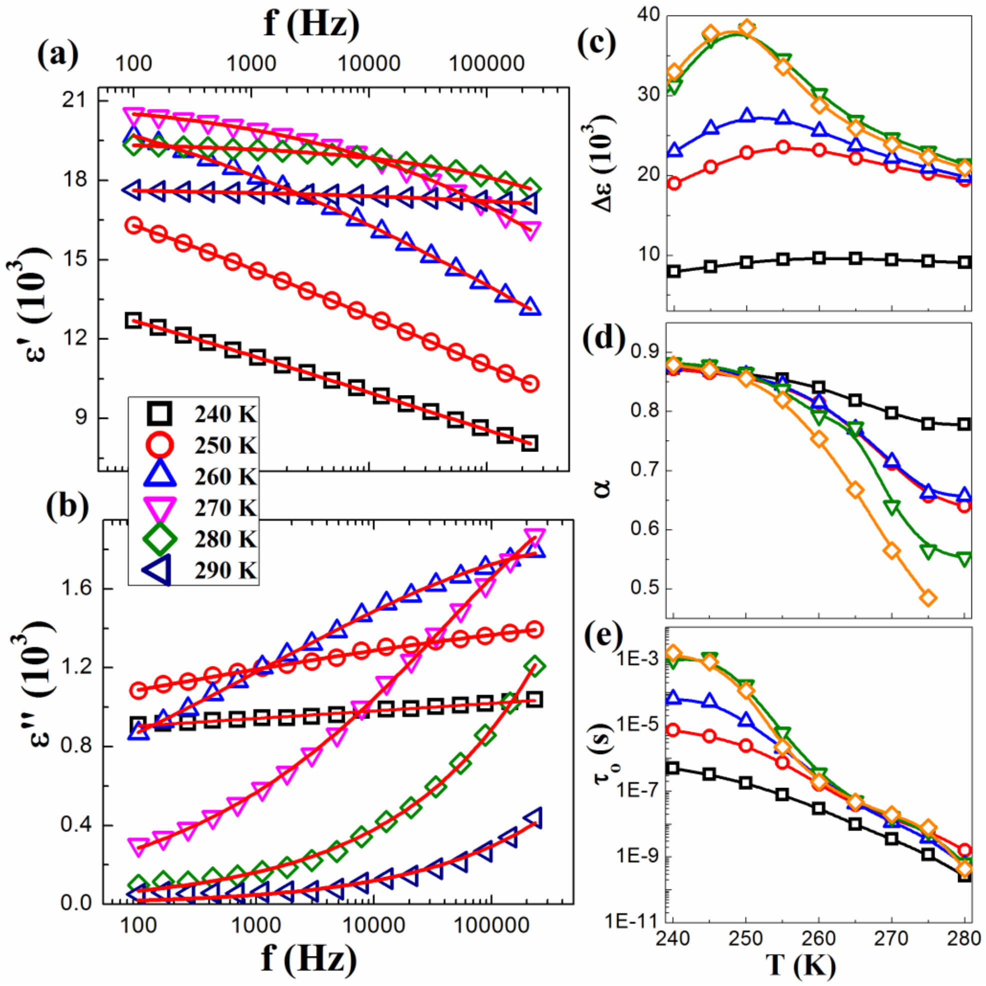

Fig. 3.10. (a,b) Frequency dependence of real (ε') and imaginary (ε'') parts of complex dielectric constant at selected temperatures between 240 K - 280 K for HP 900 PMN ceramic sample, where symbols represent the experimental data points and red solid lines are fitting to Eq. (3.10), (c-e) Variation of the Cole-Cole fitting parameter: (c) $\Delta\varepsilon$, (d) α, and (e) τ_o with temperature for HP PMN ceramics sintered from 800 °C to 1200 °C.

Table 3.4. Parameters of the (a) Vogel-Fulcher [Eq. (3.7)] and (b) power law [Eq. (3.8)], and (c) critical slowing down model [Eq. (3.9)] fit of frequency dependent T_m for various HP sintered PMN ceramics.

PMN Samples	**Vogel-Fulcher model** [Eq. (3.7)]			**Adj. R-square**
	T_f (K)	**E_a (eV)**	**f_o (Hz)**	
HP800	248.8(±1.6)	0.055(±0.006)	2.72(±1.08) x 10^{12}	0.99956
HP900	241.9(±0.9)	0.049(±0.003)	2.83(±1.58) x10^{11}	0.99982
HP1000	230.6(±1.2)	0.076(±0.005)	1.02(±0.68) x 10^{13}	0.99987
HP1100	220.1(±1.3)	0.097(±0.003)	6.09(±3.9) x 10^{13}	0.99991
HP1200	216.4(±1.7)	0.105(±0.007)	2.26(±1.0) x 10^{14}	0.99987

PMN Samples	**Power Law** [Eq. (3.8)]			**Adj. R-square**
	p	**E_a (eV)**	**f_o (Hz)**	
HP800	16.6(±1.1)	0.028(±0.004)	2.53(±0.76) x 10^{8}	0.99945
HP900	16.1(±0.7)	0.033(±0.002)	7.48(±0.39) x 10^{7}	0.99973
HP1000	12.3(±0.4)	0.029(±0.003)	5.47(±0.48) x 10^{8}	0.99988
HP1100	11.7(±0.3)	0.028(±0.001)	3.06(±0.40) x 10^{8}	0.99991
HP1200	9.7(±0.4)	0.030(±0.001)	3.84(±0.55) x 10^{9}	0.99987

PMN Samples	**Critical slowing down model** [Eq. (3.9)]			**Adj. R-square**
	zv	**T_g (K)**	**f_o (Hz)**	
HP800	10.0(±0.4)	264.5(±0.6)	8.56(±7.06) x 10^{15}	0.99967
HP900	8.9(±0.2)	257.6(±0.3)	2.96(±1.12) x 10^{14}	0.99988
HP1000	10.8(±0.4)	250.7(±0.6)	2.49(±1.32) x 10^{15}	0.99984
HP1100	11.7(±0.3)	243.8(±0.6)	2.55(±1.04) x 10^{15}	0.99991
HP1200	12.3(±0.4)	241.0(±0.8)	6.55(±3.44) x 10^{15}	0.99987

In addition, relaxation behaviour is also investigated using Cole-Cole dielectric relaxation model. Figure 3.10(a,b) shows frequency dependence of real (ε') and imaginary (ε'') parts of the complex dielectric constant for HP900 at selected temperatures in between 240 K to 280 K, respectively. The dispersion in the $\varepsilon'(f)$ is observed to decrease with increasing temperature. Correspondingly, a broad peak is observed in the $\varepsilon''(f)$, which shifts to lower frequency with decreasing temperature. A symmetric and narrow distribution of relaxation time has been reported in PMN-PSN-PZN relaxor ferroelectrics only at high temperature ($\geq T_m$(100Hz) +15°C) [93]. Similarly, frequency dependent complex dielectric constant has been fitted to the Cole-Cole relation [34];

$$\varepsilon^*(\omega) = \varepsilon_\infty + \frac{\Delta\varepsilon}{(1+i\omega\tau_o)^{1-\alpha}} \tag{3.9}$$

where $\Delta\varepsilon = \varepsilon_S - \varepsilon_\infty$, ε_S and ε_∞ are the low and high frequency limits of dielectric constant, τ_o is the mean relaxation time, and the parameter α ($0 < \alpha < 1$) indicates the distribution width of relaxation time. Solid lines in Fig. 3.10(a,b) denote the fitting to Eq. 3.9, which shows that Cole-Cole relations give a reasonably good approximation to frequency dependent complex experimental data. Temperature dependence of the Cole-Cole parameters, $\Delta\varepsilon(T)$, $\alpha(T)$, and $\tau_o(T)$ are compared in Fig. 3.10(c-e) for all HP ceramics. Figure 3.10(c) shows increase in the $\Delta\varepsilon(T)$ with decrease in the temperature, which is due to less thermal disordering effect at low temperature. Assuming same value of the higher frequency dielectric constant (ε_∞), the $\Delta\varepsilon(T)$ depends only on static dielectric constant (ε_S), which shows a peak at T_c, below which the dynamics of the PNRs are sluggish and not responding easily to the external stimuli. The T_c shifts to lower temperature with increase in the HP-temperature, which shows that the PNRs are either larger in size or co-operative interaction is increasing with HP-temperature. For HP800, the parameter α is small (~0.78) at 275 K and saturates to 0.9 around ~240 K on cooling, depicting broadness in the distribution of relaxation times. Similar trend is observed for all other HP ceramics and shown in Fig. 3.10(d). The parameter α at T_m(100Hz) +15 °C is

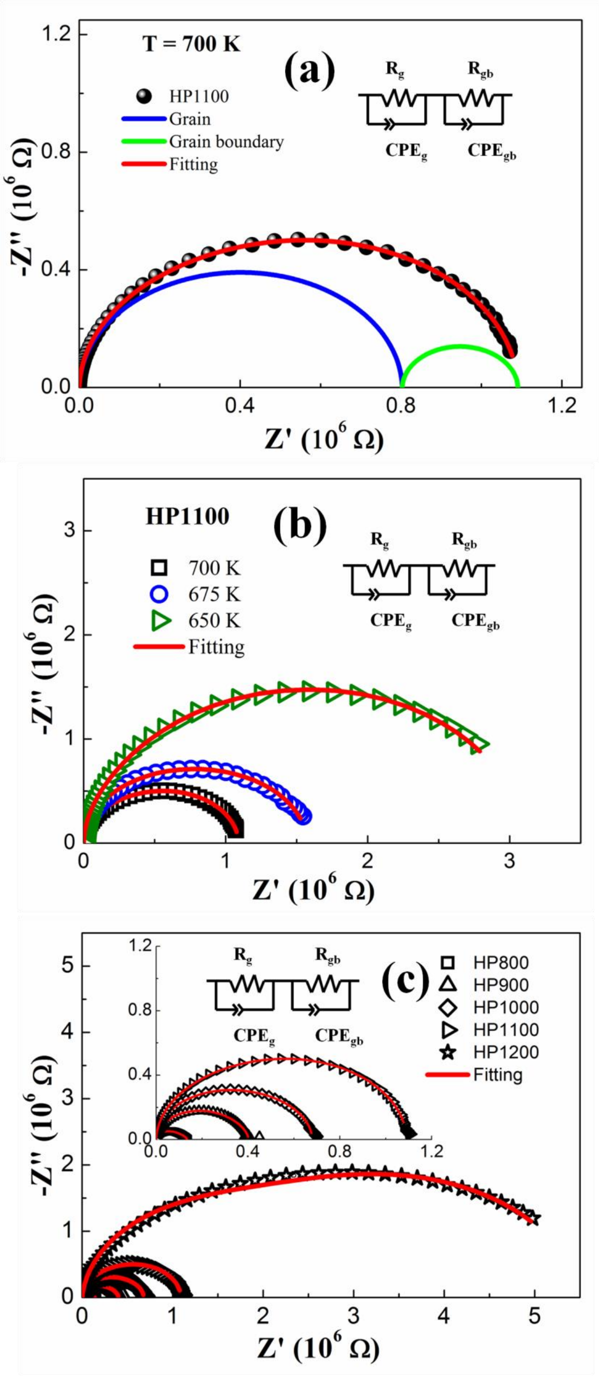

Fig. 3.11. (a) Impedance spectra of HP1100 measured at 700 K (black solid spheres) is fitted using equivalent circuit scheme using grain and grain boundary contributions, (b) Temperature evolution of impedance spectra of HP1100 measured at 650 K, 675 K, and 700 K fitted using equivalent circuit scheme, (c) Impedance spectra of different HP sintered ceramics measured at 700 K fitted using equivalent circuit scheme.

found to decrease from 0.85 to 0.53 with increasing HP-temperature, which imply decrease in the width of distribution of relaxation time, increase in size of the PNRs and their co-operative interaction. The mean relaxation time, τ_o increases from 10^{-7} s for HP800 to 10^{-3} s for HP1200 at 240 °C and remain nearly same τ_o ~10^{-10} s at high temperature ~280 K, as shown in Fig. 3.10(e). This study clearly shows that increase in the HP-temperature decreases the cation site-disorder at B-site leading to enhanced co-operative interaction among the PNRs, which is consistent with degree of diffuseness δ_A and $\Delta\varepsilon_m$ parameter.

Table 3.5. (a) Grain and grain boundary resistance (R_g (Ω) and R_{gb} (Ω)), (b) Grain and grain boundary capacitance (C_g (f) and C_{gb} (f)) of HP-PMN ceramics obtained from equivalent circuit fitting.

Ceramics		700 K	675 K	650 K
HP800	R_g (Ω)	8.81 x 10^{4}	1.50 x 10^{5}	3.69 x 10^{5}
	R_{gb} (Ω)	4.55 x 10^{4}	1.28 x 10^{5}	2.12 x 10^{5}
HP900	R_g (Ω)	3.20 x 10^{5}	3.20 x 10^{5}	1.04 x 10^{6}
	R_{gb} (Ω)	8.2 x 10^{4}	2.77 x 10^{5}	1.48 x 10^{5}
HP1000	R_g (Ω)	4.65 x 10^{5}	7.06 x 10^{5}	2.18 x 10^{6}
	R_{gb} (Ω)	2.14 x 10^{5}	7.84 x 10^{5}	1.00 x 10^{6}
HP1100	R_g (Ω)	8.03 x10^{5}	6.21 x 10^{5}	2.93 x 10^{6}
	R_{gb} (Ω)	2.88 x 10^{5}	9.51 x 10^{5}	1.64 x 10^{5}
HP1200	R_g (Ω)	1.84 x10^{6}	7.08 x 10^{6}	1.55 x 10^{7}
	R_{gb} (Ω)	3.69 x10^{6}	1.30 x 10^{6}	9.783 x 10^{5}

Ceramics		700 K	675 K	650 K
HP800	C_g (f)	1.073 x 10^{-10}	9.40 x 10^{-11}	1.2821 x 10^{-10}
	C_{gb} (f)	3.365 x 10^{-9}	5.13 x 10^{-9}	3. 8969 x 10^{-9}
HP900	C_g (f)	1.564 x 10^{-10}	1.20 x 10^{-10}	1.3083 x 10^{-10}
	C_{gb} (f)	4.0098 x 10^{-9}	1.17 x 10^{-9}	3.3247 x 10^{-10}
HP1000	C_g (f)	1.388 x 10^{-10}	4.39 x 10^{-9}	2.6454 x 10^{-10}
	C_{gb} (f)	8.665 x 10^{-10}	1.73 x 10^{-10}	2.5507 x 10^{-10}
HP1100	C_g (f)	2.49 x10^{-10}	6.18 x 10^{-10}	1.8902 x 10^{-10}
	C_{gb} (f)	3.056 x 10^{-10}	1.89 x 10^{-10}	7.6583 x 10^{-10}
HP1200	C_g (f)	1.287 x 10^{-9}	2.46 x 10^{-10}	1.8786 x 10^{-10}
	C_{gb} (f)	2.475 x10^{-10}	3.25 x 10^{-10}	6.1661 x 10^{-10}

3.3.6 Impedance Spectroscopy

To get the insight of dead layer around the grain, impedance spectroscopy has been carried out in the paraelectric region for all HP ceramics. Figure 3.11(a) shows a typical

Nyquist plot of HP1100 ceramic at 700 K and its de-convoluted plots for two microstructural elements (grain and grain boundary) as well as the fitting curve along with the experimental data points. It may be noticed that both semi-circles are depressed, i.e., center of the semi-circular arc is not on the abscissa axis. Thus series combination of two parallel RQ circuit is considered instead of RC circuit. It is well known for depressed semicircle, the capacitance is replaced with Q (also called constant phase element, C_{PE}), which is the Johnscher capacitance, and is introduced to include contribution of mobile carrier's not only to conduction but also to polarization in a universal capacitor [94]. Universal dielectric response of a capacitor is defined as follows:

$$Q = C_o \omega^{n-1} \tag{3.10}$$

where C_o is the capacitance at $\omega = 1$ rad/s, ω is the angular frequency and 'n' is exponent having value in between 0 and 1. The exponent "n" reflects deviation from an ideal capacitance. The "Q" is identical to a capacitance component when the exponent n is equal to one.

Equivalent circuit consisting of two RQ elements in series [as shown in the inset Fig. 3.11(a) for HP1100] is used to fit (solid line) the complex plots. Low and high frequency arcs are ascribed to grain boundary and grain in the HP ceramic, respectively. The capacitances (C_g and C_{gb}) and exponent n (n_g and n_{gb}) due to grain and grain boundaries are obtained from fitting of Nyquist plots with the aid of commercial available software "Z-view" [95]. Radius of the de-convoluted arc in the complex impedance plot corresponds to the DC-resistance of the micro-structural element [96]. Resistances corresponding to grain (R_g) and grain boundary (R_{gb}) are evaluated at 700 K, 675 K and 650 K temperatures are compared in Fig. 3.10(b) for HP1100. The resistance of grain and grain boundary is found to increase with decreasing temperature in all HP ceramics. Similar complex impedance plots are observed for of all HP ceramics at 700 K temperature, which are compared in Fig. 3.11(c). With increasing HP-temperature the grain and grain boundary resistance at 700 K is found to increase from ~8.8x10^4 Ω to 1.8x10^6 Ω and from 4.5 x 10^4 Ω to 3.7 x 10^6 Ω, respectively. Table 3.5 compares grain and grain boundaries resistance and capacitance at 700 K, 675 K and 650 K temperatures for all HP-ceramics. It may be noticed that both grain and grain boundaries resistance is similar at 700 K for all the HP-ceramics.

3.3.7 PE Hysteresis Loop

Electrically induced polarization variation under a drive of 15 kV/cm at 50 Hz is compared in Fig. 3.12(a-c) for all HP ceramics recorded at 300 K, 220 K, and 180 K, respectively. Hysteresis loss free “s-shaped” loop with zero remnant polarization has been observed for all HP PMN ceramics at 300 K, which display non-linear dependence of the polarization to the applied field and tendency of saturation at large field. The value of P_{max} ~16.8 µC/cm^2 (P_{max} at 15 kV/cm) for HP1200 ceramic is consistent with an air sintered PMN ceramic [59], which is sintered at 1200 ^{o}C for 2 hours and has average grain size ~7-8 µm. Upon decreasing HP-temperature from 1200 to 1000 ^{o}C, small decrease in the P_{max} from ~16.8 to ~16.3 µC/cm^2 has been observed but on further decrease in HP-temperature to 800 oC, the Pmax decreases drastically from 16.3 to ~9 µC/cm^2. The value of P_{max} for all other HP ceramics are measured under similar conditions and tabulated in Table 3.1.

Typical ferroelectric like *P-E* hysteresis loop is observed for all HP ceramics except HP800 at 180 K, as shown in Fig. 3.12(d-f), which indicates development of long range order as the applied field is more than the threshold field (~2 kV/cm for single crystal along <111> direction) reported earlier [97]. For HP1200 / HP800, the P_{max}, P_r and E_c is ~30 / 9 µC/cm^2, 24 / 4 µC/cm^2 and 7.3 / 5.5 kV/cm, respectively. A drastic change in the P_{max} and P_r has been observed when the HP-temperature is increased from 800 to 900 ^{o}C and after that the polarization increases gradually up to 1200 ^{o}C HP-temperature. It is important to note that

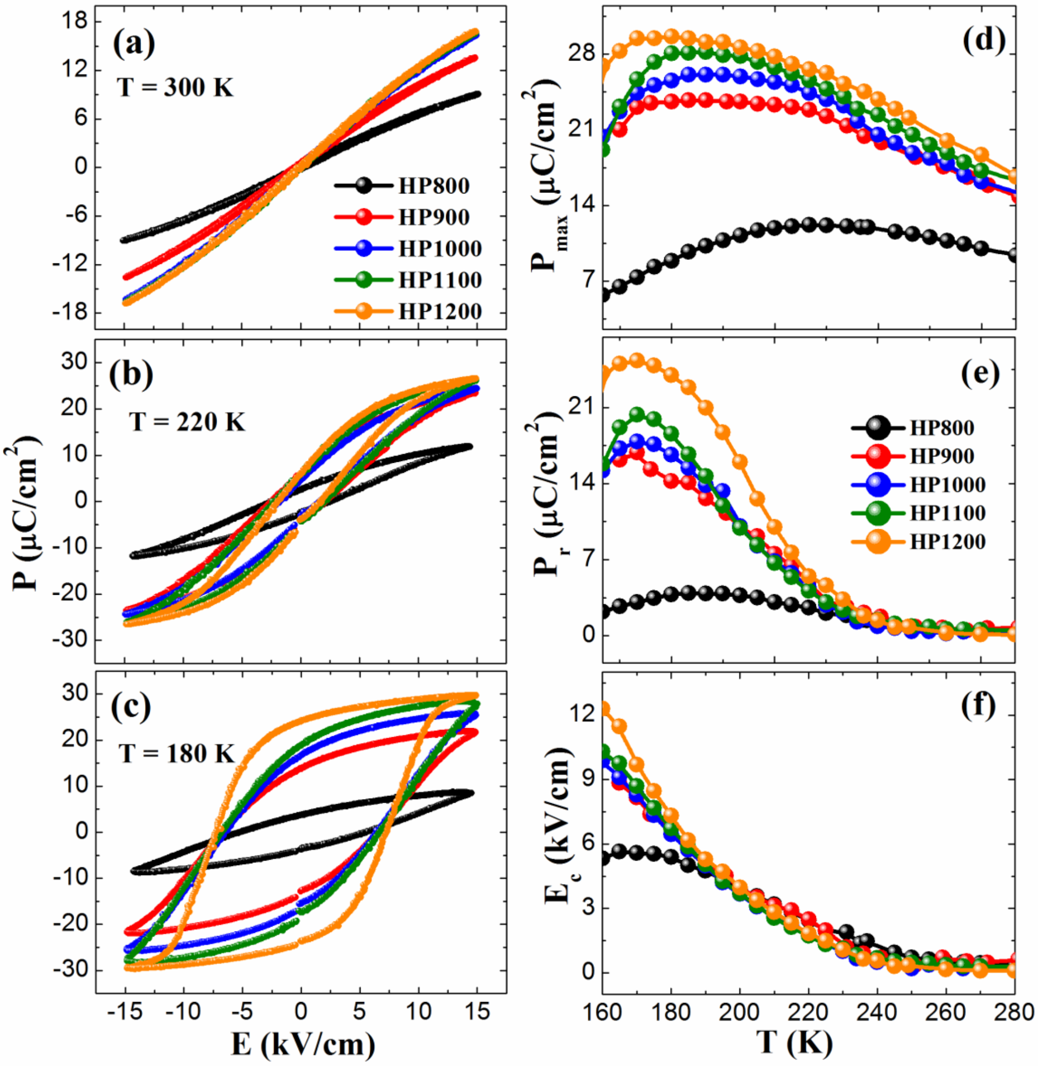

Fig. 3.12. (a-c) Comparison of PE hysteresis loop of HP sintered PMN ceramics (from 800 °C to 1200 °C) at E = 15 kV/cm and f = 50 Hz (a) T = 300, (b) T = 220 K, and (c) T = 180 K, (d-f) Comparison of temperature dependent parameters (d) P_{max}, (e) P_r, and (f) E_c of HP PMN ceramics.

HP1200 to HP900 is able to sustain P_r, which confirms transformation from short range (nano domains) to long range (macroscale domains) ordering when the applied external field is more than the random field at 180 K. The P_r is found to increase with decreasing temperature until a peak is observed around 170 K below which the P_r and P_{max} decreased. An increase in the P_r, P_{max} and E_c with decreasing temperature reveals competition between interaction among PNRs and thermal disorder. With decrease in thermal disorder effect, frustration interaction may be setting in to cause slowing down of the PNRs dynamics leading to reduction in P_r and P_{max} value. For HP800, the low P_r strongly suggests incomplete alignment of the polar nano domains, which may be due to reduced co-operative interaction among the PNRs and restriction in flipping or modifying size of PNRs near grain boundaries.

3.4 Conclusion

Grain size dependence on the ε_m and T_m has been examined using core-shell model in which the ratio of core to shell region thickness is found to increase with increasing grain size. The thickness of shell-region remains nearly same in PMN samples which are hot pressed at 800 to 1100 ^{o}C. Raman spectroscopy investigation has revealed an increase in local distortion which was not detected in X-ray diffraction study. Typical relaxor like dielectric characteristics, Super-lattice reflection (½½½) in <110> zone SAED pattern and A_{1g} mode corresponding to chemical ordered regions has been observed in HP800 sample, which was comparatively less dense, revealing formation of chemical ordered regions in the calcined powder at 800 ^{o}C. Frequency and temperature dependence of the dielectric constant reveal decrease in the distribution width of relaxation time and the degree of diffuseness, which imply increase in the size of PNRs and their co-operative interaction, which is consistent with the Mydosh-parameter, revealing that the state of PNRs ensemble is neither dipolar-glass like nor non-ergodic ferroelectric cluster-glass like.

Chapter 4

Investigation of phase formation, microstructural, vibrational, dielectric and ferroelectric properties of Gd-substituted PMN ceramics

4.1 Role of charge compensation mechanism on phase, dielectric and ferroelectric properties of aliovalent ion substitution in PMN

4.1.1 Introduction

The lead magnesium niobate (PMN), are described by nano sized cation disorder, leading to random electric/strain fields and local phase fluctuations [98]. These factors lead to unique characteristics in RFEs contrary to normal FEs, i.e., the presence of chemically ordered regions (CORs) and polar nano regions (PNRs), which are believed to be responsible for the high dielectric and piezoelectric properties of RFEs [99].

It is well known that the CORs and PNRs are correlated and henceforth, electrical properties should be influenced by thermal annealing, application of an external electric field and A/B-site chemical substitution by aliovalent ions etc. In most case of Pb-bases relaxors (viz., PSN and PNT etc.), the CORs can be controlled by thermal annealing but no influence of thermal annealing is observed in case of the PMN [100]. On the basis of the change of dielectric constant under the application of an external electric field, a phase transition from glass phase to ferroelectric phase is reported at a critical field of ~2 kV/cm in the temperature range of 160 K - 200 K [17,97]. On the other hand, B-site modification of PMN with Ti and Zr leads to reduction in the size of the CORs and enhancement in the size of polar-regions from nano to micron size i.e., relaxor to ferroelectric phase transition, whereas, A-site modification of PMN by La, Sm, Tb, Gd etc. induced the enhancement in the size of CORs and reduction in the PNRs with increasing relaxor-like dielectric characteristics [19-25].

In general, aliovalent substitution at Pb-site in PMN can be compensated by creating A-site or B-site vacancies or changing the B-site cations ratio. In this section, ceramic samples of 4 at% Gd-modified PMN where charge imbalance is compensated by considering i) vacancies in A-site ($Pb_{1-2x/3}Gd_x(Mg_{1/3}Nb_{2/3})O_3$; PGMN4-VA) or ii) vacancies in B-site ($Pb_{1-x}Gd_x(Mg_{1/3}Nb_{2/3})_{1-x/4}O_3$; PGMN4-VB) or iii) changing the ratio of B-site cations ($Pb_{1-x}Gd_x(Mg_{1+x/3}Nb_{2-x/3})O_3$; PGMN4-R) of the ABO_3 structure, synthesized by the Columbite precursor method. The aim of the present work is to study the influence of charge compensation mechanism by A/B-site vacancies or B-site cation change on the phase formation, ferroelectric and dielectric properties of Gd-modified PMN ceramic samples. This section is focused only on the relaxor behavior.

Table 4.1. Variation of the lattice parameter, % perovskite phase, grain size, dielectric properties, and field induced polarization of PGMN ceramics.

Sample	**Lattice constant '*a*' (Å)**	**% Perovskite phase**	**Average grain size (µm)**	***f* = 1 kHz**		**Δ*T* (K)**	**δ_A**	**P_{max} (µC/cm²) *E* = 20 kV/cm**
				ε_m	**T_m (K)**			
PMN	4.0467(±4)	100	11	21762	265	13.6	46	21.5
PGMN4-VA	4.0418(±5)	58	2.5	4360	247	17.9	98	5.6
PGMN4-VB	4.0419(±3)	99	4.8	7668	235	20.8	94	9.5
PGMN4-R	4.0420(±3)	99	12	7576	235	22.4	95	9.2

4.1.2 Results and discussion

4.1.2.1 Examination of phase formation using XRD, EDXS and SEM

Figure 1 illustrates comparison of room temperature XRD pattern of sintered PMN ceramics with Gd-substituted PMN (PGMN4-VA/VB/R) ceramics. It shows that single perovskite phase is present for pure PMN but minor second phase along with pure perovskite phase are present in PGMN4-VA/VB/R. All the major diffraction peaks of sintered powders have been indexed with perovskite phase of the PMN (JCPDF 22-1199) and other minor peaks have been assigned to pyrochlore phase (JCPDF 37-0071), marked by '*'), $GdNbO_4$ phase (JCPDF 22-1104, marked by '+'), and MgO (JCPDF 89-4248, marked by an arrow), and shown in the inset of Fig. 4.1. The volume fraction of pyrochlore, $GdNbO_4$, and perovskite phase have been evaluated using the relative intensities of the (222) pyrochlore peak (I_{Pyro}), (-121) $GdNbO_4$ peak (I_{GdNbO4}) and the (110) perovskite PMN peak (I_{PMN}) using the following Eq. 4.1

$$GdNbO_4/Pyro/PMN(\%) = \frac{I_{GdNbO_4/Pyro/PMN}}{I_{GdNbO_4}+I_{Pyro}+I_{PMN}} x100 \tag{4.1}$$

The inset of Fig. 4.1, clearly reveals formation of the pyrochlore phase for PGMN4-VA in which the charge imbalance is compensated by creating A-site vacancies. No diffraction peak corresponding to the pyrochlore phase is noticed for PGMN4-VB and PGMN4-R. Few minor peaks (marked by '+') are related to another secondary $GdNbO_4$ phase, whose concentration is less than 1 %. Segregation of the $GdNbO_4$ phase in PGMN4-VB and PGMN4-R ceramics is consistent with earlier proposed solubility limit (~2-3%) of Gd in PMN [29]. Further, the lattice parameter is decreased from 4.0467(±4) Å to 4.0419(±3) with 4 at.% Gd-substitution, which is consistent with smaller ionic radii of Gd^{3+} for 12 co-ordination (r_{Gd3+} ~1.276 Å) than Pb^{2+} (r_{Pb2+} ~1.49 Å). The lattice parameter is found invariant to the charge compensation mechanism used for Gd-ion substitution at Pb-ion site in PMN.

Enlarged view of diffraction peak within 2θ range from 15 ^{o} to 27 ^{o} (left panel of the inset of Fig. 1) reveal a noticeable peak for PGMN4-VB and PGMN4-R specimen, which has been assigned to the super-lattice reflections resulting from the CORs induced doubling of unit cell. It is widely known that the 1:1 non-stoichiometric chemical ordered regions (CORs) are coexisted with the PNRs in PMN. The size of the CORs varies 2-5 nm in PMN and remain unaffected in temperature range 5 to 800 K. Recently Gd-ion substitution in PMN has

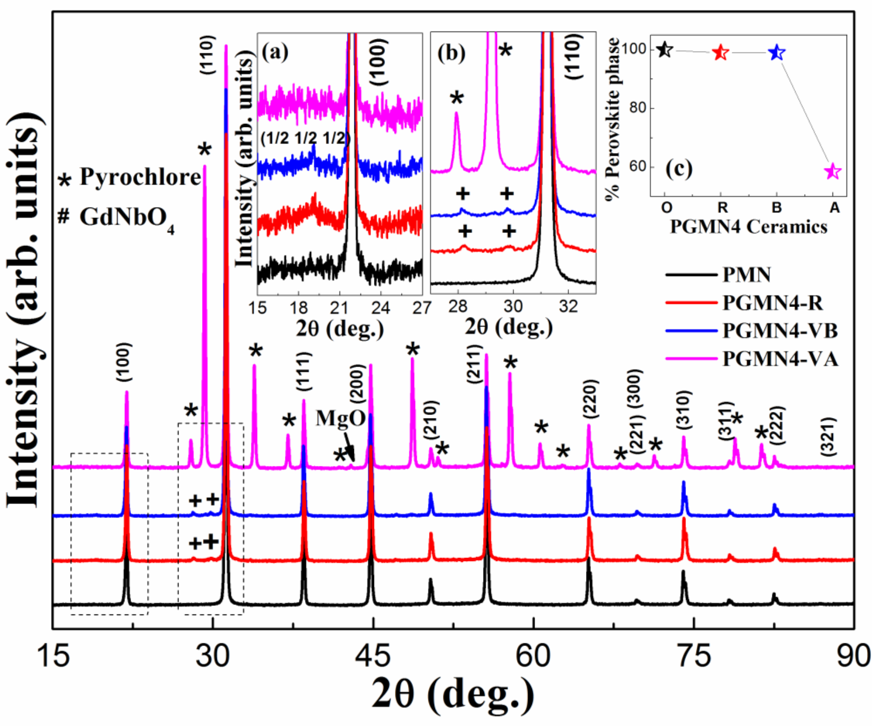

Fig. 4.1. Comparison of XRD pattern of the PGMN4 powders sintered at 1200 ºC, where the perovskite phase is indexed by JCPDS 27-1199 and few minor peaks pyrochlore phase are marked by "*"and GdNbO4 marked by "+" MgO is marked by an arrow; inset (a) shows the (½ ½ ½) supperlattice reflection resulting from the doubling of unit cell (Fm3m crystal symmetry), inset (b) is enhanced view in 2θ ragne27° - 33° to depict the secondary phases, and inset (c) shows formation of % perovskite phase in PGMN4 ceramics in comparison to PMN.

shown an enhancement in the size of the CORs, which has been related to an increase in the intensity of the super-lattice reflection spots at <½ ½ ½> along <111> unit axis direction. No peak corresponding to the superlattice has been observed for pure PMN and for PGMN4-VA. Absence of the superlattice diffraction peak in pure PMN is consistent with earlier reports [34]. However, absence in the PGMN4-VA is related to precipitation of the pyrochlore phase. It is believed that non-stoichiometric ordering of Mg^{2+} and Nb^{5+} ions in the CORs is a charged state, which is encapsulated by appositively charged state in PMN limiting its size to 2-5 nm. Alio-valent doping in PMN disrupts the charge neutrality, which leads to either precipitation of the pyrochlore phase (Nb-rich) or enhancement of the CORs region (Mg-rich). Creation of the A-site vacancy for PGMN4-A causes precipitation of the pyrochlore phase as a natural way for the charge imbalance compensation mechanism without influencing the CORs size and hence absence of the diffraction peak near ~19° 2θ angle.

Enhancement in intensity of the supperlattice peak is consistent with earlier report of alio-valent doped La-PMN, Nd-PMN, Sm-PMN and Pr-PMN etc. ceramics in which the charge imbalance is compensated with changing B-site cation ratio [34-37].

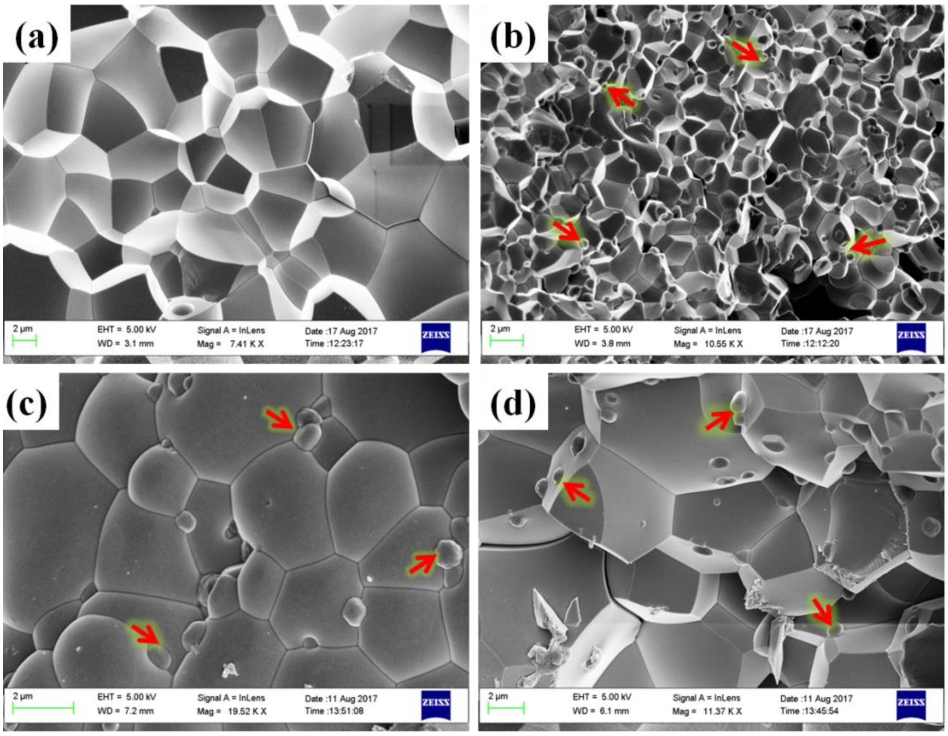

Fig. 4.2. Comparison of scanning electron micrographs of the fractured surface of sintered ceramics (a) PMN, (b) PGMN-VA, (c) PGMN-VB, and (d) PGMN-R and the spherical grains (size < 1 µm) confirming the second phase are marked by arrow.

Figure 4.2(a-d) compares scanning electron microstructure (SEM) images of the fractured surface of PMN, PGMN4-VA, PGMN4-VB, and PGMN4-R, respectively. Both inter-granular and intra-granular fractures along with negligible porosity indicating good sintered density are depicted. Linear intercept method has revealed average grain size ~ 11 µm for pure PMN and smaller average grain size ~2.5-12 µm for Gd-substituted PMN. The least average grain size, 2.5 µm is noticed for PGMN4-VA. The average grain size for PGMN4-VB, 4.8 µm is found smaller than 12 µm for PGMN4-R (Table 4.1), which can be explained by defect inhibited grain growth. In PGMN4-VA, the charge imbalance is compensated by creating Pb-ion vacancies. It may be noticed that for every $2Gd^{3+}$ ion substitution one Pb^{2+} ion vacancy is created, whereas one B-site ion vacancy is created for every 4 Gd^{3+}-ion substitution in PGMN4-VB. Large concentration of the Pb-vacancies in PGMN4-VA has resulted in reduced grain growth in comparison to the B-site vacancies in PGMN4-VB. No-vacancies are created for PGMN-R and hence the grain growth during sintering is not influenced. Similar grain size variations have been reported for rare-earths doped in PMN and PMN-PT systems with similar doping level [38-40].

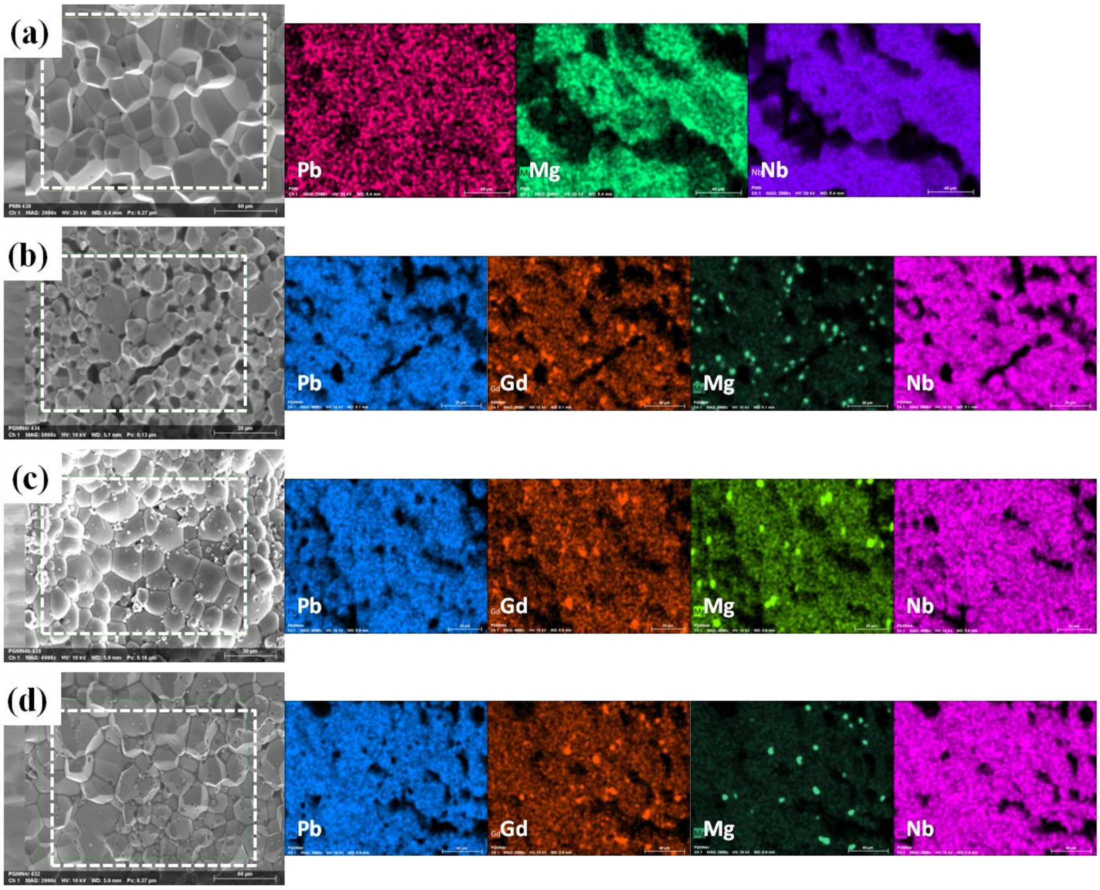

Fig. 4.3. SEM micrograph of the fractured surface of (a) PMN, (b) PGMN-VA, (c) PGMN4-VB, and (d) PGMN4 ceramic sample along with Pb, Gd, Mg, and Nb elemental mapping showing uniform distribution of these ions in the perovskite grains and presence of the $GdNbO_4$ and MgO phases.

Apart from well-developed large grains of the perovskite phase, few spherical grains (< 1 μm), as indicated by an arrow in Fig. 4.2(b-d), are also present for PGMN4-VA/VB/R ceramics. Figure 4.3(a-d) depicts the Pb, Gd, Mg, and Nb elemental mapping on the fractured surface of the pure PMN and PGMN4-VA/VB/R ceramics. Figure 4.3(a) confirms uniform distribution of Pb, Mg and Nb in the grains of PMN. Segregation of the Gd-ions and Mg-ions is noticed for Gd-substituted PGMN4-VA/VB/R ceramics [Fig. 4.3(b-d)]. Segregation of the Gd-ion is due to formation of the $GdNbO_4$ phase and consistent with the XRD-analysis. Formation of the $GdNbO_4$ phase has been reported [31,33] to result precipitation of the MgO phase, which is confirmed in the elemental mapping for all Gd-doped PMN ceramics. It may be noticed that segregation of the Gd-ion in the form of $GdNbO_4$ phase is not observed in the XRD spectra of PGMN4-VA, which is due to masking of the diffracted peak related to the $GdNbO_4$ phase by the diffracted peak related to the pyrochlore phase. Another interesting observation is large segregation of the Mg-ion for the PGMN4-VA compared to the PGMN4-VB and PGMN4-R ceramics. It is also noticed that the Mg-rich and the Gd-rich regions are close to each other, which is consistent with the proposed reaction [26,31] about the formation of the $GdNbO_4$ phase from reaction of the Gd_2O_3 with the Nb-rich pyrochlore phase resulting in the MgO segregation. The detailed microstructural investigation demonstrates an important role of the charge imbalance compensation mechanism on the secondary pyrochlore and $GdNbO_4$ phase in Gd-substituted PMN. This study also reveals non-dependence of the $GdNbO_4$ phase on the charge compensation mechanism. Further, temperature dependent dielectric and ferroelectric measurements are carried to study the influence of charge compensation mechanism on electrical properties.

4.1.2.2 Comparison of dielectric and ferroelectric properties

Temperature dependent dielectric properties at different frequencies are performed to investigate effect of the charge compensation mechanism on the relaxor dielectric behaviour. Figure 4.4(a-d) shows temperature dependent of the dielectric constant and loss tangent at selected frequencies for pure PMN and PGMN4-VA/VB/R ceramics, respectively. Typical relaxor like dielectric characteristics i.e., broad dielectric maxima (ε_m) with strong frequency dispersion near T_m (T of ε_m peak) i.e. T_m shifts progressively towards higher temperature with increasing frequency have been observed. This indicates that relaxation process of dynamic the PNRs occurs at multiple time scale. The temperature dependence of ε' and $Tan\ \delta$ at 1 kHz for PMN and PGMN4-VA/VB/R are compared in Fig. 4.5(a) and the ε_m and T_m are presented in Table 4.1. The ε_m ~ 21762 and T_m ~265 K for PMN are in good agreement with earlier reports [2,6,26]. The 4 at% Gd-ion substitution in PMN has reduced the T_m (~30 K) and ε_m (~7600) and is consistent with increase in size of the CORs, decrease in number or/and sizes of the PNRs and presence of the secondary pyrochlore and $GdNbO_4$ phases leading to reduction in correlation among PNRs [26,33], which is also in good agreement with earlier reports on A-site substitution by aliovalent ions [37]. The least value of the ε_m ~4360 is observed for PGMN4-VA compared to ~7600 for PGMN4-VB/R, which is due to presence of ~ 48% pyrochlore phase. It is also observed that PGMN4-VA shows higher value of the T_m ~247 K compared to 235 K for PGMN4-VB/R, which is attributed to low Gd-ion substitution at Pb-site in perovskite lattice because of the precipitation of $GdNbO_4$ from reaction between the pyrochlore and Gd_2O_3 [26,31].

Relaxor dielectric characteristics are generally demonstrated by degree of diffuseness (δ_A), degree of relaxation (ΔT_m) and correlation length among the polar nano-regions. Interacting polar nano-regions is known to grow below the T_B and enhance their correlation length during cooling. Depending upon the correlations among the PNRs, slowing down of polarization fluctuation at $T < T_m$ into random orientation of the polar domains also called super dipolar glass state has been reported [91]. Figure 4.5(b) compares the $\varepsilon'(T)$ curves at 1 kHz frequency in reduced form $\varepsilon'/\varepsilon'_m$ vs T/T_m for the PMN and PGMN4-VA/VB/R ceramics. Degree of diffusion is observed to increase with Gd-substitution and also relate with the defect concentration. The broadness around the 0.8*T/T_m clearly reveals large degree of diffusion for the PGMN4-VA compared to the PGMN4-VB/R, which is due to the presence of the pyrochlore phase. Larger broadness is observed for the PGMN4-VB compared to the PGMN4-R, which is attributed to large defect concentrations.

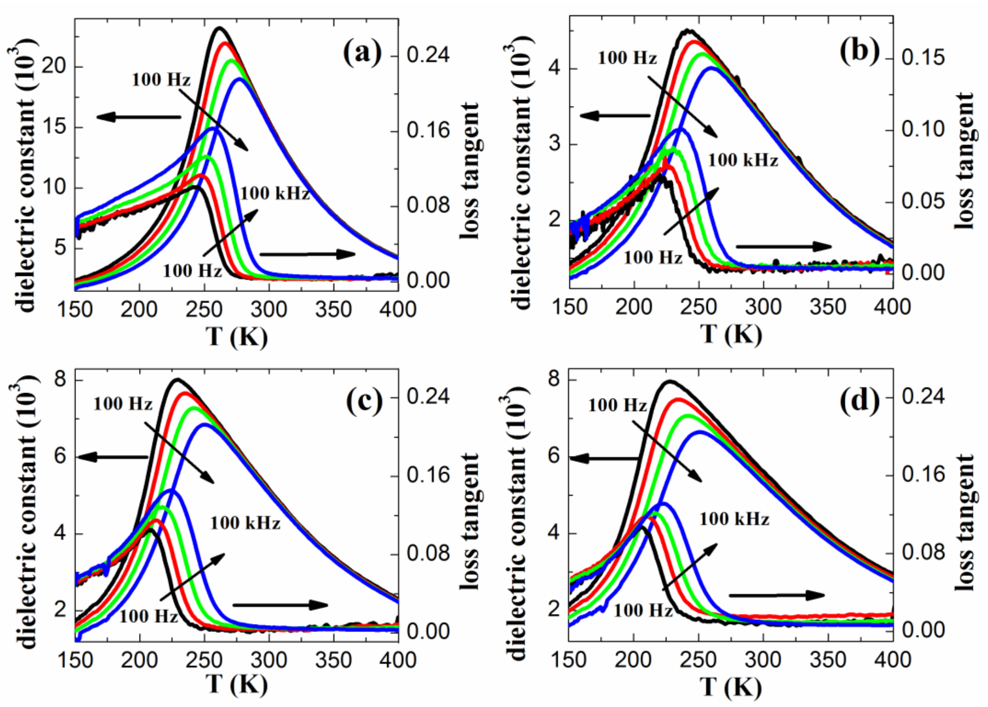

Fig. 4.4. Temperature dependence of the dielectric constant and loss tangent variations at different frequencies in the 100 Hz to100 kHz range for (a) PMN, (b) PGMN-VA, (c) PGMN-VB, and (d) PGMN-R ceramics, respectively.

Further, the modified Curie-Weiss relation (Eq. 2) has been used to fit the *ε'*(*T*) above T_m [85]

$$\frac{\varepsilon_A(\omega)}{\varepsilon'(T,\omega)} = 1 + \frac{(T-T_A(\omega))^2}{2\delta_A^2} \tag{4.2}$$

where, ε_A (> ε_m), T_A (< T_m) and δ_A (diffuseness) are the fitting parameters, practically independent of frequency and valid for long range of temperatures above the ε_m. Inset of the Fig. 4.5(b) depicts the diffuseness parameter δ_A, calculated by fitting of the $1/\varepsilon_m$ data above T_m to Eq. 4.2. The diffuseness parameter δ_A is also presented in Table 4.1 for different charge compensation methods. The δ_A parameter of Gd-substituted PMN is approximately double of that of the PMN, which is attributed to enhancement in the degree of cation's site chemical/charge disorder at the A/B-sites. Further, ΔT_m (= $T_{m,100kHz}$ - $T_{m,100Hz}$) is related to degree of relaxation and observe to increase from 13.6 (PMN) to 22.4 (PGMN4-R) suggesting enhancement in relaxor characteristics (Table 4.1).

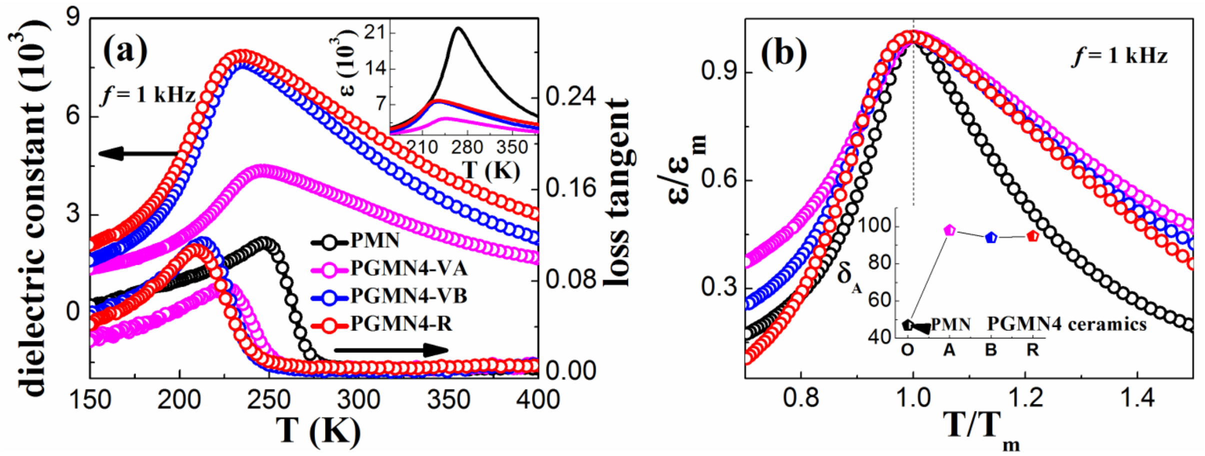

Fig. 4.5. (a) Comparison of temperature dependence of dielectric constant and loss tangent at 1 kHz frequency for PGMN4 ceramics, (b) Comparison of normalized plot $\varepsilon'/\varepsilon'_m$ vs T/T_m of PGMN4 ceramics; inset plots shows variation of diffuseness parameter, δ_A, calculated using Eq. (4.2).

Figure 4.6(a-b) compares *PE*-loop measured at temperature 300 K and 180 K when 20 kV/cm field is switched at 50 Hz frequency for PGMN4-VA/VB/R ceramic samples. At 300 K, the *PE*-loop is “S-shaped” and hysteresis loss free displaying nonlinear nature of the polarization to the applied field and tendency of saturation at large field, as shown in upper side of the inset of Fig. 4.6(a). The value of maximum polarization, P_{max} ~ 21.5 μC/cm^2 at 20 kV cm for PMN [shown in the lower side of the inset of Fig. 4.6(a)] is consistent with the earlier reported result [2,11,105]. Also no change in the *P-E* loop is observed when 20 kV/cm external field is switched at lower frequencies up to 1 Hz. A significant drop in the P_{max} is noticed with 4at% Gd-substitution, which is consistent with earlier study [105]. It may be noticed from the Table 1 that lower P_{max} ~5.6 μC/cm^2 value for PGMN4-VA in comparison to P_{max} ~9.5 μC/cm^2 for PGMN4-VB and PGMN4-R is due to presence of the pyrochlore phase.

Figure 4.6(b) shows the *P-E* hysteresis loop at 180 K for PGMN4-A/B/R. Inset of the Fig. 4.6(b) reveals typical ferroelectric like *P-E* hysteresis loop for PMN, which indicates the development of long range order. The P_{max}, P_r, and E_c is 35.7 μC/cm^2, 30.7 μC/cm^2, and 10.5

kV/cm, respectively for PMN is consistent with the earlier report [2,11,105,106]. It is important to note that PMN is able to sustain P_r at 180 K, which confirms the slowing down of polar nano-domains dynamics, but when the applied external field is more than the random field, the nano-polar domains convert into macroscopic domains. The P_r, P_{max} and the area under the curve is decreased with 4at% Gd-substitution in PMN, which is due to enhancement in size of the CORs and reduction in correlation among PNRs. The least value of P_r and P_{max} for PGMN4-VA compared to PGMN4-VB/R is due to presence of the pyrochlore phase. This study clearly demonstrates that the charge imbalance created by alio-valent ion substitution at Pb-site in PMN must be carried out by changing B-site cation ratio instead of by creating A-site and B-site vacancies.

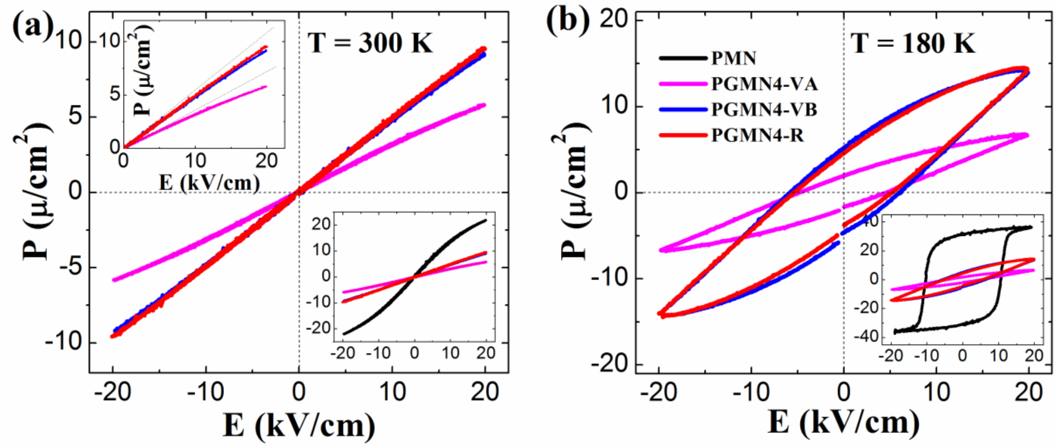

Fig. 4.6. Comparison of PE-loop recorded at (a) 300 k and (b) 180 K when 20 kV/cm field applied at 50 Hz frequency for PGMN4 ceramics along with PMN.

4.1.3 Conclusion

Systematic studies on the charge compensation mechanism concludes that the charge imbalance created by 4 at.% Gd-ion substitution at Pb-site in PMN relaxor ferroelectric must be carried out by changing the B-site cations ratio. Phase analysis confirms the formation of the pyrochlore secondary phase in PGMN4-VA in which charge imbalance is compensated by creating A-site vacancies. Elemental mapping of the fractured surface reveals that all three charge compensation mechanisms are unsuccessful in circumventing minor $GdNbO_4$ phase, which is formed due to the low solubility limit of Gd-ion at Pb-site in perovskite lattice of PMN. Microstructure analysis reveals linear relation between the grain size and the vacancies defect concentration. The lower P_{max} and ε_m for PGMN4-VA is consistent with the presence of pyrochlore phase.

4.2 Critical slowing down dynamics of nano-polar dynamics in Gd-doped PMN $Pb_{1-x}Gd_x(Mg_{1+x/3}Nb_{2-x/3})O_3$ ($0 \leq x \leq 0.1$) ceramics

4.2.1 Introduction

The PMN exhibits frequency dependent diffused dielectric maxima (high dielectric constant ~20 000 at 1 kHz), which does not correspond to any structural phase transition, analogous to spin glasses or structural glasses [3,98,99]. Other interesting properties of the PMN include hysteresis loss free polarization-electric field (*PE*) loop at room temperature, inability to sustain a remnant polarization until temperatures are significantly below the temperature of dielectric maxima (T_m), and the presence of polar nano-domains in zero-field (ZF) condition is below T_m.

Present widely accepted depiction about the PMN comprises (i) existence of non-polar paraelectric phase at all temperatures above the Burns temperature (T_B ~600 K), where temperature dependence of the dielectric constant is related with the Curie-Weiss law, and (ii) coexistence of the CORs and the PNRs below the T_B [3,10,11]. Recently, it has been found that the CORs are formed during calcination stage [107], but it is not known if these CORs disappear at high temperature.

The CORs and the PNRs are believed to be correlated and have been reported to be influenced by chemical substitution with aliovalent ions at A and B-sites [19-25]. The A-site modification of the PMN with lanthanum (La) has been shown to enhance the size of the CORs and reduce the size of the PNRs [19-22]. Similarly, B-site cation substitution with Ti or Zr in the PMN has been reported to reduce the size of the CORs, which results in the growth of the PNRs from nano to micron size [22-25]. Correspondingly, relaxor like dielectric behaviour is changed to normal ferroelectric like when the size of the CORs decreases and the size of the PNRs increases. Thus, the relaxor behavior is a consequence of the static structural disorder and a statistical distribution of the PNRs over a wide range of temperatures. The nano scale heterogeneity seems to be an inherent part of relaxors, but mechanisms of how the PNRs appear and evolve upon cooling are currently pursued worldwide.

Studies related to aliovalent gadolinium ion (Gd^{3+}) substitution in the PMN are very scanty. Purpose of the present study is to bring in a correlation among the microstructure, B-site cations ordering, dielectric, and ferroelectric properties for Gd-doped PMN, where the charge imbalance due to Gd-substitution at Pb-site is compensated with a change in the B-site cation ratio ($Pb_{1-x}Gd_xMg_{(1+x)/3}Nb_{(2-x)/3}O_3$).

Table 4.2. Phase analysis of $Pb_{1-x}Gd_xMg_{(1+x)/3}Nb_{(2-x)/3}O_3$, for $0.00 \le x \le 0.1$, (designated as PMN to PGMN10) calcined and sintered powders at 800 °C and 1200 °C, respectively.

%Gd	Calcined Powder			Sintered Powder		
	%Perovskite	**%Pyrochlore**	**%Gd_2O_3**	**%Perovskite**	**%$GdNbO_4$**	**MgO**
0	100	-	-	100	-	-
1	98.57	1	0.43	100	-	-
3	96.32	2.57	1.11	99.5	0.5	-
5	95.69	2.16	2.15	99.14	0.86	-
8	92.19	5.81	2	97.12	2.58	0.3
10	88.21	7.36	4.43	95.16	3.67	0.46

4.2.2 Results and discussion

4.2.2.1 Phase formation and structure analysis

In the present study, the charge imbalance due to Gd^{3+} substitution at the Pb^{2+} site is compensated by changing the Mg/Nb ratio as depicted in the formula $Pb_{1-x}Gd_xMg_{(1+x)/3}Nb_{(2-x)/3}O_3$, for $0.01 < x < 0.1$, (designated as PGMN1 to PGMN10). Figure 4.7 compares the XRD pattern of the Columbite precursor for different Mg/Nb ratio. Phase analysis confirms the coexistence of orthorhombic (Pbcn space group) $MgNb_2O_6$ and hexagonal (P-3c1 space group) $Mg_4Nb_2O_9$ phases. The peak intensity (104) corresponding to the $MgNb_4O_9$ increases with the increase in the Mg/Nb cationic ratio from 0.50 to 0.58. The concentration of the hexagonal Mg4Nb2O9 phase is calculated from the peak ratio using Eq. 4.3 and it increases from 0% to 3.5% with increasing Mg^{2+}/Nb^{5+} cations ratio, as shown in the inset of Fig. 4.7,

$$MgNb_2O_6/Mg_4Nb_2O_9(\%) = \frac{I_{MgNb_2O_6/Mg_4Nb_2O_9}}{I_{MgNb_2O_6}+I_{Mg_4Nb_2O_9}} x100 \qquad (4.3)$$

The suitable Columbite precursor is mixed with the required quantity of Gd_2O_3 and PbO, and the mixed powder is calcined at different temperatures for examining the phase evolution. Figure 4.8 compares the XRD pattern of the PGMN10 powder calcined at different temperatures between 800 and 1200 °C (designated as CP800 to CP1200). All the major diffraction peaks have been indexed with the perovskite phase of the PMN (JCPDS 27-1199). Few minor peaks are due to the presence of the pyrochlore phase (JCPDS 37-0071, marked by *) and the un-reacted Gd_2O_3 (JCPDS 83-2037, marked by #) in Fig. 4.8(b). The relative intensities of the (222) pyrochlore peak (I_{Pyro}), (222) Gd_2O_3 peak (I_{Gd2O3}), (-121) $GdNbO_4$ peak (I_{GdNbO4}), and the (110) perovskite PMN peak (IPMN) have been used to determine the volume fraction of the pyrochlore, Gd_2O_3, $GdNbO_4$, and perovskite phase using following relation

$$GdNbO_4/Pyro/Gd_2O_3/PMN(\%) = \frac{I_{GdNbO_4/Pyro/Gd_2O_3/PMN}}{I_{GdNbO_4}+I_{Pyro}+I_{Gd_2O_3}+I_{PMN}} x100 \qquad (4.4)$$

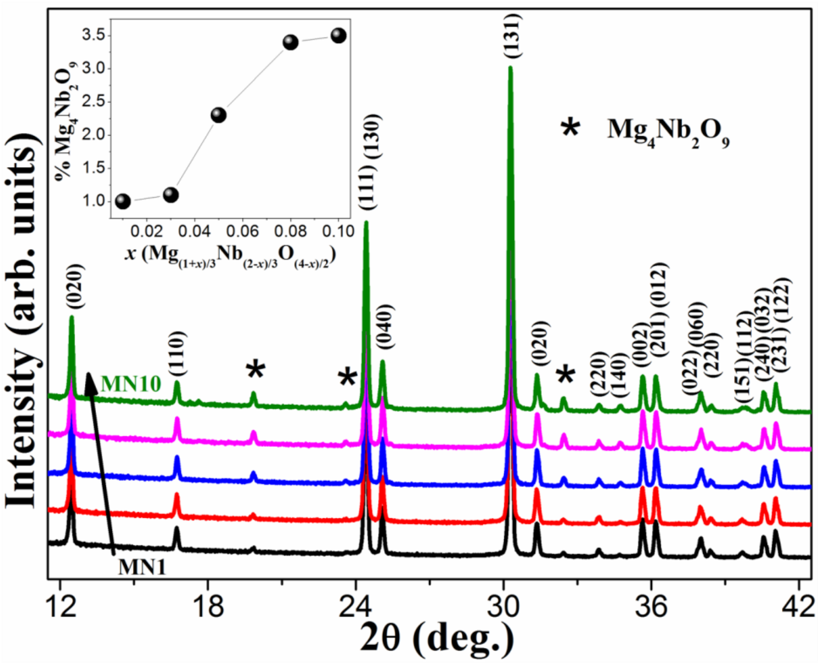

Fig. 4.7. Comparison of the XRD patterns of $Mg_{(1+x)/3}Nb_{(2-x)/3}O_{4-x/2}$, compositions $x = 0.01$ to 0.1 (MN1 to MN10) calcined at 1200 °C revealing coexistence of orthorhombic (Pbcn space group) $MgNb_2O_6$ and hexagonal (P-3c1 space group) $Mg_4Nb_2O_9$ phases, where $Mg_4Nb_2O_9$ phase is marked by "*;" Inset of figure depicts $Mg_4Nb_2O_9$ phase variation with increasing Mg^{2+}/Nb^{5+} cations ratio.

The phase analysis of the CP800 powder clearly reveals few minor peaks corresponding to the pyrochlore and the unreacted Gd_2O_3 phases along with the major peaks corresponding to the perovskite phase. The concentration of different phases is calculated from the XRD pattern of the calcined powders (figure not shown) using Eq. 4.4, and the values are tabulated in Table 4.2. It may be noticed that the concentration of the unreacted Gd_2O_3 phase is lower than the starting concentration, which implies that a small amount of the Gd_2O_3 might have incorporated in the lattice. The concentration of the pyrochlore and the unreacted phase decreases with the increase in the calcination temperature up to 1000 °C. Above 1000 °C, the peaks corresponding to the $GdNbO_4$ (JCPDF 22-1104, designated as GNO), marked by "+" appear, but the peaks corresponding to the pyrochlore and the Gd_2O_3 phase disappear, which implies reaction between the pyrochlore and the Gd_2O_3 at temperature greater than 1000 °C. These results are consistent with the earlier report [29,59].

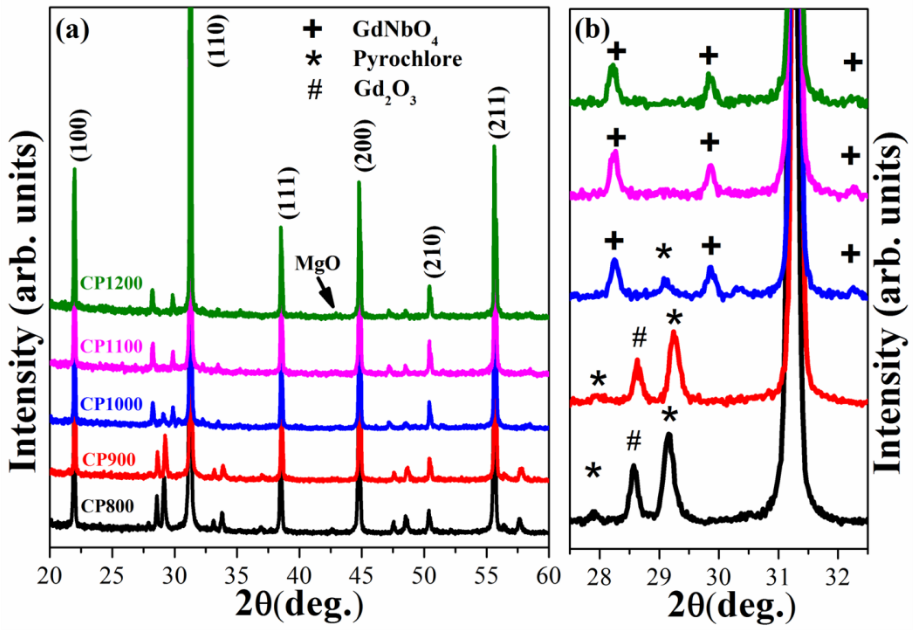

Fig. 4.8. Comparison of XRD pattern of the PGMN10 powder calcined at different temperatures between 800 and 1200 °C (designated as CP800 to CP1200), where the perovskite phase is indexed by JCPDS 27-1199 and few minor peaks pyrochlore phase are marked by "*" un-reacted Gd_2O_3 aremarked by "#" and $GdNbO_4$ marked by "+", MgO is marked by an arrow.

The powder XRD pattern of the PGMN1 to PGMN10 sintered samples are compared in Fig. 4.9, which reveals only the perovskite phase for the PGMN1 and the secondary phase GNO along with the perovskite phase is observed for $x \geq 0.03$. The concentration of the GNO increases from 0.5% to 3.7% with the increase in "*x*" from 0.03 to 0.1. It is clear from Fig. 4.9 that peaks corresponding to the pyrochlore phase or the Gd_2O_3 are not present in the sintered specimens, which is due to the reaction between the pyrochlore and the Gd_2O_3 at a high temperature (>1000 °C) to form the perovskite and the $GdNbO_4$. This study clearly shows that precipitation of the $GdNbO_4$ phase cannot be eliminated by changing the B-site cations ratio. In contrast to this, Gupta *et al.* has shown in the La-substituted PMN-PT that changing B-site cation ratio eludes the formation of the secondary phase [108]. It seems there is a solubility limit ~2%-3% of the Gd^{3+} substitution at the Pb^{2+}-site in the perovskite pseudocubic lattice, which cannot be enhanced by any charge imbalance compensation mechanisms. The solubility limit is consistent with the earlier report [29,59]. However, the

XRD pattern of higher Gd-ions substitution ($x \geq 0.05$) has also revealed a small peak corresponding to MgO (JCPDF89-4248), as marked by an arrow in Fig. 4.9.

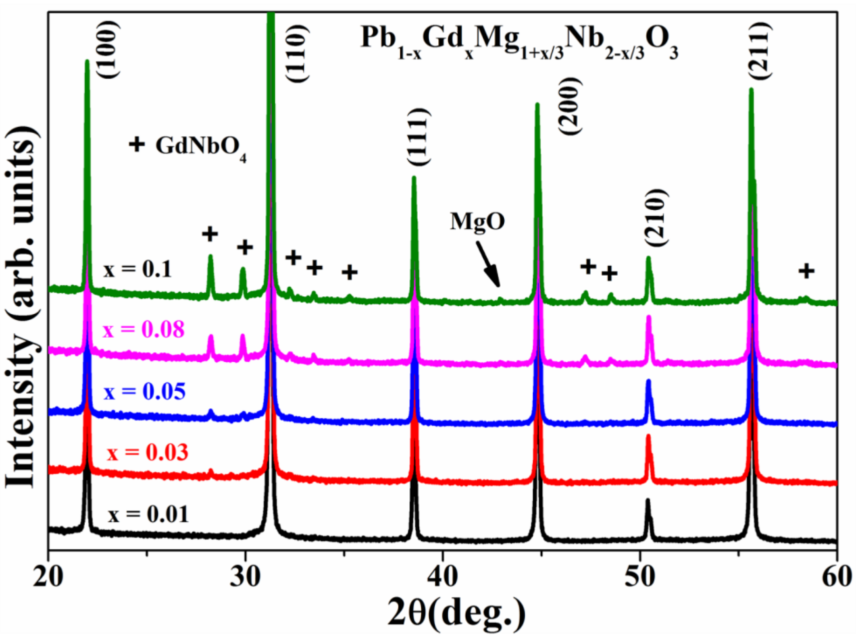

Fig. 4.9. Comparison of room temperature XRD pattern of ceramics $Pb_{1-x}Gd_xMg_{(1+x)/3}Nb_{(2-x)/3}O_3$, for $0.01 \leq x \leq 0.1$, (designated as PGMN1 to PGMN10) sintered at 1200 °C for 2 h; where secondary phase $GdNbO_4$ marked by "+" and MgO is marked by an arrow.

The crystal structure and the lattice parameters are determined by the Rietveld refinement fitting of the XRD pattern of the sintered powders using the Fullprof software [109]. In the structural analysis, Pm3m and I2/a symmetry are considered for the perovskite phase and the GNO, respectively. Large atomic displacement parameters (B_{iso}) of the Pb^{2+} and O^{2-} compared to the Mg^{2+}/Nb^{5+} have been observed, which indicate local site static disorder of the Pb^{2+} and O^{2-} from their average crystallographic positions and have been found to be consistent with the earlier studies on the PMN and other Pb-based mixed perovskites [109,110]. A split-atom approach is used to find the most probable disorder, where the Pb^{2+} and O^{2-} ions are shifted in various crystallographic directions and the most probable disorder is decided on the basis of improvement in the reliability factors from the Rietveld fitting [109]. Figure 4.10 shows that the simulated pattern satisfactorily matches with the experimental data for PMN to PGMN10 ceramics and the calculated reliability factors (R_p, R_{wp}, and χ^2) have also confirmed reasonable accurate fit. The lattice parameter is found decreasing from 4.0470 Å (PMN) to 4.0428 Å (PGMN10) with increasing "*x*", presented in Table 4.3. On comparing the ionic radii of Pb (1.49 Å) with Gd (1.276 Å) for 12 coordination and the ionic radii of Mg (0.72 Å) and Nb (0.64 Å) with Gd (0.94 Å) for 6 coordination, it is noticed that if the Gd-ion substitutes at the B-site, the lattice parameter should increase and if Gd-ion substitutes at the Pb-site, the lattice parameter should decrease. The decrease of the lattice constant with increasing "*x*" up to 0.05 indicates that the Gd^{3+} (1.276 Å) substitutes for the Pb^{2+} (1.19 Å) cation. It may also be noted that there is no change in the lattice parameter for $x \geq 0.05$ in the PMN, which can be inferred as a possibility of the Gd-ion substituting at the Mg-site. It is already reported earlier that the Gd-ion has similar probabilities of substituting at the A and B-site in the PMN [29]. The present study clearly reveals that the Gd-ion substitution takes place at the A-site up to $x \leq 0.05$ and possibly also at the Mg-site for $x \geq 0.05$. It is anticipated that the Gd-ion substitution at the Mg-site should lead to segregation of MgO in the sintered sample, which is consistent with the XRD pattern in Fig. 4.9 for x = 0.05, 0.08, and 0.1. A microstructural analysis is also performed to confirm the Gd-ion substitution at the Mg-site.

Table 4.3. Variation of the lattice parameter, grain size, dielectric properties and field induced polarization of $Pb_{1-x}Gd_xMg_{(1+x)/3}Nb_{(2-x)/3}O_3$, for $0.00 \leq x \leq 0.1$ ceramics.

%Gd	**Lattice Constant (Å)**	**Average grain size (μm)**	***f* = 1 kHz**			**δ_A**	**T_A (K)**	**ε_A**	**"*K*"**	**P_{max} (15 kV/cm)**
			ε'_m	**T_m (K)**	**Tan δ at T_m**					
0	4.0470(±2)	8	21762	265.0	0.0310	45.6	22028	247.0	0.017	15.1
1	4.0457(±1)	12	18030	250.7	0.0401	53.5	18411	236.6	0.022	11.4
3	4.0440(±3)	8	8218	240.8	0.0323	72.5	8317	226.5	0.027	7.2
5	4.0429(±3)	10	5764	240.9	0.0279	91.6	6004	217.6	0.029	4.6
8	4.0430(±1)	10	3785	244.7	0.0264	97.8	3991	217.3	0.030	3.5
10	4.0428(±3)	8	4237	243.2	0.0267	96.0	4435	218.7	0.030	4.2

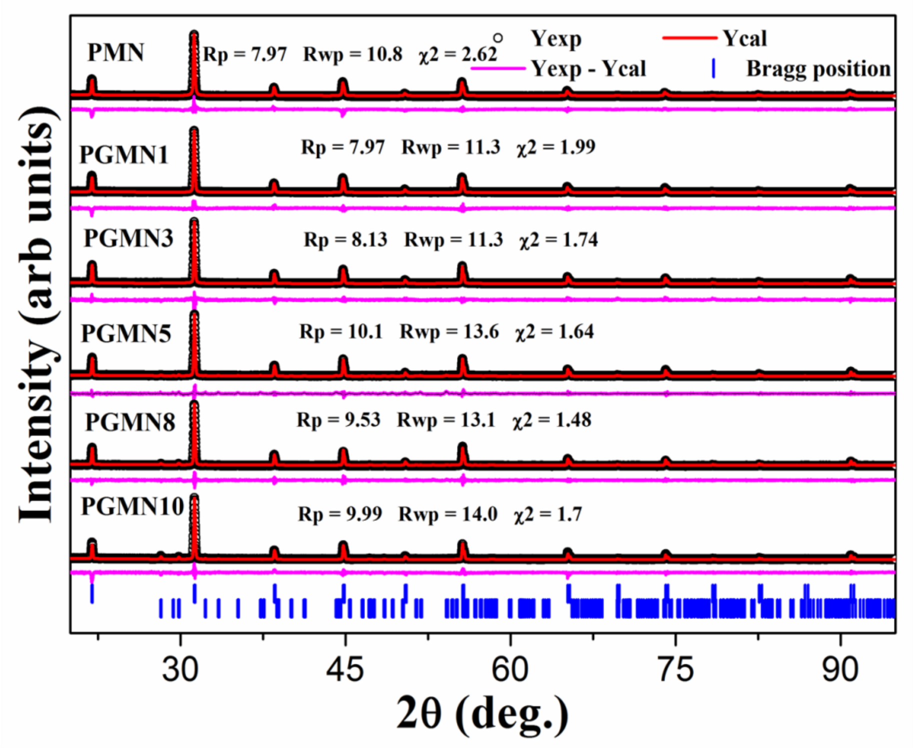

Fig. 4.10. Rietveld fitted XRD pattern of sintered $Pb_{1-x}Gd_xMg_{(1+x)/3}Nb_{(2-x)/3}O_3$, for $0 \leq x \leq 0.1$ ceramics, where open black circles represent the raw data, the solid red line is the fitted data using space group Pm3m for perovskite PMN and space group I2/c for $GdNbO_4$ along with the difference between the observed and calculated intensity.

4.2.2.2 Microstructural examination

Figure 4.11(a-e) show scanning electron micrographs of fractured surface for x = 0.01, 0.03, 0.05, 0.08, and 0.1, respectively. These images clearly reveal minimal porosity indicating good sintered ceramics. Linear intercept method has revealed no effective change in the average grain size with increasing "x" from 0.01 to 0.1. Similar grain size dependencies have been reported for rare-earths doped in PMN-PT system with similar doping level [102-104].

Apart from well developed large grains of the perovskite phase, few spherical grains (1–2 lm), as indicated by an arrow in Fig. 4.11(c-e), are also present for $x \geq 0.05$. The concentration of these small spherical grains increases with $x \geq 0.5$. Figure 4.11(f) energy dispersive spectra of the spherical grains confirming the $GdNbO_4$ phase. Figure 4.12 depicts

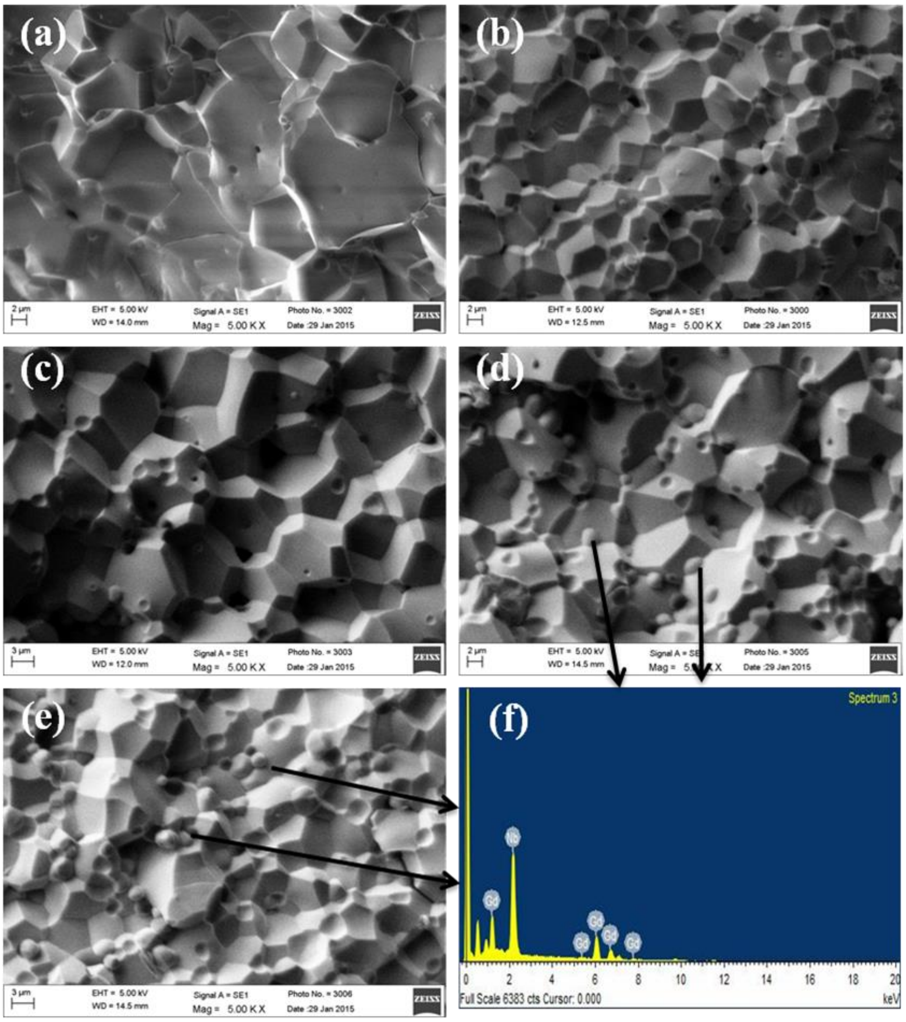

Fig. 4.11. (a-e) Comparison of scanning electron micrographs of the fractured surface of sintered $Pb_{1-x}Gd_xMg_{(1+x)/3}Nb_{(2-x)/3}O3$, for $x = 0.01, 0.03, 0.05, 0.08,$ and 0.1 ceramics, respectively; (f) energy dispersive spectra taken from the spherical grains confirming the $GdNbO_4$ phase.

the micrograph of the fractured surface of the PGMN5 sample along with Pb, Gd, Mg, and Nb elemental mapping. The elemental mapping of Pb, Gd, Mg, and Nb confirms uniform distribution of these ions in the perovskite grains. The black patches are due to the valley present in the ceramic. Further, it may also be noticed that there is clear evidence of the Gd-ion segregation in spherical shape grains, which is due to the presence of the $GdNbO_4$ phase. Similarly, the Mg-ions segregation may also be seen in Fig. 4.12(d), which is due to the presence of the MgO for $x \geq 0.05$ samples. These results are consistent with the phase analysis in which the presence of $GdNbO_4$ and MgO is observed. It is also found that the MgO and the $GdNbO_4$ grains are close to each other, which strengthen our conjecture that the

$GdNbO_4$ is formed during the reaction of the Gd_2O_3 with the Nb-rich pyrochlore phase and the MgO is segregated in this process. Further, detailed Raman spectroscopic analysis of PGMN samples is carried out to explore the local changes in assigned modes.

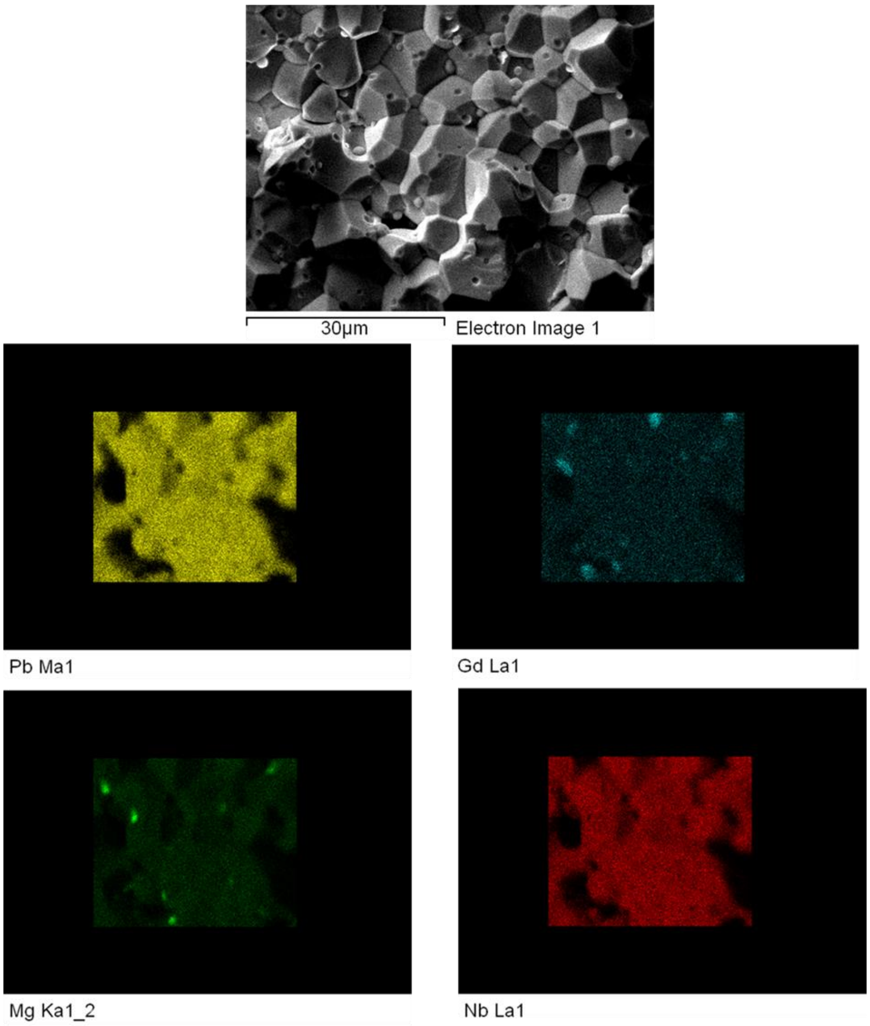

Fig. 4.12. (a) SEM micrograph of the fractured surface of PGMN5 ceramic sample along with (b) Pb, (c) Gd, (d) Mg, and (e) Nb elemental mapping showing uniform distribution of these ions in the perovskite grains and presence of the $GdNbO_4$ and MgO phases.

4.2.2.3 Raman spectroscopy

Room-temperature Raman spectra of the $Pb_{1-x}Gd_x(Mg_{1+x/3}Nb_{2-x/3})O_3$ (for $0 \leq x \leq 0.1$) ceramic are shown in Fig. 4.13. These spectra are corrected by Bose factor and normalized by the intensity of 780 cm^{-1} A_{1g} mode of PMN. The Raman spectrum of PMN reveals many broad and overlapping Raman bands, implying the presence of large disorder and different local structure, because, for an ideal cubic perovskite ABO_3 structure with Pm3m space group, the first-order Raman modes are forbidden by symmetry [76-81,111,112]. Origin of the Raman bands of PMN is due to the 1:1 non stoichiometric ordering of Mg/Nb along <111> direction with Fm3m space group – CORs and PNRs, having rhombohedral symmetry with R3m space group, formed due to correlated off-center displacement of ferro-active ions. Group theory analysis on the basis of space group suggests the presence of 20 active modes: 4 active Raman modes for Fm3m symmetry and 16 active Raman modes originating from R3m symmetry (Z = 2, doubling of unit cell). The multiple heterogeneities i.e., site disorder, presence of the CORs and off-center ionic displacements, cause the broadening and overlapping of the Raman active modes [76,78,111].

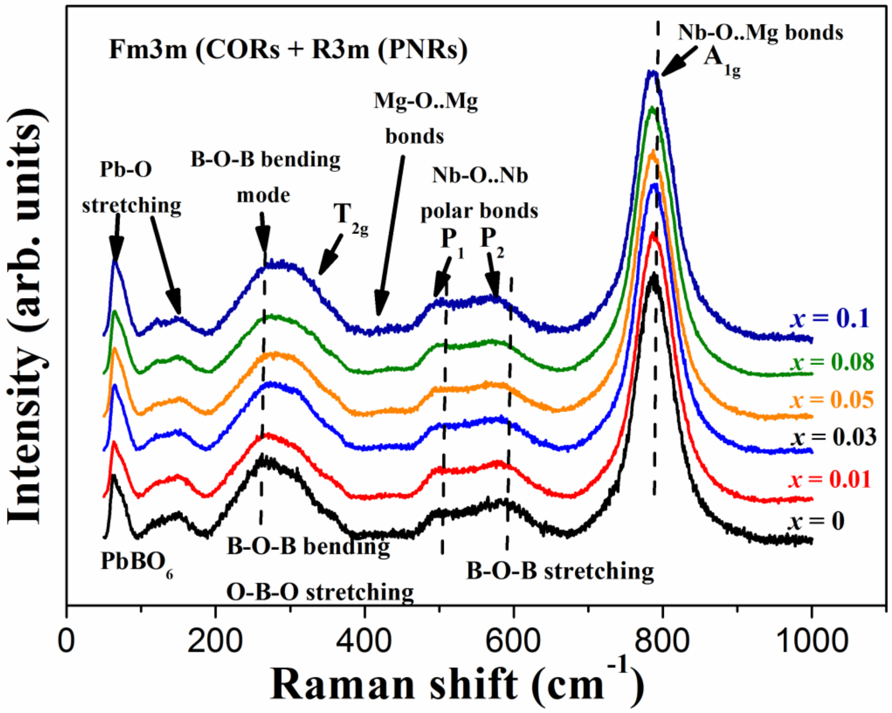

Fig. 4.13. Raman spectra of pure PMN and Gd^{3+}-substituted PMN $Pb_{1-x}Gd_x(Mg_{1+x/3}Nb_{2-x/3})O_3$ (for $0 \leq x \leq 0.1$) ceramics

In consistency with earlier reports [76,78], the Raman spectra are divided into three regions (i) the low frequency region (up to ~ 150 cm^{-1}) attributed to the Pb-BO_6 stretching modes, (ii) intermediate frequency region (from ~ 150 to 600 cm^{-1}) classified as stretching mode of Nb-O-Nb bond (at 500 to 600 cm^{-1}) and Mg-O-Mg bond (at 420-430 cm^{-1}) and bending mode of O-B-O bond (at 260-270 cm^{-1}) and (iii) high frequency region (from ~ 600 to 1000 cm^{-1}) assigned to the stretching mode of Nb-O-Mg bonds which are the most rigid in the structure.

The Raman spectra have been de-convoluted using the mixture of Gaussian and Lorentzian distribution peak profile called Pseudo-Voigt peak shape function. Fig. 4.14(a,b) shows representative Raman spectra of PGMN5 de-convoluted into 14 peaks with varying intensity, wave number and FWHM. The soft modes at ~50 cm^{-1} are not clearly visible, due to the experimental limitation. Likewise, the Raman spectra are de-convoluted for all PGMN0 to PGMN10 samples. It is noted that the number of the modes is less than that expected from the group theory analysis. This difference is attributed to the overlapping of the Raman modes due to the presence of disorder [76,78,111].

Noticeable changes in the de-convoluted Raman spectra of PGMN samples are reflected in the characteristic parameters: peak position, line width and intensity. In region 1, low frequency mode at ~150 cm^{-1} is assigned to relative motion of Pb against the rigid oxygen octahedrons, called Pb-O stretching mode. Gd substitution shifts the peak position of the Pb-O stretching mode to higher frequency, as shown in Fig. 4.14(c). This can be explained from simple harmonic model, $\omega = (k/m^*)^{1/2}$, where k is related to force constant and m* is the reduced mass of assigned mode. It has been shown from the XRD analysis that lattice parameter of Gd^{3+}-doped PMN decreases monotonically from 4.0459(±3) Å (PMN) to 4.0427(±1) Å (PGMN10), because of the ionic radii difference between Gd^{3+} (0.94 Å) and Pb^{2+} (1.19 Å). Therefore, decrease in the bond length enhances the force constant of the Pb-O bond. Along with increase in force constant, effective mass m* of the Pb-O bond also decreases (as $m_{Gd} < m_{Pb}$), which results in blue shifts and is consistent with that observed in La-doped PMN Raman [80].

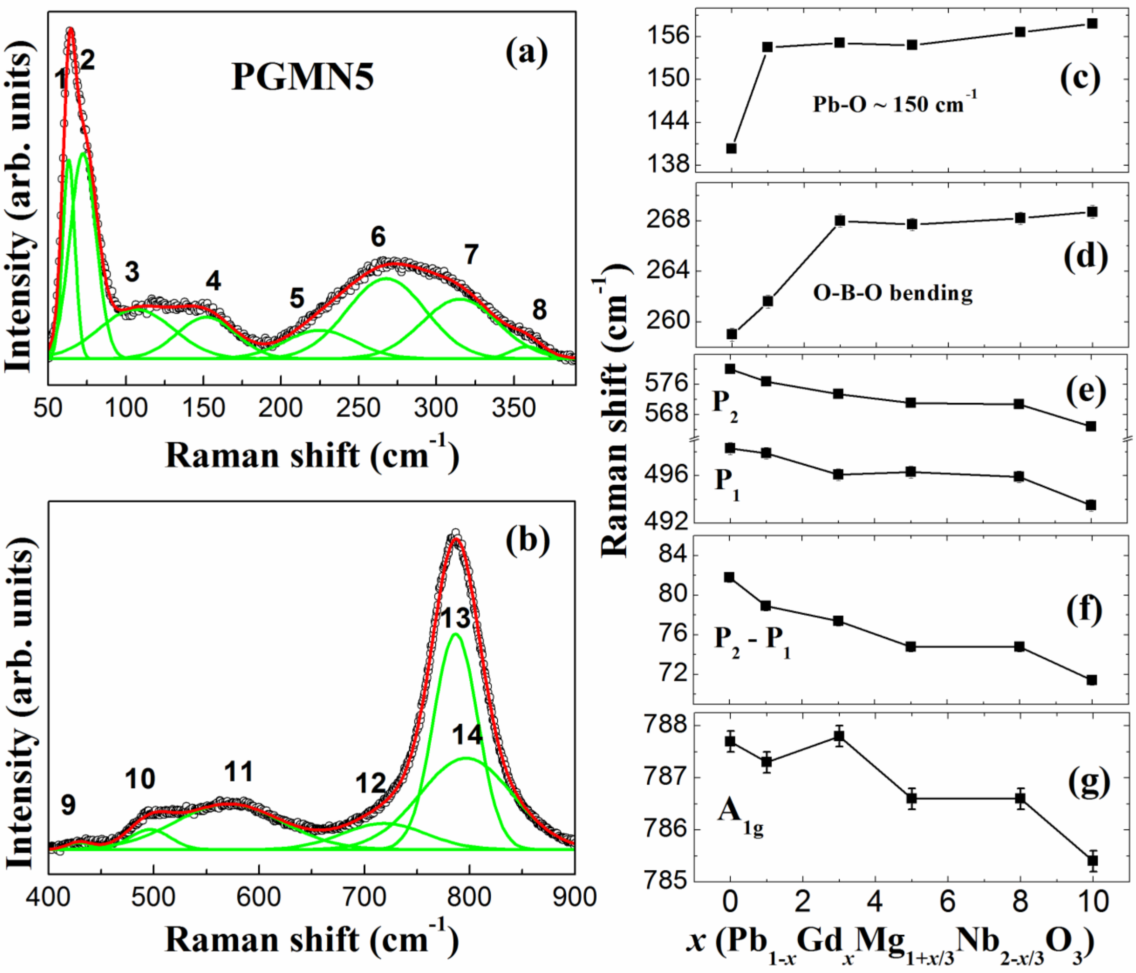

Fig. 4.14. (a,b) Deconvolution of Raman spectra of PGMN5 ceramic sample, where open circle represent the raw data, solid red line is the fitted data using Pseudo-Voigt peaks (green colour) and the linear background line is given for clarity. The composition (for $0 \leq x \leq 0.1$) evolutions of (c) bending mode of O-B-O near 260 cm^{-1}, (d) stretching mode of Pb-O bond near 150 cm^{-1}, (e) peak position around 490 cm^{-1} (P_1) and 580 cm^{-1} (P_2), (f) peak position difference of P_1 and P_2 and (g) variation of A_{1g} mode (~780 cm^{-1})

Similarly, in region 2 (~ 150 to 600 cm^{-1}), the peak position of modes 5 to 11 are assigned to bending modes of the O-B-O bonds and stretching of the Nb-O-Nb, or Mg-O-Mg bonds. The peak at ~ 260 cm^{-1} shows blue shift with increasing Gd concentration, as shown in Fig. 4.14(d). This can also be explained using the simple harmonic model. According to the formula, the charge imbalance due to Gd^{3+} ion substitution at Pb^{2+} site is compensated by changing the cation ratio of B-site ($Mg_{1+x/3}Nb_{2-x/3}$), which leads to a reduction in the effective mass of B-site from 61.937 gm/mol to 58.841 gm/mole, when Gd-concentration is increased from 0 to 10 at.%. The decrease in m^* of the O-B-O bending mode and enhancement in the binding strength (*k*) due to decrease of bond distance result in a shift of frequency to higher value, with increasing Gd concentration. The blue shift is also consistent with that in La-doped PMN [81].

In the frequency range of ~ 500-600 cm^{-1}, two broad peaks (10 and 11) are assigned to the Nb-O-Nb stretching mode, as denoted by P_1 and P_2 in Fig. 4.13. An increase in Gd-substitution has resulted in the red shift of P_1, P_2 modes [Fig. 4.14(e)]. Fig. 4.14(f) shows a decrease in separation of the frequency of P_1, P_2 modes with Gd substitution, which suggests a reduction in polarization. The origin of the Nb-O-Nb stretching mode is attributed to the displacement of Nb^{5+} from the center of NbO_6 octahedral cage, which is responsible for the formation of PNRs. This mode has been reported to evolve below the Burns temperature [77]. The separation between P_1, P_2 broad peaks is increased upon cooling, which has been related to the size of static PNRs [77,78]. A decrease in the separation of P_1, P_2 modes with increasing Gd content implies a reduction in the PNRs size, which is consistent with that reported for La-substituted PMN [81].

In region 3, the most intense mode is observed near 780 cm^{-1}, which has been designated to A_{1g} mode. This mode is a simple breathing type mode of oxygen atoms that has been observed in many complex perovskites, such as PMN, lead scandium tantalate (PST), lead scandium niobate (PSN), lead indium niobate (PIN), lead nickel niobate (PNN), lead magnesium tungstate (PMW) and lead iron tantalite (PFT) [111]. This mode has been assigned to the stretching mode of the B-O-B bond (here Nb-O-Mg), which corresponds to Fm3m symmetry observed for the CORs [76,77,81]. This A_{1g} mode is very sensitive to the B-site ordering [81]. Fig. 4.14(g) indicates that the A_{1g} mode is shifted to lower frequency with increasing Gd substitution. The red shift of this mode implies an important role of the m^*. To explain this, the origin of the CORs in the PMN is considered.

There are two models proposed to describe the CORs [12]: (i) “space charge model” where Mg and Nb occupy (111) adjacent plane in such a way that Nb-deficient negatively charged region is surrounded by Nb-rich positively charged disordered non-stoichiometric matrix and (ii) “random-layer model” where every other (111) plane of B-site sublattices is occupied by Nb cations and the rest of the planes of the B-site sublattices are occupied randomly by Mg and Nb in a ratio of 2:1. High-resolution Z-contrast image investigations have strongly supported the random-site model [13]. However, this model does not explain why the CORs in PMN do not grow with thermal annealing. This favors the space charge model, in which the local charge imbalance created by the short range CORs is compensated by the Nb-rich disordered regions. In space charge model, B-site is occupied by equal number of Mg (B_1-site) and Nb (B_2-site) and the atomic mass of B-site (58.5 gm/mol) does not change with Gd concentration. Thus the reduced mass (m^*) should remain same and frequency of A_{1g} mode should increase with Gd concentration, because of the increased force constant. This is just opposite what has been observed in Fig.4.14(g).

The red shift of A_{1g} mode can be explained if the CORs are described by random-layer model. According to this model, the CORs are applicable to $Pb[(Mg_{2/3}Nb_{1/3})_{1/2}Nb_{1/2}]O_3$, in which B_1 and B_2 sub-lattice are occupied by 2/3Mg + 1/3Nb and 1/2Nb, respectively. The average atomic mass of B_1 sub-lattice is 47, which is two times the atomic mass of the B_1 sub-lattice proposed by the space charge model. The reduced mass is expected to increase remarkably if the Nb ion diffuses at B_1-site with increasing Gd substitution. The Nb ion diffusion at B_1 site is possible if the B_1-O bond length is decreased with increasing Gd doping, while B_2-O bond length remains unchanged. The oxygen octahedral cage of B_1 cation will no longer hold large Mg ion without distortion, due to the decrease in the lattice constant. Local compositional changes may take place in which small size Nb ion can replace the large Mg ion. Consequently, m^* of A_{1g} mode also enhances, due to the variation in the distribution of Mg/Nb at B-site, which shifts this mode to the lower side. The red shift of A_{1g} confirms the increase in the 1:1 ordering of B-site due to Gd doping [80,81].

Table 4.4. Parameters of the Vogel-Fulcher (Eq. 5), strecthed exponential power law (Eq. 6) and Cluster glass model (Eq. 7) fit of frequency dependent T_m and a parameter $t^* = (T_f - T_o)/T_f$ calculated by replacing $T_f(\omega)$ by $T_m(\omega)$ and Vogel-Fulcher temperature (T_o).

%Gd	**Vogel-Fulcher Model (Eq. 5)**			
	T_f (K)	**E_a (eV)**	**ω_o (Hz)**	**Adj. R-square**
0	229.2(±0.7)	0.070(±0.002)	$3.20(\pm0.40) \times 10^{13}$	0.99990
1	190.6(±2.2)	0.140(±0.003)	$1.02(\pm0.15) \times 10^{16}$	0.99997
3	155.8(±1.5)	0.242(±0.002)	$1.41(\pm0.09) \times 10^{18}$	0.99996
5	164.3(±2.4)	0.194(±0.004)	$3.65(\pm0.13) \times 10^{16}$	0.99977
8	139.5(±1.2)	0.334(±0.003)	$6.97(\pm0.21) \times 10^{19}$	0.99993
10	117.4(±1.1)	0.473(±0.005)	$5.59(\pm0.15) \times 10^{22}$	0.99983

%Gd	**Stretched Exponential Model (Eq. 6)**			**Adj. R-square**
	p	**E_a (eV)**	**ω_o (Hz)**	
0	12.8(±0.3)	0.027(±0.001)	$1.12(\pm0.21) \times 10^{10}$	0.99994
1	7.0(±0.2)	0.032(±0.002)	$1.17(\pm0.23) \times 10^{11}$	0.99997
3	4.5(±0.3)	0.041(±0.001)	$6.85(\pm0.17) \times 10^{12}$	0.99996
5	5.1(±0.2)	0.037(±0.003)	$4.62(\pm0.37) \times 10^{11}$	0.99979
8	3.6(±0.1)	0.052(±0.004)	$2.14(\pm0.24) \times 10^{14}$	0.99993
10	2.8(±0.1)	0.070(±0.002)	$6.15(\pm0.17) \times 10^{16}$	0.99985

%Gd	**Cluster Glass Model (Eq. 7)**			***Adj. R-square***	t^*
	$z\nu$	**T_g (K)**	**ω_o (Hz)**		
0	10.5(±0.2)	248.4(±0.3)	$9.79(\pm0.30) \times 10^{15}$	0.99996	0.11
1	13.4(±0.3)	221.9(±0.6)	$5.16(\pm1.23) \times 10^{15}$	0.99996	0.22
3	14.0(±0.5)	205.0(±1.4)	$2.79(\pm0.71) \times 10^{14}$	0.99991	0.34
5	14.0(±0.8)	204.3(±2.2)	$1.87(\pm0.69) \times 10^{14}$	0.99976	0.30
8	14.0(±0.9)	205.2(±2.6)	$7.94(\pm2.79) \times 10^{13}$	0.99972	0.41
10	14.0(±1.5)	203.8(±4.3)	$6.80(\pm3.80) \times 10^{13}$	0.99923	0.50

It has been reported that the chemical ordered regions can be enhanced by aliovalent ion (e.g. La^{III}, Eu^{III}, Er^{III} etc.) doping with Pb^{II} or W^{VI} site for Nb^{V} and Mg^{II}- cations. For example, when the ordered regions are increased, the intensity of the stretching mode of Nb-

O-Mg bond (~ 780 cm^{-1}) is increased whereas the intensity of the stretching mode of Nb-O-Nb bond (~ 600 cm^{-1}) is decreased [76]. The intensity ratio of these two modes is reported to relate directly to the enhancement of the chemically ordered region. Furthermore, dielectric spectroscopy of PGMN samples is investigated, which complements the Raman results. Similarly, the intensity ratio of the stretching mode of Nb-O-Mg bond (~ 780 cm^{-1}) and the intensity of the starching mode of Nb-O-Nb bond (~ 600 cm^{-1}) is calculated from the background subtracted Raman data, which are listed in Table 1. The ratio is found to increase from 6.9 to 8.2. The intensity ratio calculated from Raman spectra of PMN is similar to that of La-doped PMN [76]. The Raman spectroscopy clearly shows that Gd substitution for Pb site enlarges the chemical ordered regions, thus leading to an enhancement in random internal electric field. Polar nano regions/domains are mainly responsible for the relaxor like dielectric characteristics.

4.2.2.4 TEM

The presence of the PNRs and the CORs in PGMN ceramics are observed under transmission electron microscope using bright and dark field imaging. Further, selected area electron diffraction (SAED) pattern along the <110> unit axis has been used to examine the effect of the Gd-substitution on the local chemical ordering of the B-site cations. Figure 4.15(a-i) illustrate room temperature bright field images, SAED pattern, and dark field images for PMN, PGMN5, and PGMN10, respectively. Local random contrasts representing polar nano-domains have been observed at room temperature, which is evident from Fig. 4.15(a-c). The average size of these polar nano-domains is less than 5 nm, which has been reported earlier to appear below the Burns temperature (T_B ~650K). In comparison to PMN, the number density of dark regions is reduced with increasing Gd-concentrations implying a reduction of the PNRs. These PNRs are an order of magnitude smaller than typical ferroelectric (FE) domains. It is in good agreement with the earlier reported TEM studies of the PMN and other Pb-based relaxors [12,13,21,19,72,113-116].

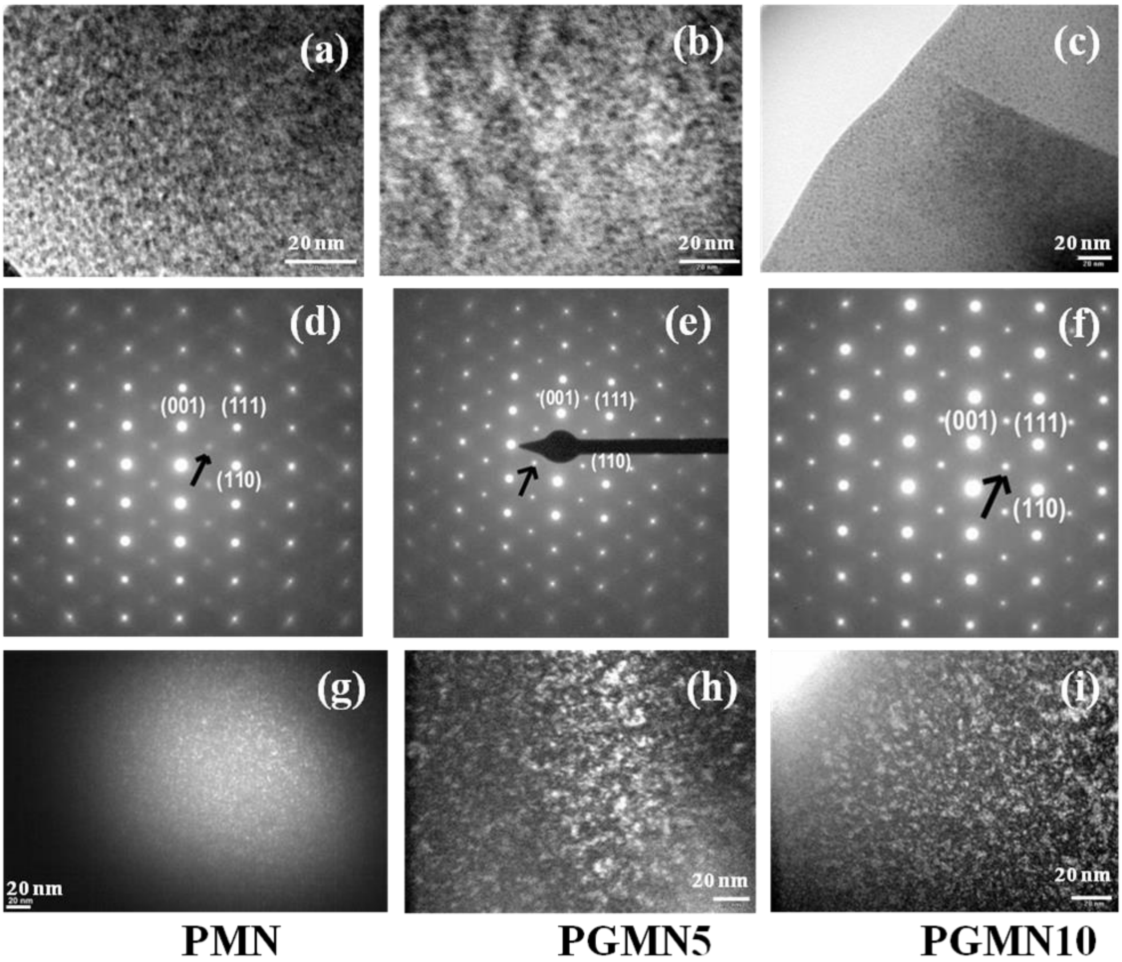

Fig. 4.15. Comparison of the bright field images (a)–(c), selected area electron diffraction along <110> unit axis (d)-(f) and dark field images (g)-(i) for PMN, PGMN5, and PGMN10 ceramics. The presence of superlattice reflection along ½<111> axis is shown by an arrow.

According to the chemical formula of PMN ($PbMg_{1/3}Nb_{2/3}O_3$), 1:2 ordering of Mg/Nb is expected as reported for $BaMg_{1/3}Nb_{2/3}O_3$. Instead of 1:2, non-stoichiometric 1:1 ordering has been reported for the PMN so far, which indicates FCC symmetry of the super-structure with doubling of unit cell in real space, where Mg and Nb are sitting alternately along h111i according to the widely accepted “random layer model”. Figure 4.15(d-f) compares the room temperature SAED pattern of PMN, PGMN5, and PGMN10 ceramics along the <110> unit axis. Apart from the allowed strong reflections originating from the cubic perovskite structure, extra weak spots along ½<111> (F-spots, super-lattice reflections), as marked by an arrow, are also clearly evident. These super-lattice reflections spots depict local ordering in some regions of the sample, which results into doubling of the unit cell. Any change in the intensity of F-spot corresponds to change in the size of CORs. It is evident from Fig. 4.15(d-f) that intensity of the F-spots enhances with increasing Gd-substitution. The effect of Gd-substitution in PMN on the intensity of ½<111> super-lattice reflections is similar to the well documented studies of the La-PMN, La-PMT ceramics and rare earth Tb, and Sm doped PMN [12,13,21,19,72,113-116].

Figures 4.15(g-i) show dark field image collected at room temperature using the (½<111>) superlattice reflections for PMN, PMN5, and PMN10 ceramics, respectively. In these images, the 1:1 CORs (shown as white spots) are confined to domains less than 5 nm in size for the PMN and the size of these CORs increases to more than 10nm with Gd-substitution. These CORs are dispersed randomly in the disordered matrix and found to be consistent with the previous investigations of the La-doped PMN [12]. Inability of the system to undergo phase separation into a mixture of perovskite and pyrochlore has been reported to be the cause of stability of the CORs in the PMN against coarsening upon thermal annealing.

This TEM analysis shows that Gd-substitution increases the intensity of superlattice reflection spots ½<111> in SAED pattern along the <110> unit axis and bright spots in the dark field images implying the enhancement of 1:1 Mg/Nb non-stoichiometric CORs, which is consistent with the earlier studies of A-site aliovalent ion substitution in PMN [12,13,21,19,72,113-116]. The consequences of this enhancement of the CORs and decrease of the PNRs on dielectric properties are discussed in Sec. 4.2.2.5.

4.2.2.5 Dielectric properties

Dielectric measurements are performed to analyse the influence of the Gd-substitution on the relaxor-like dielectric behaviour of the PMN. Figures 4.16(a-f) depict temperature dependence of dielectric constant [$\varepsilon'(T)$] and loss tangent [Tan $\delta(T)$] for x¼0, 0.01, 0.03, 0.05, 0.08, and 0.1 PGMN ceramics at selected frequencies in the frequency range of 100 Hz to 100 kHz and temperature range of 150 K-400 K. The $\varepsilon'(T)$ and Tan $\delta(T)$ for all the PGMN samples show diffused $\varepsilon'(T)$ peak with strong frequency dispersion near T_m (T of ε_m peak), i.e., T_m shifts progressively towards higher temperature with increasing frequency, which is the signature of typical relaxor behaviour. The ε_m reduces from ~21800 to 4200 and T_m from 265 K to 241 K at 1 kHz with increasing "*x*" The decrease in the ε_m is due to the presence of $GdNbO_4$ phase, reduction in number or/and size of the PNRs, and enhancement in the size of the CORs. Figure 4.17 compares the $\varepsilon'(T)$ curves at 1 kHz frequency for different PGMN ceramics in reduced form ($\varepsilon/\varepsilon_m$ vs T/T_m). The broadness around the Tm is enhanced with increasing "*x*" It can also be noticed from the inset of Fig. 4.17 that T_m (at 1 kHz) decreases from 265 K to 241 K up to $x = 0.03$. The decrease in the value of Tm is consistent with the Gd-substituting at the Pb-site in the perovskite lattice, which reduces the correlation among the PNRs. Above $x > 0.03$, a marginal increase in T_m from 241 K to ~244 K indicates substitution of the Gd-ion at the Mg-site. A similar increase in the T_m has been reported in high concentration Gd-doped PZT, which is attributed to a possibility of the Gd occupying the B site [118,119]. It is also well reported that the rare earth substitution at the A or the B-site in the PMN shifts the T_m to lower or higher temperatures, respectively [29]. Recently, Bikyashev et al. have related the size of the substituting cation to its occupancy at the A or B-sites in the PMN [29]. Large sized cations are expected to substitute at the A-site, whereas small sized cation ions are reported to substitute at the B-site. Since the Gd^{3+} ion has an intermediate size, there is a possibility of the Gd substitution at both the A or B-site depending upon the concentration. For higher "*x*" (~0.05), the Gd-ions are believed to replace the Mg-site when the charge imbalance due to the Gd-substitution at the Pb-site is compensated by adjusting the Mg/Nb cations ratio. The Gd-ion substitution at the Mg-site should lead to segregation of the MgO near to grain boundary, which is consistent with the scanning electron microstructural observation reported in Sec. 4.2.2.2.

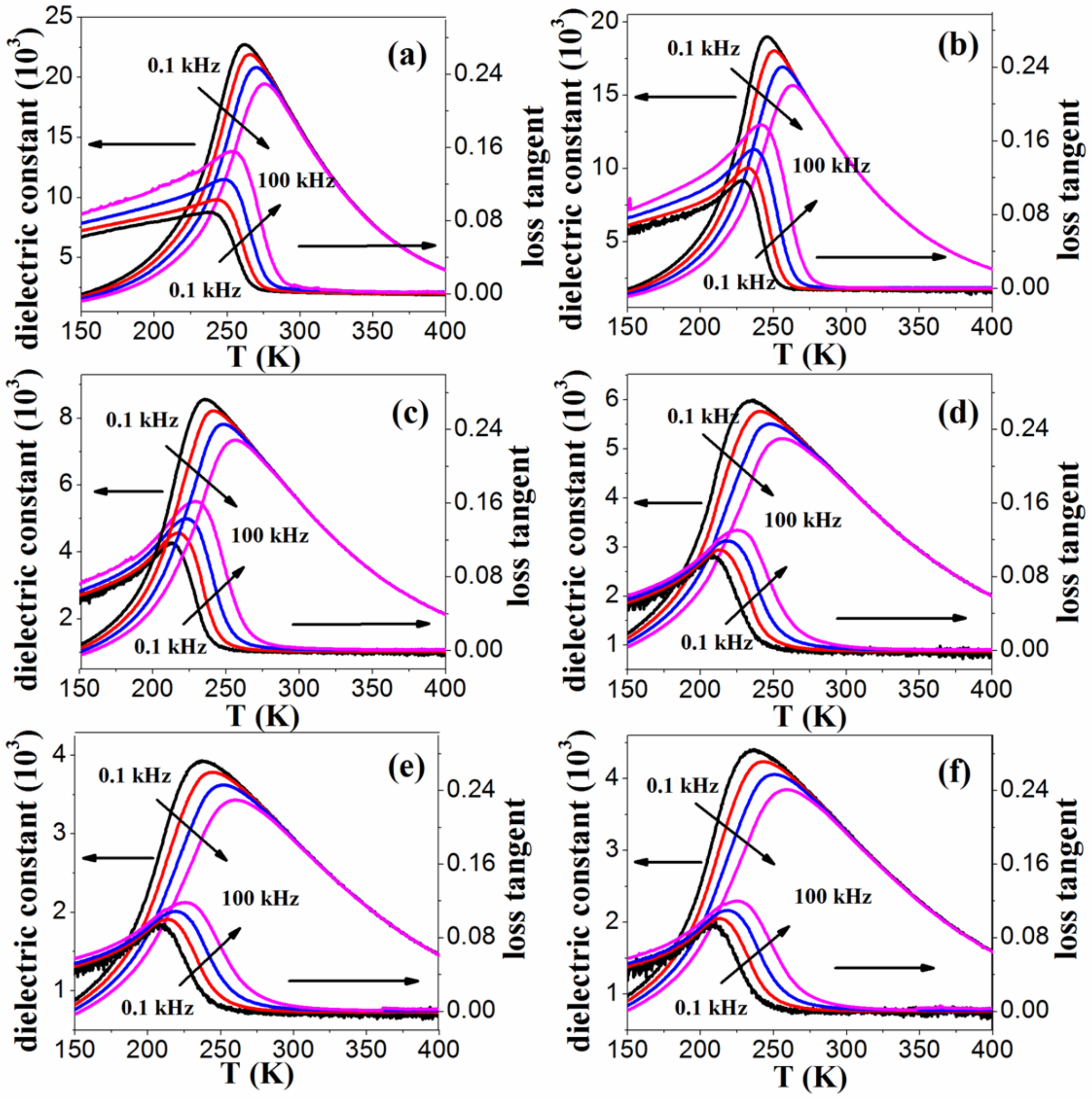

Fig. 4.16. (a)-(f) Temperature dependence of the dielectric constant [$\varepsilon'(T)$] and loss tangent [$\tan\delta(T)$] behavior at different frequencies in the 0.1-100 kHz range for $Pb_{1-x}Gd_xMg_{(1+x)/3}Nb_{(2-x)/3}O_3$, for $x = 0$, 0.01, 0.03, 0.05, 0.08, and 0.1 ceramics, respectively.

Relaxor dielectric characteristics are generally expressed by the degree of diffuseness and correlation length among the polar nano-regions. Interacting polar nano-regions should grow and enhance their correlation length during cooling. Depending on the correlation length or the size of the polar regions, the sample may undergo (a) ferroelectric phase transition at T_c (for large correlation length) or (b) slowing down of polarization fluctuation at

$T < T_m$ leading to random orientation of polar domains (for smaller correlation length). It is already known for ferroelectrics that the temperature dependence of $\varepsilon'(T)$ in paraelectric regions can be related with the Curie-Weiss law, whereas for relaxor ferroelectric, it is only related well above the T_B. Below T_B, deviation from the Curie-Weiss fitting is reported as proof of the development of the dipolar regions. Recently, a modified form of the Curie-Weiss relation (Eq. 4.2) has been shown to fit the $\varepsilon'(T)$ in a long range of temperatures above the ε_m, and this relation is reported to fit all other relaxor ferroelectrics [85]. Figure 4.18 depicts fitting of the $\varepsilon'(T)$ above the ε_m to Eq. 4.2 for $x = 0.1$, and the fitting parameters are reported in Table 4.3 along with that for other $x = 0$ to 0.1 samples. The inset of Fig. 4.18 shows the dependence of the δ_A with "x". The δ_A is shown to increase rapidly from 46 to 92 with increasing "x" up to 0.05, and above 0.05, it tends to slow down gradually to almost independent of "x" The high value of the δ_A is reported to relate directly with the enhancement of the degree of diffuseness [85]. Thus, increase in "x" leads to enhancement in the degree of diffuseness, which is due to higher chemical/charge disorder. Recently, the COR's effect on dielectric properties of the lanthanum (La^{3+}) substituted PMN is reported in which the charge imbalance due to La^{3+} substitution at the Pb-site is compensated by changing Mg/Nb cations ratio [120]. A large size of the CORs (~100 nm) is observed for 3 at.% La-doped PMN ceramic and degree of diffuseness (δ_A) is reported to increase from 45 to 77. It is believed that the random field associated with the COR's control size of the PNRs. Larger size CORs are expected to further reduce the size of the PNRs. A larger value of the δ_A (> 77) for "x" ~0.05 is believed to be due to the presence of an additional disorder, apart from the effect of the CORs on the PNRs dynamics. This additional disorder is due to Gd-substitution at the Mg-site for "x" ~0.05, which leads to a reduction in the cooperative interaction among the PNRs, resulting in a critical slowing down of the PNRs dynamics.

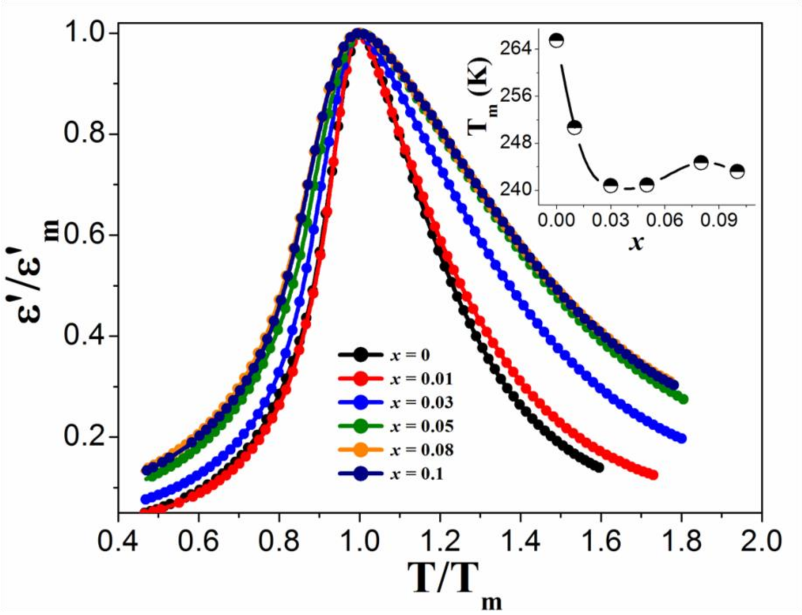

Fig. 4.17. Comparison of the $\varepsilon'(T)/\varepsilon'_m(T)$ versus T/T_m curves at 1 kHz frequency for different "x". Inset of figure depicts the variation of temperature of dielectric maxima (T_m at 1 kHz) with "x".

The strong frequency dispersion of the ε'_m near T_m is the consequence of spontaneous nucleation and thermal endurance of polarization of the PNRs below the T_B in the PMN. Frequency dispersion of the T_m can be fitted with the number of relations depending upon the strength of interaction among the polar nano-domains. The Arrhenius relation (Eq. 4.5) is generally used if there is no correlation among the PNRs, but the Vogel-Fulcher relation (Eq. 4.6) has been reported if frustrated interaction among the PNRs leads to freezing of the polar cluster fluctuations at finite temperature (T_f), similar to that in the spin glasses [54]. Stretched exponential relation (Eq 4.7) is used if continuous slowing down dynamics of PNRs the PNRs is considered and freezing of the PNRs takes place only at T = 0 K [88]. Another relation (Eq. 4.8) is suitable if frustrated interaction among the PNRs result into a critical slowing down of PNR's dynamics at a temperature (T_g) [89].

$$\omega = \omega_o e^{\left(\frac{-E_a}{k_B T_m}\right)} \tag{4.5}$$

$$\omega = \omega_o e^{\frac{-E_a}{k_B (T_m - T_f)}} \tag{4.6}$$

$$\omega = \omega_o e^{\left(\frac{-E_a}{k_B T_m}\right)^p} \tag{4.7}$$

$$\omega = \omega_o \left(\frac{T}{T_g} - 1\right)^{zv} \tag{4.8}$$

where ω_o is the attempt frequency ($\tau_o = \omega_o^{-1}$ is the microscopic time associated with flipping of fluctuating dipole entities), k_B is Boltzmann constant, E_a is the activation energy, T_f is Vogel-Fulcher temperature, where freezing of the polar cluster fluctuations takes place, T_g is the glass transition temperature, and zv is the critical dynamic exponent.

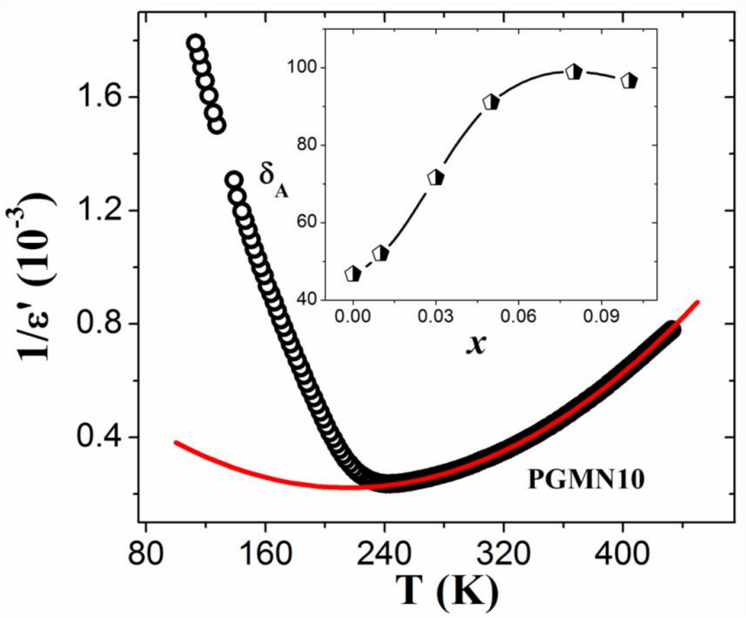

Fig. 4.18. Temperature dependence of $1/\varepsilon'(T)$ and $\varepsilon'(T)$ along with its fitting to Eq. (4.2) for $x = 0.1$, Inset of figure shows variation δ_A fitting parameter calculated by fitting temperature dependent dielectric constant ($f = 1$ kHz) with Eq. (4.2) against "x".

It has already been reported that the fitting parameter (ω_o and E_a) obtained from the Arrhenius relationship fitting do not correspond to any physical significance [3,54]. Figure 4.19(a) compares fitting of frequency dependence of the $T_m(f)$ to Eq. 4.6-4.8 for "x" equal to 0 and 0.1. The corresponding fitted parameters for $0 \leq x \leq 0.1$ are reported in Table 4.4 along with the goodness of fit. The solid line represents the fitted curve, and the open symbols represent the experimental data points. The fitting parameter of the T_f, determined from Eq. 4.6 for $x = 0$, is in close proximity of ergodic to non-ergodic transition reported earlier for PMN [3,90]. The fitting parameters ω_o and E_a for the PMN are consistent with the earlier report [85]. The attempt frequency (ω_o) is found to increase from 10^{13} Hz to 10^{22} Hz with increasing of "x" from 0 to 0.1. The attempt frequency (ω_o) beyond $>10^{14}$ has no physical significance.

The fitting parameters obtained from the fitting of $T_m(f)$ with Eq. 4.7 shows decrease of the value of p from 12.8 to 2.8 with increasing x, which is consistent with its inverse relation against dielectric strength, as reported among normal ferroelectric, Debye medium, pure glassy or relaxor ferroelectrics [88]. The attempt frequency is also reasonable to its physical process except for $x = 0.1$. The stretched exponential power law fitting suggests enhancement in the dielectric relaxation strength with increasing "x" but the value of $\omega_0 \sim 10^{16}$ Hz for $x = 0.1$ is in unacceptable range. Figure 4.19(b) compares the fitting of $T_m(f)$ with Eq. 4.8 for $0 \leq x \leq 0.1$. It is observed that the fitting of $T_m(f)$ data with bounding zv value to ~14 yields more reasonable ω_o, zv parameters, which are presented in Table 4.4. The fitted parameters of PMN are ω_o ~$9.8 \pm 0.3 \times 10^{15}$ Hz, $T_g = 248.4 \pm 0.3$ K, and $zv = 10.5 \pm 0.2$. With increasing "x" the ω_o decreases from $\sim 10^{15}$ Hz to $\sim 10^{13}$ Hz. For $x \geq 0.5$, the values of the fitting parameters ω_o are more reasonable from the point of the view of a thermally activated process in comparison to that obtained from Eq. 4.6. The best fitting parameters for PGMN10 are $\omega_o = 6.8 \pm 3.8 \times 10^{13}$ Hz, $T_g = 207.9 \pm 4.3$K, and $zv = 14.0 \pm 1.46$. Recently, in PMN, nonergodic ferroelectric cluster glass ground state (also known as "super-dipolar" glass) is reported to emerge from high temperature PNR ensemble under random electrostatic interaction [91]. A static glass temperature ($T_g = 238$ K) is reported from the fitting of the $T_m(f)$ of ε' to Eq. 4.8 in the frequency range 1×10^{-3} Hz to 2×10^{-2} Hz. The prefactor "τ_o" and zv values are in accordance with the mesoscopic size of the PNR around T_g. The fitting of the temperature dependence of the permittivity ε' to Eq. 4.8 in frequencies 10^2 Hz to 10^5 Hz has shown a strong deviation above ~245K for PMN. The parameters "τ_o", T_g, and zv of PMN reported in Table 4.4 are different because of the limited frequency range used. It may be noticed that reduction in "τ_o" from 10^{-16} to 10^{-12} s and T_g from 248 K to 204 K with increasing

"x" can be inferred as a critical slowing down of the dynamics of PNRs ensemble (cluster) resulting in "super-dipolar" glass state.

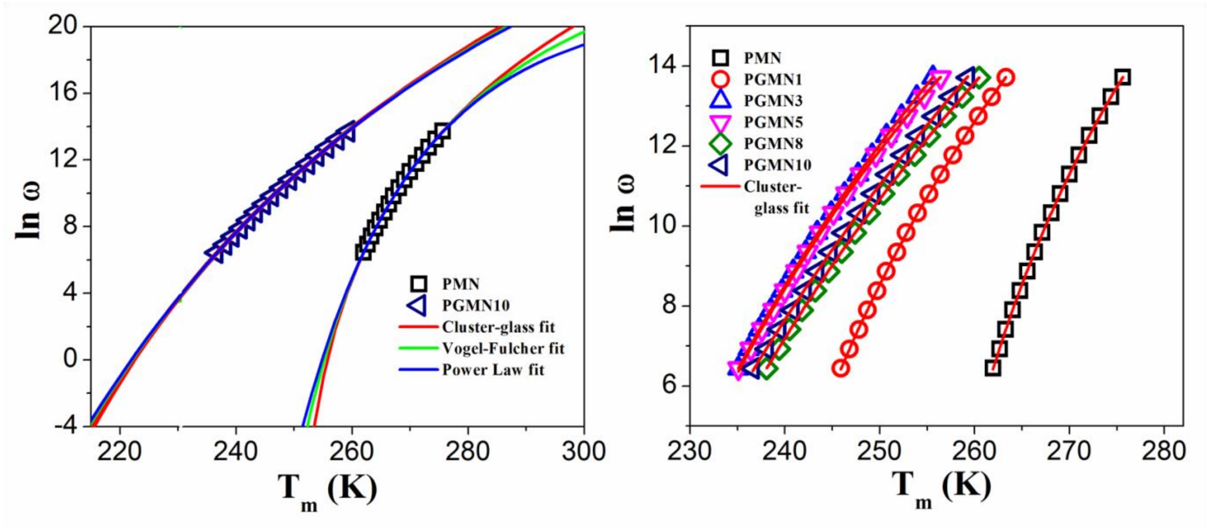

Fig. 4.19. (a) Comparison of the Vogel-Fulcher (green curve) and critical slowing down dynamics (red curve) fitting of PMN and PGMN10 ceramics, (b) All PGMN ceramics fitted by critical slowing down dynamics with bounding $z\nu$ high value to ~14, where open symbols represent the temperature of ε_m (T_m) in the frequency range of 0.1–100 kHz and the red solid line is fitting to Eq. (4.8).

The frequency dependent $\varepsilon'(T)$ data are analysed to get more insight into the glassy phase. The frequency dependent T_m (T of ε_m peak) between two frequencies is defined by an empirical (also known as Mydosh) parameter "K" = $\Delta T_m/(T_m \text{ x } \Delta\log(f))$, which has been reported to distinguish between spin glass (SG), cluster glass (CG), and superparamagnetic (SPM) states in magnetic materials [92]. The smaller values of "K" ~0.005-0.01 are generally reported for SG with strongly interacting spins, ~0.03-0.06 for CG weakly interacting spins and larger value > 0.1 for non-interacting spins for SPM system. Similarly, the value of "K" can be used to distinguish between dipolar glass, super-dipolar glass (CG), and super-paraelectric (SPE) states. The related shift $\Delta T_m/T_m$ is calculated with a change of frequency between 100 Hz and ~150 kHz. The values of "K" are presented in Table 4.3 for $0 \leq x \leq 0.1$. A non-ergodic ferroelectric cluster-glass state or "super-dipolar" glass state is expected for $x \geq 0.05$ with "K" value ~0.03. In order to further confirm the CG system, a parameter $t^* = (T_f - T_o)/T_f$ is generally reported to distinguish the SG system (where $t^* < 0.1$) from the CG system (where $t^* \geq 0.5$) in magnetic material [121]. Here T_o is the Vogel-Fulcher temperature, which relate intercluster interaction strength and T_f is represented by maxima in real part of susceptibility at particular frequency, which shifts to lower temperature with decreasing frequency analogous to that has been seen in the present temperature dependence of the dielectric constant. The parameter t^* has been calculated by replacing $T_f(\omega)$ by $T_m(\omega)$ and the values are reported in Table 4.4. It is observed that t^* parameter increases from 0.11 to 0.5 with "x" suggesting formation of super-dipolar glass state for $x \geq 0.05$.

This study clearly shows that the Gd-substitution in high concentration enhances the size of the chemical ordered regions, which is responsible for enhancement in the random field causing a reduction in the size of the PNRs. The additional disorder is observed above $x \geq 0.05$, when Gd-ions are also substituting at the Mg-site, which results in a reduction in the co-operative interaction among the PNRs leading to critical slowing down of the PNRs ensemble at static glass temperature. It seems increased chemical/charge disorder along with the weak co-operative interaction among the PNRs resulting in "superdipolar glass" state in high Gd-substituted PMN.

4.2.2.6 PE hysteresis loop

Figures 4.20(a) and 4.20(b) compare PE-loop recorded at 300 and 170 K when 15 kV/cm field is applied at 50 Hz frequency for $0 \leq x \leq 0.1$. Figures 4.20(c) and 4.20(d) compare dependence of the polarization (P_{max} and P_r) with the electric field at 300 and 170 K, respectively. The hysteresis loss free non-linear P-E loop is observed for $0 \leq x \leq 0.1$ at 300 K. The PE-loop at 300K is "S-shaped" for $x < 0.05$ displaying nonlinear dependence of the polarization to the applied field and tendency of saturation at large field. Inset of Fig. 4.20(a) shows a significant decrease in the P_{max} from 15.7 to 4.6 μC/cm^2 with increasing "x" from 0 to 0.05. With a further increase in "x" (> 0.05), the P_{max} is decreased slowly from 4.6 to 3.5

μC/cm^2. Typical ferroelectric like P-E hysteresis loop is observed at 170 K for PMN, which indicates the development of long range order because the applied field is more than the threshold field (~2 kV/cm for single crystal along <111> direction) reported earlier [97]. The P_{max}, P_r, and E_c is 30.1 μC/cm^2, 25.7 μC/cm^2, and 7.4 kV/cm, respectively (for PMN). It is important to note that PMN is able to sustain P_r, which confirms the slowing down of polar nano-domains dynamics, but when the applied external field is more than the random field, the nano-polar domains convert into macroscopic domains. Figure 4.20(d) shows the exponential decrease in P_r and P_{max} at 170 K with increasing "x". The P_r is decreased drastically from 25.7 to 1.67 μC/cm^2, in contrast, to change in the P_{max} from 30.1 to 9.1 μC/cm^2 with increasing "x" from 0 to 0.03. The area under the curve reveals the hysteresis loss, which is found to decrease with increasing "x". The enclosed area of the *PE* loop suggests a phase lag between the applied field and the polarization response, which implies sluggish response of the polar nanoregions. Small opening of the *PE* loop can be considered non-linear activity of sluggish PNRs response to the external stimuli in which the PNRs do not flip, but just change shape in the sense of a breathing mode reported for the dipolar glass $K_{1-x}Li_xTaO_3$ [122].

The P_{max} 24.5 μC/cm^2 (at 50 kV/cm) of the PGMN1 is found to be close to 27.7 μC/cm^2 (at 50 kV/cm) of PMN, which indicates a near complete alignment of the polar nanodomains at 300K [Fig. 4.20(c)]. It may be noticed for $x > 0.05$ that there is no transformation from short range (nano domains) to long range (macroscale domains) ordering up to 50 kV/cm applied field because no remnant polarization is observed. For PMN, the P_{max} strongly varies non-linearly with the applied field, which indicates complete alignment of the polar nano domains, but a near linear dependence is observed for PGMN10. Linear dependence between *P* and *E* suggests that the correlation within the PNRs is weak because of reduction in the size of the PNRs. Correlation among the PNRs is also diminished due to the enhancement of the CORs, presence of MgO and $GdNbO_4$ second phases.

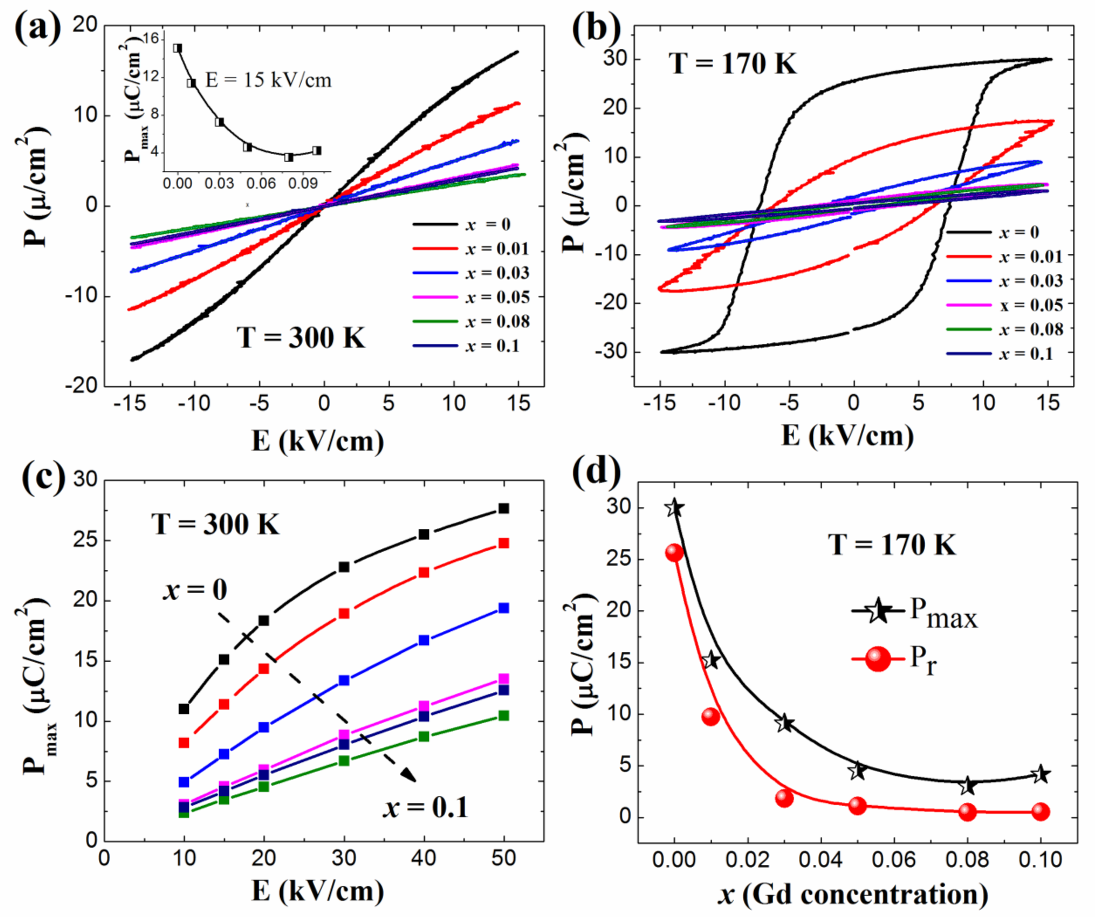

Fig. 4.20. Comparison of PE-loop recorded at (a) 300 K and (b) 170 K when15 kV/cm field applied at 50 Hz frequency for PMN to PGMN10 ceramics. (c) Comparison of the effect of Gd-concentration on the (c) P_{max} and (d) P_r and P_{max} against ac-drive amplitude applied at 50 Hz at 300 K and 170 K, respectively.

It is well reported in the literature that the La-substitution at the Pb-site in PMN leads to single perovskite phase without any secondary phase, when the charge imbalance is compensated by changing the B-site cation ratio [108]. In the present study, Gd substitution onto the Pb-site with similar charge compensation mechanism seems unable to control the precipitation of secondary phase. This peculiarity in Gd-substituted PMN system is due to lower solubility limit of Gd-ions in comparison to that of the La-substituted PMN. Enhancement in relaxation behaviour is directly correlated with the size of the CORs and the PNRs, which has been demonstrated by TEM (enhancement in the intensity of F-spot) and

RAMAN (red shift of A_{1g} mode ~780 cm^{-1}). Gd-substitution at the Pb/Mg-site is responsible for creating enhanced randomness/disorder along with weak interaction among the PNRs leading to its critical slowing down resulting in super-dipolar glass state.

4.2.3 Conclusion

Critical slowing down of PNRs ensemble resulting in a super-dipolar glass state has been observed in Gd-substituted PMN for $x \geq 0.05$. The fitting parameters obtained from the fitting of $T_m(f)$ to the power law of critical dynamics are consistent with the super-dipolar glass state. A large degree of diffuseness parameter "δ_A" > 90 for $x \geq 0.05$ is due to an additional disorder arising by the Gd-ions substitution at the Mg-site, which is also confirmed by phase analysis and elemental mapping. Raman spectroscopy has revealed red-shift in the stretching mode of Nb-O-Mg (A_{1g} mode) and Nb-O-Nb (P_1 and P_2 modes in ~500-600 cm^{-1}), which has been related to the variation in size of CORs and PNRs, respectively. The red shift in A_{1g}, as well as the Nb-O-Nb stretching modes and the intensity ratio of A_{1g} and P_2 modes, has been shown to increase with increasing Gd concentration, due to the enhancement of CORs and the reduction in PNRs size. A microstructural investigation using selected area electron diffraction (SAED) pattern along <110> unit axis has revealed enhancement in intensity of the superlattice reflection spots along ½<111> with increasing Gd-substitution, which also reveals an enhancement in the size of the CORs and reduction in the size of PNRs. Sluggish response of the polar region is exhibited in the low temperature hysteresis *P-E* loop study of $x \geq 0.05$, suggesting a reduction in the co-operative interaction within the PNRs leading to a reduction in its size. An empirical parameter "*K*" calculated from the temperature dependence of AC permittivity asserts the existence of super-dipolar glass state for $x \geq 0.05$. The segregation of second gadolinium niobate phase in Gd-substituted PMN for $x > 0.03$ is independent of the charge compensation mechanisms, which is in contrast to La-doped PMN study where precipitation of the second phase was successfully controlled by changing the B-site cation ratio.

4.3 Electrocaloric behaviour of Gd-substituted PMN $Pb_{1-x}Gd_x(Mg_{1+x/3}Nb_{2-x/3})O_3$ $(0 \leq x \leq 0.1)$ ceramics

4.3.1 Introduction

Currently ferroelectric materials showing electrocaloric (EC) effect are in focus because of their promising usage for future generation cooling technologies as an alternative to the conventional vapour-compression refrigeration technology [123]. Current impetus is on exploration of new ways to enhance the EC effect, so that solid state cooling devices may find its uses in temperature regulations for sensors, electronic devices, medical equipment, and on-chip cooling etc. [123]. Refrigeration based on the EC effect is proposed to be superior to thermoelectric effect based solid state electric-cooling devices, due to the absence of current-conduction in the ferroelectric materials.

The EC effect has been first proposed in 1887 and experimentally observed 40 years later in the Rochelle Salt, which is now considered to be relatively weak (ΔT = 3 mK) [37]. After that, many ferroelectric, antiferroelectric, and relaxor systems have been explored for the next ~60 years, without any significant improvement in the EC effect. Recent advancement in EC effect is due to the observation of giant EC response (ΔT = 12K) around 222 ^{o}C in PZT ferroelectric thin films, and in ferroelectric/relaxor copolymer in temperature range 30-70 ^{o}C, which is measured indirectly at high electric fields [124,125]. These two pioneer works have introduced new and upcoming era of electrocaloric cooling. At present, several lead-based and non-lead based perovskite materials are known to show strong EC effect. An indirect measurement on thin films of PMN-PT has reported strong EC-response

(ΔT = ~31 K) for the applied voltage of 10 volt at 140 °C [126]. However, it is believed that only bulk materials with strong EC response would exhibit enough cooling power for new-generation cooling devices.

The EC effect is related to the adiabatic temperature change (ΔT_{EC}) or isothermal entropy change (ΔS) of a material upon the application or withdrawal of an external electric field. Generally, under isothermal conditions, application of electric field orders the dipoles, accompanied by a decrease of the dipolar-subsystem entropy, leading to enhancement in the lattice-vibration entropy, resulting in an increase in temperature of the ferroelectric materials, to dissipate heat. Similarly, during the removal of field, an increase in the dipolar-subsystem entropy will cause reduction in the lattice-vibration entropy, resulting in decrease in the temperature of the ferroelectric materials, to absorb heat. Ferroelectrics with large pyroelectric coefficient $(dP/dT)_E$ are generally known to exhibit strong EC response compared to the dielectrics. For a ferroelectric, temperature dependence of the EC effect (ΔT_{EC}) at constant change of the electric field (ΔE) shows a maximum at the transition temperature (T_c), where ferroelectric to paraelectric phase transition takes place. This positive EC effect is generally found in most of the ferroelectric materials, *i.e.*, FE-material heats up (cools down) with increase (removal) of the electric field [124-130]. Solid solution of lead magnesium niobate-lead titanate near the morphotropic phase boundary is reported to show appreciable positive EC effect, due to the presence of polar nano-domains, which carry an extra entropy contribution pertinent to strong EC response [123].

Recently, an unusual/negative EC effect is observed in relaxor ferroelectrics (RFE) and antiferroelectric (AFE) ceramics, where cooling is produced by the application of an electric field.[10] Similar negative EC effect has also been reported in a number of perovskites, solid state solutions, thin films, and multi-layered nanostructures, e.g., $Sr_xBa_{(1-x)}Nb_2O_6$, $Pb(Mg_{1/3}Nb_{2/3})O_3$-$32PbTiO_3$, $Pb_{0.8}Ba_{0.2}(Zn_{1/3}Nb_{2/3})_{0.7}Ti_{0.3}O_3$, $PbZrO_3$, $BaTiO_3$, $PbTiO_3$ and

$PbZr_{0.53}Ti_{0.47}O_3/CoFe_2O_4$, $Hf_{0.5}Zr_{0.5}O2$ etc. [132-153]. Existence of both positive and negative EC effects, in which reversal of the sign of the ΔT_{EC} occurs at a certain temperature, has also been reported for compositions near the MPB of 0.94BNT-0.06BT, 0.7PMN-0.3PT, and 0.5BT-0.5ST solid solutions. Underlying mechanisms for the observance of the negative or both positive & negative EC effects is not yet established. However, it is proposed that materials exhibiting both (+ve & -ve) EC effects are preferred, in order to develop more efficient refrigeration technologies [131].

It has been previously mentioned that Gd-substitution in PMN ceramics enhances the dielectric relaxation strength, which has been correlated with enhancement in non-stoichiometric chemical ordered regions (COR's) [59,79,105]. Large concentration of Gd-ions at Pb-site is reported to induce critical slowing-down of dynamics of the polar nan-domains, which should cause anomalous EC effect, based on strong dependence of the dipolar entropy on the applied electric field [59,105]. The purpose of this study is to investigate the EC effect in $Pb_{1-x}Gd_x(Mg_{1+x/3}Nb_{2-x/3})O_3$, for $x = 0$, 0.01, 0.05 and 0.1 ceramics indirectly from the temperature dependent heat capacity and *P-E* hysteresis loop measurements on the ceramic compositions.

4.3.2 Electrocaloric behaviour

A systematic study on Gd-doped PMN has already been reported, in which the Gd-ion is shown to substitute both at the Pb-site and Mg-site for Gd-concentrations ≥ 5 at.%, resulting in enhancement of size of the chemically ordered regions (COR's); degree of relaxation and diffuseness causing reduction in the correlation among the PNR's, leading to reduction in the maximum dielectric constant at T_m (ε'_{max}) and saturation polarization (P_{sat}) [59,105]. It is believed that the size of COR's control the size of the PNR's and the random field associated with the COR's control correlations among the PNR's. It has also been revealed that an additional disorder is induced when Gd-substitutes the Mg-site, resulting in higher value of degree of diffuseness δ_A (> 77) for Gd-concentration $\geq$ 5 at.%. This additional disorder is believed to be responsible for the reduction in the cooperative interaction among the PNR's, resulting in the critical slowing down of the PNR's dynamics, which ultimately leads to non-ergodic ferroelectric cluster glass ground state (also known as "super-dipolar" glass) [91]. This is also consistent with an earlier report in which super-dipolar glass emerges from high temperature PNR's ensemble under random electrostatic interaction in PMN [91]. Figure 4.21 depicts representative dielectric behaviour of PGMN10 ceramic and inset of the Fig. 4.21 compares fitting of the T_m vs τ plot to Eq. 1 for all PGMN ceramics.

$$\tau = \tau_o \left(\frac{T}{T_g} - 1\right)^{-zv} \tag{4.9}$$

where $\tau_o = \omega_o^{-1}$ is the microscopic time associated with flipping of fluctuating dipole entities, zv is critical dynamic exponent and T_g is glass transition temperature. As reported, reasonableness of the fitting parameters reveal interaction among the PNRs resulting into a critical slowing down of PNRs dynamics at finite temperature []. Having this background, EC effect is evaluated for Gd-substituted PMN ceramics.

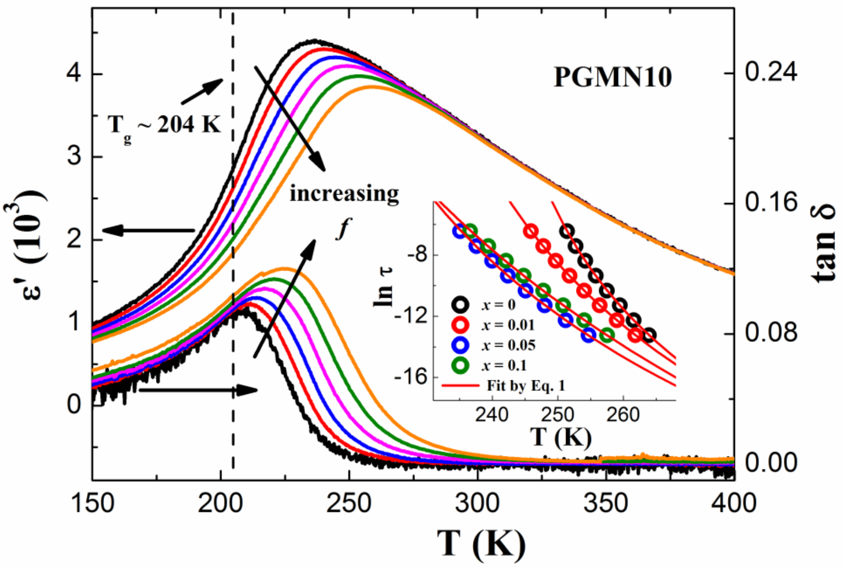

Fig. 4.21. Temperature dependent ε' and tan δ of $Pb_{1-x}Gd_xMg_{1+x/3}Nb_{2-x/3}O_3$ ceramic of x = 0.1 at different frequency. Inset of the figure shows fitting of all PGMN ceramics to the Eq. 1.

In order to evaluate the electrocaloric (EC) effect by “indirect method”, *P-E* hysteresis loop is measured at different temperatures. Figure 4.22 compares the *P-E* hysteresis loops for $x = 0$ to 0.1 PGMN ceramics, traced at several temperatures in 150 K to 240 K range. Hysteresis-loss-free non-linear *P-E* loop is observed at 300 K for $0 \leq x \leq 0.1$ when the external applied field is switched at 50 Hz. Small opening in the *P-E* loop at 210 K for $0.01 \leq x \leq 0.1$ is attributed to non-linear activity of sluggish PNR’s response to the applied electric field, in which the PNR’s do not flip but just change shape, similar to a breathing mode reported for dipolar glass $K_{1-x}Li_xTaO_3$ [122]. The hysteresis loss implies sluggish response of the polar nano-regions. For $x < 0.05$, the *P-E* loop at 300 K is “*s*-shaped”, which tends to saturate at the larger field and also exhibits non-linear dependence between the polarization and the applied field. Below 210 K, a typical ferroelectric like *P-E* hysteresis loop is observed for the PMN, indicating the development of long range order and the PMN is able to sustain P_r at low temperatures. The coercive field increases with decreasing temperature, confirming the slowing down of polar nano-domains’ dynamics.

For $x \geq 0.05$, no transformation from short range (nano-domains) to long range (macroscale domains) ordering is noticed up to 50 kV/cm applied field. The maximum polarization (P_{max}) vs. the applied field is observed to vary non-linearly for $x < 0.05$ and linearly for $x \geq 0.05$, signifying complete and incomplete alignment of the polar nano domains, respectively. Linear dependence between P and E suggests that the correlation within the PNR’s is weak, due to reduction in the size of the PNR’s, rooted in the enhancement of COR’s and the presence of second phases e.g., MgO and $GdNbO_4$, as reported earlier [105].

Figure 4.23 shows the temperature dependence of polarization under different electric fields (5, 10, and 15 kV/cm) and the P_{max} is calculated using the upper/descending part of the hysteresis loops, similarly as reported by Mischenko *et. al.* [124] The temperature dependence of P_{max} reveals a broad peak, which shifts linearly toward higher temperature with increasing electric field for $x \geq 0.01$. This anomalous behaviour is observed in very few materials, which show re-entrant behaviour [154]. Field-induced alignment of PNR's will depend upon the combination of applied field and thermal agitation or dynamics of PNR's.

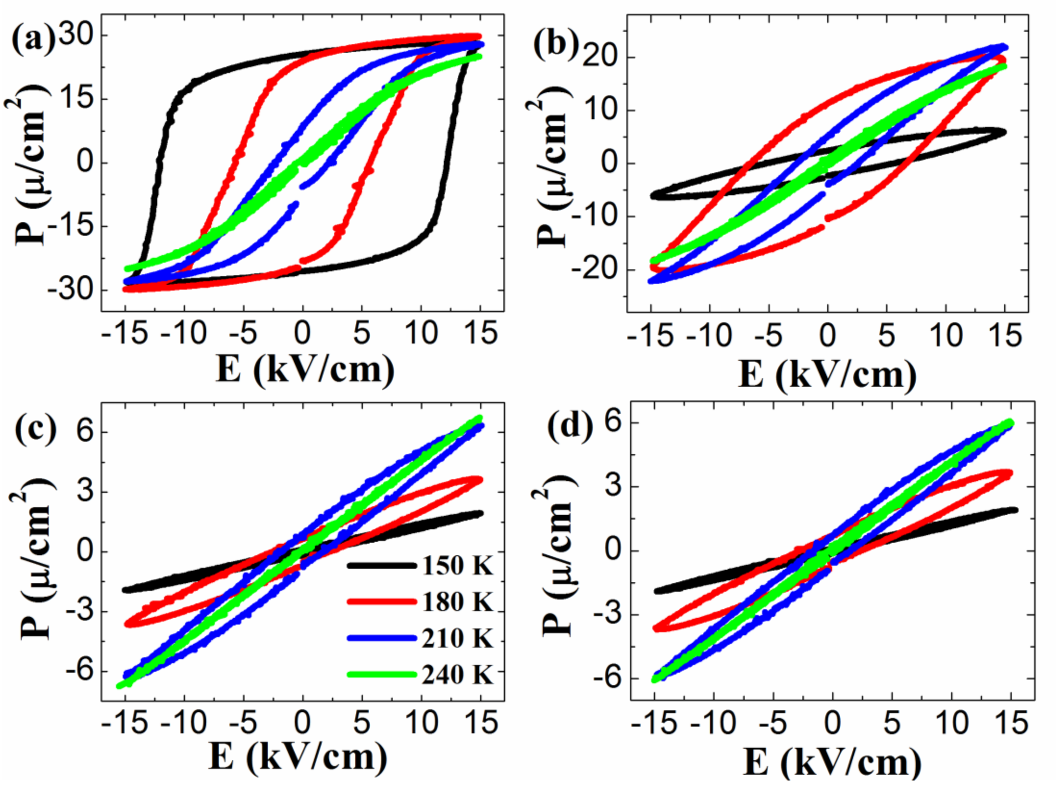

Fig. 4.22. Temperature dependent *P-E* hysteresis loop of $Pb_{1-x}Gd_xMg_{1+x/3}Nb_{2-x/3}O_3$ ceramics recorded at 50 Hz; **(a)** x =0, **(b)** x = 0.01, **(c)** x = 0.05, and **(d)** x = 0.1.

Higher field (15 kV/cm) should overcome the agitation effect and cause alignment of the PNR's at higher temperature, compared to that at lower field (5 kV/cm). It is believed that the anomalous behaviour observed for $0.01 \leq x \leq 0.1$ ceramics associates with the dynamics of polar domains. Two distinct regions are noticed in Figs. 4.23(a-d). In region II, the P_{max} is observed to increase with cooling, which is attributed to the enhanced alignment of nano-polar regions in the direction of electric field at lower temperatures. Depending upon the composition, long range ordering is developed for x = 0, but the extent of co-operative interaction decreases with increase in the Gd-ions concentration. For $x \geq 0.5$, no long range ordering is observed as shown in Fig. 4.22(c-d); an increase in the P_{max} value with decreasing temperature is attributed to the alignment of smaller nano-domains. The P_{max} decreases with further cooling in region I, which is attributed to the non-ergodic behaviour and critical slowing down of PNR's dynamics for $x = 0$ and $x > 0.1$, respectively. The critical slowing-down of PNR's dynamics is due to the enhanced disorder observed with Gd-substitution at Mg-site for $x \geq 0.5$. Further, the EC effect is calculated from the temperature dependent *PE* loop and heat capacity measurements, across the glass transition temperature.

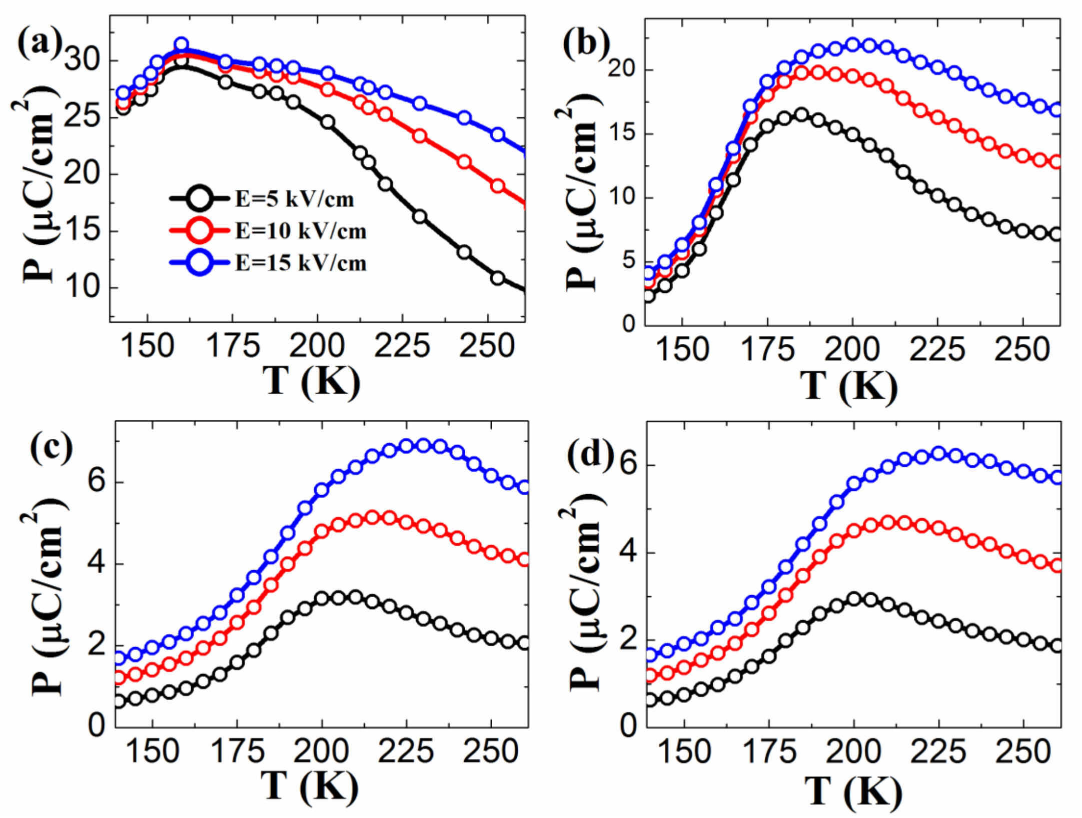

Fig. 4.23. Temperature dependent polarization behaviour of $Pb_{1-x}Gd_xMg_{1+x/3}Nb_{2-x/3}O_3$ ceramics at different electric fields; **(a)** $x = 0$, **(b)** $x = 0.01$, **(c)** $x = 0.05$, and **(d)** $x = 0.1$.

The EC effect is adiabatic temperature change (ΔT_{EC}) of a dielectric material in response to the change in electric field (ΔE). Assuming the Maxwell's relation $(\partial P/\partial T)_E = (\partial S/\partial E)_T$, for a dielectric material having density (ρ) and heat capacity (C_p), ΔT_{EC} due to an applied field E is given as follows [123]

$$\Delta T_{EC} = -\frac{1}{\rho}\int_{E_1}^{E_2} \frac{T}{C_p(T)}\left(\frac{\partial P}{\partial T}\right)_E dE \qquad (4.10)$$

where P is the polarization, and E_1, E_2 are respectively the starting and final applied electric fields. The values of $(\partial P/\partial T)_E$ are calculated from the derivative of P vs. T plot (Fig. 4.23). For the density 'ρ' (= mass of unit cell/(lattice constant)^3) of the ceramic, lattice constant is determined from the Rietveld refinement of XRD pattern using Fullprof software (ρ ~ 8.066 gm/cm^3) [109]. Temperature dependent heat capacity for $x = 0$ to 0.1 PGMN is determined by differential scanning calorimeter, which are compared in Fig. 4.24. The heat capacity initially varies linearly from 0.22 J/gm K to 0.34 J/gm K below ~ 160 K and then tends to saturate to ~ 0.40 J/gm K in the temperature range 160 K to 280 K. Absence of any structural phase transition in 130-290 K temperature range is also noticed for $x = 0$ to 0.1 PGMN ceramics.

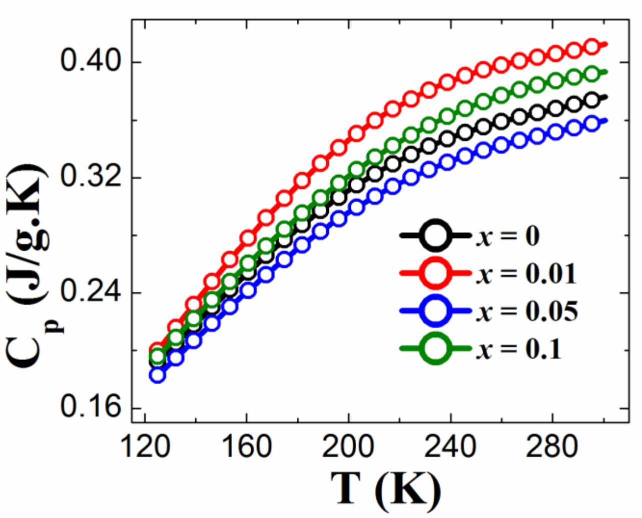

Fig. 4.24. Heat capacity (C_p) as a function of temperature for $Pb_{1-x}Gd_xMg_{1+x/3}Nb_{2-x/3}O_3$ ($0 \leq x \leq 0.1$) ceramics measured using differential scanning calorimetry (DSC).

The ΔT_{EC} is calculated by using Eq. 1, where ΔE ($=E_2-E_1$) is 5, 10, and 15 kV/cm when E_1 is set as zero for $x = 0$ to 0.1 PGMN ceramics. Figure 4.25 shows ΔT_{EC} as a function of temperature at 5, 10, and 15 kV/cm values of ΔE. Earlier, Rozic *et. al.* [155] reported the EC effect of PMN in the temperature range of 220 K-340 K and found consistent ΔT_{EC} value with that of x =0. But as a consequence of the anomalous polarization-change with temperature, all PGMN ceramics have exhibited a crossover from positive to negative ΔT_{EC} in the vicinity of the temperature dependent P_{max}-peak, as observed in Figs. 4.25(a-d).

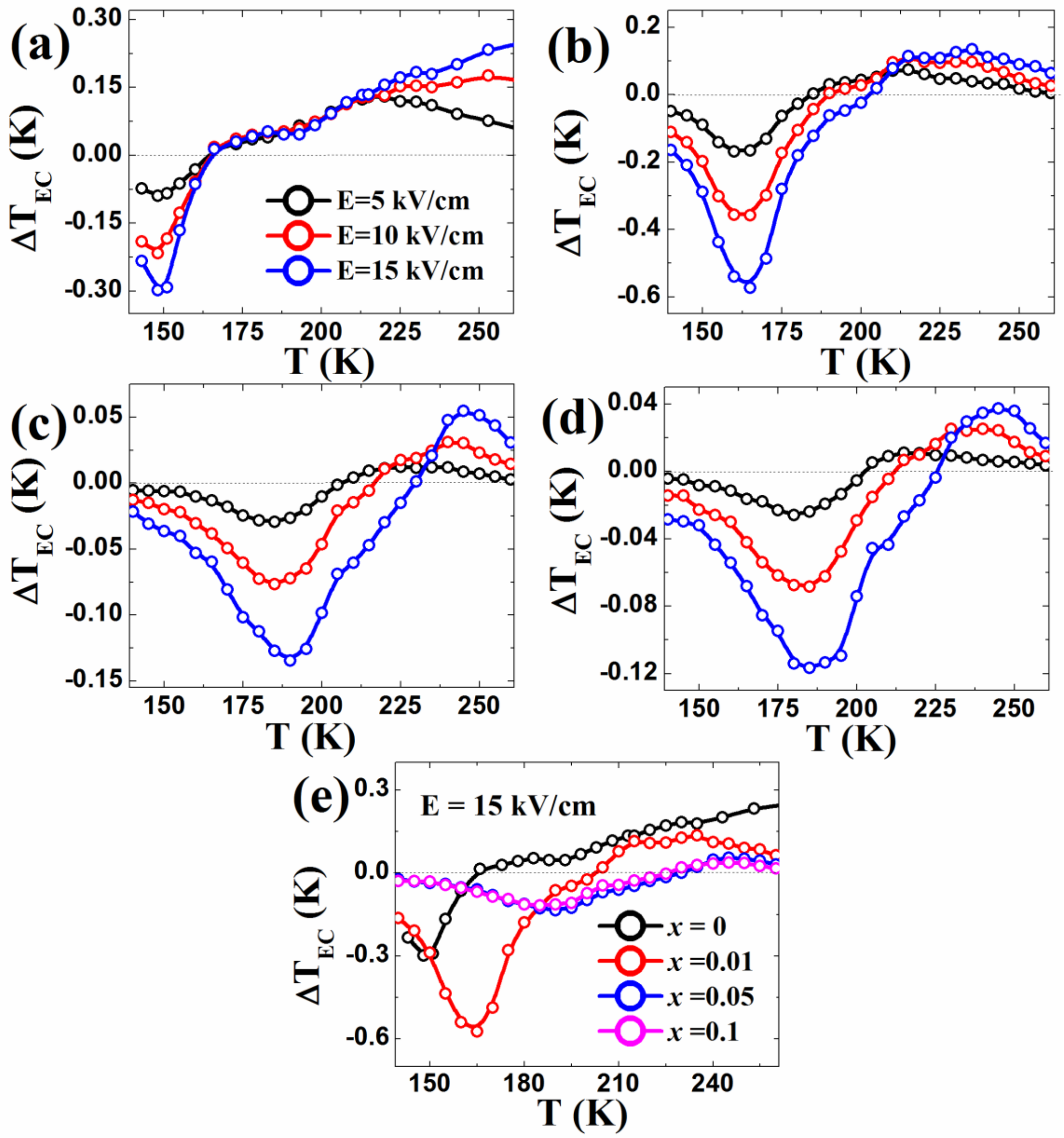

Fig. 4.25. Electrocaloric temperature change (ΔT_{EC}) as a function of temperature at different applied electric field for $Pb_{1-x}Gd_xMg_{1+x/3}Nb_{2-x/3}O_3$ ceramics **(a)** $x = 0$, **(b)** $x = 0.01$, **(c)** $x = 0.05$, and **(d)** $x = 0.1$, **(e)** comparison of ΔT_{EC} as a function of temperature for different compositions ($0 \leq x \leq 0.1$) at $\boldsymbol{E} = 15$ kV/cm.

The observed negative EC effect in region I is the outcome of decrease of polarization with cooling where $(\partial P/\partial T)_E$ decreases. According to the Maxwell relation $(\partial P/\partial T)_E = (\partial S/\partial E)_T$, the entropy should decrease with the applied field upon cooling, hence the decrease of temperature is observed. Moreover, the crossover temperature (T_{co}) of ΔT_{EC} shifts toward higher temperature with increase in electric field. A shift of large ΔT_{co} ~ 24 K is observed as the electric field is increased from 5 to 15 kV/cm. In contrast to this, in the case of AFE La-doped PZT thin films, Geng *et. al.* [136] reported that the T_{co} shifts to lower temperature side with increase of electric field. However, Bhaumik *et. al.* [138] for relaxor FE $Sr_xBa_{(1-x)}Nb_2O_6$ single crystals, and Ramesh *et. al.* [145] for relaxor FE 0.67PIN-0.33PT ceramic observed similar analogous behaviour of T_{co} with the field. Also, Zhou *et. al.* [139] reported the coexistence of multiple negative and positive electrocaloric effects in $(Pb,La)(Zr,Sn,Ti)O_3$ single crystals. The anomalous crossover and negative electrocaloric effect is recently reported in many AFEs and RFEs [131-153]. However, the mechanism for the negative EC effect is not yet clearly understood.

A negative EC effect is expected if there is a transition between the two states of the system, where the lower-temperature state has a smaller polarisation than the higher-temperature state. Generally, electric-field-induced phase transition is believed to relate with the negative ΔT_{EC}. The negative EC effect is also reported in 0.72PMN-0.28PT crystal and attributed to field-induced structural transformation from monoclinic to orthorhombic phase [132]. In the case of NBT, formation of incommensurate AFE phase is responsible for the negative EC effect, where application of electric field favours AFE or increased dipolar disorder [131]. Statistical mechanics based microscopic model by Axelsson *et. al.* [150] implied two phase transitions, which are very close in temperature, resulting in the coexistence of a dual-nature EC effect in PMN-PT. The first-principles based simulations by Ponomareva *et. al.* [152] attributed the non-linearity between the electric field and the polarization as the origin of negative EC effect in $Ba_{0.5}Sr_{0.5}TiO_3$. Moreover, there is a broad minimum value of ΔT_{EC} ~ -0.15 K, observed under an applied field of 15 kV/cm towards negative region around 152 K. A remarkable feature is that the position of negative minimum temperature is independent of the applied electric field. Recently, Wu *et. al.* [148] demonstrated that high efficiency in EC based solid state cooling devices is achieved through coexistence of positive and negative EC effects near pseudo first order phase transition in perovskite ferroelectric materials. For practical applications, EC materials show that change of small electric field generates large temperature change. The strength of EC effect, also called EC coefficient or responsivity (ξ_{max}), is calculated according to $\xi_{max} = \Delta T_{ECmax}/\Delta E_{max}$ where ΔT_{ECmax} is the maximum temperature change and ΔE_{max} is the corresponding electric field change. The value of maximum negative EC coefficient (ξ_{max}) is observed to decrease from ~ 0.4 K-mm/kV at 164 K to ~ 0.1 K-mm/kV with increasing Gd-content [Fig. 4.25(e)]. The ξ_{max} ~ 0.2 K-mm/kV at 150 K for PMN is consistent with earlier report [155]. In contrast, ξ_{max} decreases consistently in region I with increase of Gd-substitution. Similar EC behaviour i.e., crossover from positive to negative values near Vogel-Fulcher freezing temperature (T_{VF}) is reported for $Pb_{0.8}Ba_{0.2})[(Zn_{1/3}Nb_{2/3})_{0.7}Ti_{0.3}]O_3$ and for 0.2 at% Gd-doped $Na_{0.5}Bi_{0.45}TiO_3$ relaxor ferroelectric ceramic [142,153].

It has already been reported [105] that 5 at.% Gd-doped PMN has both polar nano-domains and chemically-ordered regions, which are randomly distributed within the grain. Polar nano-domains tend to align along the external electric field direction. Above room temperature, thermal energy overcomes the alignment of polar domains which are unable to sustain remnant polarization. However, at low temperatures, thermal energy is not sufficient to disrupt this alignment, but below a certain temperature (T_g), the dynamics of polar nano-regions slow down causing incomplete alignment, which results in lower polarization and crossover from positive to negative ΔT_{EC}. Further decrease in temperature results in more out-of-phase response of the polar nano-domains, leading to a minimal around 150 K. Therefore, the crossover between positive to negative EC with temperature change is believed to relate to the critical slowing down of PNR’s into super-dipolar glassy dynamics of polar-domains. At present, it is not clear if CORs are responding to the external electric field and how this response varies with temperature. Increase in ΔT_{EC} below 150 K suggests active role of COR’s, which requires confirmation.

4.3.3 Conclusion

The EC effect of relaxor-ferroelectric $Pb_{1-x}Gd_x(Mg_{1+x/3}Nb_{2-x/3})O_3$; $0 \leq x \leq 0.1$ ceramic is investigated by calculating the adiabatic temperature change (ΔT_{EC}) from temperature dependent *P-E* hysteresis loop and heat capacity measurements. The EC effect exhibited a field dependence and an anomalous crossover from low temperature negative EC effect to high temperature positive EC, near the glass transition temperature T_g ~ 204 K at 5 kV/cm for $x \geq 0.05$, calculated from $f(T_m)$ dielectric response, and is related to the critical slowing-down of the PNR dynamics. The presence of bipolar EC effect makes it a promising and more efficient material for refrigeration technologies. The maximum value of negative EC coefficient (ξ) for PGMN1 is 0.4 K-mm/kV at 195K. The crossover temperature is shifted towards higher temperature (ΔT_{co} ~ 24 K for ΔE = 10 kV/cm) with increasing electric field, which is explained by critical slow-down glassy dynamics of polar nano-domains.

Chapter 5

Investigation of magnetic and magnetodielectric properties of Gd-substituted PMN ceramics and its comparison with PCN

5.1 Magnetic and magnetodielectric properties of relaxor $Pb_{1-x}Gd_x(Mg_{(1+x)/3}Nb_{(2-x)/3})O_3$ ceramics

5.1.1 Introduction

The purpose of this study is to investigate temperature and field dependent magnetic responses when rare-earth magnetic ion Gd^{3+} is substituted at Pb-site in PMN and the charge imbalance is compensated with B-site vacancies. Recently, magnetic ion (transition metals or rare-earths) doping in ferroelectric ceramics induces new functionality termed as multiferroics, i.e., simultaneous electricity and magnetism ordering, which has revived the study of magnetodielectric effect [28,43-47]. Apart from type I and type II multiferroics (MFs), a new class of disordered multiferroics (type III MFs) revealing multiglassy or multirelaxor behaviour demonstrating magnetodielectric (MD) coupling in quadratic or higher order is come into existence [156-158]. As stated earlier, Gd-ion substitution can take place at A and/or B-site depending upon the concentration. In this section, temperature dependent susceptibility and field induced magnetization as well as MD effect of $Pb_{1-x}Gd_x(Mg_{1/3}Nb_{2/3})_{1-x/4}O_3$ for x = 0.01 to 0.1 are discussed.

5.1.2 Results and discussion

5.1.2.1 Magnetic properties

Figure 5.1(a) compares the temperature dependence of the magnetization, $\chi(T)$ measured during heating from 5 K to 300 K in a magnetic field of 100 Oe [zero field cooling (ZFC)] for $x = 0.01$ to 0.1 Gd-PMN ceramics. Susceptibility is found to decreases sharply with increasing temperature below ~50 K and then smoothly above 50 K without displaying any evidence of ferromagnetic or antiferromagnetic transitions. The susceptibility at all temperature increases with Gd-concentration. Figure 5.1(b) reveals temperature dependence of inverse of magnetic susceptibility χ^{-1} (T) measured in ZFC regimes for “x” varies from 0.01 to 0.1. Linear dependence is clearly evident for $x \geq 0.05$, which depicts paramagnetic behaviour. The magnetization displays small thermal history dependent and a bifurcation between ZFC and FC is observed at a temperature T_{irr} for all “x”. The T_{irr} is the temperature at which change in the susceptibility between ZFC and FC becomes diverse from zero. In the inset of Fig. 5.1(a), black arrow depicts the T_{irr} for $x = 0.02$ below ~250 K. The T_{irr} is found to shift lower temperature with increasing “x”.

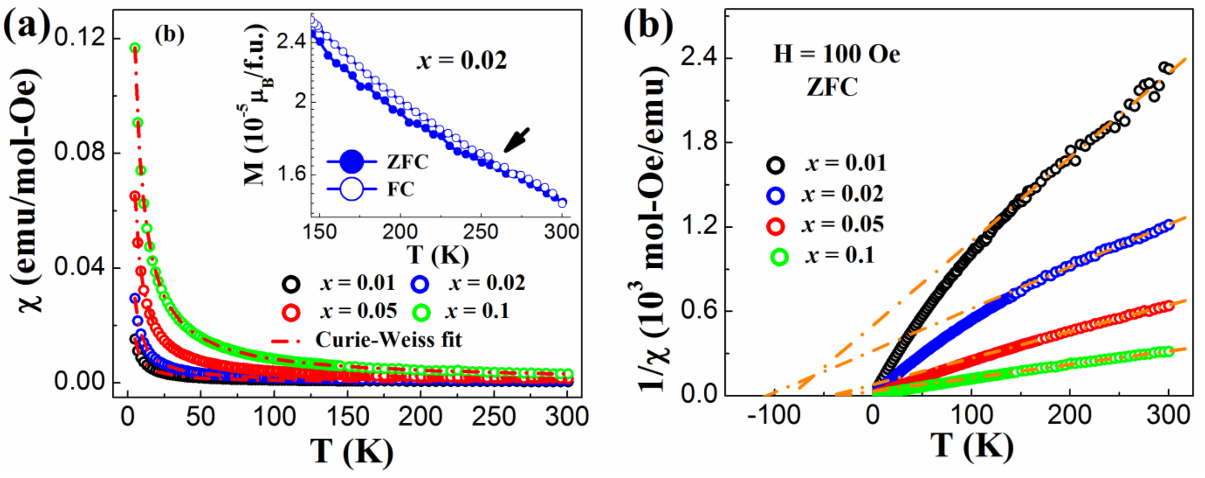

Fig. 5.1. (a) Temperature dependence of susceptibility plot $Pb_{1-x}Gd_x(Mg_{1/3}Nb_{2/3})_{1-x/4}O_3$ for $x = 0.01$ to 0.1 fitted by the Curie-Weiss law; inset shows ZFC-FC magnetization plot for $x = 0.02$ sample, (b) Temperature dependence of inverse susceptibility plot $Pb_{1-x}Gd_x(Mg_{1/3}Nb_{2/3})_{1-x/4}O_3$ for $x = 0.01$ to 0.1 showing deviation from linear dependence.

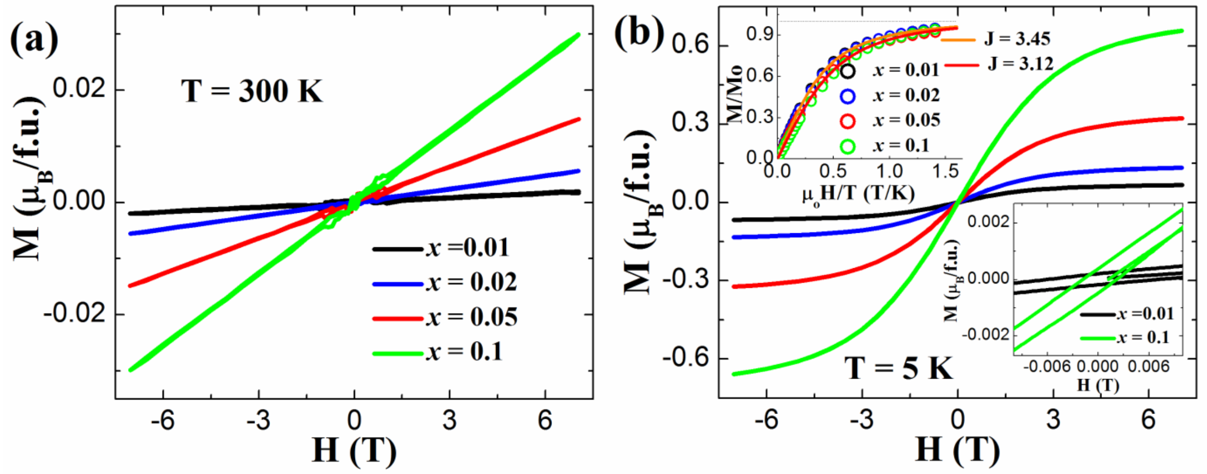

Fig. 5.2. *M-H* curve of Gd-substituted PMN ceramics [$Pb_{1-x}Gd_x(Mg_{1/3}Nb_{2/3})_{1-x/4}O_3$ for $x = 0.01$ to 0.1] at a) T = 300 K, b) T = 5 K; upper inset shows normalized M/M_o vs μ_oH/T plot of Gd-PMN ceramics fitted by Brillouin function and lower inset depicts the enlarge view of *M-H* hysteresis plot of 1Gd-PMN and 10Gd-PMN ceramics.

Further, the $\chi(T)$ curve of Gd-PMN has been fitted in full range of temperature 5 K - 300 K by the Curie-Weiss law given as follows [41,65,159],

$$\chi = \chi_o + \frac{C}{(T - \theta_p)} \tag{5.1}$$

where χ_o is temperature independent magnetic susceptibility, is a constant and composed of Pauli paramagnetism, Van Vleck paramagnetism, and Larmor dia-magnetism of the core electrons [6], C is the Curie constant and θ_p is the paramagnetic Curie temperature. The Weiss temperature depicts the strength of the interaction between the paramagnetic centres. Figure 5.1a shows the validity of the modified Curie-Weiss law. The fitting parameters, χ_o, C, θ_p and μ_{eff} are summarized and compared with the $GdNbO_4$ ceramic in Table 5.1. Here, the effective magnetic moment per Gd^{3+} ion is calculated from the Curie constant by using the following formula [159],

$$C = \frac{N\mu_{eff}^2}{3k_BT} \tag{5.2}$$

where N (N_A/W, N_A is the Avagadro number and W is molecular weight) is the number of magnetic atoms per unit volume, μ_{eff} is the effective moment per atom, and k_B is the Boltzmann constant. From Table 5.1, the fitted parameters χ_o, C and θ_p is observed to increase with Gd-concentration. The calculated values of effective magnetic moments for different Gd- doped samples lies close to the theoretical value of a free Gd^{3+} ion ~7.94 μ_B (the electronic ground state Gd^{3+} is $8S_{7/2}$) [160,161]. The fact that the experimental μ_{eff} value is close to the theoretical value confirms that the magnetic moment is localized on the Gd^{3+} ion and that, as expected, is not affected by neighbouring atoms because these atoms do not carry any permanent magnetic moment. Moreover, the small negative value of the Weiss temperature θ_p indicates the predominantly weak antiferromagnetic interaction between the Gd^{3+} spins. Further isothermal magnetization and ac-susceptibility of Gd-PMN ceramics examined to get deeper insight of magnetic behaviour.

Table 5.1. Variation of the parameters, temperature independent magnetic susceptibility (χ_o), curie constant (C), paramagnetic Curie temperature (θ_p) and μ_{eff} of $Pb_{1-x}Gd_x(Mg_{1/3}Nb_{2/3})_{1-x/4}O_3$, for $0.01 \leq x \leq 0.1$ ceramics.

Gd-PMN ceramics	χ_o **(emu/mol-Oe)**	C **(K-emu/mol-Oe)**	θ_p **(K)**	μ_{eff} **(μ_B/Gd^{3+})**
$x = 0.01$	1.95×10^{-4}	0.079	- 2.5	7.95
$x = 0.02$	3.03×10^{-4}	0.156	- 2.7	7.89
$x = 0.05$	2.95×10^{-4}	0.377	- 2.8	7.77
$x = 0.1$	5.51×10^{-4}	0.790	- 2.8	7.95
$GdNbO_4$	11.7×10^{-4}	8.077	-3.0	8.04

Figure 5.2(a,b) compares *M-H* hysteresis curves of Gd-PMN ceramics for $x = 0.01$, 0.02, 0.05, and 0.1, recorded at 300 K and 5 K, respectively. The room temperature *M-H* curves of all "x" exhibit a linear behavior implying the nature of the paramagnetic state [Fig. 5.2(a)]. The maximum induced magnetization at 7 T magnetic field increases with increasing "x". But the M-H curve at 5 K shows a nonlinear dependence and are "S-shaped", which become nonlinear above ~2 T applied field and tends to saturate at higher fields. A deviation from the linear dependence is generally observed for paramagnetic materials at low temperature and high magnetic field. No hysteresis or remanent magnetization is observed but a weak coercive field for $x = 0.01$ and 0.1 can be seen in the enlarged view depicted in the lower inset of Fig. 5.2(b). From Fig. 5.2(b), it is noticed that saturated magnetization (M_o)

increases with increasing Gd-concentrations, which can be described by the field dependence of magnetization with the Brillouin function, $B_J(x)$ given as follows [65],

$$M = M_o B_J(x)$$

$$M_o = NgJ\mu_B;\ B_J(x) = \left(\frac{2J+1}{2J}\right)coth\left(\frac{(2J+1)x}{2J}\right) - \frac{1}{2J}\coth\left(\frac{x}{2J}\right)\ and\ x = \frac{gJ\mu_B H}{k_B T} \qquad (5.3)$$

Here, N is the number of Gd^{3+} per unit volume, μ_B is the Bohr magneton, g (= 2, theoretical value) is the spectroscopic splitting factor or Lande factor, and J is the total angular momentum. The universal plot of M/M_o vs $\mu_o H/T$ is fitted with Eq. (5.3) and shown in upper inset of the Fig 5.2(b). The result of the Brillouin function fitting to M-H curves relate, J = 3.45 for x = 0.01, 0.02 and J = 3.12 for x = 0.05, 0.1 ceramics. The effective magnetic moment (μ_{eff}) per Gd^{3+} calculated using $g[J(J+1)]^{1/2}\mu_B$ is 7.84μ_B (for x = 0.01, 0.02) and 7.17μ_B (for x = 0.01, 0.02), which is smaller than the theoretical value. The observed smaller value of J in later case is due to the enhanced disorder at B-site and presence of $GdNbO_4$ phase, which has smaller field induced magnetization in compared to Gd-PMN ceramic [161].

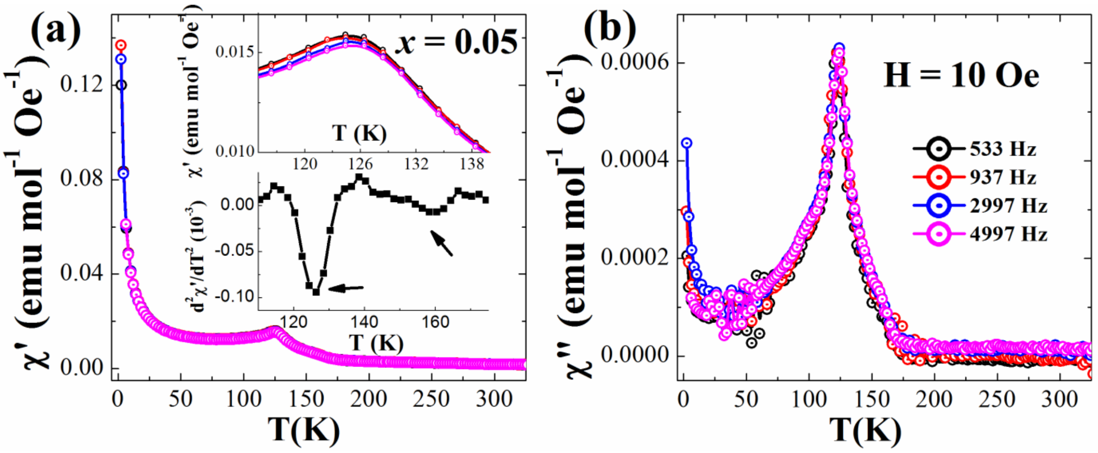

Fig. 5.3. Temperature dependence of (a) real (χ') and (b) imaginary (χ'') parts of ac magnetic susceptibility at H = 10 Oe field and at different frequencies; upper inset shows enlarged view of χ' around the peaks and lower inset depicts the second derivative plot of χ' for 5Gd-PMN ceramic sample.

Figure 5.3(a,b) shows the temperature dependence of real (χ') and imaginary (χ'') parts of complex ac-magnetic susceptibility of 5Gd-PMN ceramic at four different frequencies.

The $\chi'(T)$ displays gradual increase on cooling initially and then sharply below 50 K without leading to any saturation. A well-defined peak at 125 K is clearly observed in $\chi'(T)$ and $\chi''(T)$ plots, which exhibits a weak frequency dependence and is shown in the inset of Fig. 5.3(a). This peak is also accompanied with a weak hump at ~160 K, which is clearly evident in second derivative plot of χ' in lower inset of the Fig. 5.3(a). This very weak frequency dependent χ' and χ'' indicates the presence of dynamic nature of isolated stoichiometric correlated regions. These regions might be very small in size and quite unstable in temperature regime, $T > 125$ K, where random distributions of Gd^{3+} ions magnetic moment exist. Since for low Gd-ions concentration ($x < 0.05$), the distance between Gd^{3+} ion is too large for stability of the spin glass structure mainly by frustrated super-exchange. It is believed that frustrated interaction develops with increase in the Gd-ion concentrations, when the Gd-ions starts substituting at B-site for high Gd-ion concentration ($x > 0.05$) below 160 K. These results are found consistent with earlier reported Mn-doped SrTiO$_3$ ceramic [158].

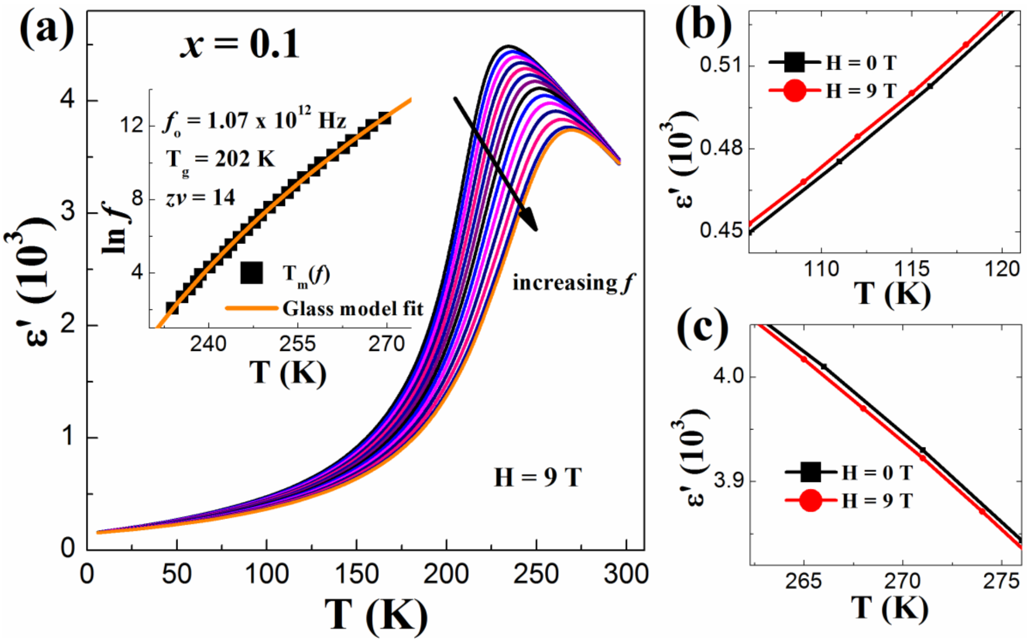

Fig. 5.4. (a) Temperature dependence of real (ε') permittivity of 10Gd-PMN ceramic sample at H = 9 T magnetic field at different frequencies from 10 Hz - 200 kHz; inset shows cluster glass model fitted to ln f vs T_m plot, Temperature dependence of ε', (b) below 250 K and (c) above 250 K at H = 0 T and H = 9 T field of "x" = 0.1 (10Gd-PMN) ceramic sample at 1 kHz.

5.1.2.2 Magnetodielectric studies

The temperature dependent dielectric permittivity of 10Gd-PMN ceramic sample is performed in H = 9 T magnetic field, which clearly manifests the relaxor dielectric behaviour. Figure 5.4(a) depicts the real (ε') part of the dielectric permittivity of "x" = 0.1 ceramic sample in the frequency range of 10 Hz - 2 MHz and in the temperature range of 5 K - 300 K in the presence of magnetic field, H = 9 T. The temperature dependent dielectric permittivity, $\varepsilon'(T)$ shows broad dielectric maxima (ε_m) with strong frequency dispersion near T_m (T of ε_m peak) i.e. T_m shifts progressively towards lower temperature from 269.6 K to 233.8 K with decreasing frequency from 200 kHz to 10 Hz. It is already mentioned that the strong frequency dependent dielectric permittivity of Gd-ion substituted PMN ceramics is a consequence of statistical distribution of the PNRs over wide temperatures range. It has been already shown in earlier sections that Gd-doping in PMN has enhanced the size of the CORs, degree of relaxation and diffuseness, which is attributed to reduction in the correlation among the PNRs leading to reduction in the maximum dielectric constant at T_m (ε'_{max}) and saturation polarization (P_{sat}). It has also been revealed that an additional disorder is induced when Gd-substitutes the Mg-site, resulting in higher value of degree of diffuseness (δ_A) in comparison to PMN. This additional disorder is believed to be responsible for the reduction in the cooperative interaction among the PNR's, resulting in the critical slowing down of the PNR's dynamics, which ultimately leads to non-ergodic ferroelectric cluster glass ground state (also known as "super-dipolar" glass) [59,79, 91,105]. Inset of the Fig. 5.4(a) shows fitting of the $f(\mathrm{T_m})$ vs T plot to critical slowing down glass model (Eq. 5.4) for "x" = 0.1 ceramic, given below

$$f = f_o\left(\frac{T}{T_g} - 1\right)^{zv} \tag{5.4}$$

where f_o is the Debye frequency, zv is critical dynamic exponent and T_g is glass transition temperature. The open symbols represent experimental data points and solid line represents the fitted curve. Accurate value of the T_m is determined by fitting the $\varepsilon'(T)$ curve for each frequency in a narrow temperature range around the T_m. The fitted parameters of “x” = 0.1, $f_o \sim 1.07 \pm 0.47 \times 10^{12}$ Hz, $T_g = 202 \pm 3$ K, and $z\nu = 14 \pm 1$ and are in agreement with mesoscopic size of the PNRs near T_g and within the limit of its physical significance.

Figure 5.4(b,c) compares the $\varepsilon'(T)$ with H = 0 T and 9 T below and above 250 K depicting positive and negative variation of dielectric permittivity dependence on the magnetic field. The $\varepsilon'(T)$ and $\varepsilon''(T)$ value increases with application of magnetic field below T ~250 K but it decreases above 250 K. The frequency and temperature dependent bipolar magneto-dielectric behaviour is calculated using Eq. 5.5 and magneto-dielectric (%MD) and magneto-loss (%ML) coefficients are given as follows

$$\%MD = \frac{\varepsilon'(H=9\,T) - \varepsilon'(H=0\,T)}{\varepsilon'(H=0\,T)} x100, \;\; \%ML = \frac{\varepsilon''(H=9\,T) - \varepsilon''(H=0\,T)}{\varepsilon''(H=0\,T)} x100 \qquad (5.5)$$

where $\varepsilon'(H = 9\text{ T})$ and $\varepsilon''(H = 9\text{ T})$ are dielectric permittivity and dielectric loss in H = 9 T magnetic field, respectively, and $\varepsilon'(H = 0\text{ T})$ and $\varepsilon''(H = 0\text{ T})$ are dielectric permittivity and dielectric loss, respectively, in absence of magnetic field. Figure 5.5(a,b) depicts frequency dependent bipolar magneto-dielectric and magneto-loss effect for “x” = 0.1 ceramic.

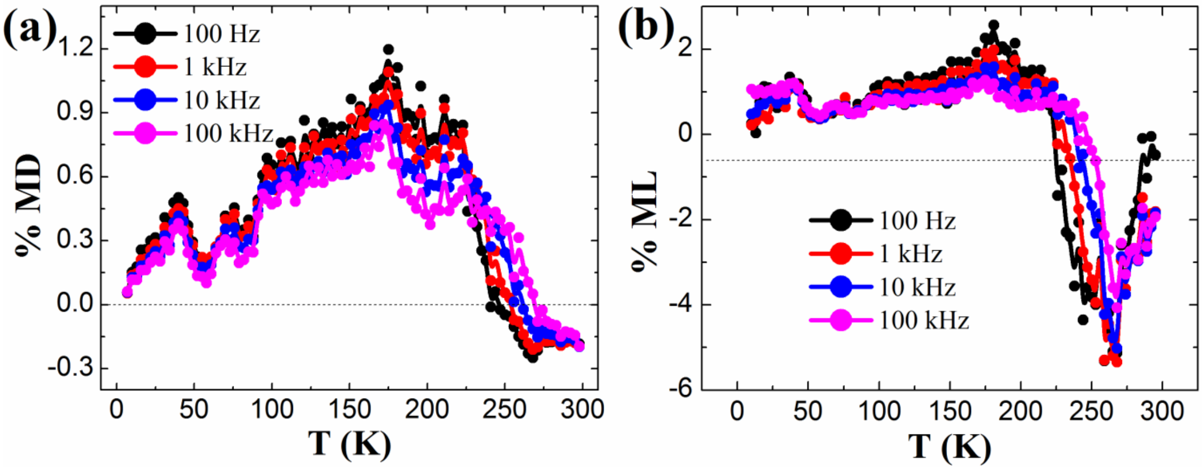

Fig. 5.5. Temperature dependence of (a) magneto-dielectric (%MD), and (b) magneto-loss (%ML) behaviour of “x” = 0.1 at different frequencies from 100 Hz to 100 kHz.

This effect appears to be more prominent at low frequency (f = 100 Hz) of a measuring field, and found decreasing with increasing frequency. Below 250 K, the %MD and %ML first increases and reach the maximum value near ~180 K and then decreases below 180 K. The temperature of maximum positive MD and ML effect is independent of frequency, however maximum positive MD and ML at T = 180 K are frequency dependent, i.e., %MD increases from 0.8 (100 kHz) to 1.18 (100 Hz) and similarly, %ML increases from 1.13 (100 kHz) to 2.51 (100 Hz). It is believed that weak interaction of the magnetic field with magnetic moments of moving nano-domains walls is responsible for small magneto-dielectric effect. The change from negative to positive MD effect around 250 K seems to be related with the PNRs size and initiation of the magnetic field influence on the dynamic characteristics of the nano-domains walls. As these nano-domains grow in size, the MD-effect increases up to a temperature T_g, where the dynamics of the domains are known to critically slow down. The peak %MD value is also close to the glass transition temperature, T_g ~200 K estimated from critical slowing down glass model, Eq. 5.4. The dynamic nature of the PNRs is further examined in isothermal aging analysis, which is performed at 40 K in the absence and presence of external magnetic field.

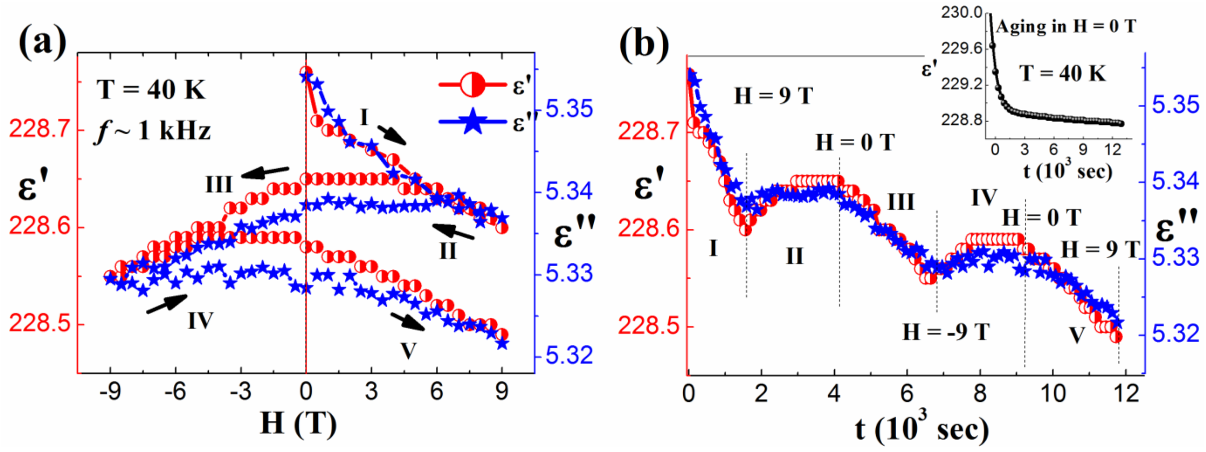

Fig. 5.6. a) Magnetic field dependence of real (ε') and imaginary (ε") parts of complex permittivity at T = 40 K and 1 kHz frequency, b) Time dependence of ε' and ε" in variation of magnetic field; inset depicts aging of 10Gd-PMN ceramic sample at 40 K.

Figure 5.6(a) shows isotherm curves of the dielectric permittivity [ε'(T)] and dielectric loss [ε"(T)] at 40 K for various applied magnetic fields. Inset of Fig. 5.6b illustrates the dependence of ε' (at 1 kHz) with time during an aging study at T = 40 K. The ε' is found to decrease with time, which clearly shows metastable characteristics of the PNRs at 40 K, akin to structural and spin glasses [162-164]. Generally, with increase of magnetic field (H), ε’ and ε” increases or decreases from virgin state and with decrease of magnetic field to $H = 0$, ε’ and ε” should have the same value of zero field virgin state. Figure 5.6(a) depicts an anomalous behaviour in isotherm curve of ε’ and ε” vs H. In the first cycle, the ε’ and ε” decreases with increasing magnetic field up to $H = 9$ T and then in second cycle ε’ and ε” increases slightly with decreasing magnetic field but does not reach to the same initial value of $H = 0$ T. In third cycle, with reversal of field to $H = -9$ T, ε’ and ε” again decreases and in fourth cycle, ε’ and ε” slightly increases akin to second cycle. Similar to the first and third cycles, ε’ and ε” again decreases with increasing magnetic field to $H = 9$ T in the V cycle. Close observation of magnetodielectric isotherm measurement in time, i.e., ε’(H) and ε”(H) vs time plot in Fig. 5.6(b) depicts overall decreasing trend with cycle nature in time and magnetic field implying metastable behaviour of relaxors. A decrease in the ε’(H) with the application of magnetic field and increase in the ε’(H) with decrease in the magnetic field clearly reveals that the dynamics of the PNRs are influenced by the magnetic field. Therefore, it is believed that the aging behaviour is superimposed with the MD effect.

5.1.3 Conclusion

Temperature and field induced magnetization $M(T/H)$ investigations revealed paramagnetic behaviour for Gd-substituted PMN. However, few very small sized correlated regions are believed to form, where Gd-ions are present at the A-site and B-site in the same lattice. Temperature dependent MD and ML revealed bipolar change of dielectric properties with magnetic field. In conclusion, it is demonstrated that introducing Gd^{3+} ion into the lattice of relaxor ferroelectric $Pb(Mg_{1/3}Nb_{2/3})O_3$ may be considered as an alternate way to get magnetization and magnetodielectric effect.

5.2 Magnetic and magnetodielectric properties of relaxor $PbCo_{1/3}Nb_{2/3}O_3$ ceramic

5.2.1 Introduction

Relaxor materials in which the B-site is occupied mainly by a transition metal ion e.g., Fe, Co and Ni are already reported. Out of these relaxors, lead cobalt (II) niobate (PCN) is chosen because it is one of the oldest but poorly studied, analysed and reported. The structure is cubic at room temperature and octahedral sites are randomly occupied by Co^{2+} and Nb^{5+} ions, as reported by Bokov and Myl'nikova on single crystal [165]. Dielectric study has been reported to reveal relaxor behaviour with strong frequency dispersion, ε'_m ~ 6000 at T_m ~-70 ^{o}C (for 1 kHz). Temperature dependent PE loop has indicated polarization due to domain reorientation in sufficiently large field. Malkov *et el.* [166] have indicated large deviation in T_m for single crystal and ceramic form but no explanation is reported. Recently Popova *et al*. has observed dielectric anomaly near antiferromagnetic transition temperature T_N ~130 K, which is due to the presence of magnetic ion Co^{2+} in the lattice at B-site [167]. Others researcher has reported temperature dependent magnetization of single crystal and ceramic PCN depicted paramagnetic behaviour with no short range ordering down to 2 K. The PCN is synthesised in the same conditions of Gd-PMN and well characterized before comparing the magnetic properties with Gd-doped PMN.

5.2.2 Results and discussion

5.2.2.1 Microstructural and structural studies

Figure 5.7(a-d) reveals phase, microstructural and structural characterization of PCN synthesised using the Columbite route similar to Gd-PMN ceramic. Rietveld refinement of PCN using Pseudo-Voigt pattern function has revealed pseudo cubic Pm-3m symmetry having lattice parameter, ‘*a*’ = 4.0496(2) Å [Fig. 5.7(a)]. The thermal parameters of Pb^{2+} and O^{2-} ions are improved by considering a split-atom approach. In this approach, Pb^{2+} and O^{2-} ions are allowed to shift statistically in various crystallographic directions rather than fixing them on high symmetry cubic positions. Significant improvement in the thermal parameters have been observed when atomic positions of Pb and O are isotropically shifted along <111> and <110> directions, respectively [Table 5.2]. The isotropic shift of ~0.045 Å for Pb^{2+} along <111> direction and ~0.046 Å for O^{2-} along <110> direction has improved isothermal parameters by an order of magnitude. Microstructure observed under scanning electron microscope (SEM) of fractured surface of PCN ceramic has revealed inter granular fractured grains in the size of 10-15 μm and shown in Fig. 5.7(c). The sample was free from any secondary phase and presence of spherical pores is consistent with the density measurement by the Archimedes liquid displacement method.

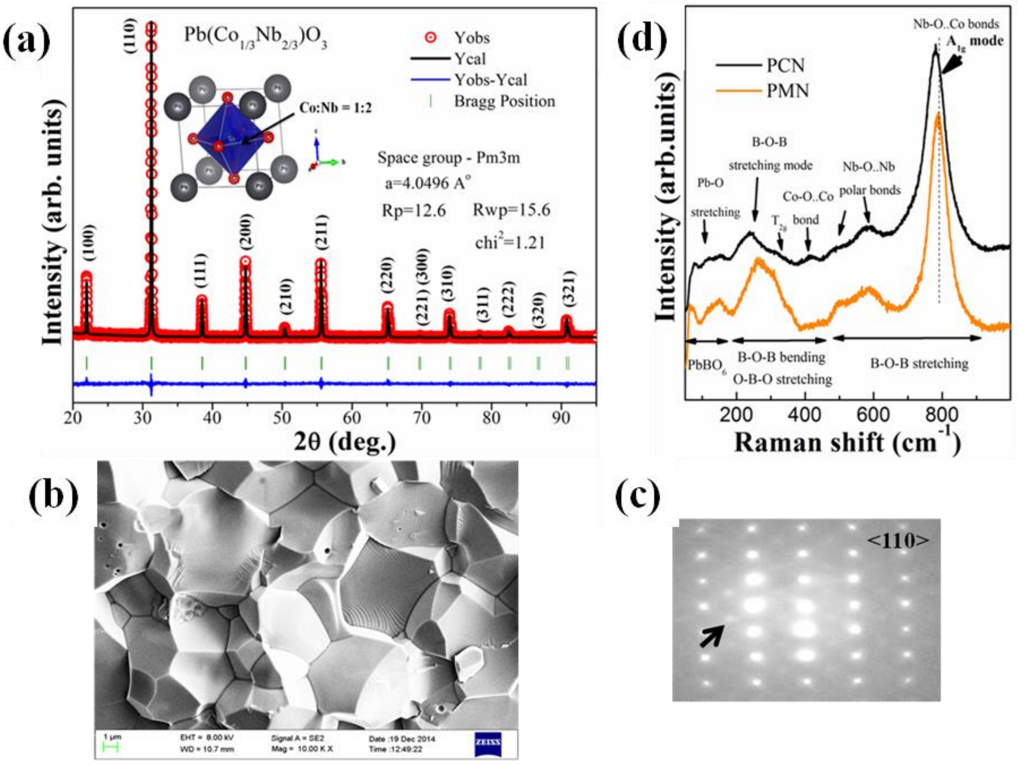

Fig. 5.7. Room temperature (a) XRD, (b) Raman spectra, (c) SEM micrograph and (d) SAED pattern along <110> pattern of PCN ceramic sample

Figure 5.7(d) shows selected area electron diffraction pattern in <110> zone axis, which reveals extra spots along <111> unit axis representing doubling of unit cell and B-site non-stoichiometric ordering of Co^{2+} and Nb^{5+} ions. This ordering is also confirmed by using the Raman spectroscopy. Figure 5.7(b) represents room temperature Raman spectrum of the PCN and for the sake of easy understanding; it is compared with already analysed similar mixed perovskite PMN compound. Qualitatively both spectra are similar except red shifting of few modes with different intensities and FWHM. The A_{1g} mode ~ 780 cm^{-1} is observed in the PCN, which is related to B-site ordering and consistent with earlier report of complex Pb-based mixed perovskites [79,81]. Red shift of A_{1g} and few other modes can be explained using simple harmonic approximation model, $\omega = (k/m^*)^{1/2}$ where ω is Raman shift, k is bond constant and m^* is effective mass of modes. Atomic mass of Co is higher; hence modes involving Co have been red shifted due to large effective mass of Co in comparison to Mg.

Table 5.2. Structure parameters obtained after Rietveld refinement of lead cobalt niobate ceramic sample for Pm3m crystal symmetry

Lattice Parameter (Å)	**Wyckoff Positions**				**Isothermal parameter ($Å^2$)**	**Occupancy**	**Agreement Factors**
4.0496(2)	Atoms	*x*	*y*	*z*			
	Pb	0	0	0	3.298	1	$\chi^2 = 1.21$
	Co/Nb	0.5	0.5	0.5	0.308	0.33/0.67	$R_B = 3.89$,
	O	0.5	0.5	0	2.114	3	$R_F = 4.52$
4.0496(2)	Pb	0.04458	0.04458	0.04458	0.210	1	$\chi^2 = 1.20$
Pb<111>	Co/Nb	0.5	0.5	0.5	0.280	0.33/0.67	$R_B = 3.28$,
O<110>	O	0.54638	0.54638	0	0.216	3	$R_F = 3.87$

5.2.2.2 XANES

XANES is an element specific spectroscopic tool which provides information about oxidation states, local coordination and electronic structure (hybridization effect of orbitals) of the elements present in the sample [168]. Edge step normalized Co K-edge XANES spectra of PCN, Co metal foil and cobalt oxide standards are shown in Fig. 5.8(a). K-edge XANES spectrum of Co describes the transitions, 1s→4p and 1s→3d called main and pre-absorption edges, respectively, which provides information about the chemical shift and unoccupied density of states. Energy position of the main absorption line is determined from maximum energy value of first order differentiated spectrum. The spectra clearly show that the main edge position of PCN sample lies between that of CoO and CoF_3, which means Co is in mixed states of Co^{2+} and Co^{3+} in ~ 38% and 62% concentrations, respectively. A simple linear combination is used to calculate the concentration of Co^{2+} and Co^{3+} and shown in the inset of Fig. 5.8(a). Figure 5.8(b) shows step normalized XANES spectra for Nb K-edge 1s→5p with two standard references for Nb^{4+} (NbO_2) and Nb^{5+} (Nb_2O_5). The XANES spectra reveals that Nb exists in multiple oxidation sate $Nb^{3+}/Nb^{4+}/Nb^{5+}$. The XANES measurement of the Columbite precursors, cobalt niobate ($CoNb_2O_6$) at Co and Nb K-edges reveals that Co exists in multiple valance state (Co^{2+}/Co^{3+}) but Nb exists in Nb^{5+} oxidation state.

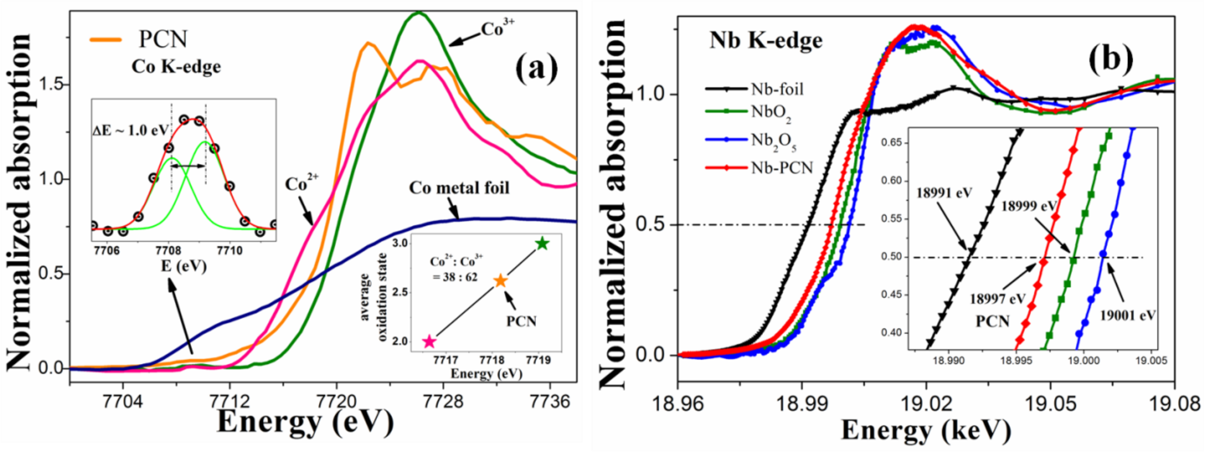

Fig. 5.8. Room temperature (a) Co K-edge and (b) Nb K-edge XANES spectra of PCN ceramic along with their respective standard samples

5.2.2.3 Dielectric spectroscopy

Figure 5.9(a-c) illustrates the temperature variation of real [$\varepsilon'(T)$], imaginary [$\varepsilon''(T)$] parts of dielectric permittivity and loss tangent [$\tan\delta(T)$], respectively, measured in temperature range of 80 K to 480 K and at different frequencies in the range of 100 Hz to 1 MHz. Dielectric and loss spectra of PCN show three distinctive dielectric anomalies marked I, II, III. At higher temperatures (above region III), dielectric loss suddenly rises due to space charge or ionic conduction loss. The dielectric behaviour of ceramic sample of PCN matches with earlier reports on the PCN ceramic [169]. As the sample is cooled, the dielectric constant increases and a broad diffused maximum in dielectric constant (ε_m ~4400) is observed at temperature T_m ~ 260 K, which indicates the existence of a phase transition [169]. Below T_m ~260 K, there are two frequency dependent ε''-T peaks marked by I (~120 K) and II (~200 K) as shown in Fig. 5.9(b). On further cooling below T_m dielectric constant decreases down to 80 K, a frequency dependent weak and broad hump is observed below ~120 K.

The $1/\varepsilon$-T plot shows deviation from its linear dependence near ~420 K [Fig. 5.9(d)]. Therefore, the temperature variation of dielectric constant of PCN above 420 K is fitted by Curie-Weiss law [Eq. (5.6)] and broad diffused maximum is described using quadratic form of Curie-Weiss law [Eq. (5.7)] given as follows [85,107]

$$\frac{1}{\varepsilon(T,\omega)} = \frac{T-T_{cw}}{C} \tag{5.6}$$

$$\frac{\varepsilon_A(\omega)}{\varepsilon'(T,\omega)} = 1 + \frac{(T-T_A(\omega))^2}{2\delta_A^2} \tag{5.7}$$

where, C is the Curie constant, T_{cw} is Curie-Weiss transition temperature, ε_A (> ε_m), T_A (< T_m) and δ_A are fitting parameters, practically independent of frequency and valid for long range of temperatures [85]. Figure 5.9(d) shows the fitted curve of $1/\varepsilon$ vs T by Eq. (5.6) and (5.7); yield parameters, $C = 2.6 \times 10^5$ K, $T_{cw} = 250$ K, and $\delta_A \sim 90$. The value of T_{cw} is close to the temperature of ε_m, 260 K implying paraelectric to ferroelectric or antiferroelectric phase transition temperature. The value of degree of diffuseness, δ_A is almost double of well-known relaxor PMN (δ_A ~45) implying larger disorder at B-site in PCN ceramic [59,85].

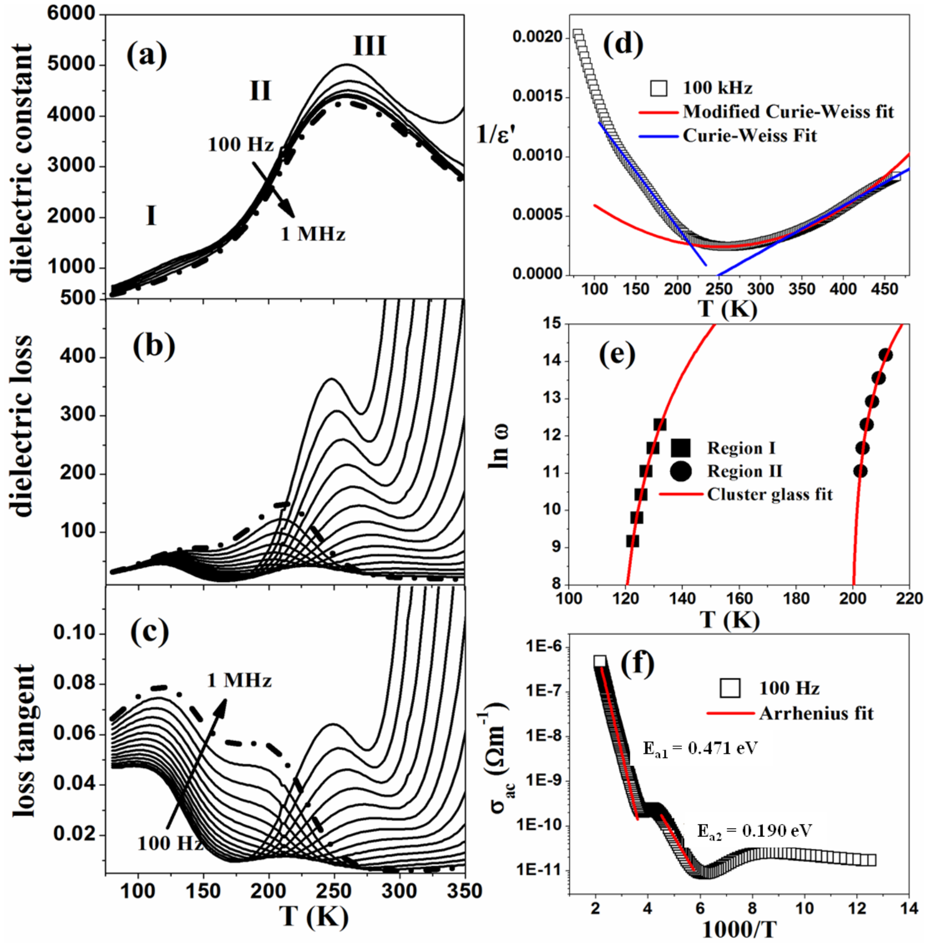

Fig. 5.9. Temperature dependence of (a) real part (ε'), (b) imaginary part (ε''), (c) loss tangent (tan δ) of complex permittivity, (d) Curie-Weiss and Modified Curie-Weiss fit to 1/ε' vs T plot, (e) temperature dependence of relaxation frequency fitted using cluster glass model in region I and II for PCN ceramic sample, and (f) temperature dependence of ac-conductivity of PCN at 100 Hz is fitted by Arrhenius law.

Table 5.3. Model fitting to dielectric data of PCN ceramic sample in various regions

Region I	Region II	Region III
Cluster glass model		**Curie-Weiss Law**
ω_o = 2.05 x 10^8 Hz	ω_o = 8 x 10^8 Hz	C = 2.6 x 10^5 K; T_{cw} = 250 K
T_g = 115.7 K	T_g = 199.5 K	**Modified Curie-Weiss Law**
$z\nu$ = 3.5	$z\nu$ = 2.27	ε_A = 4113 ; T_A = 252 K; δ_A = 90

Careful observation of region I suggest that ε''_{m1} and T''_{m1} increases with increase of frequency akin to relaxors. In region II, ε''_{m2} and T''_{m2} behaves akin to region I, but this hump is present only above 10 kHz frequencies. The observed low temperature glassy phase appeared below phase transition temperature is called re-entrant phase. It has already been revealed that an additional disorder is induced when Gd-substitutes the Mg-site, resulting in higher value of degree of diffuseness (δ_A). It is believed that the development of magnetic correlation near 150 K resulting in the reduction of the cooperative interaction among the polar regions leading to frequency dependent $\varepsilon'(T)$ behaviour.

Figure 5.9(e) depicts the temperature dependence of relaxation frequency, $\omega = \omega(T''_m)$ and it's fitting with cluster glass model [89,91]. The cluster glass model [Eq. (5.8)] is reported, based on critical slowing down dynamics of PNRs, which is well known in magnetic cluster glasses and structural glasses.

$$\omega = \omega_o \left(\frac{T}{T_g} - 1\right)^{zv} \tag{5.8}$$

where ω_0 is the Debye frequency ($\tau_0 = \omega_0^{-1}$ is the microscopic time associated with flipping of fluctuating dipole entities), T_g is glass transition temperature also called blocking temperature and zv is critical dynamic exponent for the correlation length. A good agreement between fitted curve (solid line) and the experimental data (open circle) can be observed for two I and II regions. The parameters presented in Table 5.3 are well within the limit of its physical significance.

At high temperature regime (above region III) value of tan δ is large and it suddenly starts increasing with increasing temperature, which may correspond to hopping electrons and ionic conduction. To understand the different physical mechanism of conduction processes in regions III, the temperature variation of ac-conductivity is analysed. The ac-conductivity is calculated as follows

$$\sigma_{ac}(T) = \omega_o \varepsilon_o \varepsilon'(T) tan\delta(T) \tag{5.9}$$

The plot of ln σ_{ac} versus 1000/T is shown in Fig 5.9(f). The height of potential barrier i.e. activation energies corresponding to various thermally activated processes is calculated from the Arrhenius relationship. The calculated values of the activation energies in different temperature regimes are $E_{a1} \sim 0.471(4)$ eV and $E_{a2} \sim 0.196(3)$ eV. The activation energies in the range 0.1-0.3 eV, 0.3-0.5 eV and 0.6–1.2 eV is attributed to localized hopping of polarons, single-ionized and doubly-ionized oxygen vacancies, respectively [170]. The value of activation energies, $E_{a1} \sim 0.471(4)$ eV and $E_{a2} \sim 0.196(3)$ eV is associated with hopping of single-ionized oxygen vacancies and with the two-site polaron hopping process of charge transfer between Co^{2+}–Co^{3+}sites [171].

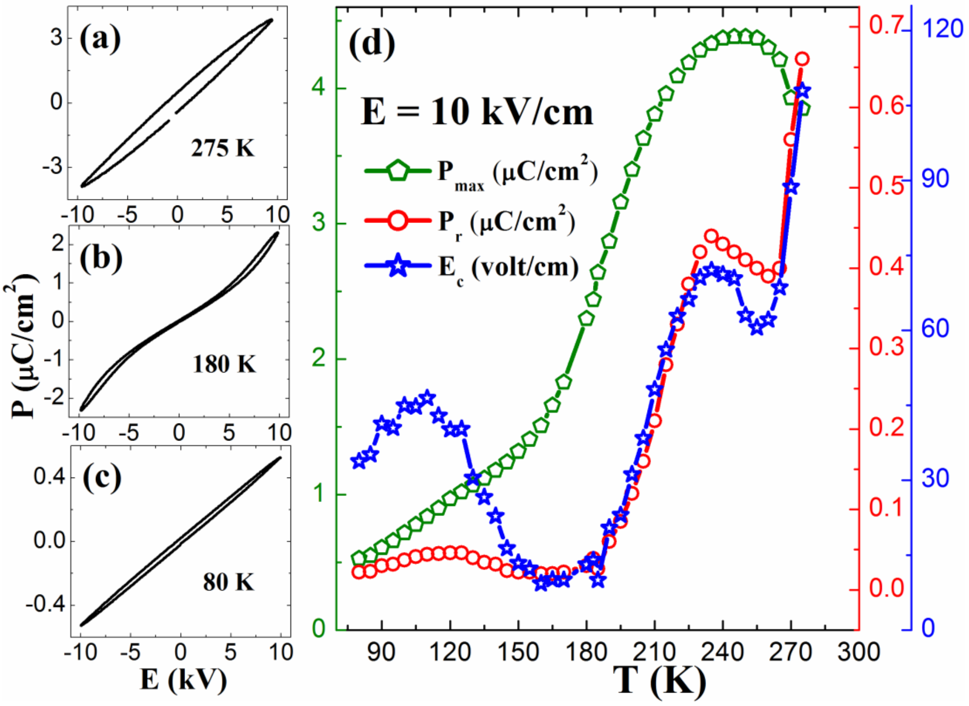

Fig. 5.10. *P-E* hysteresis of PCN ceramic sample at different temperatures, (a) 275 K, (b) 180 K and (c) 80 K, (d) Temperature dependence of P_{max}, P_r and E_c of PCN ceramic sample for E = 10 kV/cm applied electric field.

5.2.2.4 Polarization

Figure 5.10(a-c) shows *P-E* loop traced for PCN at 275 K, 180 K and 80 K when 10 kV/cm external field is switched at 50 Hz. The *P-E* loop at 275 K is consistent with switching of field induced polar regions displaying low coherent length among the polar regions. On cooling to 180 K, the coherent length increases and the cooperative interaction leads to anti-ferroelectric phase transition, which is clearly shown by double *P-E* hysteresis loop at 180 K. Further cooling to 80 K, leads to development of frustration among the polar regions, which resulting into critically slowing down of the polar nano-regions dynamics. The frustration is believed to develop near 150 K, where correlations among magnetic moment is observed. Figure 5.10(d) compares the temperature dependence of the maximum polarization (P_{max}), remnant (P_r) and coercive field (E_c) revealing the paraelectric to antiferroelectric transition. The coupling between the polar regions is believed to become frustrated below 150 K leading to reduction of polar region size, i.e., re-entrant behaviour. The dynamics of the polar nano-regions slows down below 110 K, which is consistent with reduced P_{max} and hysteresis loss.

5.2.2.5 Magnetization

Temperature dependence of zero-field-cooled (ZFC) dc susceptibility measurement in temperature range of ~5 to 300 K under an applied field of ~ 100 Oe is carried out. There are contradictory reports about the magnetic ordering of PCN, e.g., Venevtsev *et al.* [172] has reported AFM phase transition at T_N ~ 130 K but Chillal *et al.* [173] have observed paramagnetic behaviour in single crystal of PCN with an additional anomaly near 50 K, which is reported to be suppressed by the application of high magnetic field.

Figure 5.11(a) shows temperature dependent susceptibility [$\chi(T) = M/H$] and inverse susceptibility ($1/\chi$) for PCN ceramic. No anomalies in $\chi(T)$ near ~130 K or 50 K are observed between 5 K - 300 K. However, a deviation from the Curie-Weiss fitting is noted at ~150 K in the $1/\chi(T)$ plot. The deviation from linearity is due to development of weak correlation between the magnetic moments of Co^{2+}/Co^{3+}, which may not be strong enough to grow to long range ordered phase upon cooling.

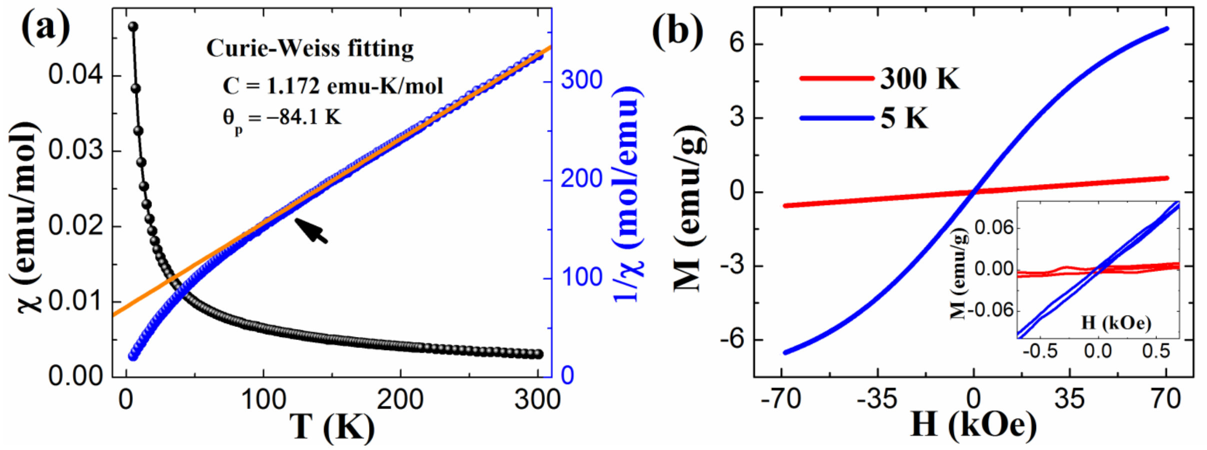

Fig. 5.11. (a) Temperature dependent susceptibility and inverse susceptibility plot of PCN ceramic where high temperature linear region above ~150 K is fitted using Curie-Weiss law, (b) Field dependent magnetization at 300 K and 5 K

The Curie-Weiss law is fitted in linear region of $\chi^{-1}(T)$ i.e. in the temperature range of ~170 K to 300 K and the Curie–Weiss temperature (θ_p), the Curie-Weiss constant (C) and effective magnetic moment (μ_{eff}) are calculated. The Curie-Weiss constant and effective magnetic moment 1.172 emu-K/mol and 5.33 μ_B are calculated, which is consistent with earlier report [168,174,175]. The large negative value of -84.1 K for θ_p reveals local weak predominant AFM interactions in the PCN. These results are consistent with the earlier reported results in which no long range magnetic ordering is observed. It is not clear why the magnetic transition from paramagnetic to AFM is not observed because the concentration of Co-ions is well above the percolation threshold required to form long range magnetic order in the disordered PCN [176]. Here, the percolation threshold means the minimal concentration of magnetic ions distributed in non-magnetic matrix below which the individual magnetic moments do not correlate to form long range order. The absence of long range magnetic ordering is believed to be due to the presence of enhanced degree of disorder at the B-site. The magnetization versus magnetic field (*M-H*) curve recorded at 300 K and 5 K and are compared in Fig. 5.11(b). The room temperature *M-H* curve of the PCN shows linear dependence. The dependence between magnetization and magnetic field become non-linear, which tends to saturate at low temperature 5 K suggesting co-existence of anti-ferromagnetic correlations in paramagnetic matrix [Fig. 5.11(b)]. The magnetic correlation is believed to develop at low temperature, which may be originating from super-exchange correlations between the Co^{2+}-Co^{3+} or Co^{2+}-Co^{2+} and Co^{3+}-Co^{3+} [168,173,174].

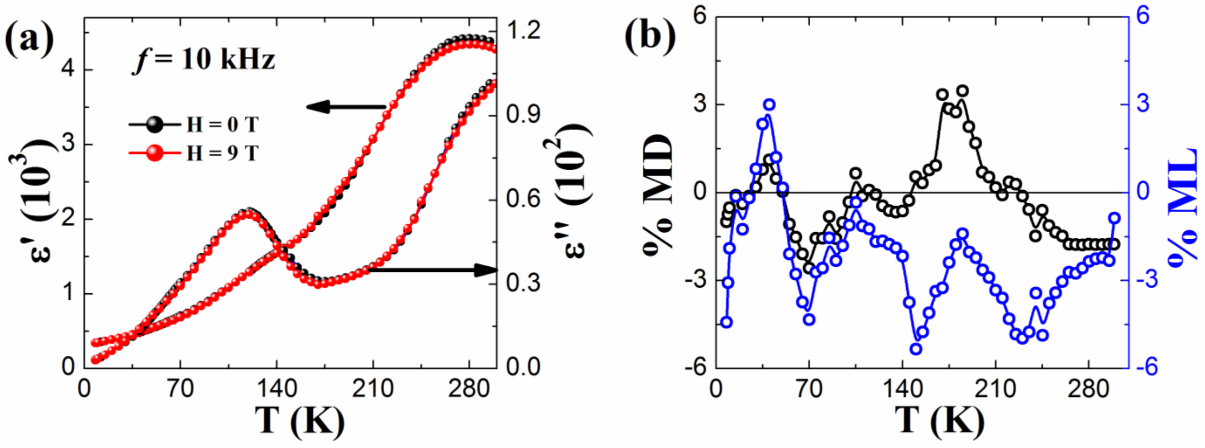

Fig. 5.12. a) Temperature dependence of real (*ε*') and imaginary (*ε*") parts of complex dielectric permittivity of PCN ceramic sample at H = 0 T and H = 9 T magnetic field at 10 kHz frequency, b) Temperature dependence of magnetodielectric (%MD) and magnetoloss (%ML) of PCN at 10 kHz.

5.2.2.6 Magnetodielectric effect

Figure 5.12(a) compares the temperature dependent dielectric constant and loss (at 10 kHz frequency) of the PCN ceramic in the present and absence of the 9 T magnetic field. The temperature dependent dielectric permittivity, *ε*'(*T*) clearly reveals an abnormally near 160 K, which is related to the development of magnetic correlations leading to re-entrant behaviour due to reduction in the correlation among the polar regions. Figure 5.12(b) compares the temperature dependent magnetodielectric (%*MD*) and magneto-loss (%*ML*) coefficient for PCN sample. Below 300 K, the MD first increases up to ~4% near ~170 K and then decreases to -3% below 170 K, which then increases to 2% around 40 K. The %*ML* remains negative in all the temperature except between 25 to 50 K. It is believed that weak interaction of the magnetic field with magnetic moments of moving nano-domains walls is responsible for small magneto-dielectric effect. As stated earlier. the change from negative to positive MD effect around 250 K seems to be related with the PNRs size and initiation of the magnetic field influence on the dynamic characteristics of the nano-domains walls. As these nano-domains grow in size, the MD effect increases up to a temperature 170 K and then decreases due to development of magnetic correlation. Such positive and negative MD behaviour are also observed in disordered double perovskite Pr_2CoMnO_6 ceramic whereas single %*MD* peak is reported in B-site ordered phase [177]. Similarly, Imamura *et al.* [178] observed positive and negative MD effect in A-site ordered oxide, $(BiMn_3)Mn_4O_{12}$. They suggested that the anomalous MD behaviour is due to occupation of magnetic ion Mn^{3+} at A and B both sites are the important crystal chemical factor.

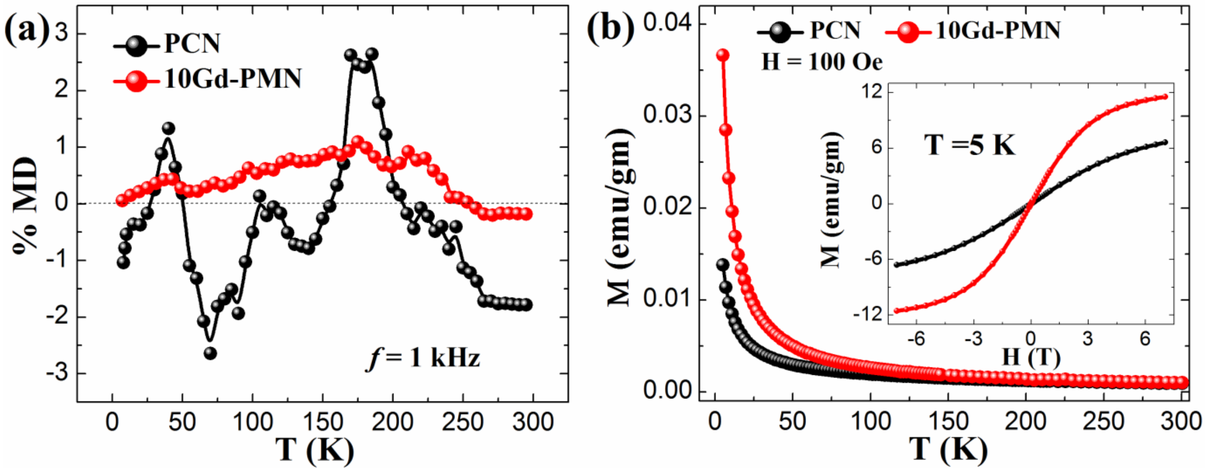

Fig. 5.13. (a) Comparison of magnetodielectric effect, and (b) magnetization of 10Gd-PMN and PCN ceramic samples

Figure 5.13(a) compares the %*MD* curve of 10Gd-PMN with PCN revealing the similar bipolar magnetic field dependence on the dielectric properties. The M(T) plots of PCN and 10Gd-PMN are compared in Fig. 513(b) revealing similar paramagnetic behaviour. The field induced *M-H* at 5 K is compared in the inset of the Fig. 5.13(b) revealing higher saturation M_{sat} for 10Gd-PMN compared to PCN, which is due to the larger effective magnetic moment of Gd-ion compared to that of Co-ion. It may be noticed that frustration created by anti-ferromagnetic correlations, which starts to develop around 150 K is believed to result into re-entrant behaviour in PCN, whereas no such magnetic correlation is established in Gd-PMN because of $GdNbO_4$ precipitation. However, few very small sized correlated regions are believed to form in those regions, where Gd-ions are present at the A-site and B-site in the same lattice.

5.2.3 Conclusions

Temperature dependent dielectric and ferroelectric properties revealed re-entrant low temperature relaxor behaviour near T_m ~120 K for 1 kHz along with a diffused transition, T_c ~250 K. The local and average structural properties suggest chemical, structural and spatial heterogeneities. K-edge XANES spectra analysis has revealed two oxidation states Co^{2+} and Co^{3+} in 38:62 ratio and Nb in Nb^{3+} oxidation state. Raman spectroscopy suggests strong disorderness and presence of nano scale 1:1 Co and Nb non stoichiometric chemical ordering (CORs), which is supported by A_{1g} (780 cm^{-1}) mode and presence of superlattice reflections at <½½½> in <110> SAED pattern. The multiple heterogeneities viz., chemical, structural and spatial observed by local and structure characterization are believed to play a crucial role in producing re-entrant relaxor behaviour. Magnetization and magnetodielectric (MD) effect of PCN ceramics has revealed bipolar magnetic field dependence on the dielectric properties. Weak anti-ferromagnetic correlations are believed to develop around 150 K in PCN, which results in re-entrant behaviour in PCN.

Chapter 6

Conclusions and future works

6.1 Conclusions

It is widely accepted that the presence of chemically ordered regions (CORs) and polar nano regions (PNRs) is responsible for anomalous dielectric and ferroelectric behaviour in disordered in lead magnesium niobate (PMN) relaxors. Following conclusions are drawn from Gd-doped PMN relaxor ferroelectric study in this thesis.

- Origin of the CORs is investigated in uni-axial hot-pressed (HP) PMN ceramics, which are sintered at different temperatures from 800 °C to 1200 °C. Microstructural analysis shows an increase of average grain size from 1.1 μm to 2.8 μm, the presence of (½½½) superlattice reflections along <111> in <110> zone axis SAED pattern, bright nano-meter regions in corresponding dark-field images and Raman active stretching mode of Nb-O-Mg (A_{1g}, ~ 780 cm^{-1}) in 800 °C hot pressed PMN, which concludes formation of the CORs as soon as perovskite phase is formed during calcination and remain invariant with HP sinterng temperetaure.
- Dielectric and ferroelectric properties analysis reveals an increase in the ε_m from 8000 to 25000, shifting of the T_m from 278 K to 263 K, reduction in the degree of diffuseness (δ_A) from 57.7 to 44.1 and increase in the P_{max} from 9 to ~17 μC/cm^2 with increase in the hot-pressed temperature, which implies increase in the size of PNRs and their co-operative interaction and is consistent with the Mydosh-parameter revealing that the state of PNRs ensemble is neither dipolar-glass like nor non-ergodic ferroelectric cluster-glass like.
- Grain size dependence on the ε_m and T_m has been analysed using the core-shell model in which the ratio of core to shell region thickness is found to increase from 15 to 139 with

increasing grain size. The thickness of shell-region remains unaffected by the hot-press temperature.

- Structure, microstructure, dielectric and ferroelectric properties are examined in rare-earth magnetic Gd^{3+} ion-substituted PMN ceramic. Study of the charge imbalance compensation by creating A-site or B-site vacancies or changing the B-site cations ratio reveals the formation of unwanted secondary pyrochlore phase when the compensation is made with creating A-site vacancies.
- No appreciable change is observed in the X-ray diffraction patterns, dielectric and ferroelectric hysteresis loops when the compensation is carried out with B-site vacancies or changing B-site cations ratio.
- Comprehensive study on Gd-substituted PMN $Pb_{1-x}Gd_x(Mg_{1+x/3}Nb_{2-x/3})O_3$ $(0 \leq x \leq 0.1)$ ceramics has revealed the segregation of second $GdNbO_4$ and MgO phases for $x \geq 0.05$, which is confirmed through phase analysis and elemental mapping.
- Raman active stretching mode of Nb-O-Mg (A_{1g}, ~ 780 cm^{-1}) and Nb-O-Nb (~ 500-600 cm^{-1}) have been used as probe to determine the effect of Gd-ions on the size of chemical ordered regions (CORs) and polar nano-regions (PNRs) in PGMN ceramics. The red shift in the A_{1g} and Nb-O-Nb stretching modes and increase in the intensity ratio of A_{1g} and P_2 modes has been related with enhancement of the CORs and reduction in the PNRs size, which is also consistent with the enhanced intensity of (½½½) superlattice reflections along <111> in <110> zone axis SAED pattern, bright nano-meter regions in corresponding dark-field images.
- The fitting parameters obtain from the fitting of T_m (f) to the power law suggests critical slowing down of PNRs ensemble resulting in a super-dipolar glass state for $x \geq 0.05$. This outcome agrees well with sluggish response of the polar region in the hysteresis P-E loop,

which suggests reduction in the correlation within the PNRs leading to reduction in its size.

- Electrocaloric temperature change (ΔT_{EC}) is measured from the temperature dependent PE hysteresis loop using thermodynamic Maxwell equation, which reveals an anomalous behaviour around glass transition temperature T_g where crossover from low temperature negative EC effect to high temperature positive EC effect is observed.
- Temperature and field induced magnetization $M(T/H)$ investigations revealed paramagnetic behaviour for Gd-substituted PMN. However, few very small sized correlated regions are believed to form in those regions, where Gd-ions are present at the A-site and B-site in the same lattice.
- Temperature dependent dielectric and ferroelectric properties revealed re-entrant low temperature relaxor behaviour near T_m ~120 K for 1 kHz along with a diffused transition, T_c ~250 K. The local and average structural properties suggest chemical, structural and spatial heterogeneities. The multiple heterogeneities viz., chemical, structural and spatial observed by local and structure characterization are believed to play a crucial role in producing re-entrant relaxor behaviour.
- Magnetization and magnetodielectric (MD) effect of Gd-PMN ceramics has revealed similar bipolar magnetic field dependence on the dielectric properties. Weak anti-ferromagnetic correlations are believed to develop around 150 K in PCN, which results in re-entrant behaviour in PCN, whereas no such magnetic correlation is established in Gd-PMN because of $GdNbO_4$ precipitation.

6.2 Future work

This research work provides important finding of controlling size of the CORs and PNRs by rare-earth magnetic Gd-ion in PMN ceramic.

1. It is observed that dielectric constant maximum shifts to lower temperature with Gd-substitution. For any practical applicability, optimum Gd-ions substitution may be found in PMN-PT solid solution, so that temperature of dielectric maximum is around room temperature.
2. Compositional analysis of the PNRs and CORs in Gd-doped PMN using TEM should be carried out to know if the Gd-ion is present in the CORs. Temperature dependent bright and dark field image analysis will provide more insight to critical slowing down dynamic behaviour of the PNRs.
3. Higher Gd-ions concentration $x \geq 0.05$ in PMN is observed to occupy B-site along with A-site due to intermediate size of Gd^{3+} ion in comparison to Pb^{2+}/Mg^{2+}/Nb^{5+} ions. Magnetic correlation between Gd-ions should be examined when both A and B-site of the same lattice is occupied by the Gd-ion in suitable perovskite where second phase $GdNbO_4$ precipitation is minimal.

References

[1] K. Uchino, S. Nomura, L. E. Cross, S. J. Jang, and R. E. Newnham, J. Appl. Phys. 51, 1142 (1980); K. Uchino, Ferroelectrics 151, 321 (1994).

[2] L. E. Cross, Ferroelectrics 76, 241 (1987); Y. Yamashita, K. Harada, and S. Saitoh, Ferroelectrics 219, 29 (1998).

[3] A. A. Bokov and Z. -G. Ye, J. Mater. Sci. 41, 31 (2006); A. A. Bokov and Z.-G. Ye, J. Adv. Dielectrics 2[2], 1241010 (2012).

[4] P. Bonneau, P. Garnier, G. Calvarin, E. Husson, J. R. Cavarri, A. W. Hewat, and A. Morell, J. Solid State Chem. 91, 350 (1991).

[5] B. Hehlen, M. Al-Sabbagh, A. Al-Zein, J. Hlinka, Phys. Rev. Lett. 117, 155501 (2016).

[6] G. Xu, G. Shirane, J. R. D. Copley, P. M. Gehring, Phys. Rev. B 69, 064112 (2004).

[7] H. B. Krause, J. M. Cowley, J. Wheatley, Acta Crystallogr. Sect. A 35 (1979) 1015-1017.

[8] G. Burns and F. Dacol, Solid State Commun. 48[10] 853 (1983); G. Burns and F. Dacol, Solid State Commun. 58[9], 567 (1986).

[9] C. Stock, P. M. Gehring, H. Hiraka, I. Swainson, G. Xu, Z.-G. Ye, H. Luo, J.-F. Li, and D. Viehland, Phys. Rev. B 86, 104108 (2012).

[10] R.A. Cowley, S.N. Gvasaliyac, S.G. Lushnikov, B. Roessli and G.M. Rotaru, Advances in Phys. 60, 229 (2011).

[11] D. Fu, H. Taniguchi, M. Itoh, S.-ya Koshihara, N. Yamamoto, and S. Mori, Phys. Rev. Lett. 103, 207601 (2009); D. Fu, H. Taniguchi, M. Itoh, and S. Mori, in: Aime Pelaiz-Barranco (Ed.), Advancesin Ferroelectrics, InTech, 2015, ISBN 978-953-51-0885-6.

[12] J. Chen, H. M. Chan, and M. P. Harmer, J. Am. Ceram. Soc. 72[4], 593-598 (1989).

[13] Z. Xu, S. M. Gupta, D. Viehland, Y. Yan, and S. J. Pennycook, J. Am. Ceram. Soc. 83(1), 181-188 (2000).

[14] M. J. Cabral, S. Zhang, E. C. Dickey, and J. M. LeBeau, Appl. Phys. Lett. 112, 082901 (2018).

[15] C. Stock, R. J. Birgeneau, S. Wakimoto, J. S. Gardner, W. Chen, Z.-G. Ye, and G. Shirane, Phys. Rev. B 69, 094104 (2004).

[16] V. Westphal and W. Kleemann, and M. D. Glinchuk, Phys. Rev. Lett. 68, 847 (1992).

[17] E. V. Colla, E. Yu. Koroleva, N. M. Okuneva, S.B. Vakhrushev, Phys. Rev. Lett. 74[9], 1681-1684 (1995).

[18] Z.-G. Ye and H. Schmid, Ferroelectrics 145[1], 83-108 (1993).

[19] A. D. Hilton, D. J. Barber, C. A. Randall, T. R. Shrout, J. Mater. Sci. 25(8), 3461-3466 (1990).

[20] B.-K. Kim and S.-B. Cha, Mat. Res. Bull. 32[6], 743-747 (1997); B.-K. Kim, S.-B. Cha, and J.-W. Jang, Mater. Lett. 35[1-2], 1-3 (1998); B.-K. Kim, Mater. Sci. Eng. B 94, 102 (2002).

[21] K.-M. Lee, H. M. Jang, and W.-J. Park, J. of Mater. Res. 12, 1603-1613 (1997).

[22] O. Bidault, E. Husson, P. Gaucher, Philos. Mag. B 79[3], 435-448 (1999).

[23] H. Q. Fan, L. T. Zhanga, L. Y. Zhang, X. Yao, Solid State Commun. 111, 541-546 (1999).

[24] A. D. Hilton, C. A. Randall, D. J. Barber and T. R. Shrout, Ferroelectrics 93 (1989) 379-386.

[25] G. Singh, V. S. Tiwari, V. K. Wadhawan, Solid State Commun. 118[8], 407 (2001); G. Singh, Dielectric, Thermal and Structural Studies on $(1-x)Pb(Mg_{1/3}Nb_{2/3})O_3-xPbZrO_3$ Ferroelectric Ceramics, PhD thesis, Devi Aahilya Vishwavidyalaya (2007).

[26] W. Kleemann, Phys. Status Solidi B 251[10], 1993-2002 (2014).

[27] M. J. Krogstad, P. M. Gehring, S. Rosenkranz, R. Osborn, F. Ye, Y. Liu, J. P. C. Ruff, W. Chen, J. M. Wozniak, H. Luo, O. Chmaissem, Z.-G. Ye, and D. Phelan, Nat. Mater. 17, 718-724 (2018); H. Takenaka, I. Grinberg, and A. M. Rappe, Nat. Mater. 17, 657-658 (2018).

[28] M. Fiebig, T. Lottermoser, D. Meier, and M. Trassin, Nat. Rev. Mater. 1, 16046 (2016).

[29] E. A. Bikyashev, I. V. Lisnevskaya, and I. V. Zhorina, Inorganic Mater. 42, 1006 (2006).

[30] J. C. Anderson, Dielectric, Chapman and Hall Ltd., London (1964).

[31] L. L. Hench and J. K. West, Principles of Electronic Ceramics, Wiley, New York (1990).

[32] W. D. Kingery, H. K. Bowen and D.R. Uhlmann, Introduction to Ceramics, 2nd ed., John Wiley & Sons, New York (1926).

[33] P. Debye, Z. Phys. 13, 97 (1912); P. Debye, Polar Molecules, Dover, New York (1945).

[34] K. S. Cole and R. H. Cole, J. Chem. Phys. 9, 341 (1941).

[35] D. W. Davidson and R. H. Cole, J. Chem. Phys. 18, 1417 (1950).

[36] S. Havriliak and S. Negami, Polymer 8, 161-210 (1967).

[37] P. Kobeko, J. Kurtschatov, Zeit. Phys. 66, 192 (1930).

[38] T. Mitsiu, I. Tatsuzaki and E. Nakamura, An introduction to the physics of ferroelectrics, Gordon and Breach Science Publishers Ltd., London (1976).

[39] M. E. Lines and A. M. Glass, Principles and Applications of Ferroelectrics and Related Materials, Clarendon Press, Oxford (1977).

[40] A. J. Moulson and J. M. Herbert, Electroceramics, Wiley, London (2003).

[41] S. Blundell, Magnetism in Condensed Matter, Oxford University Press, New York (2001).

[42] N. A. Spaldin, Magnetic Materials, Fundamentals and Device Applications, Cambridge University Press, Cambridge, England (2003).

[43] H. Schmidt, Ferroelectrics 162, 317-338 (1994).

[44] M. Fiebig, J. Phys. D: Appl. Phys., 38[8], 123-158 (2005).

[45] W. Eerenstein, N. D. Mathur, and J. F. Scott, Nat. Rev. 442[17], 759-765 (2006).

[46] W. F Brown, R. M Hornreich, and S. Shtrikman, Phys. Rev., 168[2], 574-577 (1968).

[47] D. I. Khomskii, J. Magn. Magn. Mater. 306, 1 (2006); D. Khomskii, Phys. 2, 20 (2009).

[48] P. Ondrejkovi, Studies of Relaxor Ferroelectrics with Spontaneous Polar Nanoregions, PhD thesis, Institute of Physics of the Czech Academy of Sciences (2017).

[49] C. W. Ahn, C.-H. Hong, B.-Y. Choi, H.-P Kim, H.-S. Han, Y. Hwang, W. Jo, K. Wang, J.-F. Li, J.-S. Lee, and I. W. Kim, J. Kor. Phys. Soc. 68[12], 1481-1494 (2016).

[50] J. Hlinka, J. Adv. Dielectrics 2, 1241006 (2012).

[51] G. A. Smolenski and A. Agranovskaya, Sov. Phys. Solid State 1, 1429 (1960); V. A. Isupov, Sov. Phys. Solid State 5, 136 (1963); G. A. Smolenski, J. Phys. Soc. Jpn. 51, 4356 (1970).

[52] J. Bell, J. Phys.: Condens. Matter 5, 8773 (1993).

[53] V. Kirrillov and V. Isupov, Ferroelectrics 5, 3 (1973).

[54] D. Viehland, S. J. Jang, L. E. Cross, and M. Wuttig, J. Appl. Phys. 68, 2916 (1990); D. Viehland, J. F. Li, S. J. Jang, L. Eric Cross, and M. Wuttig, Phys. Rev. B 43[10], 8316 (1991).

[55] A. K. Tagantsev, Phys. Rev. Lett. 72[7], 1100-1103 (1994).

[56] A. K. Tagantsev and A. E. Glazounov, Phys. Rev. B 57, 18 (1998).

[57] T. Nattermann, in Spin Glasses and Random Fields, edited by A. P. Young, World Scientific, Singapore (1998).

[58] S.L.Swartz and T.R.Shrout, Mater, Res. Bull. 17[10], 1245-1250 (1982).

[59] A. H. Pandey, A.K. Srivastava, A.K. Sinha, and S.M. Gupta, Mater. Res. Express 2, 096303 (2015).

[60] P. J. Goodhew, J. Humphreys, and R. Beanland, Electron microscopy and analysis, 3rd ed., London and New York: Taylor & Francis (2000).

[61] D. B. Williams and C. B. Carter, Transmission Electron Microscopy: A Textbook for Materials Science Plenum, New York (1996).

[62] B. D. Cullity, Elements of x-ray difraction. Massachusetts: Company, Addison-Wesley Publishing (1956).

[63] R. A. Young, The Rietveld Method; International Union of Crystallography, Oxford University Press: New York (1995).

[64] C.N. Banwell, E.M. McCash, Fundamentals of Molecular Spectroscopy, 4th ed., Tata McCraw-Hill Publishing Co. Ltd (2000).

[65] B. D. Cullity, Introduction to Magnetic Materials, Addison Wesley, Reading, MA (1972).

[66] J. Petzelt, Ferroelectrics 400, 117-134 (2010).

[67] Z. Zhao, V. Buscaglia, M. Viviani, M. T. Buscaglia, L. Mitoseriu, A. Testino, M. Nygren, M. Johnsson, and P. Nanni, Phys. Rev. B 70, 024107 (2004).

[68] J. Carreaud, P. Gemeiner, J. M. Kiat, B. Dkhil, C. Bogicevic, T. Rojac, and B. Malic, Phys. Rev. B 72, 174115 (2005); J. Carreaud, C. Bogicevic, B. Dkhil, and J. M. Kiat, Appl. Phys. Lett. 92, 242902 (2008).

[69] R. Grigalaitis, M. Ivanov, J. Macutkevic, J. Banys, J. Carreaud, J. M. Kiat, V. V. Laguta, and B Zalar, J. Phys.: Condens. Matter 26, 272201 (2014).

[70] V. Bovtun, S. Kamba, S. Veljko, D. Nuzhnyy, J. Kroupa, M. Savinov, P. Vanek, J. Petzelt, J. Holc, M. Kosec, H. Amorin, and M. Alguero, Phys. Rev. B 79, 102111 (2009).

[71] A. Bhakar, A. H. Pandey, M. N. Singh, A. Upadhyay, A. K. Sinha, S. M. Gupta, T. Ganguli, and S. K. Rai, Acta Crystallogr. B 73, 1095-1104 (2017).

[72] C. Ghica, L. Nistor, and G. Van Tendeloo, J. Optoelectron. & Adv. Mat. 10(9), 2328-2333 (2008).

[73] A. D. Hilton, D. J. Barber, C. A. Randall, and T. R. Shrout, J. Mater. Sci. 25 (1990) 3461-3466.

[74] J. Chen, H. M. Chan, and M. P. Harmer, J. Am. Ceram. Soc. 72 (1989) 593-598.

[75] Y. Yan, S. J. Pennycook, Z. Xu, and D. Viehland, Appl. Phys. Lett. 72(24), 3145-3147 (1998).

[76] E. Husson, L. Abello, and A. Morell, Mater. Res. Bull. 25, 539-545 (1990).

[77] O. Svitelskiy, J. Toulouse, G. Yong, and Z.-G. Ye, Phys. Rev. B 68, 104107 (2003).

[78] A. Slodezyk, P. Daniel, and A. Kania, Phys. Rev. B 77, 184114 (2008).

[79] A. H. Pandey, V.G. Sathe, and Surya M. Gupta, J. of Alloys and Comp. 682, 182-187 (2016).

[80] T. Li, J. Liu, H. Li, and Y. Xu, J. Mater. Sci. Mater. Electron. 22, 1188-1194 (2011).

[81] F. Jiang, S. Kojima, C. Zhao, and C. Feng, J. Appl. Phys. 88, 3608-3612 (2000); F. Jiang, S. Kojima, C. Zhao, and C. Feng, Appl. Phys. Lett. 79, 3938-3940 (2001).

[82] N. Waeselmann, B. Mihailova, M. Gospodinov, and U. Bismayer, J. Phys.: Condens. Matter 25, 155902 (2013).

[83] B. Mihailova, U. Bismayer, B. G. Uttler, M. Gospodinov, and L. Konstantinov, J. Phys.: Condens. Matter 14, 1091-1105 (2002).

[84] D. Viehland, S. J. Jang , L. E. Cross, and M. Wutting, Phys. Rev. B 46, 8003 (1992).

[85] A. A. Bokov and Z.-G. Ye, Solid State Comm. 116(2), 105-108 (2000); A. A. Bokov, Y.-H. Bing, W. Chen, Z.-G. Ye, S. A. Bogatina, I. P. Raevski, S. I. Raevskaya, and E. V. Sahkar, Phys. Rev. B 68, 052102 (2003).

[86] D. F. Rushman and M. A. Striven, Proc. Phys. Soc. 59(6), 1011-1016 (1947).

[87] K. Lichtenecker, Phys. Z. 10, 1005 (1909); Y. Wu, X. Zhao, F. Li, and Z. Fan, J. of Electroceram. 11, 227-239 (2003).

[88] Z.-Y. Cheng, L.-Y. Zhang, and X. Yao, J. Appl. Phys.79, 8615–9 (1996); Z.-Y. Cheng, L.-Y. Zhang, and X. Yao, J. Appl. Phys. 80 5518 (1996); Z.-Y. Cheng, R. S. Katiyar, X. Yao, and A. Guo, Phys. Rev.B 55, 8165-8174 1997.

[89] V. V. Shvartsman, J. Dec, Z. K. Xu, J. Banys, P. Keburis, and W. Kleemann, Phase Trans. 81[11-12], 1013-1021 (2008); W. Kleemann, S. Miga, J. Dec, and J. Zhai, Appl. Phys. Lett. 102, 232907 (2013).

[90] A. Levstik, Z. Kutnjak, C. Filipic, and R. Pirc, Phys. Rev. 57[18], 11204-11211 (1998).

[91] W. Kleeman and J. Dec, Phys. Rev. B 94, 174203 (2016).

[92] J. A. Mydosh, Spin Glasses: An Experimental Introduction, Vol. 125, Taylor & Francies, London, (1993).

[93] J. Macutkevic, S. Kamba, J. Banys, A. Brilingas, A. Pashkin, J. Petzelt, K. Bormanis, and A. Sternberg, Phys. Rev. B 74, 227-239 (2006).

[94] A. K. Jonscher, Dielectric Relaxation in solids, Chelsea Dielectrics Press in London (1983).

[95] D. Jonhson, Software Zview- v.2.3d, Scribner Associates, Inc. (2000).

[96] S. Rachna, S. Bhattacharyya, and S. M. Gupta, J. of Phys. and Chem. of Solids 69, 822-829 (2008).

[97] E. V. Colla, E. Yu. Koroleva, N. M. Okuneva, and S.B. Vakhrushev, Phys. Rev. Lett. 74[9], 1681-1684 (1995).

[98] D. Wang, X. Ke, Y. Wang, J. Gao, Y. Wang, L. Zhang, S. Yang, and X. Ren, Phys. Rev. B 86, 054120 (2012).

[99] F. Li, S. Zhang, T. Yang, Z. Xu, N. Zhang, G. Liu, J. Wang, J. Wang, Z. Cheng, Z. Ye, J. Luo, T.R. Shrout, and L. Chen, Nat. Commun. 7, 13807 (2016).

[100] P. K. Davies and M. A. Akbas, J. Phys. Chem. Solids 61, 159 (2000).

[101] D. M. Fanning, I. K. Robinson, S. T. Jung, E. V. Colla, D. D. Viehland, and D. A. Payne, J. Appl. Phys. 87[2], 840-848 (2000).

[102] A. S. Deliormanls, E. Celik, and M. Polat, J. Mater. Sci.: Mater. Electro 19[6], 577-583 (2008).

[103] J. R. Zhang, Y. C. Zhang, C. J. Lu, W. N. Ye, and J. Su, J Mater. Sci.: Mater. Electron. 25, 653-658 (2014).

[104] N. Zhong, P.-H. Xiang, D.-Z. Sun, and X.-L. Dong, Mater. Sci. Eng. B 116[2], 140-145 (2005).

[105] A. H. Pandey, S. M. Gupta, N. P. Lalla, and A. K. Nigam, J. of Appl. Phys. 122, 044101 (2017).

[106] X. Zhao, W. Qu, X. Tan, A. A. Bokov, and Z.-G. Ye, Phys. Rev. B 75, 104106 (2007).

[107] A. H. Pandey, S. M. Gupta, V. G. Sathe, and N. P. Lalla, Unpublished (2018).

[108] S. M. Gupta and D. Viehland, J. Appl. Phys. 80, 5875 (1996); S. M. Gupta and D. Viehland, J. Am. Ceram. Soc. 80(2), 477 (1997).

[109] A. Bhakar, A. H. Pandey, M. N. Singh, A. Upadhyay, A. K. Sinha, S. M. Gupta, and T. Ganguli, Acta Crystallogr. B 72(3), 404 (2016).

[110] G. Singh and V. S. Tiwari, J. Appl. Phys. 101, 014115 (2007).

[111] I. G. Siny, R.S. Katiyar, Ferroelectrics 223, 35-42 (1999).

[112] H. Idink, W. White, J. Appl. Phys. 76, 1789-1793 (1994).

[113] A. A. Bokov, B. J. Rodriguez, X. Zhao, J.-H. Ko, S. Jesse, X. Long, W. Qu, T. H. Kim, J. D. Budai, A. N. Morozovska, S. Kojima, X. Tan, S. V. Kalinin, and Z.-G. Ye, Z. Kristallogr. 226, 99 (2011).

[114] L.-J. Lin and T.-B. Wu, J. Am. Ceram. Soc. 73, 1253 (1990).

[115] A. Sakar-Deliormanli, E. Celik, and M. Polat, J. Mater. Sci: Mater. Electron. 19, 577 (2008).

[116] C. Stock, L. Van Eijck, P. Fouquet, M. Maccarini, P. M. Gehring, G. Xu, H. Luo, X. Zhao, J.-F. Li, and D. Viehland, Phys. Rev. B 81, 144127 (2010).

[117] M. A. Akbas and P. K. Davies, J. Am. Ceram. Soc. 81(8), 2205 (1998); Y. Yan, S. J. Pennycook, Z. Xu, and D. Viehland, Appl. Phys. Lett. 72, 3145 (1998); J. K. Montgomery, M. A. Akbas, and P. K. Davies, J. Am. Ceram. Soc. 82(12), 3481 (1999).

[118] L. Pdungsap, S. Boonyeun, P. Winotai, N. Udomkan, and P. Limsuwan, Eur. Phys. J. B 48, 367 (2005).

[119] S. K. S. Parashar, R. N. P. Choudhary, and B. S. Murty, Mater. Sci. Eng. B 110, 58 (2004).

[120] X. Zhao, W. Qu, X. Tan, A. A. Bokov, and Z.-G. Ye, Phys. Rev. B 79, 144101 (2009).

[121] A. Kumar, R.P. Tandon, and V.P.S. Awana, Eur. Phys. J. B 85, 238 (2012); A. Kumar, R. P. Tandon, and V. P. S. Awana, J. Appl. Phys. 110, 043926 (2011).

[122] W. Kleemann, J. Dec, S. Miga, and D. Rytz, Z. Kristallogr. 226, 145 (2011).

[123] T. Correia and Q. Zhang (eds.), Electrocaloric Materials, Engineering Materials 34, Springer-Verlag Berlin Heidelberg (2014).

[124] A.S. Mischenko, Q. Zhang, J.F. Scott, R.W. Whatmore, and N.D. Mathur, Science 311 (5765), 1270 (2006).

[125] B. Neese, B. Chu, S.-G. Lu, Y. Wang, E. Furman, and Q.M. Zhang, Science 321 (5890), 821 (2008).

[126] D. Saranya, A. R. Chaudhuri, J. Parui, S. Krupanidhi, Bull. Mater. Sci. 32, 259 (2009).

[127] G. Singh, and V. S. Tiwari, J. of Alloys Compnds. 523, 30 (2012); G. Singh, V. S. Tiwari, and P. K. Gupta, Appl. Phys. Lett. 103, 202903 (2013); G. Singh, I. Bhaumik, S. Ganesamoorthy, R. Bhatt, A. K. Karnal, V. S. Tiwari, and P. K. Gupta, Appl. Phys. Lett 102, 082902 (2013).

[128] S. K. Upadhyay, V. R. Reddy, P. Bag, R. Rawat, S. M. Gupta, and A. Gupta, Appl. Phys. Lett. 105, 112907 (2014).

[129] B. Asbani, J.-L. Dellis, A. Lahmar, M. Courty, M. Amjoud, Y. Gagou, K. Djellab, D. Mezzane, Z. Kutnjak, and M. El Marssi, Appl. Phys. Lett. 106, 042902 (2015).

[130] Y. Bai, X. Han, X.-C. Zheng, & L. Qiao, Sci. Rep. 3, 2895 (2013).

[131] Y. Bai, G. Zheng, and S. Shi, Appl. Phys. Lett. 96, 192902 (2010); Y. Bai, G.-P. Zheng, and S.-Q. Shi, Mat. Res. Bull. 46, 1866 (2011).

[132] J. Perantie, J. Hagberg, A. Uusimäki, and H. Jantunen, Phys. Rev. B 82, 134119 (2010).

[133] S. Uddin, G.-P. Zheng, Y. Iqbal, R. Ubic, and J. Yang, J. of Appl. Phys. 114, 213519 (2013); G.-P. Zheng, S. Uddin, X. Zheng, J. Yang, J. of Alloy. Comp. 663, 249 (2016).

[134] B. Li, J. B. Wang, X.L. Zhong, F. Wang, Y. K. Zeng, and Y.C. Zhou, Eur. Phys. Lett. 102, 47004 (2013).

[135] W. P. Cao, W. L. Li, D. Xu , Y. F. Hou, W. Wang, and W. D. Fei, Cerm. International 40, 9273–9278 (2014); W. P. Cao, W.L. Li, X.F. Dai, T. D. Zhang, J. Sheng, Y. F. Hou, W. D. Fei, J. of Eur. Cerm. Soc. 36, 593 (2016).

[136] W. Geng, Y. Liu, X. Meng, L. Bellaiche, J.F. Scott, B. Dkhil, and A. Jiang, Adv. Mater. 27 (20), 3165 (2015).

[137] A. Chauhan, S. Patel, and R. Vaish, Acta Mater. 89, 384 (2015).

[138] I. Bhaumik, S. Ganesamoorthy, R. Bhatt, A.K. Karnal, P.K. Gupta, S. Takekawa, and K. Kitamura, Eur. Phys. Lett. 107, 47001 (2014).

[139] F. Zhuo, Q. Li, J. Gao, Y. Wang, Q. Yan, Y. Zhang, X. Xi, X. Chu, and W. Cao, Appl. Phys. Lett. 108, 082904 (2016); F. Zhuo, Q. Li, H. Qiao, Q. Yan, Y. Zhang, X. Xi, X. Chu, X. Long, and W. Cao, Appl. Phys. Lett. 112, 133901 (2018).

[140] G. Vats, A. Kumar, N. Ortega, C.R. Bowen, and R.S. Katiyar, Energy Environ. Sci. 9, 1335 (2016).

[141] R. Pirc, B. Rozic, J. Koruza, B. Malic, and Z. Kutnjak, Eur. Phys. Lett. 107, 17002 (2014).

[142] A. Pelaiz-Barranco, F. Calderon-Pinar, and Y. Mendez-Gonzalez, J. Adv. Dielect. 06, 1620002 (2016).

[143] Z. Xu, Z. Fan, X. Liu, and X. Tan, Appl. Phys. Lett. 110, 082901 (2017).

[144] Q. Lia, J. Wanga, L. Maa, H. Fana, and Z. Li, Mater. Res. Bull. 76, 57-61 (2016).

[145] G. Ramesh, M.S. Ramachandra Rao, V. Sivasubramanian, and V. Subramanian, J. of Alloys and Comp. 663, 444-448 (2016).

[146] E. Birks, M. Dunce, J. Perantie, J. Hagberg, and A. Sternberg, J. of Appl. Phys. 121, 224102 (2017).

[147] T. Zhang, W. Li, Y. Hou, Y. Yu, W. Cao, Y. Fenga, and W. Fei, RSC Adv. 6, 71934-71939 (2016).

[148] H. H. Wu, J. Zhu, and T. Y. Zhang, Phys. Chem. Chem. Phys. 17, 23897 (2015).

[149] Z.-H. Niua, Y.-P. Jianga, X.-G. Tanga, Q.-X. Liua, W.-H. Lia, X.-W Linb, and S.-G. Lub, Mater. Res. Lett. 6(7), 384-389 (2018).

[150] F. Le Goupil, A. Berenov, A.-K. Axelsson, M. Valant, and N. McN. Alford, J. of Appl. Phys. 111, 124109 (2012); A.-K. Axelsson, F. Le Goupil, L.J. Dunne, G. Manos, M. Valant, and N. McN. Alford, Appl. Phys. Lett. 102, 102902 (2013).

[151] Y. Liu, J.F. Scott, and B. Dkhil, Appl. Phys. Reviews 3, 031102 (2016).

[152] I. Ponomareva and S. Lisenkov, Phys. Rev. Lett. 108, 167604 (2012).

[153] M. Zannen, A. Lahmar, Z. Kutnjak, J. Belhadi, H. Khemakhem, M. El Marssi, Solid State Sci. 66, 31-37 (2017).

[154] K. Li, X.L. Zhu, X.Q. Liu, and X.M. Chen, J. of Appl. Phys. 114, 044106 (2013); K. Li, X.L. Zhu, X.Q. Liu, and X.M. Chen, Appl. Phys. Lett. 102, 112912 (2013); C.J. Huang, K. Li, S.Y. Wu, X.L. Zhu, X.M. Chen, Journal of Materms 1, 146 (2015).

[155] B. Rozic , B. Malic, H. Ursic, J. Holc, M. Kosec, and Z. Kutnjak, Ferroelectrics 421, 103-107 (2011); B. Rozic, M. Kosec, H. Ursic, J. Holc, B. Malic, Q.M. Zhang, R. Blinc, R. Pirc, and Z. Kutjnak, J. of Appl. Phys. 110, 0644118 (2011).

[156] W. Kleemann, P. Borisov, S. Bedanta, and V. Shvartsman, IEEE Trans. Ultrason. Ferroelectr. Freq. Control 57, 2228 (2010); W. Kleemann, S. Bedanta, P. Borisov, V. V. Shvartsman, S. Miga, J. Dec, A. Tkach, and P. M. Vilarinho, Eur. Phys. J. B 71, 407 (2009).

[157] V. V. Shvartsman, S. Bedanta, P. Borisov, W. Kleemann, A. Tkach, and P. M. Vilarinho, J. Appl. Phys. 107, 103926 (2010).

[158] V. V. Shvartsman, S. Bedanta, P. Borisov, W. Kleemann, A. Tkach, and P. M. Vilarinho, Phys. Rev. Lett. 101, 165704 (2008).

[159] G. Amoretti and J. M. Fournier, J. Mag. and Mag. Mater. 43, 217-220 (1984).

[160] B. Sitharaman, B. D. Jacobson, Yo. Z. Wadghiri, H. Bryant, and J. Frank, J. Appl. Phys. 113, 134308 (2013).

[161] U. S. Alaan, P Shafer, A. T. N'Diaye, E. Arenholz, and Y. Suzuki, Appl. Phys. Lett. 108, 042106 (2016).

[162] K. Binder and A. P. Young,Rev. Mod. Phys.58, 801 (1986).

[163] E. V. Colla, L. K. Chao, M. B. Weissman, and D. D. Viehland, Phys. Rev. Lett. 85[14], 3033-3036 (2000).

[164] O. Kircher and R. Bohmer, Eur. Phys. J. B 26, 329 (2002).

[165] A. I. Agranovskaya, Akad. Nauk Izvestiya, Physical Ser. 24, 1275 (1960); V. A. Bokov, I. E. Mylnikova, Sov. Phys. Solid State (Eng. Transl.) 2, 2428 (1961).

[166] B. A. Malkov and Yu N. Venevtsev, Izv. Akad. Nauk Neorg. Mater. 13, 1468 (1977).

[167] E. A. Popova, V. G. Zalessky, T. A. Shaplygina, S. N. Gvasaliya, S. G. Lushnikov, and S. V. Krivovichev, Ferroelectrics 412, 15-22 (2011).

[168] H. Singh, H. Ghosh, T. V. Chandrasekhar Rao, A. K. Sinha, and P. Rajput, J. Appl. Phys. 116, 214106 (2014).

[169] T. Hachigat, S. FujimotoS, and N. Yasuda,J. Phys. D: Appl. Phys. 20, 1291-1296 (1987).

[170] Preeti, Adityanarayan Pandey, Rachna Selvamani, Chander Shekhar, and S. M. Gupta, Ferroelectrics 517, 1-7 (2017).

[171] E. Iguchi, K. Ueda, and W. H. Jung, Phys. Rev. B 54[24], 17431-17437 (1996).

[172] Yu. N. Venevtsev, E. D. Politova, and S. A. Ivanov, Ferro- and antiferroelectrics of the barium titanate family, Moscow, Khimiya, 1985, 256 (in Russian).

[173] Shravani Chillal, PhD thesis, Microscopic Coexistence of Antiferromagnetic and Spin glass States in Disordered Perovskites, ETH Zurich (2015).

[174] M. Sikora, Cz. Kapusta, K. Knızek, Z. Jirak, C. Autret, M. Borowiec, C. J. Oates, V. Prochazka, D. Rybicki, and D. Zajac, Phys. Rev. B 73, 094426 (2006).

[175] G. Vanko, J. Rueff, A. Mattila, Z. Nemeth, and A. Shukla, Phys. Rev. B 73, 024424 (2006).

[176] X. Zuo, J. Yang, B. Yuan, D. Song, X. Tang, K. Zhang, X. Zhu, W. Song, J. Dai, and Y. Sun, RSC Adv. 4, 46704 (2104).

[177] L. Yu Wang, Q. Li, Y. Y. Gong, D. H. Wang†, Q. Qi Cao, and Y. W. Du, J. Am. Ceram. Soc. 97[7], 2024-2026 (2014).

[178] N. Imamura, M. Karppinen, T. Motohashi, D. Fu, M. Itoh, and H. Yamauchi, J. Am. Chem. Soc. 130, 14948-14949 (2008).